Primary open-angle glaucoma: on the development of novel therapeutic approaches

A Thesis Submitted to Trinity College Dublin for the Degree of Doctor of Philosophy

by Darragh Crosbie

Supervised by Professor Peter Humphries

Smurfit Institute of Genetics

Trinity College Dublin

September 2017

Declaration

I declare that this thesis has not been submitted as an exercise for a degree at this or any other university and it is entirely my own work except where noted. I agree to deposit this thesis in the University's open access institutional repository or allow the Library to do so on my behalf, subject to Irish Copyright Legislation and Trinity College Library conditions of use and acknowledgement.

Signed:

Acknowledgements

I would like to take this opportunity to thank every person that has helped me throughout the course of my PhD study. Firstly, to Prof. Pete Humphries, thank you so much for the opportunity to embark on this challenging project and for your continued support. I am also hugely grateful to Dr. Lawrence Tam who offered continued guidance throughout this project, meeting any stumbling blocks along the way. Special thanks to Dr Sophie Kiang, Dr Marian Humphries, Dr. Ester Reina-Torres, Dr Matthew Campbell, and Dr James Keaney. In particular to James for guidance early on in my studies and for contributing hugely to the MRI project. I must offer sincere thanks to Marian for developing any AAV constructs and offering her expertise in any PCR related problems, and Sophie for looking out for me ever since I entered the lab. To Dr. Paul Kenna I offer my gratitude for any help with animal work, and thanks to all those working in the animal unit Dave, Charlie and Caroline for taking care of my animals. I would like to thank Rustam Rakhmatullin and Christian Kerskens, who run the mouse MRI facility. This work was greatly helped by our collaborators, Prof Colm O'Brien, Dr. Darryl Overby, Dr. Joseph Sherwood, Prof. Daniel Stamer, and Kristin Perkumas. Dr. Joseph Sherwood established the eye perfusion system for our group and Prof. Daniel Stamer supplied primary human cells with the help of Kristin Perkumas.

To all my friends I must offer thanks for keeping life fun throughout my PhD studies. Firstly to Paul, Jeff we had some adventures and some fantastic photoshoots. Thanks to all my friends on the third floor, we've had some great chats at coffee: Danny, Adrian, Killian, Ciara, and Natalie. To all those running partners and tag teammates, thanks for keeping me somewhat in shape: Darragh, Evan, Eric, Lara, Bennett, and Russell. Thanks to all my other friends at home and abroad: George, Roger, Leanne, Micheal, and Cormac. Finally a big thank you to all my family for never letting me get a big head, and to my girlfriend Cecilia who constantly puts up with me and with whom I can never remain worried or to serious.

Summary

Glaucoma is one of the most prevalent forms of preventable blindness, affecting more than 60 million people worldwide. While normotensive forms of the disease do exist, the majority of cases are caused by elevations in intraocular pressure. The open-angle form of the disease is the most common and the primary standard of care is the use of topically-applied pressure reducing medications. Such medications work either by slowing down the production of aqueous humour, or increasing its outflow from the eye. Interestingly, none of these medications target the major route of aqueous humour outflow, the conventional outflow pathway, comprised of the trabecular meshwork and Schlemm's canal. Current therapies often fail to meet adequate IOP reduction and surgical intervention is required in these cases, which can result in significant side effects. There is, therefore, a distinct unmet clinical need for therapies primarily targeting the conventional outflow pathway and the work presented in this thesis directly addresses this issue using the mouse as an animal model.

Chapter 2 (after the general introduction of Chapter 1) describes work in which tight junctions of the eye are studied as targets for glaucoma therapy. The inner wall of SC is an intact barrier joined by tight junctions that contributes to AH outflow resistance (Overby et al. 2009). The tight junction components joining SC endothelial cells were characterized in *in vitro* and *in vivo* studies in human, primate and mouse with a view to then down-regulating these via siRNA delivery to the mouse AC (results of overall project reported in Tam et al., (2017). Furthermore, a similar approach was used down-regulate claudin-5 and occludin tight junction proteins in endothelial cells of the inner retina in the DBA/2J glaucoma mouse, resulting in increased clearance of soluble amyloid-β (1-40) from the ganglion cell layer.

Adeno-associated viruses (AAV) are vectors that offer long-term transgene expression with little immunogenicity (Daya & Berns 2008). In Chapter 3 the transduction efficacies of six different AAV pseudotypes were examined in the mouse AC. Very little eGFP expression was found in the mouse outflow tissues, in contrast to studies in other species (Buie et al. 2010a). However, AAV-2/9 was found to widely transduce the mouse corneal endothelium, offering a reservoir to introduce soluble recombinant proteins to the AH and hence to the outflow tissues.

As part of a group effort, this virus was further used to deliver MMP-3 to the outflow pathway, enhancing aqueous humour outflow, as reported in O'Callaghan, Crosbie, et al. (2017). Increased plasminogen activator inhibitor-1 (PAI-1) levels were observed in POAG patient AH. PAI-1 is a downstream effector of TGF-β2, which has a role in glaucomatous pathogenesis (Fuchshofer & Tamm 2012). PAI-1 increased the trans-endothelial electrical resistance across both SC endothelial cell (SCEC) and TM cell monolayers, increasing ECM deposition and cell contractility. Previously, virally expressed TGF-β2 has been used to create a mouse model of glaucoma (Shepard et al. 2010), and so mouse recombinant PAI-1 was placed into the AAV-2/9 vector and expressed from the mouse corneal endothelium with the goal of creating a novel glaucoma model. After 12-weeks no increase in IOP or decrease in outflow facility was evident in AAV-PAI-1treated eyes, potentially due to low PAI-1 secretion.

Assessment of AH dynamics in a model is important in novel treatment discovery. Magnetic resonance imaging (MRI) is a non-invasive technique that allows real-time measurement of morphology and fluid movement (Townsend et al. 2008). Chapter 4 reports data on the use of MRI to evaluate the glaucoma mouse eye. The effect of the glaucoma medication, latanoporst, was measured using Gd-MRI, with treated eyes displaying enhanced clearance of contrast agent. Age-related changes in aqueous humour dynamics, morphology and blood-aqueous barrier integrity were detected in the DBA/2J pigmentary glaucoma mouse model. Use of MRI in this scenario is in its infancy, and the results obtained clearly indicate a great potential for the use of this technique in glaucoma research.

Hopefully, these approaches will be of use in development of clinical therapies, targeting those large numbers of individuals currently resistant to conventional medications.

Table of contents

Abbreviations

AAV	Adeno-associated virus
AAV-null	AAV2/9 with no transgene
AAV-PAI-1	AAV2/9 with mouse PAI-1 transgene
AAV2/2	AAV with AAV2 genome and AAV2 capsid
AAV2/5	AAV with AAV2 genome and AAV5 capsid
AAV2/9	AAV with AAV2 genome and AAV9 capsid
AV	Adenovirus
AC	Anterior chamber
AH	Aqueous humour
ALT	Argon laser trabeculoplasty
AMD	Age-related macular degeneration
APP	Amyloid precursor protein
AV	Adenovirus
Aβ	Amyloid-beta
BBB	Blood-brain barrier
BOLD	Blood oxygenation level dependent
BRB	Blood-retinal barrier
CAI	Carbonic anhydrase inhibitors
CB	Ciliary body
CNV	Choroidal neovascularisation
C_r	Reference facility
CTGF	Connective tissue growth factor
DN	Double negative
DP	Double positive
dsDNA	Double-stranded deoxyribonucleic acid
FACS	Fuorescence-activated cell sorting
FSC-A	Forward scatter area

FSC-W	Forward scatter width
GAG	Glycosaminoglycan
Gd-BOPTA	Gadobentate dimeglumine
Gd-DTPA	Gadopentetic acid
Gd-MRI	Gadolinium enhanced MRI
GV	Giant vacuoles
H&E	Hematoxylin and eosin
ICAM-1	Intercellular adhesion molecule-1
indAAV2/9	AAV2/9 with a doxycycline inducible promoter
IOP	Intraocular pressure
ITR	Inverted terminal repeat
JAM	Junctional adhesion molecule
JCT	Juxtacanalicular tissue
LLC	Large latent complex
MAD	Median absolute dispersion
MRI	Magnetic resonance imaging
MSP1	Mucopolysaccharidosis type I
NMDA	N-methyl-D-aspartate
NTG	Normal tension glaucoma
ONL	Outer nuclear layer
OCT	Optical coherence tomography
PACG	Primary angle closure glaucoma
PAI-1	Plasminogen activator inhibitor-1
PI	Propidium iodide
POAG	Primary open angle glaucoma
PXG	Pseudoexfoliative glaucoma
rAAV	recombinant Adeno-associated virus
RGC	Retinal ganglion cell
RPE	Retinal pigment epithelium
RT-PCR	Real-time polymerase chain reaction
SC	Schlemm's canal
scAAV	Self-complementary adeno-associated

	virus
scAAV2/2	scAAV with scAAV2 genome and AAV2 capsid
scAAV2/5	scAAV with scAAV2 genome and AAV5 capsid
scAAV2/9	scAAV with scAAV2 genome and AAV9 capsid
SCEC	Schlemm's canal endothelial cell
SLT	Selective laser trabeculoplasty
SPARC	Secreted protein acidic and rich in cysteine
SSC-A	Side scatter area
SSC-W	Side scatter width
ssDNA	Single-stranded deoxyribonucleic acid
t-PA	Tissue plasminogen activator
TGF-β2	Transforming growth factor-β2
TJ	Tight juncion
TUNEL	Terminal deoxynucleotidyl transferase dUTP nick-end labeling
u-PA	Urokinase plasminogen activator
ZO-1	Zonula occludens-1
ZONAB	Zolnula occludens-1 associated nucleic acid binding protein

Chapter 1

General Introduction

Chapter 1: General Introduction

Glaucoma is a progressive optic neuropathy that accounts for 2.1 million cases of blindness worldwide. The most common form of glaucoma is primary open angle glaucoma (POAG), which is characterized by glaucomatous retinal damage with an open iridocorneal angle. In POAG the major risk factor is increased intraocular pressure (IOP), caused by a dysregulation in aqueous humour (AH) production and drainage (Bourne et al. 2016; Tham et al. 2014; Braunger et al. 2015). AH drainage occurs via two pathways, the uveoscleral and the conventional pathway. Drainage of AH occurs primarily through the conventional outflow pathway with a smaller fraction of AH outflow draining through the uveoscleral pathway. The fraction of uveoscleral drainage decreases with age (Goel et al. 2010). Despite this, the majority of current glaucoma therapies that increase AH outflow primarily target the uveoscleral pathway.

The overall focus of this thesis has been to explore, through murine systems, concepts relating to the discovery of novel glaucoma therapies that target the conventional AH outflow pathway. In this introductory chapter, the prevalence of glaucoma worldwide is outlined, together with an overview of different clinical forms of disease. The regulation of AH homeostasis that controls IOP is discussed, along with a detailed appraisal of the anatomy and structure of the conventional outflow pathway. Resistance to outflow facility is key in increased IOP, and therefore the role of the tissues of the conventional outflow pathway in resistance generation is explored. Use of animal models in glaucoma is central to understanding biological reactions to IOP- lowering therapies, and the suitability of the mouse as a model is covered. The final section of this introduction focuses on current therapies, their efficacies and modes of action, along with recent progress in the development of novel glaucoma medications.

Global blindness and glaucoma

In 2010 it was estimated that some 223 million people suffer from visual impairment globally. This can be separated into moderate and severe vision impairment affecting 191 million people, and blindness, affecting 32.4 million. A large proportion of those with vision impairment or blindness, 65% and 76% respectively, are afflicted by a preventable or treatable cause. Avoidable vision loss

is defined as any visual impairment caused by cataract, uncorrected refractive error, trachoma, glaucoma or diabetic retinopathy. Cataract is the leading cause of blindness worldwide, being responsible for 33.4% of recorded blindness, with uncorrected refractive error being the second largest cause. Both of these are largely preventable by surgery in the case of cataract, and by spectacles, contact lenses and refractive surgery in relation to uncorrected refractive error and hence these conditions are more prevalent in the developing world where there is less access to medical intervention. Outside of these, glaucoma is the next leading cause of preventable blindness, responsible for 6.6% of global blindness – more in fact than trachoma and diabetic retinopathy combined. From 1990 to 2010 the number of cases of blindness caused by cataract reduced from 12.3 to 10.8 million. In contrast, the proportion of people affected by glaucoma rose from 4.4% to 6.6%, relating to an increase from 1.3 million in 1990 to 2.1 million cases in 2010 (Bourne et al. 2013; Bourne et al. 2016; Congdon 2003). The number of patients presenting with glaucoma in 2013 was estimated at 64 million, predicted possibly to increase to 112 million by 2040, most of these increases being attributable to Asia and Africa (Tham et al. 2014).

Overview of glaucoma

Glaucomatous optic neuropathies

The term glaucoma refers to a diverse group of diseases that are associated with characteristic structural deformation at the optic nerve head that may lead to progressive retinal ganglion cell (RGC) death. When left untreated glaucoma typically leads to chronic, progressive, and irreversible visual field loss, which can result in tunnel vision and, finally, loss of central vision (Gupta & Chen 2016). Glaucomatous optic neuropathies are generally defined by optic disc abnormalities such as cup/disc ratio (CDR) asymmetry and characteristic visual field defects (**Fig. 1.1**); they are often associated with high IOP, one of the greatest risk factors linked to glaucoma (Sun et al. 2017). Normal IOP is controlled by the balance of AH production by the ciliary processes and drainage through Schlemm's canal (SC) and uveoscleral routes, and is generally between 12-22mmHg. High IOP is a result of the dysregulation of these two processes. Broadly, glaucoma is split into two

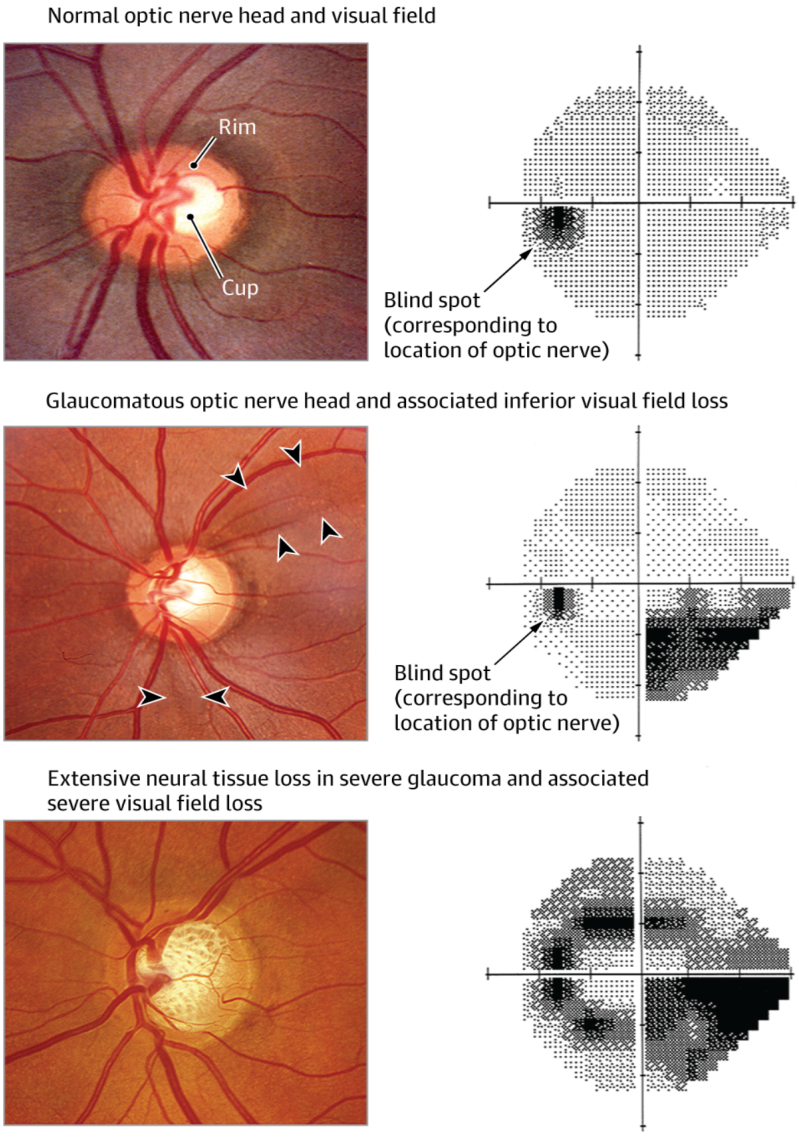

Fig. 1.1. Normal, glaucomatous, and severe glaucomatous optic nerve heads and visual field tests.

In the normal optic nerve head the pink area of neural tissue forms the neuroretinal rim and the empty central space is the 'cup'. In the glaucomatous optic nerve head the retinal rim is thinning, with cup enlargement. The arrowheads point to retinal nerve fibre layer defect, which appears as a wedge-shaped dark area emanating from the optic nerve head. The superior neural loss corresponds to the inferior defect (black scotoma) seen on the visual field. In the severe glaucomatous eye there is more extensive neural loss with severe reduction of the neuroretinal rim, and cup enlargement, with considerable visual field loss in both the superior and inferior hemifield. Image taken from Weinreb et al. (2014).

main categories; open- and closed- angle. With open-angle glaucoma the iridocorneal angle is unobstructed, whereas in closed-angle glaucoma the angle is obscured by the iris, blocking the outflow tissues (**Fig. 1.2.b-c**). Both of open-angle and closed-angle glaucoma can occur as primary or secondary conditions (Leske 2007).

The global prevalence of glaucoma is 3.54% with 3% of this consisting of patients with primary open angle glaucoma (POAG) and 0.5% patients with primary angle closure glaucoma (PACG). Regional analysis of glaucoma shows that the highest prevalence of POAG is found in Africa (4.79%) and of PACG in Asia (1.09%). Similarly, between ethnic groups, prevalence of POAG is highest in those of African ancestry (5.40%) and PACG prevalence is highest in people of Asian ancestry (1.20%) (Tham et al. 2014). Clinically, in closed angle glaucoma the AC angle is occluded around more than 180° of the circumference of the eye causing a severe rise in IOP. In the case of acute angle closure, patients experience a sharp increase in IOP, that can lead to sudden and painful loss of vision, which can be accompanied by nausea and vomiting due to the iris completely covering the entire trabecular meshwork (Gupta & Chen 2016).These individuals must get immediate medical intervention to avoid permanent vision loss. PACG has a high prevalence among Asian populations and risk factors include: small cornea, shallow AC, thick lens, anteriorly shifted lens position and short axial length (Sun et al. 2017). In the majority of cases angle closure is caused by pupillary block. Briefly, increased resistance at the iris-lens junction to the flow of AH from the posterior to the anterior chamber forms a pressure gradient across the iris and ultimately results in forward bowing of the iris and AC angle closure (**Fig. 1.2c**).

Other causes are termed non-pupillary blocking. Examples are anteriorly rotated ciliary processes and plateau iris, both of which cause the base of the ciliary process to crowd the outflow tissues or via iris crowding mechanisms not associated with a posterior-anterior pressure gradient. In Asian populations it has been estimated that the majority of the cases of angle closure glaucoma result from multiple mechanisms with varying combinations of pupillary block, ciliary body rotation and iris crowding (Sun et al. 2017). In comparison, POAG, which occurs at a higher prevalence in the population, has no physical obstruction at the AC angle. Patients with POAG show an increased resistance to AH outflow that generally

results in increased IOP, ocular deformation and RGC death. Though primary congenital and juvenile forms of POAG exist, the most common form is adult onset (>35 years); a chronic disease that is often linked with high IOP. However, in some cases the disease progresses and patients can develop optic neuropathy without ever exhibiting high IOP. This is known as normal-tension glaucoma (NTG) and patients generally have consistent IOP measurements of less than 21mmHg. The work presented in this thesis focuses on the mechanisms and treatments associated with POAG involving high IOP.

POAG and increased outflow resistance

POAG is characterized as any nerve damage that meets the criteria discussed above and decreased AH outflow, but without angle closure (**Fig. 1.2b**) (Foster et al. 2002). There are numerous risk factors associated with POAG such as myopia, increased age, a family history of glaucoma, race, and ethnicity. With age, other risk factors associated with glaucoma increase, such as blood pressure, cardiovascular disease and thinner central corneas. POAG prevalence is 5 times higher in those of African descent in comparison to other ethnic groups (Harasymowycz et al. 2016; Hollands et al. 2013). In addition to the above, high IOP is one of the most common risk factors for development for POAG and reduction thereof is the main mode of treatment to retard disease progression (Harasymowycz et al. 2016).

IOP is controlled by the homeostatic regulation of AH production and drainage. AH is produced in the processes of the ciliary body (CB) and is an active process. The ciliary arterial supply is derived from the major arterial circle of the iris and it delivers water, ions, proteins and plasma components to the fenestrated capillaries of the CB. The AH components are extracted from the blood, by ultrafiltration and diffusion, into the stroma of the ciliary processes by hydrostatic pressure and concentration gradients. AH is then driven into the basolateral spaces between the non-pigmented epithelial cells of the CB and into the posterior chamber through the formation of an osmotic gradient. At this point the practically protein-free AH is drawn through the pupil into the AC, where plasma proteins diffuse into the AH at the anterior iris root. AH has around 1% of the total protein concentration of blood plasma and supplies the avascular tissues of the AC with nutrients before drainage through the trabecular meshwork (TM)/ SC and

uveoscleral pathways (Freddo 2013; Kiel et al. 2011). The conventional pathway drains AH through the TM/SC and out through collector ducts and back into the vascular system to the episcleral veins, whereas in the unconventional pathway, the AH passes through the base of the CB into the suprachoroidal space (see **Fig. 1.2a**)(Alm & Nilsson 2009; Tamm 2009).

AH that passes through the unconventional pathway passes through the interstitial spaces between the longitudinal ciliary muscle bundles and into the supraciliary spaces. In other words, the unconventional pathway must pass through the ciliary muscle and as a result, factors affecting its contraction or relaxation affect outflow. For example pilocarpine (which is used to treat acute ACG) causes ciliary muscle contraction, decreasing the spaces between these muscle fibres thereby reducing unconventional outflow. Conversely atropine acts as a cholinergic antagonist, relaxing the ciliary muscle and increasing unconventional outflow. The effect of CB muscle tone on unconventional outflow appears to influence AH drainage with age. The unconventional pathway accounts for approximately 10-35% of AH drainage in humans, which has shown to decrease with age. The high variances in outflow estimates are due to indirect measurements of human AH outflow. In eyes at age 60, there is a significant increase in connective tissue in the anterior section of the ciliary muscle, which reduces interstitial space, and this may well contribute to the unconventional outflow reduction associated with increasing age. Another feature of unconventional outflow is that it is relatively pressure insensitive and for this reason it was originally thought that the amount of flow through the unconventional pathway was completely independent of changes in IOP. However, the uveoscleral pathway does contribute a small amount (~5%), to the pressure dependent change in outflow, known as outflow facility, which is an important feature to take into account when measuring AH flow through the trabecular meshwork (Alm & Nilsson 2009; Johnson et al. 2017; Goel et al. 2010). It is of relevance to note that the unconventional outflow accounts for only 10 – 35% of AH drainage in humans and yet traditionally the majority of intraocular pressure (IOP)-lowering drugs directly target this pathway (Nilsson 1997).

The conventional outflow pathway

The trabecular meshwork (TM) and juxtacanalicular tissue (JCT)

The majority of AH outflow in humans occurs through the conventional pathway located at the iridocorneal angle (**Fig. 2a**). AH is filtered from the AC through the TM, the juxtacanalicular tissue (JCT) and finally the inner wall of the SC; from here it drains through collector channels back into the limbal vasculature (Keller et al. 2011; Floyd et al. 1985). This pathway is pressure dependent and outflow resistance changes dynamically in healthy tissue to help maintain IOP within a physiologically safe range. Most of the evidence suggests that the majority of outflow resistance, the primary determinant of IOP, is generated at the inner wall of the SC and the connective tissue of the JCT (**Fig. 1.3**) (Overby et al. 2009; Llobet et al. 2003).

The TM is a highly organised tissue that is located proximal to the AC at the corneoscleral angle. The connective tissue of the TM is composed of prolongations arising from the iris and CB; the inner section consists of columns of glycoproteins, collagen, hyaluronic acid and elastic fibers covered by flattened TM cells (Llobet et al. 2003). It can be separated into regions based on anatomical location, and these differ in structure and function. From the inner to outermost regions, the TM is composed of the uveal meshwork (the first tissue encountered by exiting AH), the corneoscleral meshwork, and finally the JCT (**Fig. 1.3**). The uveal meshwork is a highly fenestrated tissue formed by trabecular beams made of elastic fibres, collagens and glycoproteins, associated with endothelial TM beam cells. These trabecular beams form a netlike structure with large interstitial spaces that have very little effect on outflow resistance generation. Next is the corneoscleral meshwork. This layer continues for a depth of around 100μm between the uveal meshwork and the outer JCT layer. Similarly to the inner uveal layer, the corneoscleral layer is composed of highly irregular layers of trabecular beams that form a meshwork of extracellular matrix (ECM), covered and maintained by a continuous layer of TM cells. As this layer continues to the outer edge, the openings between these beams gradually become smaller, that acts as a filter, funneling the AH towards SC.

The deepest, or outermost region is the JCT, also known as the cribriform region, which lies adjacent to the SC inner wall. It follows the final trabecular beam

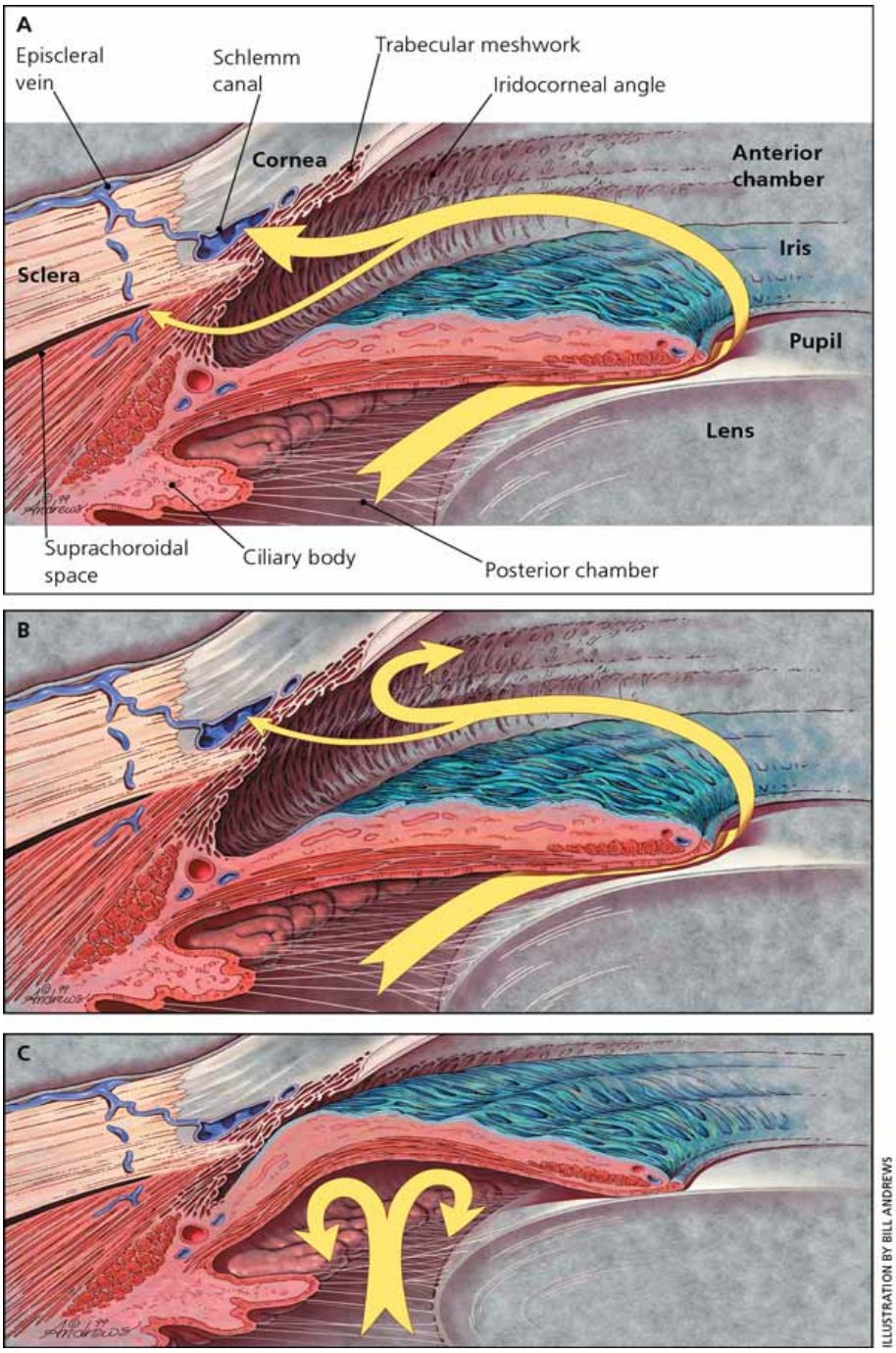

Fig. 1.2. Normal and abnormal aqueous humour (AH) flow.

(a) Normal AH flow; AH is generated in the ciliary body and flows through the pupil into the anterior chamber. AH is drained through the conventional pathway (large arrow) and the uveoscleral pathway (small arrow). **(b)** In primary open angle glaucoma outflow is reduced through these pathways resulting in increased intraocular pressure. **(c)** In angle closure glaucoma the iris is abnormally positioned against the iridocorneal outflow tissues blocking AH drainage and increasing IOP. Image taken from Gupta and Chen (2016).

and merges with the basement membrane of the SC inner wall, extending on average 10μm from the SC endothelial cells. In contrast to the uveal and corneoscleral network, the JCT is not organized into a layered structure but is composed of an amorphous ECM with a discontinuous scattering of several layers of JCT cells embedded into it. These JCT cells are separate from the SC inner wall but can form processes that make contact with SC endothelial cells and TM cells of the corneoscleral layer (Keller & Acott 2013; Acott & Kelley 2009; Overby et al. 2009; Gong et al. 2002; Llobet et al. 2003).

The ECM support of the TM is a highly dynamic structure that is regulated by its environment, with changes in the extracellular meshwork being linked to actin cytoskeletal changes in the resident cells, thus effecting cell rigidity (Fletcher & Mullins 2010). Interestingly, although the JCT region is both functionally and structurally different to the uveal and corneoscleral regions, the only known biomarker that differentiates the respective cells is the stress protein αB-crystallin (Fuchshofer et al. 2006; Siegner et al. 1996). Though often termed endothelial cells due to their flat nature, the cells of the TM show epithelial cell characteristics and are in fact derived from ocular mesenchymal cells, originating from the neural crest (Cvekl & Tamm 2004; Braunger et al. 2015).

The cells of the uveal and corneoscleral regions are actively phagocytic and act as filters, removing debris such as pigment granules, erythrocytes and degraded ECM from the AH before reaching the less porous JCT region (Saccà et al. 2016). They can also act as mechanosensors, expressing several known mechanotransduction channels. *In vivo,* high IOP has been shown to increase the pressure gradient across the TM causing cells to stretch in response. In conjunction with these observations, TM cells *in vitro* display a diverse response to mechanical stretching including alterations in ECM, cytoskeleton and induction of cytokine production (Hirt & Liton 2017). These responses are all involved in regulation of outflow resistance and in fact the region around the JCT and SC inner wall is where the majority of outflow resistance is generated (Keller & Acott 2013).

Schlemm's canal

The last barrier in the regulation of aqueous outflow is the inner wall of SC itself, consisting of a single continuous layer of endothelial cells on the inner side of the

elliptical canal. This flattened channel encircles the cornea with an average meridional diameter of 233μm and is connected to collector channels along its length, these channels ultimately drain AH into the episcleral veins. Collector channels separate into 2 different categories, those with simple oval openings and those with complex orifice structures forming bridge-like structures or tethered flaps, which may act as vascular valves that inhibit AH backflow (Bentley et al. 2016). Due to unidirectional influx of AH, not all SC endothelia share the same properties, and are separable into inner and outer wall endothelial cells. Along the canal, the inner and outer wall cells are joined by septa, especially clustered at regions with a high proportion of collector channels, and owing to their positioning these septa may prevent collapse of the canal structure. The cells of the inner and outer SC wall differ in morphology, cell biomarkers, specialized cellular organelles, and functions. Whether these differences are due to the vastly different biomechanical environment these cells experience or due to the effect of the neighbouring cells is unclear (Overby et al. 2009; C. Dautriche et al. 2015).

SC inner wall cells differ to most endothelial cells. Although they are of endothelial origin, during differentiation they acquire some lymphatic characteristics while retaining their identity as endothelial cells. Interestingly, they express both the endothelial marker PECAM-1 and the lymphatic marker PROX-1 (Park et al. 2014b). Distinct from other endothelial cells, which experience pressure in the apical to basal direction, pressure is exerted on SC cells basally to apically, i.e. from the AC to the SC lumen. Thus SC endothelial cells have unique barrier properties that allow them to regulate outflow resistance, including the formation of giant vacuoles (GV) and the presence of micron-sized pores that cross the inner wall (Johnson 2006).

GVs are invaginations of the SC endothelia into the lumen of the canal, with openings to the basal membrane apical to the endothelial lining, creating a pocket of space between the SC inner wall and the ECM of the JCT. Both size and density of GVs are pressure-dependent, with no evidence of GV formation at an IOP of 0 mmHg (Ryan M Pedrigi et al. 2011). SC cells appear to be very well suited to withstanding the pressure drop between IOP and episcleral venous pressure (Stamer et al. 2015). Within these GVs, transcellular pores often form, that connect the apical and basal extracellular fluid. Such pores traverse the cell, without

exposing the cytoplasmic space. In addition to the transcellular pores, the continuous SC endothelium is broken by paracellular pores that form between the cell junctions (Johnson 2006). A higher density of paracellular pores has been linked with areas of increased flow rate in *ex vivo* eyes and the overall pore density of the inner wall has been shown to be decreased up to 5-fold in glaucomatous tissues (Braakman et al. 2015a).

Generation of outflow resistance

It is universally recognized that elevated IOP seen in POAG is as a result of increased outflow resistance, at the conventional outflow tissues. Despite this, it is still unknown how resistance is generated in both glaucomatous and normal eyes (from here on the term glaucomatous will refer to POAG). The uveoscleral pathway carries less than 10% of total AH outflow and thus does not contribute significantly to outflow resistance in the human eye (Johnson 2006; Overby et al. 2009). In the conventional pathway it is generally accepted that very little outflow resistance is attributable to the uveal and corneoscleral meshworks. Both of these structures are incredibly porous; interstitial spaces range from 25-75μm in the inner regions of the uveal meshwork to 2-15μm within the deeper regions of the corneoscleral meshwork (Overby et al. 2009).

These opening have no effect on resistance, as demonstrated by the fact that removal of the proximal TM tissues in enucleated human eyes has no effect on outflow resistance (McEwen 1958; Grant 1963). The lumen of SC carries the total flow of AH that passes through the conventional pathway and is open at low IOPs. However, due to TM expansion during pressure increase the canal has been shown to collapse experimentally (Johnstone & Grant 1973). Collapse of the canal in this manner could potentially lead to the generation of outflow resistance. Yet outflow resistance in normal, as compared to glaucomatous eyes, at high pressure is still much lower, despite canal collapse in the both (Johnson 2006).

The collector channels and aqueous veins are large vessels in the region of 20 to 110μm in diameter, and theoretically their contribution to outflow resistance is negligible (Bentley et al. 2016). Experimental evidence on this is, in fact, mixed. For example, there is little or no pressure difference between SC and distal episcleral veins at spontaneous IOP (Mäepea & Bill 1989). Yet after complete

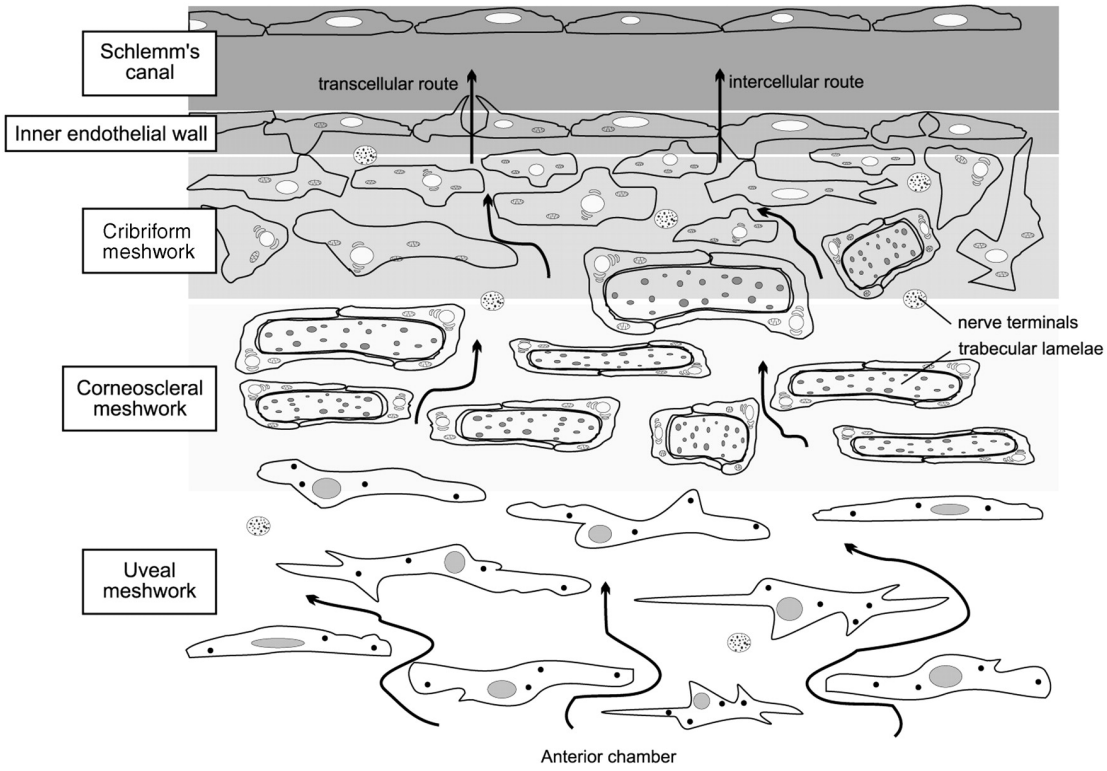

Fig. 1.3. Schematic diagram of the conventional outflow pathway. Arrows indicate the flow of aqueous humor (AH) from the anterior chamber (AC) through the trabecular meshwork (TM) toward the Schlemm's canal (SC) lumen. The separate regions of the TM are labeled; beginning with the innermost layer, the uveal meshwork, the corneoscleral meshwork, and the cribriform meshwork or juxtacanalicular tissue (JCT) region. The final barrier in this pathway is the SC inner wall, where AH flows through both transcellular and intercellular routes. Resistance to AH flow is generated by these tissues in combination, with the greatest resistance generated at the JCT-SC inner wall intersection. Image taken from Llobet et al. (2003).

trabeculectomy, which includes removal of the SC inner wall and surrounding TM, there still remains a minimum of 25% of outflow resistance distal to the SC (Rosenquist et al. 1989; Van Buskirk 1977). Despite this, it is unlikely that distal tissues play a role in increased resistance in POAG. An early study showed that all glaucomatous related increases in resistance were eliminated in glaucomatous eyes, subsequent to complete trabeculectomy (Grant 1963; Johnson 2006).

Outflow resistance at the juxtacanalicular tissue

Experimental evidence suggests that the bulk of conventional outflow resistance is generated within the vicinity of the inner SC wall, within 14μm (Mäepea & Bill 1989; Mäepea & Bill 1992). This includes the area around the JCT, the SC inner wall endothelium and the discontinuous membrane of this endothelium. The basement membrane has the potential to create significant flow resistance. Nonetheless, examination by quick freeze/deep etch electron microscopy indicates that the basement membrane is discontinuous, thereby limiting its capacity for resistance generation (Johnson 2006; Gong et al. 2002). The JCT forms a meshwork proximal to the SC inner wall and contains micron-sized pores dotted throughout, lacking visible ECM ultrastructure and presenting a rather tortuous pathway for AH to follow on its route from the AC. However, if the current model of JCT structure holds true, then the size of these spaces is too large for the JCT to offer significant impact to outflow resistance (Ethier et al. 1986; Murphy et al. 1992). Either the JCT is not the region of primary resistance generation in the conventional pathway or techniques used for visualizing this tissue do not preserve the ECM present in these pores (Johnson 2006).

Classically proteoglycans and glycosaminoglycans (GAGs) have been thought to have a role in regulating outflow resistance, and indeed, perfusion of bovine eyes with hyaluronidase decreased outflow resistance by almost 50% (Barany & Scotchbrook 1954). However, in primate and human eyes the role of GAGs are far less clear, for example testicular hyaluronidase has no effect on enucleated human eye outflow resistance (Grant 1963). Interestingly, outflow resistance can be lowered in human eyes by inhibiting GAG elongation or sulfation, but during this same study the treatment of enucleated human eyes with GAGases had no effect on outflow facility (Keller et al. 2008). In summary, it is not yet

known what fraction of outflow resistance is influenced by the JCT.

Outflow resistance at the Schlemm's canal inner wall

The final tissue capable of generating outflow resistance is the endothelium of SC, these cells being joined by tight junctions (Gong et al. 1996). AH flows through the inner wall of the canal both through paracellular routes and intracellular pores. However, based on pore density it has been estimated that the SC inner wall only contributes to about 10% of total outflow resistance (Bill & Svedbergh 1972). It should be noted however that the fixative used to visualize these pores may increase the number of apparent pores than would be present physiologically. Moreover, there is a decrease in SC pore density in glaucomatous eyes and it is likely that the portion of outflow resistance attributable to the SC inner wall is greater than previously calculated (Johnson et al. 2002; Overby et al. 2009). We are thus left with a paradox in relation to outflow resistance in the AC - the majority of outflow resistance is generated within the area surrounding the SC inner wall, but none of the relevant tissues generate sufficient resistance to account for this, even taking additive effects into account (Mäepea & Bill 1989; Mäepea & Bill 1992; Overby et al. 2009).

This has led to the proposal of a synergistic model of outflow resistance generation, in which the AH is funneled toward SC pores. SC pores are relatively widely spaced apart, with around 20 – 30μm of separation, and presumably create non-uniform flow patterns in the JCT. This funneling effect would reduce the effective filtration area of the JCT and so increase the resistance generation in this tissue (Overby et al. 2009). In this way the funneling effect would create outflow resistance greater than the combined resistance of each tissue. Supporting this model is the effect of SC endothelium disruption by EDTA, which results in greater reduction in outflow resistance than would be estimated from the pore morphology alone (Hamanaka & Bill 1987). Thus, according to the funneling model, IOP-reducing treatments targeting the SC inner wall have the greatest hope of significant outflow resistance reduction.

Segmental AH outflow

The SC is an elliptical channel that traverses the entire circumference of the eye,

and across the conventional outflow pathway are regions of active and inactive outflow (Carreon et al. 2017). Eyes perfused with cationic ferritin or fluorescent microspheres show high and low flow tracer regions within the TM (Hann et al. 2005). Differential flow patterns are not seen when these same tissues are bathed in tracer, suggesting that these differences are caused by regions of variable flow rate in the conventional pathway. In humans the conventional tissues are generally composed of one third low-flow, one third medium-flow and one third high-flow regions (Vranka, Bradley, et al. 2015). Segmental outflow has been demonstrated in a recent study to be preserved in the tissues distal to the TM, such as SC and the episcleral veins. In that study the TM had an effective filtration area 86% of its total length, whereas the SC and episcleral veins had effective filtration areas of 35% and 41% respectively (Cha et al. 2016). As of yet it is unknown what factors influence segmental outflow, though there is evidence to suggest tracers accumulate preferentially in regions of the TM proximal to collector channels (Hann & Fautsch 2009; Cha et al. 2016).

Another factor may be the funneling effect in action. It has been suggested that untethering of the SC and TM will relieve outflow resistance by negating the funneling effect and variable tethering of these tissues along the eye circumference influences segmental outflow (Overby et al. 2009). Bovine eyes treated with the rho-kinase inhibitor (Y-27632) demonstrated an increase in total high-flow region area, in conjunction with increased separation between the SC inner wall and JCT. Rho-kinase inhibitors target the SC inner wall and reduce cell-cell interactions (Lu et al. 2008).

Cell contractility also appears to effect segmental outflow (Carreon et al. 2017). One study found in monkey eyes treated with the serine-threonine kinase inhibitor H-7, that outflow facility is greatly increased. Regions of high flow were traced using colloidal gold particles, and it was found that after H-7 treatment the tracer went from sparse foci to a much broader and uniform distribution. In these eyes the SC remained continuous but with distension of the JCT and SC tissues, associated with the 'relaxation' of the actin cytoskeleton, and loss of the JCT ECM, resulting in loss of the funneling effect and segmental outflow (Sabanay et al. 2000). Moreover, the effects of H-7 are fully reversible and on rescue of outflow facility these morphological changes are also recovered only hours after drug

removal (Sabanay et al. 2004).

Segmental flow is also influenced by ECM composition and regulation of ECM turnover. The expression of ECM associated glycoprotein versican is inversely related to labeling of high flow regions in the TM (Keller et al. 2011). In another instance, the most highly expressed gene product of the TM is secreted protein acidic and rich in cysteine (SPARC), which is a matricellular glycoprotein involved in ECM remodeling. SPARC null mice show a 15-20% decrease in IOP and outflow is much more uniform across the circumference than in wild-type mice (Haddadin et al. 2017; Swaminathan et al. 2017). In summary, the conventional outflow pathway is composed of regions of variable AH flow, dependent on SC inner wall tethering, TM and SC cell contractility and ECM deposition.

Genetics of POAG

POAG is a complex multifactorial disease that exhibits some heritability that is very dependent on polygenic and gene-environmental interactions. Linkage studies have so far have identified 20 chromosomal loci linked with POAG, however these genes together account for <10% of cases in the general population (Abu-amero et al. 2015). More recently, genome wide association studies (GWAS) have found 16 gene/loci that are significantly associated with POAG in European Caucasian and Asian populations (Wiggs & Pasquale 2017). Mendelian forms of the disease do exist but account for a very small fraction of the cases. Mutations within four specific disease-causing genes having been found in myocilin (*MYOC*), cytochrome P450 family 1 subfamily B polypeptide 1 (*CYP1B1*), optineurin (*OPTN*), and TANK-binding kinase 1 (*TBK1*) (Liu & Allingham 2017; Zhou et al. 2017).

Myocillin

Mutations in *MYOC* were first identified in families with autosomal dominant POAG. The gene located on chromosome 1q, was known to be expressed in the CB and the TM (Sheffield et al. 1993; Stone et al. 1997). Mutations in this gene are associated with juvenile glaucoma, generally manifesting between 3 and 20 years of age, and account for 3-5% of POAG cases worldwide (Wang & Wiggs 2015). *MYOC* encodes an extracellular protein, myocilin, of unknown function that is expressed in multiple ocular tissues and also secreted by TM cells (Hoffman et al.

2009). Most disease-causing mutations occur in the olfactomedin domain of this gene, which inhibits protein secretion from TM cells (Jacobson et al. 2001). Dominantly-mutated *MYOC* expressed in TM cells leads to accumulation of the misfolded protein, leading to disruption of cellular protein trafficking and ER stress (Kasetti et al. 2016). Overexpression, reduction or complete loss of myocilin in mice does not lead to a glaucomatous phenotype, suggesting it does not normally play a role in IOP regulation (Liu & Allingham 2017). However, transgenic mice expressing the human or mouse Tyr437His variant develop glaucomatous features, including elevated IOP, progressive RGC loss and axonal degeneration. Some of the retinal degeneration phenotype may be IOP-independent in these animals, since myocilin is also expressed at the optic nerve head (Chou et al. 2014).

Optineurin

Mutations in the *OPTN* gene are associated with normotensive glaucoma (NTG) (Child et al. 2002; Ariani et al. 2006). OPTN is involved in membrane trafficking, protein secretion, cell division, autophagy, and host defense against pathogens (Liu & Allingham 2017). The most common variant found in this gene is the missense mutation E50K, associated with very early onset disease progression (Aung et al. 2005). The mutation may be involved in an enhancement of the interaction between OPTN and TBK1, leading to accumulation of the insoluble OPTN and ER stress in cells (Minegishi et al. 2013). Mutations in the *TBK1* gene have also been associated with hereditary forms of glaucoma. *TBK1* encodes a serine/threonine kinase involved in the regulation of inflammatory responses to foreign agents, specifically regulating the expression of genes in the NF-κB signaling pathway (Fingert 2011). Duplication of the *TBK1* gene has been associated with ~1% of all NTG cases, sharing its pathway of pathogenesis with OPTN. TBK1 is expressed in the RGCs, with duplication of *TBK1* in mice leading to progressive RGC loss without increased IOP (Fingert et al. 2016). While the exact mechanism by which *OPTN* and *TBK1* affect glaucoma is unknown, these mutations may act through dysregulation of autophagy and the NF-κB pathway.

GWAS and POAG

Other genes discovered by association analysis with POAG include *WDR36, NTF4, ASB10*, *EFEMP1* and *IL20RB*. Genome-wide association studies (GWAS) have increased the extent to which we can understand the genetic component of glaucoma. It must be noted that all GWAS studies to date have been in populations of Asian and European derivations despite the high prevalence of POAG in those of African descent (Liu & Allingham 2017). Of the genes to come from these studies, the most examined are the caveolins, *CAV1* and *CAV2.* Caveolins are integral membrane proteins that are the principal components of caveolae membranes. They are involved in cellular transport, mechanotransduction, cell proliferation, and signal transduction, and are expressed in the retina, CB, TM and SC endothelial cells (Gu et al. 2017; Liu & Allingham 2017). Reduced expression of caveolins in glaucomatous tissues may be indicative of their pathological role in POAG (Surgucheva & Surguchov 2011). Interestingly, $Cav^{-/-}$ mice display ocular hypertension, with decreased AH outflow. In these mice TM and SC cells lack caveolae and display a greater susceptibility to rupture through mechanical stress (Elliott et al. 2016). More than 50 other genes have been identified using the GWAS approach including those with significant associations: *CDKN2BAS, TMCO1, SIX6, 8q22, AFAP1, ABCA1, GMDS, TGFBR3, FNDC3B, ARHGEF12, TXNRD2, ATXN2, PMM2, GAS7, FOXC1, .* These genes are involved in a variety pathways such as actin signalling, ER stress, cytokine signalling, membrane trafficking, mitochondrial function, cell division and ocular development all of which could have a role in the progression of the disease (Abu-amero et al. 2015; Liu & Allingham 2017; Wiggs & Pasquale 2017; Bailey et al. 2016).

The mouse as a model for glaucoma

The mouse is an attractive model to use in research owing to its well-characterised genetic variability, ease of genetic manipulation, inexpensive cost, and ease of use in drug studies. In relation to glaucoma research, mice have advantages over other non-primate models. They have a lamellar TM and SC with both conventional and unconventional pathways (Chowdhury et al. 2015). Both mice and humans have cyclical IOP patterns with similar AH production and turnover rates (Aihara et al. 2003). Importantly for glaucoma research, mice also have similar mechanisms for

AH formation, regulation and outflow, have similar responses to IOP-lowering drugs, and also have no washout rate, a trait so far known only to be shared between mouse and human eyes (Fernandes et al. 2015). In relation to the AC, the differences between mice and primates include; a larger AC in relation to total eye size and a narrower angle with a thinner and more posteriorly placed TM containing fewer collagen beams (Chowdhury et al. 2015).

Retinal damage in human glaucoma begins at the optic nerve head. In mice, increased IOP causes similar glaucomatous retinal damage with dysfunction of optic nerve transport. Though the mouse optic nerve head is comparable to primates there are some important differences, particularly at the lamina cribrosa. In the human optic nerve head the bundled axons pass through the lamina cribrosa, a meshwork of astrocyte-covered connective tissue beams. The mouse has a poorly developed collagenous lamina cribrosa, but is supported by transversely orientated astrocytes (Abe et al. 2015; Morrison et al. 2012). Overall, mouse models are a valuable resource in glaucoma research with structurally similar outflow pathways, similar IOP regulatory mechanisms, and hypertension-induced RGC death.

Myocilin mouse model of glaucoma

Myocilin is an extracellular protein of unknown function and mutation of the *MYOC* gene is associated with autosomal dominant juvenile POAG (Menaa et al. 2011). Mutations in *MYOC* result in the prevention of myocilin secretion from TM cells, resulting in an intracellular aggregation thereof and ER stress (Kasetti et al. 2016). Myocilin is highly expressed in mouse TM cells and RGCs, which is similar to humans (Takahashi et al. 1998; Tamm 2002). The first use of a mouse model to investigate the role of myocilin in glaucoma was a *MYOC* knockout mouse, which had no IOP increase, morphological abnormalities or any other glaucomatous phenotype (Kim et al. 2001). Similarly, overexpression of the gene had no phenotype related to glaucoma (Fernandes et al. 2015). Mutated mycocilin mouse mutants have also been used to recapitulate glaucomatous phenotypes.

Tyr437His-mutated human myocilin was not secreted into the TM, unlike the WT human protein (Zillig et al. 2005). Following this finding, mice with an analogous mutation (Tyr423His) in the endogenous mouse gene were developed.

Strain-dependent differences were evident, with some strains lacking any glaucomatous phenotype and others developing a slight increase in IOP and increased RGC death in aged mice. This is despite a lack of myocilin secretion in all transgenic mice (Gould et al. 2006; Senatorov et al. 2006). However, with the use of an adenoviral vector expressing a mutated Tyr437His human myocilin gene that targeted the iridocorneal angle, Shepard et al. were able to demonstrate a very large increase in IOP. This study demonstrated the importance of the peroxisomal targeting sequence, PTS1, which is exposed in the human mutant protein (Shepard et al. 2007).

Transgenic mice expressing the human mutant have since been developed. However, only mice with the human gene under control of a CMV promoter display a distinct glaucomatous phenotype (Zode et al. 2011; Zhou et al. 2008). This CMV-driven model demonstrates that the myocilin mutant elicits an unfolded protein response in the mouse TM, and is associated with a loss of TM cells (Zode et al. 2011). It has been established that these mice have increased deposition of ECM proteins, fibronectin and laminin in the conventional outflow tissues, visible from 3 months of age (Kasetti et al. 2016). These studies only use a single *MYOC* mutation but recently novel mutations under evaluation suggest other pathways could be involved in the pathogenesis of glaucoma (McKay et al. 2013; Itakura et al. 2015).

DBA/2J mouse model of glaucoma

The DBA/2J mouse is the best-described congenital mouse model of glaucoma (Fernandes et al. 2015). These mice develop a pigment-dispersing iris disease that leads to increases in IOP and RGC loss, as well a severe age-related anterior segment anomalies including iris atrophy, peripheral anterior synechiae and pigment dispersion (John et al. 1998). The iris disease is split into two main components: iris pigment dispersion and iris stromal atrophy. The iris pigment dispersion is characterized by a deterioration of the posterior iris pigment epithelium which is mediated by a premature stop codon in the *Gpnmb* gene. A recessive mutation in the *Tyrp1* gene is responsible for iris stromal atrophy which is associated with deterioration of the anterior iris stroma (Anderson et al. 2002). Both of these mutations are necessary for the glaucomatous disease progression in

these mice, however on other mouse strain backgrounds they are not sufficient to initiate IOP increase or RGC death (Anderson et al. 2006). This indicates that other factors influence the glaucomatous phenotype in these animals, since the two mutations are sufficient to cause iris disease but not glaucoma on different strains.

In the DBA/2J mouse, as disease progresses there is a breakdown of the blood-aqueous barrier and increased leukocyte infiltration to the AC. This phenotype, along with iris dispersion, are all rescued by the transplantation of C57BL/6J bone marrow into the DBA/2J animal (Mo et al. 2003; Anderson et al. 2008). This demonstrates the possibility of a role for the immune response in the DBA/2J disease, yet to date such a role has yet to be elucidated (Nair et al. 2014). The DBA/2J mouse model shows characteristics of chronic glaucoma, with the disease progressing more rapidly in females than males. IOP begins to rise in females at ~6 months, comparative to ~8 months in males, and reaches a peak at 10 months in both sexes (Libby et al. 2005). DBA/2J animals display disruption in RGC axon transport prior to RGC cell death, as occurs in glaucoma. At 13 months of age there is no significant decrease in RGC density, however 75% of all RGCs are deficient for axonal transport. At 18 months of age these animals have significantly reduced RGC density (Buckingham et al. 2008). Despite these late changes in RGC density, apoptotic RGCs are found in the DBA/2J retina from 9 months of age (Reichstein et al. 2007; Schuettauf et al. 2004).

The DBA/2J mouse model has been used to test the potential neuroprotective effects of numerous compounds (Hines-Beard et al. 2016; Cwerman-Thibault et al. 2017; Ward et al. 2007). Though there are multiple drawbacks to this congenital glaucoma model. For one, the variability between individuals; a recent study found that not all animals demonstrate an increase in IOP, and not all animals developing optic neuropathy have high IOP (Wang & Dong 2016). Furthermore, iris pathologies in these animals make OCT, fundus imaging and AC analysis extremely difficult. Also, these animals develop other pathologies not involved in glaucoma such as auditory seizures and hearing loss. This results in a high attrition rate of animals and a need for high animal numbers, in addition to long housing duration (Turner et al. 2017). In spite of these disadvantages, DBA/2J mice proved to be extremely useful in demonstrating that co-suppression within the retina of the tight junction proteins, claudin-5 and occludin, increases

paracellular permeability and clearance of amyloid-β1-40 from the retina into the peripheral circulation (see **Chapter 2**).

Ad-TGF-β2 and Ad-CTGF mouse models

TGF-β2 is associated with glaucoma; levels are increased in POAG AH, and exogenous TGF-β2 causes changes in TM and SC cell permeability (Fuchshofer & Tamm 2012). Adenoviral vectors have been used to transduce the cells of mouse outflow tissues, including the TM and the SC (Li et al. 2013). Expression of a spontaneously active human TGF-β2 from such vectors results in a significant IOP increase at day 7 post-injection, which slowly declines but is still moderately high at day 29, with a concomitant decrease in outflow facility (Shepard et al. 2010).

The TGF-β2 mouse model has been used to demonstrate the role of Secreted Protein Acidic and Rich in Cysteine (SPARC) in glaucoma pathogenesis. SPARC is a matricellular protein of the TM and null mice have a 15-20% lower IOP compared to WT. These mice also are resistant to Ad-TGF-β2-induced IOP increases and inhibit ECM deposition in the outflow tissues (Swaminathan et al. 2014). Connective tissue growth factor (CTGF) is up-regulated in the TM after TGF-β2 treatment and mediates much of the TGF-β2-induced ECM synthesis. Increase in CTGF expression in the mouse TM results in an increase in IOP that lasts up to 63 days post injection. At day 63, there is a significant reduction in optic nerve axon density. Following these results, a transgenic mouse expressing increased CTGF in the TM was developed. These mice have increased IOP up to 3 months of age and develop reduced optic nerve axon density (Junglas et al. 2012). Adenoviral mouse models develop high IOP with axon degeneration, similar to POAG, and the phenotype develops at an early age, allowing the use of a contralateral eye as a control. This being said, the AV expression is transient and these models are therefore not suitable as models of chronic glaucoma.

Induced hypertension mouse models: vein occlusion

Laser photocoagulation leads to an increase in IOP, probably due to increased outflow resistance owing to angle closure, TM scarring and obliteration of the SC. Laser treatment results in sustained ocular hypertension and a decrease in optic nerve head axon density (Mabuchi et al. 2003; Ishikawa et al. 2015). Adversely,

this technique also results in ocular inflammation and is not suitable for research on outflow tissues owing to the damage caused. Glaucoma models have also been generated by targeting the episcleral veins via an occlusion model or with the intravenous injection of saline. In occlusion models IOP is increased by photocoagulation of the episcleral veins which results in a decrease in AH outflow. Models of this sort also cause complications, including ocular inflammation and ocular surface damage. In the saline-induced model, hypertonic saline is injected into the limbal vessels, bringing about an increase in AH outflow resistance and as a result, IOP elevation. Disadvantages of this approach are the transience of IOP elevation and the difficult technical aspect of microneedle insertion into mouse limbal vessels (Ishikawa et al. 2015).

Induced hypertension mouse models: microbeads

The microbead model of ocular hypertension is an attractive option, being cost-effective, not technically demanding, rapid in onset and applicable in a high percentage of animals. Broadly, IOP is increased by injection of microbeads (ranging in size from 1-6μm) into the AC. The beads migrate into the TM lodging in these tissues and increase outflow resistance. Such mice demonstrate increased IOP and RGC death; interestingly, RGC loss is strain-specific, with increased RGC death in the CD1 mouse compared to the C57BL/6J mouse after microbead induced IOP elevation (Morgan & Tribble 2015). The principal disadvantages in this model include physical disruption of the TM, which is inconsistent with POAG, and the fact that microbeads can be lost from the AC angle. In regard to the latter, it is interesting to note that new techniques have been developed using magnetic microbeads that can be directed via magnets to the angle (Ishikawa et al. 2015).

Induced hypertension mouse models: glucocorticoid induced glaucoma

Glucocorticoids are a commonly prescribed type of medication owing to their broad range of anti-inflammatory and immunosuppressive properties. They are often used in ocular anti-inflammatory therapy via topical, oral or intravitreal administration. Sustained treatment with glucocorticoids is associated with induced ocular hypertension and secondary open angle glaucoma, which has similarities to POAG (Patel et al. 2017). In mice, both systemic and topical

administration of the glucocorticoid dexamethasone, results in ocular hypertension that can be modulated using classical glaucoma therapies (Zode et al. 2011; Whitlock et al. 2010). These models are characterized by an increase in outflow resistance with increased ECM deposition in the JCT tissue (Overby, et al. 2014). In mixed genetic backgrounds, a proportion of the population are non-responders and do not develop ocular hypertension, implying a non-elucidated genetic component (Whitlock et al. 2010). Also, on systemic use of dexamethasone, mice can experience adverse effects including weight loss (Overby, et al. 2014).

Mouse models of retinal ganglion cell death

Several methods have been developed that are designed to induce rapid and uniform RGC death in mice. These include intraocular delivery of various compounds inducing RGC death such as staurosporine or *N*-methyl-$_D$-aspartate (NMDA), an analog of glutamate. Mouse RGCs are susceptible to glutamate toxicity and demonstrate a dose-dependent loss upon NMDA administration (McKinnon et al. 2009). In addition to these, RGC loss can also be induced in mice via direct optic nerve (ON) injury. Complete intraorbital optic nerve crush, or transection, both produce clean and replicable models of RGC degeneration. Both techniques result in two phases of RGC death, with an abrupt loss of 80-95 % of RGCs within 7-12 days post-transection. The second phase is more protracted, with 1-2 % RGC survival at the latest timepoints.

Topographically, these models have diffuse loss of RGCs throughout the retina, consistent with total ON lesion. In comparison, RGC degeneration in ocular hypertensive models is more gradual with patchy loss of RGCs throughout the retina, consistent with damage of ON bundles near the optic nerve head (Vidal-Sanz et al. 2017). These techniques offer quick and reproducible models of RGC death after ON injury, useful for testing neuroprotective treatments. However, RGC loss shows differences in temporal and spatial progression to that seen in ocular hypertensive models, and lack the major risk factor of POAG, increased IOP.

Glaucoma medications

In many instances people with high IOP never develop glaucoma and conversely, there are those who develop glaucoma with IOPs within the normal range. Despite

this, IOP remains the only treatable risk factor in glaucoma. POAG can ultimately, only be diagnosed after the detection of neuronal loss at the optic nerve head combined with visual field defect testing (Weinreb et al. 2014). Therefore, in the majority of cases treatment can only begin after RGCs have already been damaged. In one study, an average IOP reduction of 25% resulted in a 17% decrease in patients with progression of visual field defects (Heijl 2002). Treatment goals for IOP reduction vary greatly on an individual basis but in general, a target IOP reduction of 25-30% is desired. Treatments generally include pressure-reducing eye drops that either reduce AH production or increase outflow. In more severe cases surgery is required (Harasymowycz et al. 2016).

The first line of treatment in early glaucoma is the use of medications, most commonly including prostaglandin analogues, β-blockers, α-2 agonists and carbonic anhydrase inhibitors (Gupta & Chen 2016). Data obtained from a recent meta-analysis indicated that the most efficacious of these are the prostaglandin analogues such as latanoprost, bimatoprost and travoprost (T. Li et al. 2016). These medications reduce IOP by increasing outflow primarily through the uveoscleral pathway, although some evidence indicates that conventional outflow is also increased during treatment (Bahler et al. 2008; Toris et al. 2008).

Prostaglandin analogues

Prostaglandins are autacoids, hormones that are released and act locally, and are produced natively in the AC from cells of the outflow pathway (Weinreb et al. 2002). These hormones and their analogues affect AH outflow and IOP, and though the exact mechanism is yet to be elucidated, binding of the FP receptor plays a significant role. Remodeling of the ECM in the uveoscleral pathway is the most well-studied effect of prostaglandin treatment. Long-term treatment of monkey eyes with various prostaglandin drugs resulted in enlargement of all the tissue spaces within the ciliary muscle bundles increasing fluid pathways (Nilsson et al. 2006). Increases in interstitial tissue space are due to dissolution of collagen types I and III within the ECM of the ciliary muscle by stimulation of matrix metalloproteinases (MMPs). The prostaglandin effect on the TM and conventional outflow appears to act via a similar mechanism, with an increase in MMPs in treated AC explants, though some studies show no rise in MMP levels with

increased outflow (Bahler et al. 2008; Toris et al. 2008). These medications have some side effects including conjunctival hyperemia, increased pigmentation of the iris, eyelid and eyelash, and eyelash thickening. In the majority of these cases the side effects do not result in treatment discontinuation (Cracknell & Grierson 2009).

β-blockers

β-blockers have been in use clinically for over 30 years, though they are contraindicated in patients with cardiac or pulmonary conditions and have known side effects. They block β-adrenoceptor binding, reducing AH production by competitive inhibition of the sympathetic pathway of the CB. Typically β-blockers are selective or non-selective. Selective inhibitors specifically target β1-receptors whereas non-selective inhibitors can target both β1- and β2- adrenoceptors, found within the ciliary processes (Brooks & Gillies 1992; Trope & Clark 1982). The resulting decrease in AH production is likely due to the inhibition of catecholamine-stimulated synthesis of cAMP in the ciliary epithelium (Marquis & Whitson 2005). Timolol, the most widely used β-blocker, is non-selective. Some reports claim that an added benefit to treatment using selective β-blockers may be enhanced retinal blood flow, decreasing optic nerve axon loss (Collignon-Brach 1992; Messmer et al. 1991). Despite this, the role of retinal blood flow in glaucoma treatment is not yet understood (Noecker 2006).

Topical applications of these β-blockers results in systemic absorption that can lead to severe side effects. Blocking β1-receptors of the heart by Timolol may lead to bradycardia, arrhythmia, bronchospasm, and congestive heart failure. Furthermore, Timolol can pass the blood-brain barrier and block serotonin receptors in the CNS. It may also cause depression, weakness, fatigue and impotence (Noecker 2006). Nonetheless, Timolol is widely used in glaucoma treatment often in combination with prostaglandin analogues.

α-2 agonists

α-2 adrenergic agonists decrease IOP by the dual action of decreased AH production and increased uveoscleral outflow (Fudemberg et al. 2008). Originally, non-selective agonists that targeted both the α1- and α-2 receptors were used as

glaucoma therapies, but these had too many serious side effects such as systemic hypotension. Modern treatments use very selective α-2 agonists like brimonidine, which has an IOP-lowering effect comparative to the β-blockers, and is often used as an adjunctive with latanoprost and Timolol (Fudemberg et al. 2008; T. Li et al. 2016). Side effects of the selective α-2 agonists locally include allergic blepharoconjunctivitis, a systemically dry mouth, headache, and fatigue (Marquis & Whitson 2005).

Carbonic anhydrase inhibitors (CAIs) and cholinergics

Carbonic anhydrase inhibitors (CAIs) relieve ocular hypertension through reduction of AH formation by inhibiting the catalysis of the reversible hydration of CO_2 by carbonic anhydrase in the ciliary epithelium (Civan & Macknight 2004). CAIs were initially administered systemically, with acetazolamide first used for glaucoma therapy in 1954 (Gloster & Perkins 1955). Systemically, CAIs are effective IOP-lowering agents but have some severe side effects amongst which are paraesthesias of the hands and feet, nausea, vomiting, fatigue, weight loss, and off-target effects to the kidney. Due to these issues, oral medications are generally only used as a temporary therapy, such as before surgery. Topically-applied CAIs such as dorzolamide and brinzolamide, are less effective in comparison to acetazolamide, but they are additive in their IOP-lowering effect when used with other therapies such as Timolol, and therefore are often used as an adjunct treatment (Marquis & Whitson 2005). The topical CAIs cause significantly fewer adverse effects; systemically bitter taste has been reported in ~25% of patients, and locally, effects include stinging, burning and itching (Swenson 2014).

Lastly are the cholinergic drugs, which had reduced clinical use in recent years and are now not commonly used in POAG. These drugs enhance conventional outflow by stimulating CM muscle contraction, thus increasing the TM/SC angle area (Overby, et al. 2014). This however, has the added effect of reducing uveoscleral outflow. Adverse events can include a reduction in visual acuity due to effects on ciliary and pupillary muscle, migraine, and rarely, retinal detachment (Marquis & Whitson 2005).

IOP-lowering glaucoma surgeries

Laser trabeculoplasty

Generally, glaucoma is a chronic condition. Medical treatment is approached in a stepwise manner to reach the optimal treatment combination for a desirable outcome. In some cases where medical therapy does not reach optimum therapeutic goals, or if non-compliance becomes an issue, treatments such as laser therapy or incisional surgery may be required (Weinreb et al. 2014; Marquis & Whitson 2005).

Argon laser trabeculoplasty (ALT) was first proposed in 1979 and involves regularly-spaced laser burns to the anterior trabecular meshwork (Wise & Witter 1979). ALT improves outflow through the TM leading to very high initial success rate. After 5 years however, the success rate is reduced to only 50%. Complications include transient IOP elevation, inflammation of the iris and the formation of peripheral anterior synechiaes (adhesion of the iris to the AC angle) (Marquis & Whitson 2005).

Selective laser trabeculoplasty (SLT) is a similar technique that transmits energy only to the pigmented TM cells, lowering the off-target effect of the laser burn (Kagan et al. 2014). Histological examination of tissue post-ALT indicates that the ECM layers and collagen beams surrounding the TM endothelial cells, as well as the cells themselves, are disrupted and show coagulation damage. Conversely, post-SLT treatment, the disruption was far more focused to the TM cells specifically and the tissues lacked coagulation damage (Kramer & Noecker 2001; Rodrigues et al. 1982). The mechanism of SLT action has not been fully elucidated; it may be due to the protease/cytokine release that occurs after a laser burn. Outflow from the conventional pathway can be increased via ECM remodeling, and studies show that TM cells *in vitro* and in explant models show increased production of the MMP-3 and MMP-9 in response to SLT, both of which increase ECM remodeling (Parshley et al. 1995; Parshley et al. 1996). Laser treatment induces TM cells to produce the chemokine IL-8, which is linked to increased AH outflow. After SLT treatment in humans and monkeys, monocytes are recruited to the TM, and these can increase AH outflow and SC cell permeability (Alvarado et al. 2010; Kagan et al. 2014). Complications after SLT are similar to those using ALT but occur less frequently, yet transient side effects include changes in corneal

thickness and corneal hysteresis (Zhou & Aref 2017).

IOP-lowering glaucoma surgeries: trabeculectomy and stent surgeries

Incision surgeries are also commonly used in glaucoma treatment, the most frequent one being trabeculectomy. The latter involves generating a scleral flap with excision of a minute amount of the TM, forming a channel from flap to the AC and allowing the AH to exit the subconjunctival space in a bleb. Long-term scarring along the channel can lead to decreased outflow and hence this form of surgery could be greatly improved by using anti-fibrotic agents. Complications may include hypotony, cataract formation, choroidal effusion, haemorrhage, and inflammation of the eye (Weinreb & Khaw 2004; Marquis & Whitson 2005). Modern methods of glaucoma surgery utilize stent insertion to create a path for the AH to bypass the areas of greatest resistance. These stents are minimally invasive and can bypass the TM to the SC, or suprachoroidal space. Stent surgeries offer different advantages, some having fewer complications but lesser IOP-lowering effect, hence the type of stent to be used must be chosen on a case-to-case basis (Manasses & Au 2016).

Novel medications: targeting the conventional outflow pathway

Rho-kinase (ROCK) inhibitors

The goal in developing novel glaucoma therapies is to target the cells of the conventional outflow pathway, specifically those in the resistance-generating region around the SC and JCT, with the goal of lowering IOP. The Rho-kinase (ROCK) inhibitors have IOP-lowering effects in humans and have been evaluated for clinical safety and efficacy. Two ROCK inhibitor compounds, ripasudil and fasudil, have been advanced to phase 3 clinical studies (Rao et al. 2017). Ripasudil has been approved for treatment in cases where other treatments are ineffective and shows good tolerability and IOP-lowering effect after 1 year in patients (Garnock-Jones 2014; Inazaki et al. 2017). Rho-kinases are serine/threonine kinases that are involved in the regulation of actin cytoskeletal dynamics, cell adhesion, cell stiffness, and ECM reorganization (Fukata et al. 2001).

ROCK inhibitors reduce the contractile response of the outflow pathway, in addition to decreasing actin stress fibres and cell-cell interactions (Inoue &

Tanihara 2013). On ROCK inhibitor treatment, SC cells show a marked increase in permeability, alter the integrity of tight and adherens junctions, and result in F-actin depolymerisation (Kaneko et al. 2016; Kameda et al. 2012). Recently, work has commenced on a new class of ROCK inhibitors, Netarsudil, that also has activity against the norepinephrine transporter, the drug having been shown to lower IOP in preclinical studies. Netarsudil increases outflow facility, in conjunction with an increase in the active filtration area along the SC, and increases JCT thickness, which may be associated with cell relaxation (Ren et al. 2016; G. Li et al. 2016).

Adenosine receptor agonists

Adenosine receptor agonists reduce IOP by increasing outflow through the conventional pathway. There are four known adenosine receptor subtypes; A_1, A_{2A}, A_{2b}, and A_3 (Lu et al. 2017). Adenosine is produced in the extracellular space from ATP, and elevated AH levels of adenosine have been associated with PACG (Li et al. 2011; Andrés-Guerrero et al. 2017). Adenosine-receptor agonists reduce IOP by early reduction in AH secretion, followed by an increase in outflow through promotion of expression of MMP-2 via the A_1 receptor, which results in ECM degradation and turnover at the TM (Zhong et al. 2013). Trabodenson is an adenosine agonist with high affinity and specificity for A_1 receptors, and has been assessed in a Phase III clinical trial, showing well-tolerated toxicity profiles along with possible neuroprotective effect (Myers et al. 2016; Laties et al. 2016).

Novel prostaglandin analogues

Prostaglandin analogues are a novel class of drug that combine the IOP-lowering effects of the prostaglandin F2 analogues with a nitric-oxide donating mechanism (Lu et al. 2017). Nitric-oxide (NO) is a free radical produced by NO synthase (NOS) in the outflow tissue and CB, it's dysregulation being associated with glaucoma (Nathanson & McKee 1995). NO is a key regulator of vascular tone, and has a role in endothelial tight junction organization, affecting permeability. Overexpression of endothelial NOS in the SC endothelia of mice leads to a decrease in IOP and a large increase in outflow facility (Stamer et al. 2011). Interestingly, SC cells were

found to act similarly to vascular endothelial cells in response to shear stress, in that they increase NO production. However, glaucomatous SC cells were found to be shear-stress unresponsive (Elliott et al. 2016).

Latanoprostene is an updated NO-donating prostanoid FP receptor agonist, that upon topical administration is metabolized to latanaprost acid and butanediol mononitrate (Lu et al. 2017). Latanoprost acid is the active ingredient of latanoprost and acts by uveoscleral remodeling and ciliary muscle relaxation (Kaufman 2017). Butanediol mononitrate acts as an NO donor and increases outflow through the conventional pathway. NO appears to act via relaxation of the TM and SC cells, through the soluble guanylyl cyclase/cyclic guanosine monophosphate pathway, leading to downstream Rho-kinase inhibition (Kaufman 2017). This pathway leads to cytoskeletal remodeling in the cells of the conventional pathway, reducing stress fibre formation in the TM and in the SC cells (Cavet et al. 2015; Cavet et al. 2014). Latanoprostene has been through both phase II and phase III clinical trials, demonstrating greater IOP-lowering effects than both Latanoprost and Timolol, in addition to adequate safety and tolerability (Lu et al. 2017).

Actin depolymerisation agents

Actin is a monomeric unit that polymerises to form filaments that have a role in mechanical structure and motility in cells. Actin structure and formation are associated with cell stiffness and glaucomatous SC tissue is known to have increased subcortical cell stiffness (Overby et al. 2014; Andrés-Guerrero et al. 2017). Actin depolymerizing agents reduce SC and TM cell stiffness, increasing AH outflow through the conventional pathway.

Latrunculins are macrolides from the marine sea sponge *Latrunculin Magnifica,* exhibiting specific and potent actin-disrupting properties, sequestering monomeric G-actin which leads to disassembly of actin filaments (Peterson, et al. 2000). The two most common latrunculins, –A and -B, both increase outflow facility in non-human primate eyes by more than two-fold, however latrunculin-B is 10 times more potent (Peterson, et al. 2000).

Cytochalsan agents are fungal polyketides that have diverse biological functions including the capping of actin filaments. Both cytochalasan-D and

latrunculin-A treatment of HTM cells lead to the activation of MMP-2, indicating a secondary mechanism by which these actin depolymerizing agents may work (Sanka et al. 2007). The IOP-lowering effect of these cytoskeletal agents is reversible, suggesting that the effect on the outflow pathway is not due to cytotoxicity. Latrunculin-B has been studied in a Phase-I human trial and was found to significantly reduce IOP with adequate tolerability (Rasmussen et al. 2014).

All of these novel therapies show some promise with the ROCK inhibitors already in clinical use in Japan. These, and other therapeutics in development, exemplify an unmet clinical need for improved medications targeting the conventional outflow pathway.

Objectives of this study

Up to 6% of patients with open-angle glaucoma - equating to around 300,000 cases in the US and EU combined - are bilaterally, sub-optimally responsive to currently-used topical pressure-reducing medications. For the most commonly used prostaglandin analogue, latanoprost, between 25-50% of patients do not achieve greater than a 20% reduction in intraocular pressure (Kass et al. 2002; Scherer 2002; Noecker et al. 2003). These therapies largely target the uveoscleral outflow pathway, which accounts for only ~10-35% of total AH outflow, with this proportion decreasing in aged eyes (Goel et al. 2010). Therefore, there is a need to develop glaucoma therapeutics targeting the conventional outflow tissue where the majority of outflow resistance is generated.

All AH that drains through the conventional pathway must pass through the SC, which according to the funneling model, is responsible for the majority of outflow resistance generation (Overby et al. 2009). The mouse provides an excellent model for research into conventional AH drainage, as it has a similar anatomy to humans, is amenable to therapy, and has similar responses to glaucoma medications (Chowdhury et al. 2015). The aims of this study were 3-fold.

1. To characterize the tight-junction components of human and mouse SC endothelial cells with the ultimate goal of discovering targets for si-RNA mediated down-regulation, and the enhancement of pressure-dependent outflow facility. Such studies are reported in Tam et al. 2017; Campbell et al.

2017.

2. To identify an AAV construct, or constructs capable of efficiently transfecting the tissues of the mouse TM and/or SC endothelia, with the objective of delivering potentially therapeutic shRNA or recombinant proteins into the conventional outflow pathway. Such studies resulted in the identification of an AAV with strong tropism for the corneal endothelium, which enabled the development of a gene therapy strategy based on inducible expression of an AAV expressing MMP-3. This MMP-3 work is reported in O'Callaghan, Crosbie et al. (2017).
3. To investigate the capability of contrast-enhanced MRI in assessment of changes in AH dynamics in the glaucomatous mouse eye, or in response to IOP-lowering therapies *in vivo*.

Chapter 2

On manipulation of ocular endothelial tight junctions: potential applications in treatment of ocular hypertension and retinal disease pathology

Chapter 2: On manipulation of ocular endothelial tight junctions: potential applications in treatment of ocular hypertension and retinal disease pathology.

Introduction

Summary

Aqueous humour (AH) enters the Schlemm's canal (SC) via transcellular pores and between paracellular endothelial junctions. A major objective of this study was to characterize SC endothelial tight junctions, with a view to targeting these with siRNA, addressing the hypothesis that such down-regulation would increase junctional gaps in the SC endothelial cells, thus enabling an enhancement of AH outflow through the canal. To this end, levels of transcript and protein were examined by PCR arrays and by Western blotting on RNA and protein extracted from cultured SCE cells. Claudin-11, ZO-1, junctional adhesion molecule-3 (JAM-3) and tricellulin were all expressed at relatively high levels in these cells. Tight junction targets were also identified in murine tissues using immunohistochemistry. In humans SCE cells, claudin-11, ZO-1 and tricellulin were identified as potential targets. In mice, ZO-1 and tricellulin were also highly expressed, but claudin-11 was absent. These data were used by Tam et al. (2017) to validate an approach using tight junction-targeting siRNA to enhance AH outflow through the mouse SC, demonstrating it's use as a potential therapy for cases of POAG sub-optimally responsive to current pressure-reducing medications (see **Appendix I**).

The tight junctions of endothelial cells of the inner retinal microvasculature are well characterized in comparison to those of the SC endothelia, major components including claudin-5 and occludin. It has been well established that si/shRNA-mediated down-regulation of claudin-5 in the endothelial cells of the inner retinal vasculature results in reversible opening of the inner blood retina barrier (iBRB) allowing passage of compounds up to 1kDa in size. In a recent approach Keaney et al. (2015) demonstrated that co-suppression of claudin-5 and occludin increased paracellular clearance of soluble amyloid-β1-40 (Aβ1-40) across the endothelia of the blood-brain barrier (BBB), from the brain to the blood. Data are presented here (also in Keaney et al. 2015) to indicate that the same

procedure induces a reduction in potentially neurotoxic Aβ1-40 from the retinas of the DBA/2J mouse, a model of pigmentary glaucoma. These studies lay the groundwork for analysis of the effects of reducing Aβ1-40 in other glaucoma models and indeed other forms of retinal degeneration.

The blood-eye barriers

The eye is an isolated environment efficiently restricting the entry of plasma constituents. It is protected in the anterior segment by the blood-aqueous barrier (BAB) and in the vitreous body by the inner blood-retinal barrier (iBRB) (Freddo 2013; Gonçalves et al. 2013). The eye is an immune privileged tissue, dependent on maintaining an intact barrier integrity, with barrier breakdown accompanying a variety of ocular diseases (Chung et al. 2017; Eshaq et al. 2017). For example, in pseudoexfoliation glaucoma (PXG), a condition associated with an accumulation of fibrillar extracellular material which leads to IOP increase and glaucoma, patients display breakdown of the BAB at the iris (Kahloun et al. 2016). While iBRB breakdown is a feature of many degenerative retinal conditions as disease progresses, including age-related macular degeneration, diabetic retinopathy and the inherited retinal degenerations (Campbell et al. 2011). The BRB is composed of the iBRB, comprising the endothelial cells of microvessels of the neural retina (**Fig. 2.1a**), and the outer BRB (oBRB), represented by the retinal pigment epithelium (RPE) (Cunha-Vaz et al. 2011; Rizzolo 2014). The BAB is comprised of the blood vessels of the iris and ciliary body (CB), the non-pigmented epithelium of the CB, and the endothelial lining of the SC (**Fig. 2.1b**) (Freddo 2013). The iBRB and the BAB control the flow of fluids and solutes into the eye, specifically the endothelial cells of the SC inner wall play a central role in the removal of aqueous humor (AH). Key components of this control are the so-called tight junction complexes (TJs), joining the endothelial cells of the inner retinal vessels and those of the SC (Schneeberger & Lynch 2004).

Component of the tight junction complex

The TJ complex is a vertebrate specific adhesions complex, that forms intercellular contacts between individual cells of an epithelial or endothelial sheet. TJs are involved in numerous functions including: vesicle targeting, proliferation,

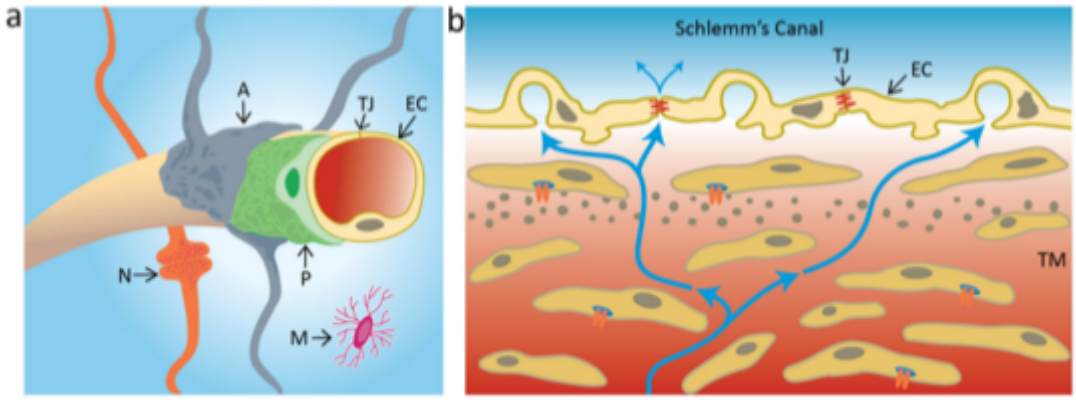

Fig. 2.1. Diagrammatic representations of the iBRB and the SC.
(a) Structure of the neurovascular unit of the inner blood retina barrier (iBRB) comprising endothelial cells (EC), pericytes (P) and atrocyte foot processes (A). The contacting point of an iBRB EC is where the tight junction (TJ) is formed. Neurons (N) and microglia (M) are located on the retina aspect of the iBRB. **(b)** Schlemm's canal endothelial cells contain TJs but also manifest giant vacuoles to allow for aqueous humour movement (see arrows for directionality of flow) into Schlemm's canal via the trabecular meshwork (TM). Diagram from Campbell et al, 2017 (see **Appendix II**)

transcription signaling, mediation of cell polarity, and most importantly the regulation of paracellular transport. The TJ complex is located at the apical periphery of the plasma membrane and acts as a gate, regulating the transport of water ions and macromolecules across the paracellular space. In freeze-fracture electron microscopy, TJs appear as interconnecting fibrils between cells formed by rows of transcellular particles. The main constituents of these transcellular strands are the 26 members (27 in mice) of the claudin family proteins, and the MARVEL proteins including: occludin, tricellulin (MARVEL D1, MARVEL D2 respectively) and MARVEL D3. In conjunction with these transmembrane proteins, there also exist cytosolic plaques associated with the TJs (Zihni et al. 2016). These are cytosolic complexes of proteins, that link the TJ proteins to the cytoskeletal structure and downstream signaling proteins. The *Zonula occludens* (ZO) proteins, ZO-1, ZO-2 and ZO-3 are a part of the MAGUK family of proteins and act as molecular adaptors that mediate this link (Van Itallie & Anderson 2014).

The claudins form the backbone of the TJ complex and mediate the charge selectivity and 'tightness' of the barrier. For example claudin-2 and -10b are cation selective, claudin-15, and -17 are anion selective, and claudin-1 and -5 are known for sealing (Zihni et al. 2016). They are made up of 4 transmembrane domains, with N- and C-terminal cytoplasmic tails; these domains form 2 extracellular loops. The first and larger extracellular loop contains several charged amino acid residues that regulate paracellular charge selectivity, whereas the shorter second loop is involved in claudin dimerization, helping to seal junctions. The intracellular C-terminal tail has the scaffold binding PDZ domain, that recruits protein such as ZO-1 (Günzel & Yu 2013). Claudins interact with each other in two ways; either head-to-head in opposing, *trans*-interactions, or in side-to-side, *cis*-interactions, within the same membrane. The claudins are capable of homo- and heterotypical interactions and this appears to be regulated by the variable region on the second extracellular loop (Van Itallie & Anderson 2013). The MARVEL proteins are essential for the formation of TJs and can act in place of one another. Occludin was the first transmembrane protein to be associated with TJs, and its loss has been linked with pathophysiological barrier loss (Furuse et al. 1993). However, this does not reconcile with the fact that occludin-deficient mice are viable with functioning barriers (Ikenouchi et al. 2005). It is hypothesized that the other MARVEL domain-containing proteins tricellulin, which is generally associated with tricellular junctions, and MARVEL D3 compensate for the loss of occludin in these mice. This is thought to be reciprocated in humans with mutations in tricellulin associated with non-syndromic hearing loss, but with no other pathologies (Mariano et al. 2011).

ZO-1 is a peripheral membrane protein with an N-terminus that has several motifs, including three PDZ domains, an SH3 domain, and a GUK domain, and a C-terminal half that associates with F-actin. The PDZ domains interact with claudins and junctional adhesion molecules (JAMs), and occludin interacts with ZO-1 via the GUK domain. In addition to these, ZO-1 also binds the adherens junction proteins, afadin and α-catenin. The SH3 domain of ZO-1 links it to junctional signaling mechanisms, through binding to ZO-1 associated nucleic acid binding protein (ZONAB), a transcriptional and post-transcriptional regulator (Zihni et al. 2016). Loss of ZO-1 results in cells that do not develop TJs; it is suggested to act as a

scaffold and is very important in proper TJ assembly. Mutations in the highly conserved U6 domain of ZO-1 lead to misplaced TJ strands localizing ectopically along the plasma membrane (Rodgers et al. 2013). ZO-1 is a crucial protein in TJ assembly and is localized to the apical junctions at the earliest cell-cell contacts, prior to the transmembrane proteins. Knockdown of ZO-1 in cells alters cytoskeletal dynamics, disrupts F-actin structures associated with junctions and delays the formation of circumferential actin bundles (Fanning & Anderson 2009).

The blood-retina barrier (BRB)

The eye is an immune privileged region of the body and TJ complexes are extremely important in the regulation of what enters and exits the eye (Taylor 2009). At the back of the eye, the retina is protected by the blood-retinal barrier (BRB). This is separable into the inner BRB (iBRB) composed of the TJs between the retinal capillary endothelial cells and the outer BRB (oBRB) formed by the TJ between retinal pigment epithelial (RPE) (Gonçalves et al. 2013). In the iBRB the prevailing claudins are claudin-1, -2, and -5, which are found throughout the blood microvessels and are present from the inner to outer areas of the neural retina (**Fig. 2.2**). The TJs of the oBRB are composed of multiple claudins throughout development, but adult human RPE express significant amounts of claudin-19 and -3. Dysregulation of the oBRB is implicated in the pathology of diabetic retinopathy and age-related macular degeneration (AMD) (Chung et al. 2017; Gonçalves et al. 2013). In diabetic retinopathy, the breakdown of the iBRB is mediated by an increase in pro-inflammatory cytokines, accompanied by alterations in claudin-5 expression, which is associated with increased vessel leakage (Klaassen et al. 2009; Kowluru & Odenbach 2004). A major pathology in wet AMD is choroidal neovascularization (CNV), where new blood vessels sprout from the choroidal vessels and penetrate into the RPE layer (Campochiaro 2000). This concludes with the local breakdown of the oBRB barrier function, these CNVs are permeable to blood components resulting in leakage to the subretinal space (Celkova et al. 2015).

The blood-aqueous barrier (BAB)

The other mechanism by which the eye separates itself from the blood supply is via the BAB. The BAB consists of the barriers in the CB, iris and SC. The AH as a whole contains 1% of the protein composition compared to plasma, whereas the ciliary process stroma has 74% of the protein content relative to plasma. This difference may be down to the difference in permeability of the ciliary vs iris vasculature (Yang et al. 2015b). The anterior iris surface is known to be a permeable sheet that allows free diffusion of AH into the iris stroma, and so the barrier of the iris vasculature would be a crucial mechanism in AC homeostasis. Following this, it is of interest to note that the iris vasculature is sealed with claudin-5, which is associated with tight barriers (Yang et al. 2015a). The blood vessels of the ciliary body stroma are fenestrated and so the non-pigmented epithelium (NPE) regulates solute flow into the AH. The cells of the NPE are joined by continuous TJ strands, which in normal eyes stop the flow of tracer into the posterior chamber. During inflammation these strands become discontinuous and the posterior chamber is flooded with tracer (Freddo 1987; Freddo 2013). Concurrent with these observations, claudin-1 is expressed across the entire NPE and not expressed by the pigmented epithelium (PE). In addition, the cells of the NPE also demonstrate expression of occludin and ZO-1 along the apico-lateral junctions and in the PE-NPE junctions (Karim et al. 2011).

In comparison to the vasculature of the CB and iris, the SC endothelium differs in various ways to that of a typical vascular endothelial cell, and in fact has some properties similar to lymphatic vessels. This unique cell type grows on a discontinuous basement membrane and expresses lymphatic specific markers such as PROX-1 and FLT-4, however it develops from the limbal blood vessels (Ramos et al. 2007; Kizhatil et al. 2014). This variation between vascular and SC endothelial cells is also consistent in the TJ formation. In freeze-fracture monkey studies TJs between the SC inner wall endothelial cells were seen as parallel intercellular stands that rarely branched or anastomosed. These junctional strands were very long but were interrupted by corridors of smooth membrane matrix that allow the passage of macromolecules such as cationised ferritin, these are the transcellular pores that were discussed earlier (Raviola & Raviola 1981; Epstein & Rohen 1991). In human eyes the junctions between SC endothelial cells are

composed of either a single tight junctional strand, two strands or, three or more strands. At zero pressure these were at almost equal ratios but as the eyes were perfused at elevating pressures this ratio shifted. As the perfusion pressure increased the junctional strands simplified, with the single strand junctions becoming almost 6 times more frequent than junctions containing three or more strands (Ye et al. 1997). This also differs in comparison to vascular endothelial cells that don't exhibit TJ changes in response to perfusion pressure and have complex anastomosing TJs (Fujimoto 1995; Schneeberger & Karnovsky 1976). To date the ZO-1 is the only member of the TJ complex that has been studied in the SC. It has been found that ZO-1 localised to the membranes of SC endothelial cells and is up-regulated after glucocorticoid treatment in conjunction with decreased hydraulic conductivity (Underwood et al. 1999). Conversely SCECs treated with ROCK inhibitors decreased transendothelial resistance (TEER) and disrupted ZO-1 membrane staining (Kaneko et al. 2016). These studies display evidence that the SC inner wall TJ complex has a role in outflow resistance generation.

In summary, SC has a highly permeable endothelial cell layer that allows diffusion of large macromolecules and has a very high hydraulic conductivity (Alvarado et al. 2004). Much of these features are due to the presence of paracellular and transcellular pores that increase in frequency in response biomechanical strain (Braakman et al. 2014). However, the current evidence suggests that SC TJs play a role in outflow resistance generation at the inner wall endothelium. In this study, the components of the human, mouse, and African Green monkey were characterized. All species expressed the ZO-1 scaffold protein and tricellulin, with both human and monkey expressing claudin-11. The ultimate goal of this characterization is the development of a novel siRNA-based therapeutic that can target the SC TJs, thus enhancing AH outflow. Published data in which siRNAs targeting the TJs of the mouse SC increased outflow facility in treated eyes, is explored further in Tam et al. (2017) (see **Appendix I)**. In addition, similar to Keaney et al. (2015), co-suppression of claudin-5 and occludin by siRNA in the DBA/2J mouse retina resulted in increased clearance of soluble amyloid-β1-40, a potential neurotoxin, into the blood from the RGC layer. A published review of the

technologies for modulation of the permeability of the iBRB and of SC endothelial cells via TJ targeting is included in **Appendix II**.

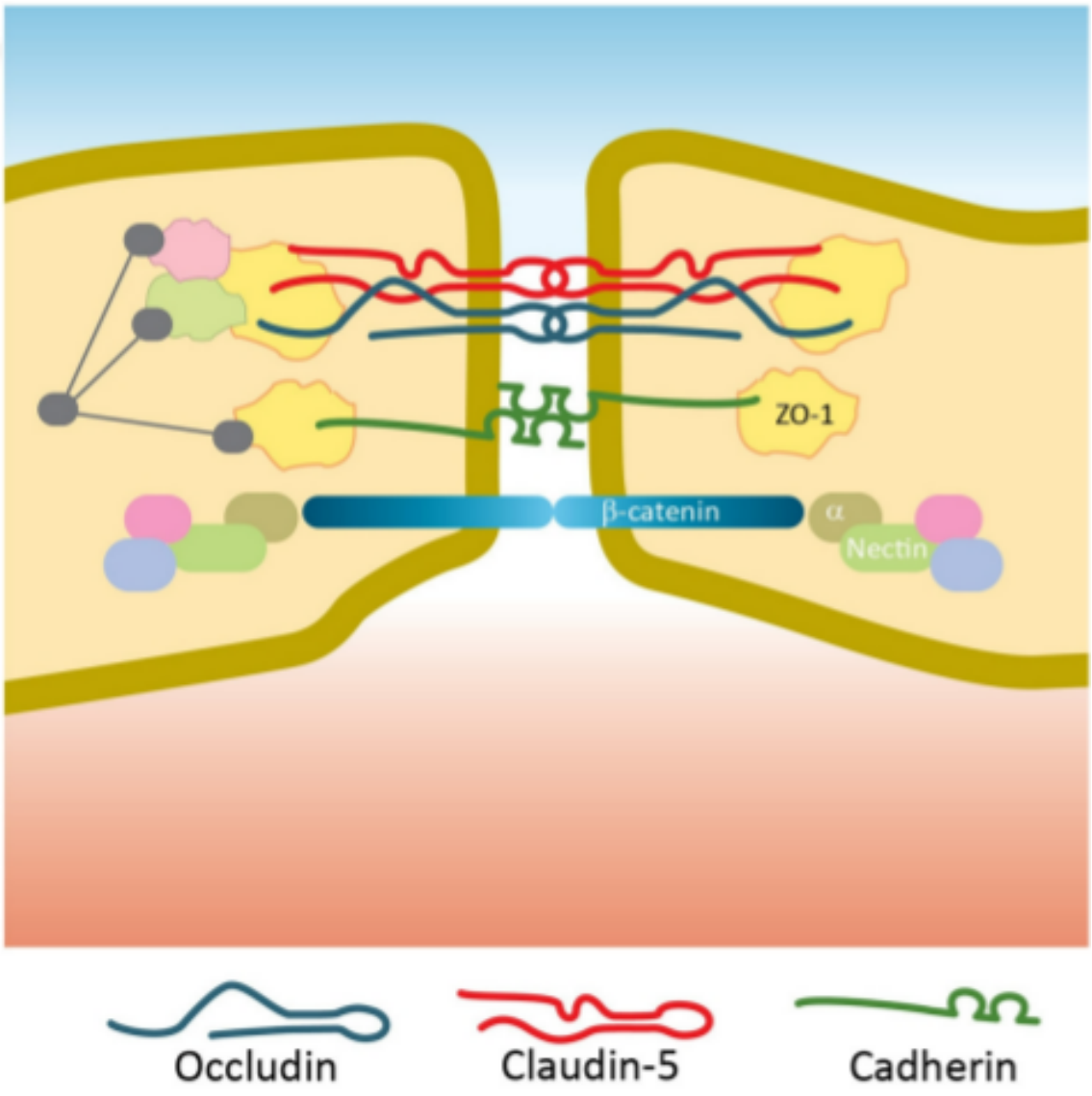

Fig. 2.2. Diagrammatic representation of the tight junction complex of the iBRB.

Tight junctions of endothelial cells associated with the inner blood retina barrier (iBRB) show an enrichment of claudin-5 and occludin at the tight junction. Diagram taken from Campbell et al. (2017) (see **Appendix II**)

Results

Characterization of the tight junction proteins in human Schlemm's canal endothelial cells (SCECs).

The objective here was to identify the TJ components of human SC cells, with the ultimate goal to use these as targets for barrier modulation in the AC. All methods used in these studies are outlined in **Chapter 5**. RNA was extracted from primary cultures of human SCECs isolated from four individual donors; the mRNA expression profile of the TJs in these cells was examined using an array (**5.3**). The mean normalized expression ($2^{-\Delta Ct}$) of genes encoding claudins, adhesion junctional proteins, scaffold proteins, and other TJ-associated proteins from four different SCEC strains is shown in **Fig. 2.3a.** The expression of the remaining targets on the array is shown in **Fig. 2.3b.** One of the highest expressed components in the TJ array was claudin-11 (or oligodendrocyte specific protein). ZO-1 was expressed to a high level, which has been previously observed in human SCECs (Underwood et al. 1999). The cell-cell adhesion molecule, junctional adhesion molecule-3 (JAM-3) was also highly expressed in human SCECs. Interestingly the other TJ proteins of the eye, such as claudin-5, claudin-1 and occludin (Campbell et al. 2010; Karim et al. 2011), were expressed at a low level. Collectively this evidence points to claudin-11 being the primary claudin in the human SCEC. Transcript levels of claudin-11 and ZO-1 were also compared between SCECs and human TM cells. mRNA expression levels ($2^{-\Delta\Delta Ct}$) were calculated relative to TM cell mRNA levels, and claudin-11 was found to be expressed 2.52-fold higher in SCEC than in TM cells (**Fig. 2.3c**)**.** No difference was found in ZO-1 expression between the two cell types.

Claudin-11 and ZO-1 protein expression was confirmed in cultured SCEC by Western blot (**Fig. 2.4a**)**.** In addition the MARVEL family protein tricellulin was also detected in cultured SCECs, which was not included in the PCR array but is a very common junctional protein. Similarly to other studies (Park et al. 2014b; Heimark et al. 2002), expression of vascular endothelial (VE)-cadherin by SCEC was confirmed (**Fig. 2.4a**)**.** Consistent with PCR array data, no claudin-5 was detected, despite expression previously observed in cultured monkey SCs (Kameda et al. 2012). In addition, no claudin-11 or tricellulin expression was observed in TM cells. Whereas ZO-1 expression was consistent in both cell types (**Fig. 2.4b**), as

has been previously reported (Underwood et al. 1999). Immunohistochemistry was undertaken in SCECs to visualize TJ component localization (**5.20**). ZO-1, tricellulin, and claudin-11 all displayed discontinuous membrane staining patterns in SCEC monolayers (**Fig. 2.4c**).

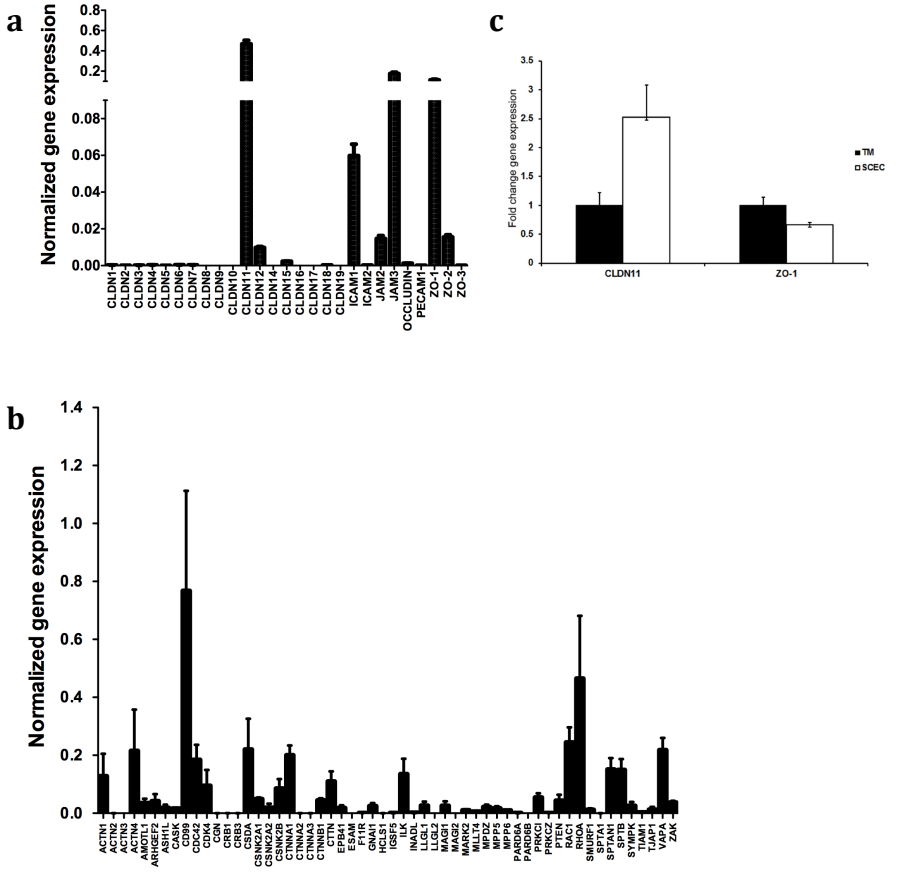

Fig. 2.3. Expression of Tight Junction Proteins in human outflow tissue. **(a)** The human TJs RT^2 Profiler PCR array was used to examine expression of claudins, adhesion junctional proteins and scaffold proteins. Note break in scale for normalized gene expression. **(b)** Expression of all remaining junction related components. Bar graphs illustrate average relative gene expression ($2^{-\Delta Ct}$) normalized to 5 housekeeping genes from 4 different SCEC strains: SC65, SC68, SC76, and SC77. Data are mean ± s.e.m. **(c)** Comparison of claudin-11 and ZO-1 gene expression between cultured TM and SCECs. Bar graph illustrates fold change in gene expression ($2^{-\Delta\Delta Ct}$). Data represents mean fold change in SC77 and TM93 cell strains ± s.e.m (n=2).

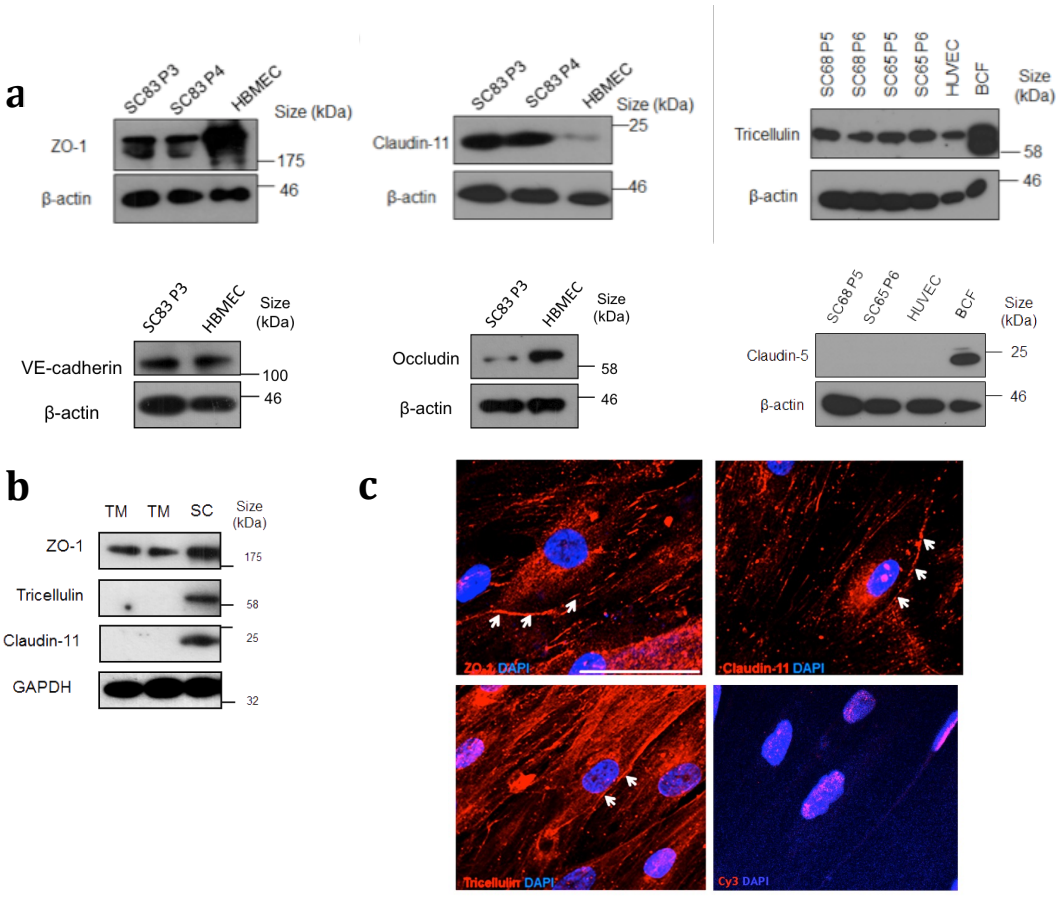

Fig. 2.4. Characterisation of tight junction protein expression in human Schlemm's canal endothelial cells.

(a) Protein expression of ZO-1, claudin-11, tricellulin, VE-cadherin, occludin, and claudin-5 in SCECs was analysed using Western blot. HBMEC = human brain microvascular endothelial cells; BCF = Mouse brain capillary fraction; β-actin as loading control. Different SCEC strains are denoted by passage (P) number. **(b)** Comparison of tight junction protein expression between human TM (TM120 and TM130) and SCEC. **(c)** Immunodetection of ZO-1, claudin-11 and tricellulin in human SCECs with a control treated with secondary antibody, but no primary antibody. White arrowhead indicates junctional staining. Cy3 = red; Blue = DAPI nuclei staining. Scale bar, 50µm.

siRNA treatment of SCECs

After TJ characterization, the efficacies of pre-designed siRNAs targeting the human transcripts of claudin-11, ZO-1 and tricellulin in cultured SCEC were investigated **5.5**. Confluent SCECs were transfected with 40nM of each siRNA, and levels of endogenous TJ expression were assessed in a time-dependent manner by Western blot. Time-dependent down-regulation of claudin-11 expression to 5 ± 3% (p<0.0001), 11 ± 1% (p<0.0001) and 9 ± 4% (p<0.0001) (mean ± s.e.m.), was achieved at 24, 48 and 72hr post-transfection respectively, as compared to NT-siRNA (**Fig. 2.5a**). ZO-1 protein expression was reduced to 72 ± 3% (p=0.005), 64 ± 4% (p=0.0004) and 49 ± 18% (p=0.02) at 24, 48 and 72hr post-transfection respectively (**Fig. 2.5b**). In addition, tricellulin expression was reduced to 75 ± 0.2% (p=0.002), 81 ± 6% (p=0.012) and 87 ± 8% (p>0.05) at 24, 48 and 72hr respectively post treatment (**Fig. 2.5c**). These siRNAs were used by Tam et al. (2017) to test SCEC layer permeability as shown in **Appendix. I.**

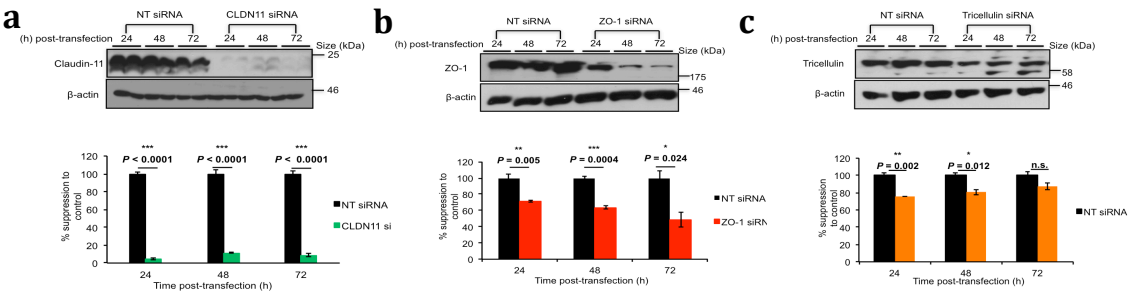

Fig. 2.5. Downregulation of human SCEC tight junction transcripts using siRNA.

Representative Western blots of **(a)** claudin-11, **(b)** ZO-1 and **(c)** tricellulin knockdown in cultured human SCEC over a 72hr period. Attached bar graphs demonstrate densitometric analysis of percentage protein normalized to β-actin. NT siRNA = non-targeting siRNA. Data shown are mean ± s.e.m; Symbols n.s, *, **, *** denote p-values of >0.05, <0.05, <0.01, <0.001 respectively.

Characterization of tight junctions in the mouse and monkey SC endothelia

SC endothelial cell TJs of other species were investigated. RNA was extracted from dissected mouse outflow tissue, and the expression of TJ transcripts from four mice was analysed on a TJ array (**5.4**). The mean normalized expression ($2^{-\Delta Ct}$) of genes encoding claudin, adhesion junctional proteins, scaffold proteins, and other TJ-associated proteins from four mouse eyes is shown (**Fig. 2.6a**)**.** High expression levels of Claudin-1,-4,-7 and -10 were consistent among tissue from all mice (n = 4); the TJ protein occludin and TJ associated proteins ZO-1,-2-,3 and JAM-3 were also expressed to a high level. To validate the presence of these target transcripts in the mouse SC, frozen mouse sections were stained with antibodies against the TJ targets. Immunofluorescent images show tricellulin, occludin, and ZO-1 staining to be predominantly localized to the SC inner wall. In particular, it was observed that ZO-1 staining was diffusely distributed in the cytoplasm, tricellulin and occludin staining was continuous along the SC endothelial cells. ZO-1, occludin, and tricellulin staining was also seen in the outer SC wall and the TM of the mouse AC (**Fig. 2.6c**). None of the claudin proteins that were stained for showed any immunoreactivity in the mouse SC (**Fig. 2.6d**). Claudin-4 was detected in corneal stroma and the SC outer wall, claudin-1 was detected in the ciliary body epithelium, claudin-7 localised to the cornea epithelium and claudin-10 to the cornea endothelium and TM, no claudin-11 staining was seen in the anterior chamber. JAM-3 staining was consistent along the cornea endothelium.

In addition, immunohistochemistry was performed on paraffin sections of African green monkey anterior segments to characterize the TJ components of the outflow region as outlined in **5.24**. Hematoxylin and eosin staining (H&E) of the AC clearly identified the iridocorneal angle and conventional outflow tissues (**Fig. 2.7a**)**.** Confocal imaging showed continuous claudin-11 staining along the monkey SC inner wall and the TM cells. Similarly, ZO-1 and tricellulin staining was observed in a punctate pattern along the SC inner wall. All the TJ proteins stained were present between the TM cells, but the staining was less intense than in the SC inner wall endothelium. In addition, no claudin-5 staining was seen in the monkey outflow tissue despite its presence being reported in cultured SC cells from cynomolgus monkey eyes (**Fig. 2.7b**) (Kameda et al. 2012)**.**

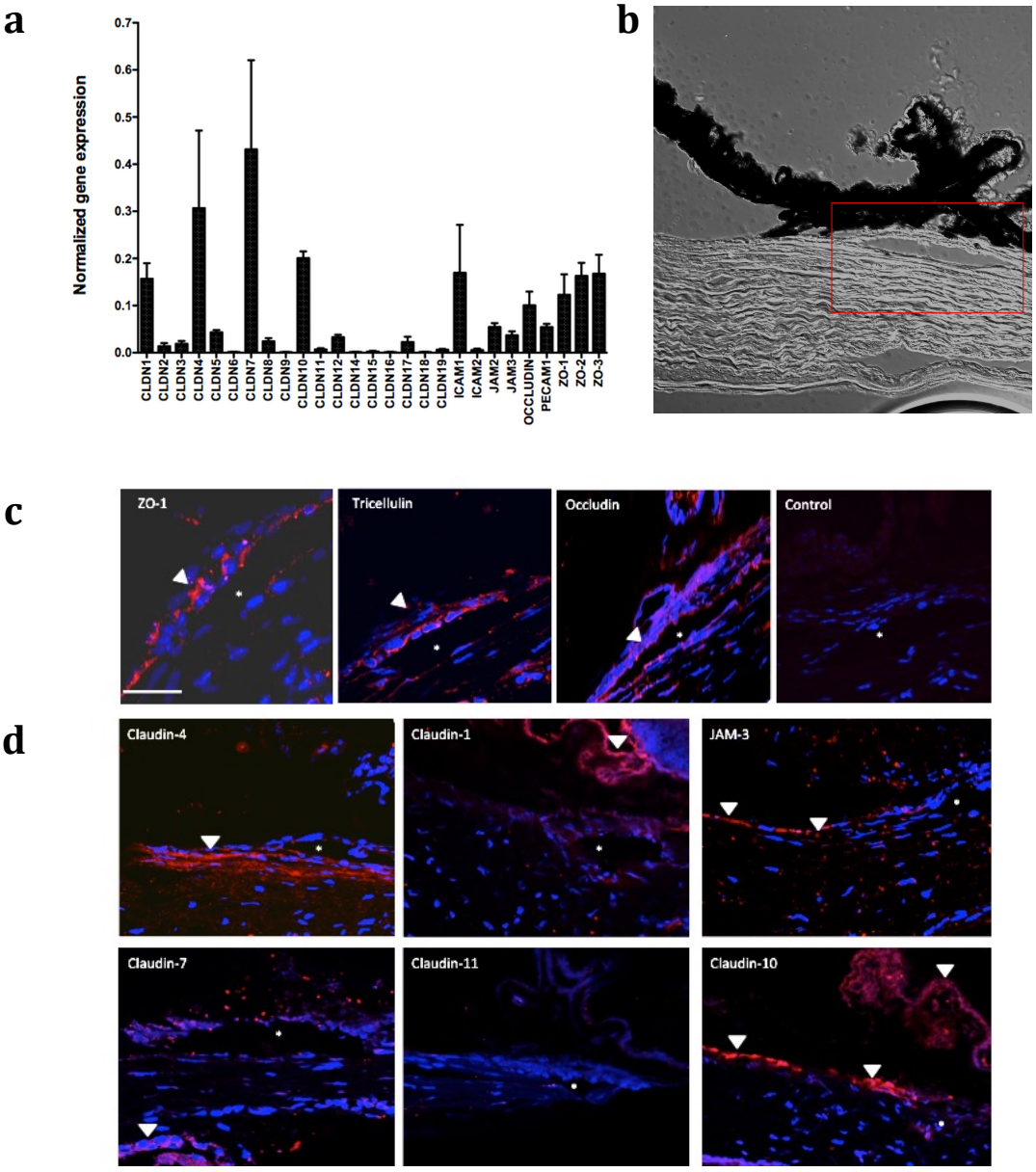

Fig. 2.6. Immunostaining of tight junctions in the mouse anterior chamber. **(a)** Normalised gene expression profile of tight junctions dissected mouse outflow tissue (2-ΔCt). **(b)** Representative image of mouse anterior chamber angle, red box denotes area displayed in stained images. **(c)** ZO-1, tricellulin and occludin staining is present in the inner wall of the SC in frozen mouse sections. **(d)** Claudin-4, JAM-3 and Claudin-10 staining is found in the corneal endothelium, with claudin-4 staining in the SC outer wall and claudin-10 detected in the TM. Claudin-7 antibody stained the corneal epithelium, claudin-1 and claudin-10 were detected in the non-pigmented epithelium (NPE) of the ciliary body. No claudin-11 staining was found in the mouse anterior chamber. White arrowheads indicate immunodetection of tight junctions (Cy3), asterisks denotes lumen of the SC, scale bar = 50μm. Blue = DAPI (nuclear stain) and red = Cy3.

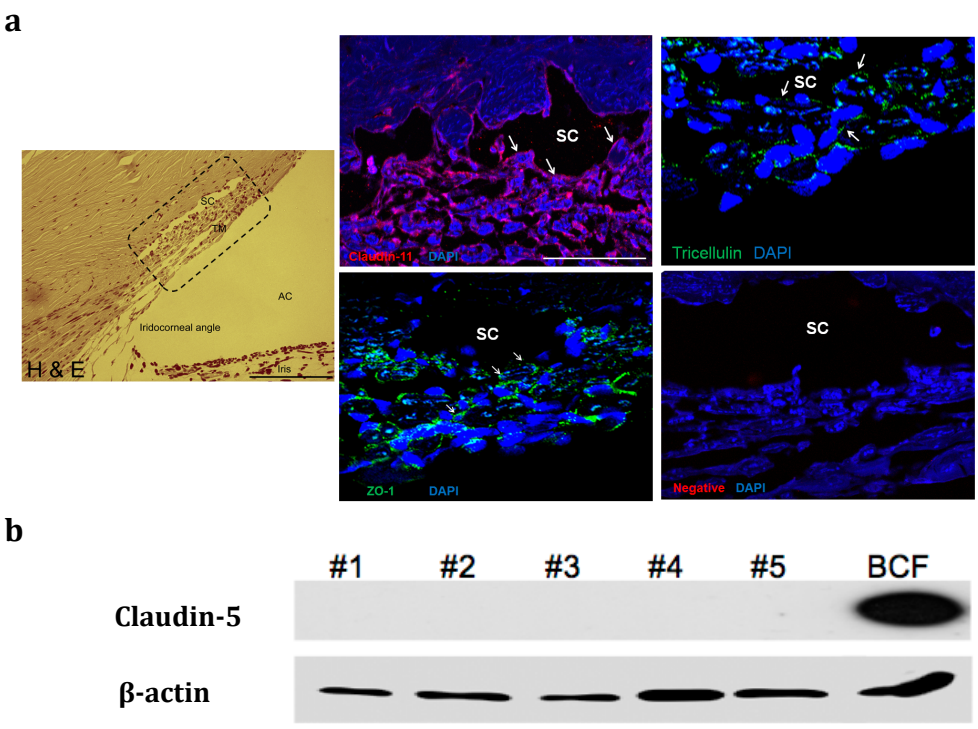

Fig. 2.7. Tight junction detection in the outflow tissues of the Africa green monkey.

(a) H&E staining of monkey paraffin sections clearly shows the location of the SC and TM (left panel). Boxed area depicts superimposed regions shown in immunofluorescence images. Claudin-11, tricellulin and ZO-1 staining was localized to the SC and TM. AC = anterior chamber; SC = Schlemm's canal lumen; TM = trabecular meshwork. Scale bar, 200μm. White arrows indicate detection of corresponding tight junctions at the inner wall of SC endothelium. Negative = no primary antibody. Scale bar, 50μm. **(b)** Western blot for claudin-5 in SC endothelial cells dissected from five different African green monkeys. β-actin was used as a loading control. BCF = mouse brain capillary fraction as positive control.

An attempt to isolate mouse SC endothelial cells

Immunostaining of mouse tissue did not detect the claudin component of the mouse SC, though it is an integral part of any TJ. The tissue, used for the TJ mRNA array, was roughly dissected and contained other tissue contaminants. Therefore, the isolation of the mouse SC was attempted. Flow cytometry sorting was attempted, to enrich dissociated mouse anterior chamber for SC endothelial cells (**5.11**). There are no SC specific markers (Ramos et al. 2007), and so two different markers, PECAM-1 (CD-31) and VEGFR-3 (Flt-4), were chosen to separate the SC cell population. Firstly frozen mouse anterior segment sections were stained with PECAM-1 and VEGFR-3 antibodies to confirm their presence in the mouse SC (**Fig. 2.8a**)**.** Next, the anterior chambers were dissected from 10 WT C57BL/6J mice and the CB and iris were removed. PECAM-1 staining had previously demonstrated the presence of SC endothelial cells in these dissected anterior chambers (**Fig. 2.8b**)**.** The anterior chamber dissections were dissociated using collagenase and then trypsin. The subsequent cell supernatant was stained with VEGFR-3 and PECAM-1 Alexa-fluor conjugated antibodies. This cell supernatant underwent FACS analysis and the total population is shown as side-scatter area (SSC-A) plotted against forward-scatter area (FSC-A), this is seen to be a highly heterogeneous mix indicating incomplete dissociation. In this regard multiple gating measures were used to enrich the number of single cells. Cell clumps were excluded using a FSC-width vs FSC-area gate, granular material such as cell debris were excluded using a SSC-area vs SSC-width gate, and dead cells were excluded using a propidium iodide (PI) stain vs FSC-area gate. The resulting double positive population that stained for both antibody conjugates was collected as well as a double negative population to be used as a control, these populations are shown with and without the excluded cell populations (**Fig. 2.9a**)**.** RNA was extracted from these cell populations and analysed for relative expression of genes expressed in anterior chamber tissues; PECAM-1 (endothelial cells), PROX-1 (lymphatic cells), keratin-12 (corneal epithelial cells), opticin (ciliary body),(Takanosu et al. 2001) claudin-7 (cornea),(Inagaki et al. 2013) JAM-3 (cornea endothelium) and VEGFR-1 (blood endothelial cells). Results demonstrated that relative to the double negative control population PROX-1, claudin-7, JAM-3 and VEGFR-3 expression was down-regulated and PECAM-1, keratin-12 and opticin expression remained stable in the

double positive population ($2^{-\Delta\Delta Ct}$), indicating minimal SC cell enrichment (**Fig. 2.9b**). Attempts were made to isolate SC endothelia using laser capture microscopy (LCM), however tissue contamination was too high and RNA yield too low. Briefly, fresh frozen mouse anterior chambers were cyro-sectioned using RNase-free methods. Within hours these sections were processed for microdissection using LCM; this includes cutting around the tissue of interest with an ultra-violet laser to release it from surrounding tissue and an infrared laser is used to heat the thermoplastic film that then isolates the target tissue. However, during this process it was found the target tissue was too small and large sections of cornea would accompany the outflow tissues, contaminating any resulting sample.

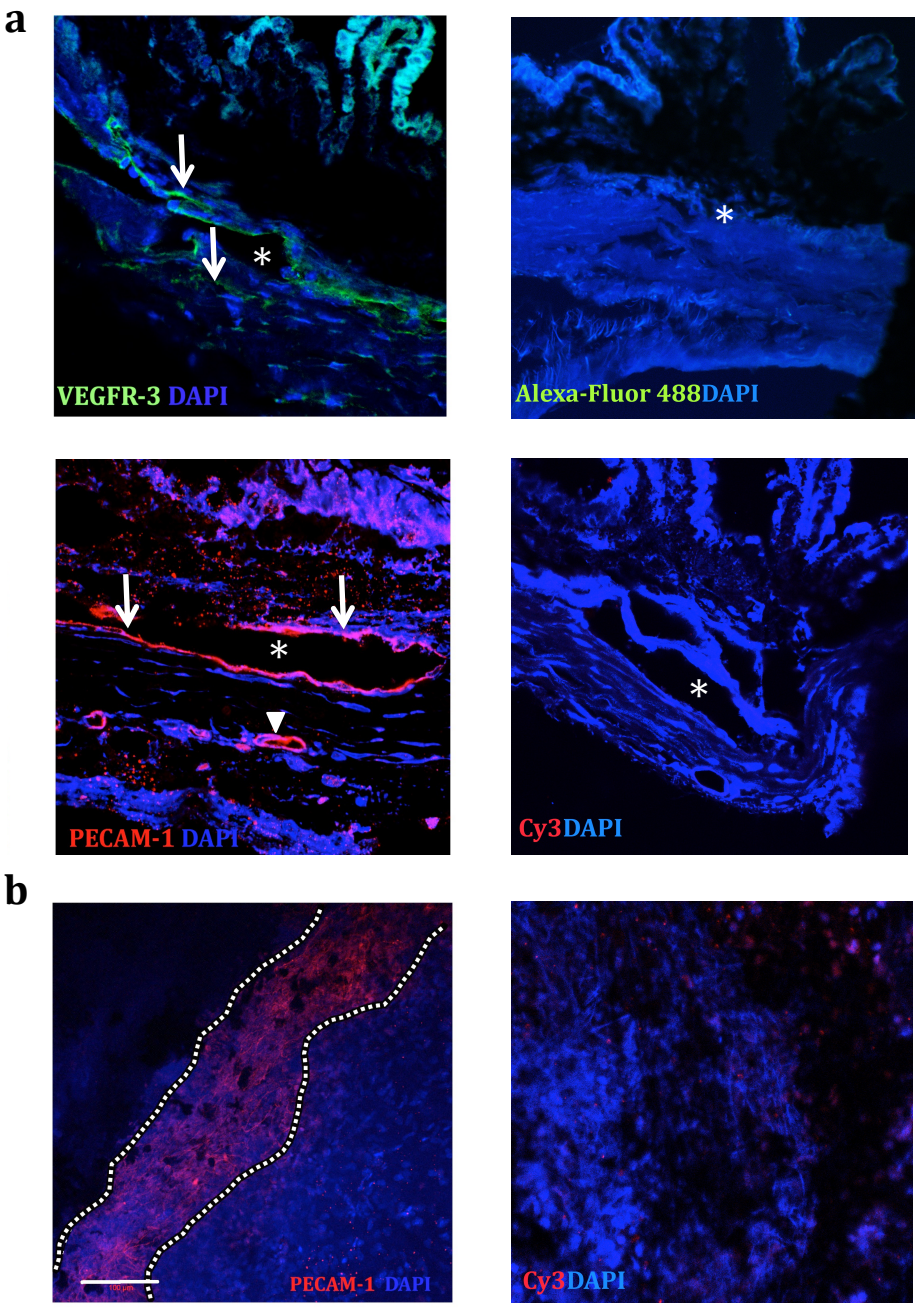

Fig. 2.8. Staining of mouse Schlemm's canal endothelial cells with PECAM-1 and VEGFR-3.

Prior to FACS analysis frozen C57 mouse AC sections were stained for the presence of VEGFR-3 (green) and PECAM-1 (red) **(a)**. White arrows = VEGFR-3 and PECAM-1 staining in the SC inner and outer wall endothelial cells; white arrowhead = PECAM-1 staining in the endothelium of the episcleral blood vessels; asterisks = SC lumen. **(b)** Flatmount C57 anterior segment stained for PECAM-1 (red) to mark the SC. Dotted line = SC border; scale bar = 100μm. Red = Cy3; Green = Alexa-fluor 488; Blue = DAPI nuclear staining.

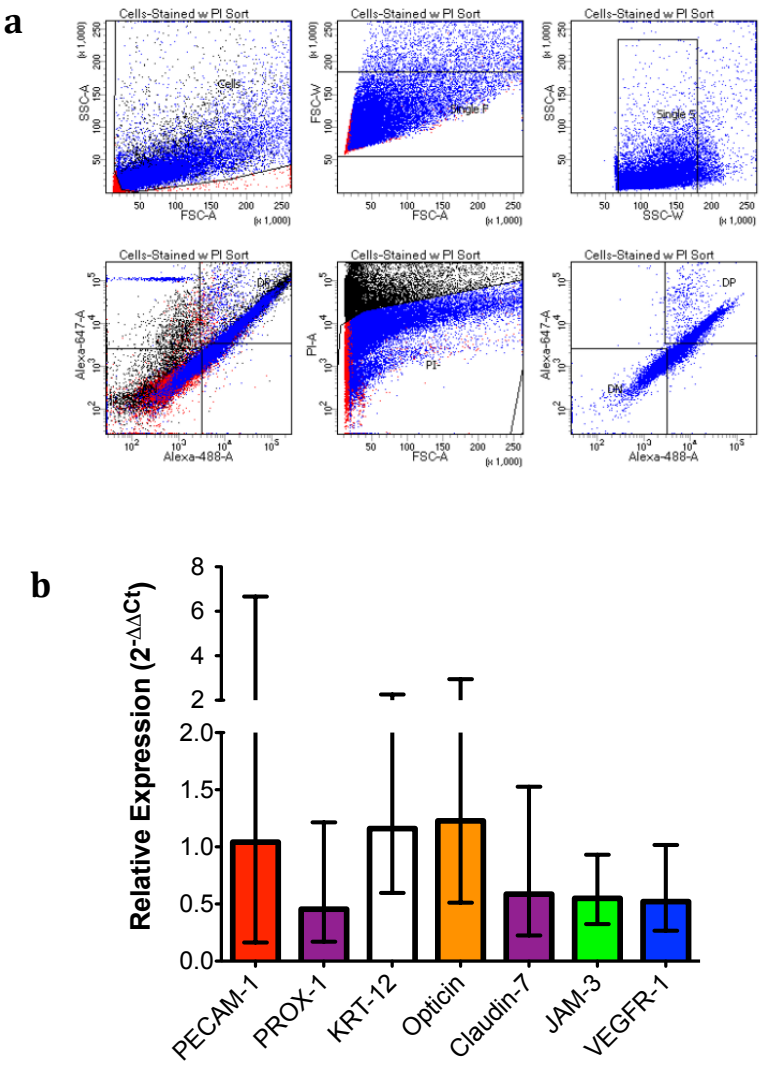

Fig. 2.9. FACS analysis of dissociated double stained mouse anterior chamber.

(a) Report of flow cytometry cell sorting describing, cell morphology, cell size, PI staining, double positive (DP) and double negative (DN) populations. Total events = 62 133; PI positive = 40 367; DP = 7 000; DN = 4 884. Alexa-647 = PECAM-1; Alexa-488 = VEGFR-3. Red = PI positive cells, Black = All events, Blue = Accepted events. PI = propodium iodide. **(b)** Fold change in expression of AC tissue genes in the double stained cell population compared to the double negative population. PECAM-1 (0.16 < 1.04 < 6.66); PROX-1 (0.17 < 0.45 < 1.21); KRT-12 (0.60 < 1.16 < 2.26); Opticin (0.51 < 1.23 < 2.94); Claudin-7 (0.22 < 0.59 <1.53); JAM-3 (0.32 < 0.55 < 0.93); VEGFR-3 (0.27 < 0.52 < 1.02). KRT-12 = Keratin-12. Data is mean fold change ($2^{-\Delta\Delta Ct}$); error bars denote min and max fold difference.

In summary, data presented above resulted in the identification of ZO-1 and tricellulin as putative targets for down-regulation in the endothelia of the mouse SC, with the goal of enhancing AH outflow through the SC. In addition claudin-11 could also serve as an attractive target in primates. These results were exploited in Tam et al. (2017), in which co-suppression of ZO-1 and tricellulin were shown to significantly enhance outflow facility in the murine eye ex vivo, see **Appendix I**.

iBRB modulation in the DBA/2J mouse model of glaucoma

As outlined in the appended article (Campbell et al. 2017), the permeability of the inner blood-retina barrier can be increased to accommodate the passage of compounds up to ~1kDa, by down-regulation of claudin-5. This approach was further developed in Keaney et al. (2015), where it was shown that co-suppression of the selected tight junctions claudin-5 and occludin results in increased blood-brain barrier permeability to ~3kDa macromolecules. Thus increasing the clearance of the potentially neurotoxic soluble-Aβ1-40 from the brains of a murine Alzheimer disease model into the peripheral circulation, with concomitant improvement in cognitive function. As a component of this work, it was of interest to explore whether or not the same technique could be of used to reduce levels of Aβ1-40 from the retinas of the DBA/2J mouse model of pigmentary glaucoma. Data outlining this study is supplied below.

The effect of retinal barrier modulation was examined in DBA/2J mice, using adjusted methods described in Keaney et al. (2015). Nine-month old DBA/2J mice are known to have high IOP and the effect of iBRB opening on IOP was examined. The baseline IOP of 9M DBA/2J mice was measured prior to tail-vein siRNA injection as in **5.31**. The control group received NT siRNA and the targeting group received occludin siRNA, 24hrs later the treatment group received tail vein claudin-5 siRNA. IOP was measured again 48 hrs after NT/occludin treatment. There was a slight increase in average IOP in both the control (20.4 to 21.3 mmHg) and targeting groups (18.2 to 19.2 mmHg), however no significant difference was found between the groups (**Fig. 2.10a**)**,** individual IOPs are shown in **Fig. 2.10b.** Knockdown of occludin (61.26 ± 8.25 %, $p = 0.008$) and claudin-5 (63.39 ± 4.55 %, $p = 0.038$) protein relative to NT siRNA treated retinas was confirmed by Western blot, which were repeated three times (**Fig. 2.11b**). DBA/2J animals show RGC degeneration at 8M, and it was examined if they also accumulate Aβ1-40 in the

retina. Retinas from 8M DBA/2J and 3M C57 wild-type (WT) mice were cryosectioned and stained for Aβ expression (**5.8**). No Aβ was seen in the WT ganglion cell layer (GCL), but was found to accumulate in the DBA/2J GCL, retinas from 4 different animals were evaluated (**Fig. 2.11a**)**.** Following this finding the levels of soluble Aβ1-40 in the retina were compared between NT siRNA and claudin-5/occludin siRNA treated mice using ELISA (**5.9**). When compared with NT controls animals treated with targeting siRNA had lower levels of soluble Aβ1-40 in the retina relative to circulating plasma Aβ1-40 (n = 12, p = 0.045)(**Fig. 2.11c**). No difference in TUNEL staining was seen in treated and untreated DBA retinas, with both displaying apoptotic retinal ganglion cells (**Fig. 2.11d**)**.**

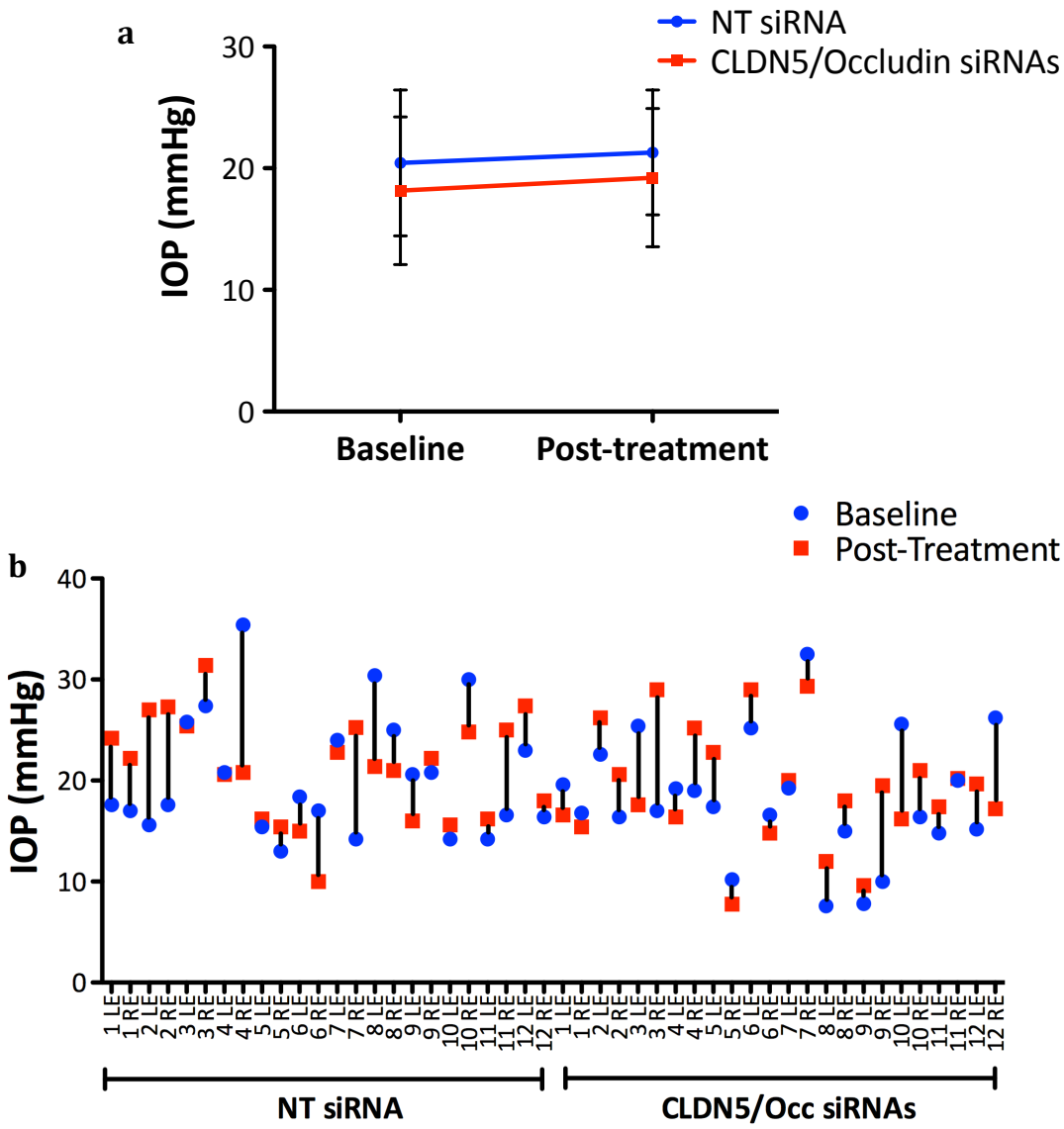

Fig. 2.10 . IOP of 9M DBA/2J Mice After siRNA Treatment.

(a) Average IOP of 9M DBA/2J mice before siRNA injection and after 48hrs after NT and occludin/claudin-5 siRNA treatment. Occludin treated mice were injected with claudin-5 siRNA after 24 hrs. IOP means (mmHg), error bars denote s.d (n=24 eyes per experimental group). **(b)** Individual IOP for each eye shown, baseline and post-treatment IOPs are shown for each eye (mmHg). Bar connects baseline and post-treatment values.

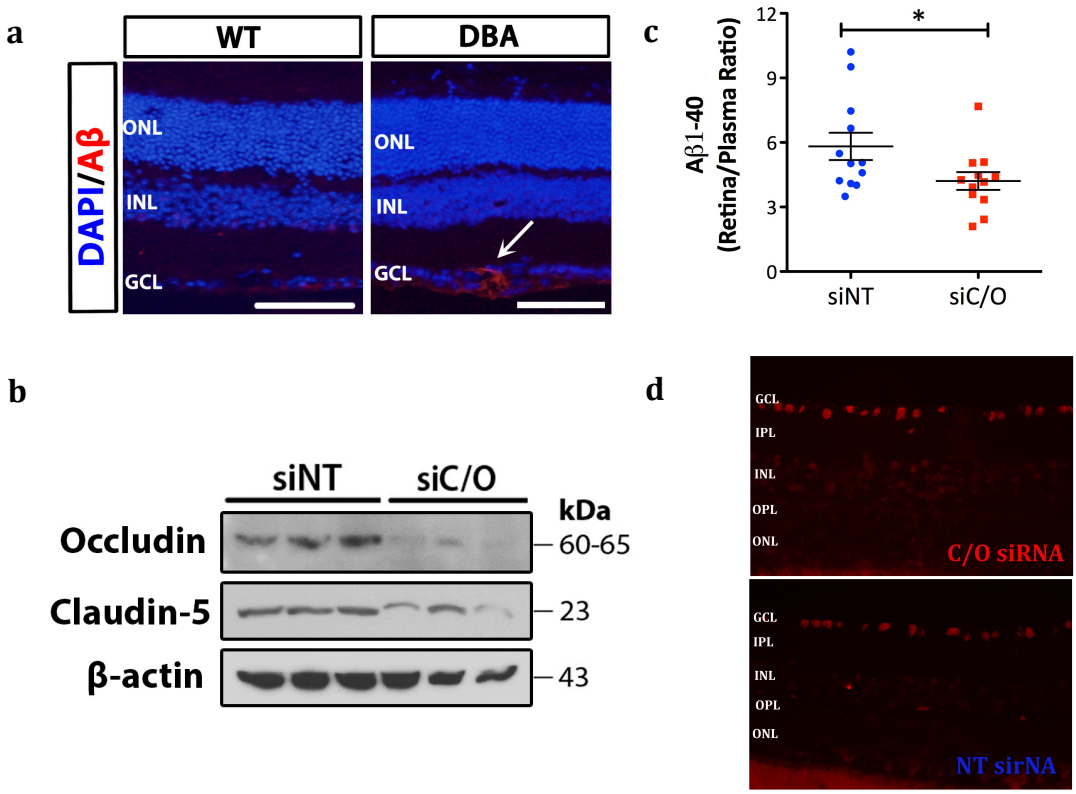

Fig. 2.11. Systemic administration of claudin-5 and occludin siRNA leads to increased paracellular clearance of amyloid-β (Aβ) 1-40 from 8-month old DBA/2J retinas.

(a) Aβ immunostaining in the ganglion cell layer of wild-type (WT) and DBA/2J mouse retinas (Scale bar = 50 μm). **(b)** Western blot analysis of claudin-5 and occludin in retinas of DBA/2J mice following systemic administration of non-targeting (NT) or claudin-5 and occludin siRNAs. **(c)** Retina/plasma ratios of Aβ(1-40) (pg/ml soluble retina Aβ(1-40) to pg/ml plasma Aβ(1-40)) in DBA/2J mice after a single round of siRNA administration (unpaired Student's *t*-test, n = 12 animals per experimental group, **p* = 0.045. Data are means ± s.e.m). **(d)** Representative image of TUNEL staining of 8M DBA retinas, the retinal ganglion cells were TUNEL positive. (ONL: outer nuclear layer, OPL: outer plexiform layer, INL: inner nuclear layer, IPL: inner plexiform layer, GCL: ganglion cell layer).

Discussion

All conventional outflow must pass through the SC and therefore pass through the barrier of the SC inner wall. In tracer studies high outflow regions of the conventional outflow tissue correlate with paracellular, but not transcellular pore density (Braakman et al. 2015a). This indicates that the paracellular flow of AH through the SC endothelia is crucial for outflow resistance generation, and tight junctions play a significant role in paracellular flow in other endothelia. While it has previously been demonstrated that antisense down-regulation of ZO-1 in SCECs increases hydraulic conductivity across a confluent monolayer (Underwood et al. 1999), TJ components of the SC in human, mouse and monkey tissue are characterized here for the first time. TJ mRNA profile indicated that claudin-11 and ZO-1 were the main components in the human SCEC TJ complex. Protein expression was confirmed with Western blot and immunostaining of cultured SCECs. Due to low occludin expression in the human SCEC, tricellulin expression was analysed using Western blot, as it has been shown that it can play a similar role, though it is usually associated with tricellular junctions (Kitajiri et al. 2014). In Western blot, tricellulin was strongly expressed in the SCECs and occludin was expressed to a low degree. Interestingly tricellulin localized in bicellular junctions in the immunostaining. Both tricellulin and claudin-11 are SC specific TJ proteins and neither was expressed in the TM, whereas ZO-1 is expressed in both tissues, as has been demonstrated previously (Underwood et al. 1999; Yang et al. 2011). As claudin-11 is expressed to such a high level in SCEC compared to the TM cells, this may also be used as a specific marker for identifying SC cells. Claudin-11 is expressed in the sertoli cells of the blood-testis barrier, the salivary gland, and in the myelin sheath of the CNS, including the optic nerve (Devaux & Gow 2008; Gow et al. 1999; Lourenço et al. 2007). Claudin-11 was found to be crucial for barrier function and for paracellular permeability in these tissues, and reduction of claudin-11 increases permeability across tissue barriers (McCabe et al. 2016; Denninger et al. 2015). Therefore, claudin-11 in conjunction with tricellulin and ZO-1 are significant targets for increasing paracellular passage across the SC inner wall. This work has been used to show that siRNA knockdown of these TJ components does in fact lead to increased permeability across the SCEC monolayer as shown in Tam et al. (2017), see **Appendix I**.

Of the readily available mammalian models, only non-human primates and rodents have an outflow pathway of analogous design to humans (Li et al. 2013). The mouse eye has similar anatomical structure, outflow pathways and response to IOP-lowering drugs in comparison to human eyes (Aihara et al. 2003). The mouse eye has similar functional properties to the human eye in that it has no detectable washout rate and a linear pressure-flow relationship over a broad range of IOPs (Lei et al. 2011). Clearly there are advantages in using the mouse as a model for investigating outflow and glaucoma, and the characterization of the mouse SC TJs is of substantial value in that regard. As with the human SC cells the expression of various TJ genes was analysed on using RT-PCR array. However, due to the small size of the mouse SC and outflow tissue, the dissection used to remove it was extremely rough. There was a number of other tissue contaminants such as the cornea and ciliary body that express high levels of TJ related genes (Karim et al. 2011; Inagaki et al. 2013). The highest expressed claudins are claudin-1, -4, -7, and -10; apart from these the other highly expressed genes are ZO-1, -2, -3, occludin and intercellular adhesion molecule 1 (ICAM-1). Due to the difficulty in isolating mouse SC tissue the TJs were characterized by immunohistochemistry. Similarly to the human SC the mouse inner wall expresses both tricellulin and ZO-1. ZO-1 shows a discontinuous and tricellulin a continuous staining pattern along the inner wall. Whereas in the African green monkey sections both ZO-1 and tricellulin staining in the SC and TM are in a punctate pattern, this is common of tricellulin staining when localized to tricellular junctions (Ikenouchi et al. 2005). Interestingly, though very little occludin was expressed in the human SC cells there was continuous staining of occludin along the mouse inner wall. Occludin expression may be decreased on culture of the SC cells and may be expressed in the *in vivo* eye, as is the case with PECAM-1, another SC membrane protein (Perkumas & Stamer 2012).

Unfortunately, none of the claudin targets that were investigated were found in the SC inner wall endothelial cells. No claudin-11 expression was found in the SC, or in any other tissue of the mouse anterior chamber, but it was found in a continuous pattern along the monkey SC endothelium and TM cells. Of the other targets claudin-1 was found in the ciliary NPE, claudin-4 and -10 and JAM-3 in the corneal

endothelium. Interestingly claudin-4 stained in the tissues distal to the SC including the SC outer wall, although staining was diffuse and did not appear membrane bound. Claudin-10 staining was seen in the TM and in the ciliary NPE, which has not been published previously. Using targets validated in this study we have now shown that delivery of ZO-1 and tricellulin targeting siRNA to the mouse outflow tissue results in increased outflow facility. Included here are EM data compiled for us by collaborator Elke Drecoll (Nuremburg) demonstrating increased paracellular gaps in the SC inner walls of treated eyes 48 hr after treatment (**Appendix I**).

As TJs require claudin molecules for their formation and the other species investigated had claudin proteins in the SC, it can be predicted that there is an unidentified claudin protein in the mouse SC (Furuse et al. 1998). Therefore attempts were made to isolate the mouse SC endothelial cells, using LCM and FACS. The LCM attempt failed as the mouse SC tissue was an extremely small area and could not be separated from the cornea and RNA yield was extremely low. For FACS analysis two markers were used to separate the SC cell population, PECAM-1 an endothelial cell marker and VEGFR-3 a lymphatic cell marker, both of which are expressed in the mouse SC (Lertkiatmongkol et al. 2016; Rakocevic et al. 2016; Kizhatil et al. 2014). There were many difficulties in the dissociation of the anterior segments and the resulting cell population sorted was extremely low ~60 000 cells, with 65% of them PI positive, a marker of cell death. Though yield of sorted double positive (DP) and double negative (DN) cells was low, there was sufficient tissue for RT-PCR analysis. To this end specific cell biomarkers were used to demonstrate SC cell enrichment in the DP population. The lymphatic marker PROX-1, corneal epithelial marker claudin-7 (Nakatsukasa et al. 2010), corneal endothelial marker JAM-3, and vascular endothelial marker VEGFR-1 were all down-regulated in the DP population relative to the DN population. However, there was no difference in PECAM-1, KRT-12, and opticin expression between the DP and DN populations. KRT-12 is highly expressed in the corneal epithelium but is also found in corneal stroma cells (Carlson et al. 2003), and opticin is expressed in the iris and ciliary body (Forrester 2004; Ramesh et al. 2004). This would indicate that there are still significant cell populations from both the cornea and CB

in the DP cell population, both of which express high amounts of TJ proteins. There is significant room for improvement in this method especially in the corneal dissociation, which must be at once more thorough to get a greater sorted population and more gentle to the cells to reduce the amount of dead cells. Future work with mice however would benefit hugely from the ability to analyse SC specific expression changes after *in vivo* treatments.

In this chapter's results section, an attempt to isolate a mouse SC population using LCM is briefly outlined. The technical challenges associated with targeting the minute mouse SC monolayer again resulted in poor SC cell enrichment. In both the FACS and LCM approach, the robust nature of the cornea resulted in a lack of tissue dissociation in the former and an inability to separate the target area from surrounding tissues in the latter. Therefore, any further approaches would profit from avoidance of corneal processing, such as used in isolation of human SC tissue populations, which is achieved with the use of a gelatin-coated suture. The SC lumen is cannulated with the suture and the entire tissue is then incubated in cell culture medium for a period of 3 weeks, over this period the SC cells adhere to the suture, which is subsequently removed and the captured cells seeded onto cell culture dishes (Stamer et al. 1998). Due to the inherent size differences between the mouse and human tissue this was not a viable method in these studies. However, those attempts at mouse SC isolation outlined here indicate that development of a method capable of such delicate SC lumen cannulation would be have the highest chance of success.

In summary, these studies have resulted in the identification of TJ targets in the SC inner wall endothelial cells of human, primate and mouse. These discoveries have significantly contributed to the demonstration of the role of TJs in the regulation of AH outflow and the proof-of-concept that siRNA-mediated down-regulation of selected TJ targets in SC endothelium provides a novel means of outflow facility enhancement (Tam et al. 2017) (**Appendix I**).

Studies have previously been reported from this laboratory on the use of siRNAs targeted against cerebral and retinal vascular endothelial TJ components to modulate barrier permeability in the blood-brain (BBB) and the inner blood-retina barriers (iBRB) (Campbell et al. 2008; Campbell et al. 2009). In addition to

facilitating systemic delivery of low molecular weight drugs, modulation of permeability at the BBB reduces cerebral oedema and to improve cognitive function following experimentally-induced traumatic brain injury (Campbell et al. 2012). In the eye opening the iBRB improved systemic delivery of therapeutic agents to the retina resulting in reduced cell death in the outer nuclear layer (ONL) in a model of retinopathy (Campbell et al. 2010). In these studies only claudin-5 was targeted for siRNA mediated down-regulation, however, in the work reported above both claudin-5 and occludin were targeted. This method improves permeability of Aβ1-40 across mouse brain endothelial cells and improves permeability of 3kDa dextran across the BBB *in vivo,* relative to the single siRNA method (Keaney et al. 2015). Hence, it appeared to be worth investigating whether down-regulation of multiple iBRB TJ proteins could in principle be used in the glaucoma field, via the removal of neurotoxic compounds, such as Aβ1-40, from the retina. Initially, the effect of iBRB opening on IOP was investigated; barrier modulation in a model of traumatic brain injury reduces oedema, allowing paracellular efflux of extra-neural water (Campbell et al. 2012). It is possible therefore that the opening of the iBRB could lead to increased fluid transfer into or out of these vessels in a hypertensive eye, either ameliorating or exacerbating the phenotype respectively. It was found that transiently opening the iBRB in a hypertensive mouse eye had no effect on IOP.

Amyloid-β (Aβ) is a pathogenic peptide associated with neurodegeneration, such as Alzheimer's disease, and has previously been linked to ocular disease. In age-related macular degeneration it is one of the main components of drusen (Huang et al. 2017), and some evidence suggests that it has a role in RGC death in glaucoma (Ito et al. 2012; Kipfer-Kauer et al. 2010; Wostyn et al. 2015). Aβ is a cleaved form of the amyloid precursor protein (APP) and exists in two forms, $A\beta_{1-42}$ which is mainly associated with fibrillar plaques, and the more soluble peptide $A\beta_{1-40}$ that is more prevalent in eye disease (Lei et al. 2017). Some studies indicate that $A\beta_{1-40}$ is the more toxic, and an intravitreal injection of $A\beta_{1-40}$ induces retinal inflammation (Lei et al. 2017; Li et al. 2014). Data accrued here indicate that the DBA/2J mouse model of glaucoma accumulates Aβ in the retinal ganglion cells. siRNA-mediated opening of the iBRB leads to a reduction of $A\beta_{1-40}$ in the retinas of

these animals as is published in Keaney et al. (2015**)**. However, both NT and treated DBA animals showed TUNEL positive staining in the RGCs implying prior damage in these RGCs, and so no immediate therapeutic benefit from this treatment was apparent. Previous studies have shown that the young DBA/2J mouse has increased Aβ levels in the optic nerve (ON), but not the retina (Wilson et al. 2016; Goldblum et al. 2007). With this in mind earlier and more frequent treatment might increase ganglion cell survival. As RGC death does not occur in 9 month C57BL/6J mice, these can be used a RGC-death negative control, demonstrating any negative side-effects of long-term treatment (Danias et al. 2003; Buckingham et al. 2008). The DBA/2J mouse model is a complicated glaucoma model with unknown immune response elements involved in pathological progression, as discussed in **Chapter 1**. Therefore, the technique could be of use in another model that better simulates the pathogenesis of glaucoma. The myocilin mouse model has high IOP and RGC cell loss from as early as 3 months of age (Zode et al. 2011). We are currently breeding a colony of transgenic *MYOC* mutant mice. If these animals demonstrate increased Aβ in their retinas at or before 3 months of age, they would be suitable candidates to ascertain the effect of regular iBRB opening on RGC survival.

Statement of collaboration

Lawrence Tam conducted TJ-profile RT-PCR arrays. Paul Cassidy and Lawrence Tam collaborated in SCEC TJ Western blot analysis and siRNA validation. Jeffrey O'Callaghan collaborated in anterior segment dissociation.

Chapter 3
AAV-mediated delivery of recombinant proteins to the outflow tissues

Chapter 3: AAV-mediated delivery of recombinant proteins to the outflow tissues.

Introduction

Summary

The eye is an isolated immune privileged environment and that is suited to viral-mediated therapeutic delivery (Lebherz et al. 2008). Adenoviral vectors have demonstrated transduction of the conventional outflow tissues and have been used in glaucoma model creation using TGF-β2, and in therapeutic delivery of MMP-1 (Shepard et al. 2010; Gerometta et al. 2010). However, expression of adenovirus (AV) vectors in the TM is transient and repeated injections are not well tolerated (Borrás et al. 2001). AAVs offer a vector with reduced immunogenicity, transfection of non-dividing cells, and long-term transgene expression (McCarty et al. 2004).

In this chapter, there is an overview of AAVs and their use in ocular therapies with a focus on transfection of the tissues of the AC. Following this, the introduction focuses on the role of TGF-β2 and its downstream regulators in POAG. This study investigated the efficacy of six AAV pseudotypes in transfection of the mouse AC. AAV2/9 was found to transfect the corneal endothelium. Further AAV2/9-mediated transgene expression was controlled with a doxycycline-inducible promoter, which was activated with doxycycline eyedrops. Both the constitutive and inducible AAV2/9 vectors were used to deliver MMP-3 into the AH and hence to the conventional outflow tissues. This treatment resulted in increased MMP-3 in the AH and increased AH outflow facility, a full report of the work involving MMP-3 is found in O'Callaghan, Crosbie, et al. (2017), which is appended to this Chapter. In as yet unpublished work the effect of TGF-β2 and it's downstream effector, PAI-1, on the outflow tissues was investigated, with a focus on SCECs. PAI-1 was found to decrease solute passage across both SCEC and TM cell monolayers; these results were associated with increased ECM deposition and cell contractility. Using these observations mouse PAI-1 was expressed from AAV2/9 in the mouse AC with the goal of creating a mouse model of POAG.

Adeno-associated virus (AAV)

AAVs were first discovered as a contaminant of adenovirus preparation and found to be nonautonomous, requiring AV co-infection for particle production (Atchison et al. 1965). AAV is one of the smallest viruses known to man, with a capsid composed of 60 subunits and a ~4,7-kb single-stranded linear DNA genome that is bookended by inverted terminal repeat sequences (ITRs) (Samulski et al. 2015). AAV is an attractive vector for therapeutic delivery as it does not appear to cause disease in humans and it remains quiescent in the absence of helper virus, typically adenovirus (McCarty et al. 2004). AAVs have the ability to integrate into the host genome, and can infect a broad range of cells including dividing and non-dividing cells. WT AAVs contain three genes (*rep, cap,* and *aap*), which are involved collectively in genome replication, site-specific integration, capsid production, and genome packaging (Samulski et al. 2015). For vector delivery, AAV particles are manufactured using a three-plasmid transfection strategy. This leads to the production of a viral genome that has a transgene flanked by the ITRs without the viral genes (Samulski et al. 2015). This produces viruses that are replication deficient and generally persist as stable episomes with low levels of random integration (McCarty et al. 2004).

Twelve natural AAV serotypes have been reported (AAV1 to AAV12) and more than 100 serotypes from nonhuman primates have been discovered to date (Daya & Berns 2008). The different AAV vectors show varying tissue-specific transfection efficiencies, and have been demonstrated to be capable of transfection in other species (Srivastava 2016). Recombinant AAV vectors can be generated using genomes and capsid proteins from the same serotype, or alternatively, pseudotyped vectors can be generated that contain the AAV2 genome and alternative serotype capsids. Pseudotyped vectors allow the vector to have the tropism of one serotype while retaining the well-characterized AAV2 genome. In these cases, vectors are named with the serotype of the genome numbered first and the number of the capsid serotype second (Surace & Auricchio 2008). Each different capsid structure has individual tropisms for infection of specific tissues and cells. Therefore, strategies have been implemented to create novel capsid structures with higher affinity for certain cell types and markers or with decreased affinity with AAV neutralizing antibodies (Kotterman & Schaffer 2014; Perabo et al.

2006; Maheshri et al. 2006). In directed evolution diverse libraries of mutated AAV *cap* genes are created and are subsequently put under a selective pressure, *in vitro* or *in vivo*, to isolate the variants that overcome gene delivery barriers. The mutated *cap* genes are produced using: error prone PCR, which inserts random point mutations (Perabo et al. 2006; Maheshri et al. 2006); chimeric capsids are made using *in vivo* viral recombination or DNA shuffling of *cap* gene libraries (Bowles et al. 2003; Li et al. 2008); or random peptides are inserted at known binding sites, such as the heparin binding domain (Perabo et al. 2003). The power of this technique is due to the wide range of selection assays possible even without the knowledge of the underlying molecular mechanisms involved in the increased tropism. *In vitro* selection was used to fabricate AAVs that selectively target: an HIV infected T-cell line (Wooley et al. 2017), neural stem cells (Jang et al. 2011), and human induced pluripotent stem cells (Asuri et al. 2012). These methods of capsid production are increasing the available AAV serotypes by an order of magnitude, allowing the targeting of a myriad of cell types.

Capsid proteins not only influence cell transfection but can also influence transgene expression. Onset of expression is delayed in the retina after AAV2/2 delivery compared to expression after treatment with AAV2/5 or, 2/1 despite these AAVs having the same genome (Auricchio et al. 2001). AAV vectors possess a unique expression profile in comparison to other vectors. After administration *in vivo,* transgene expression is low until 1-2 weeks, and then reaches a plateau some weeks later. The slow rise in AAV vector expression is thought to be due to the rate-limiting step of converting the single stranded DNA (ssDNA) vector genome into double-stranded DNA (dsDNA) before gene expression (Ferrari et al. 1996; Wang et al. 2007). Further studies have indicated that newly formed AAV dsDNA is in a transient unstable form that can be lost from the cell (Wang et al. 2007). To escape this rate-limiting step a new form of recombinant AAV (rAAV) termed self-complementary AAV (scAAV) has been developed. In these vectors the viral genome consists as both strands as a single molecule, and then these two halves of the ssDNA molecule can fold and base pair to form a dsDNA molecule, thus avoiding any DNA synthesis stop points (McCarty et al. 2001). This reduces the available vector size by half to ~2.5kb, however this can still package a vector, including transcription elements, that could code for proteins of 40-55kDa

(McCarty 2008). In summary, AAVs have been used in over 100 clinical trials for a multitude of conditions including systemic diseases such as hemophilia (Marrazzo et al. 2015), diseases of the eye (Testa et al. 2013), CNS (Janson et al. 2002), muscle (Bowles et al. 2012), and heart (Hajjar et al. 2008).

Drawbacks of AAV

Though AAV mediated transgene delivery has many advantages such as a lack of pathogenicity and the ability to transduce a broad range of tissues, including non-dividing cells, there are some aspects that still must be kept in mind when using AAV. Firstly, the small size of the AAV vector means that only ~4.7kb DNA can be inserted into the viral genome and this must include all the relevant regulatory sequences (Buie et al. 2010b). Another problem is the difficulty in delivering a systemic AAV therapy to non-immunoprivileged sites. Initial trials using AAV2 to deliver human factorIX to hemophilia B patients have suggested that the majority of transduced cells were removed by cytotoxic T lymphocytes targeted specifically to capsid proteins. Therapeutic benefit peaked at the highest AAV titer, however transgene expression was transient and decreased over time (Mingozzi et al. 2007). Vector load has a direct bearing on immune response against AAV therapies and so increasing transgene efficiency and concurrently lowering vector titre is now paramount in systemic AAV delivery. Increased factorIX transgene expression was stabilized in subsequent trials using a self-complementary codon-optimised transgene packaged in AAV8 under a liver specific promoter (scAAV2/8-LP1-hFIXco), with levels of factorIX sustained at 5% of normal levels (High & Anguela 2016; Nathwani et al. 2014). Subsequently, further work on transgene optimization using a codon-optimised gain-of function factorIX mutant under the control of the hAAT liver specific promoter has shown good expression and little evidence of a capsid-directed immune response in a phase I-IIa trial (George et al. 2017). Therefore, in these cases if transduction efficacy is improved it is hypothesized that a lower viral titer could be administered thus avoiding the immune response. To this end there are multiple strategies including avoidance of proteasome degradation, and use of topoisomerase inhibitors (Nicolson et al. 2016). Another disadvantage in the use of AAV is that the onset of gene expression is generally slow due to the requirement to convert ssDNA into dsDNA. This can be

circumvented as previously discussed with the use of scAAVs that contain the sense and antisense transgene on a ssDNA molecule. This however further decreases the transgene size. Despite these drawbacks AAV remains a highly promising candidate for transgene delivery, especially in immunoprivileged sites such as the eye.

AAV-mediated ocular therapies

The eye is an ideal site for virally-mediated gene delivery - it is accessible, compartmentalized and is an immune privileged site (Streilein 2003). Lentiviral, adenoviral and adeno-associated viral vectors have been used in the treatment of retinal neovascularization, photoreceptor and retinal ganglion cell degeneration among other disease pathologies (Liu et al. 2011). Two main routes of delivery are used in AAV therapy for the retina; intravitreal and sub-retinal injection. Using intravitreal injection both AAV2/2, AAV2/6, and AAV2/8 have the displayed good transduction of the retina, including RGC, Müller glia and photoreceptors. Compared to AAV2/2, AAV2/6 and 2/8 penetrate deeper and transduce the Müller glia and photoreceptor cells, and it seems that vitreous removal before injection greatly increases transduction (Vandenberghe & Auricchio 2012; Da Costa et al. 2016). Other AAV serotypes appear to have difficulty crossing the inner limiting membrane and so display reduced transduction efficiency. Subretinal injection has a greater transduction efficiency on administration of AAV. This technique however does carry greater risk of retinal detachment and is more technically demanding (Vandenberghe & Auricchio 2012). Using this delivery method AAV2/2 has been shown to transduce both the photoreceptors and RPE cells (Sarra et al. 2002), AAV2/5 was shown to exhibit more efficient transduction of photoreceptor cells (Auricchio et al. 2001), and AAV2/8 is more efficient again in multiple species (Vandenberghe & Auricchio 2012). In addition AAV2/9 can also transfect Müller cells, photoreceptor cells and RPE cells after subretinal injection in mice (Allocca et al. 2007).

To date the most high profile example of ocular gene therapy has been that targeting Leber's congenital amaurosis (LCA) caused by mutations in the *RPE65* gene. This gene-replacement therapy using AAV resulted in improved vision over a 3-year period in a canine model and caused no adverse effects in Phase I safety and

tolerability studies. Visual outcomes from this trial have been mixed, but have demonstrated the potential for ocular viral therapies (Ku & Pennesi 2015). Recently the results of a Phase III trial for AAV-RPE65 have been published an demonstrated an increase in visual field scores and better low-light functional navigation 1 year post-treatment (Russell et al. 2017). Other therapies utilise AAV2/2 expressing the VEGF inhibitor FLT-1 for use in wet-AMD treatment. In the preclinical safety evaluation monkeys injected with virus demonstrated good tolerability, with consistently increased sFLT-1 expression (Maclachlan et al. 2011). Subsequent to this, AAV2/2-sFLT-1 has advanced to Phase IIa clinical trials; this treatment was well tolerated, with little adverse effects, and some signs of clinical improvement in a Phase I trial (Rakoczy et al. 2015). This Phase II trial was the largest clinical trial to date involving AAV, the results re-affirming the safety of a subretinal injection of AAV2/2-FLT-1 (Constable et al. 2016). While for most of these examples the efficacy of AAV therapies in ocular disorders has still yet to be fully proven in a clinical setting, it is clear that AAV has a very good safety profile. Moreover, for the the RPE-65 therapy, a successful Phase III trial has been completed and the therapy is progressing towards market authorisation.

AAV in the AC

AC-directed AAV therapy has vast potential in multiple ocular disorders, such as corneal dystrophy, glaucoma, and corneal neovascularization (Bogner et al. 2015). Similar to the posterior chamber there are multiple administration methods, dependent on the desired outcome. The cornea has been targeted by both intrastromal injection and topical administration of viral vector. Intrastromal injection of the cornea leads to transfection of the corneal stromal keratocytes. AAV2/1, AAV2/2, AAV2/5, AAV2/6, and AAV2/9 all transfect mouse and human stromal cells, but the consensus is that AAV2/8 has the highest corneal stromal transduction efficiency (Hippert et al. 2012; Lebherz et al. 2008; Sharma et al. 2010; Mohan et al. 2003).

Topical instillation of AAV vector also leads to efficient transduction of keratocytes with AAV2/8 and AAV2/9 showing the greatest efficiency (Mohan et al. 2010; Vance et al. 2016). This delivery technique is being developed to deliver the IDUA transgene that encodes for alpha-L-uronidase that is mutated in

mucopolysaccharidosis type I (MSP1), a lysosomal storage disorder. In MSP1 95% of surviving patients develop corneal clouding with reduced vision, an AAV with a chimeric capsid, containing capsids from serotype 9 and 8, increases IDUA expression in the cornea stroma (Vance et al. 2016).

Intracameral injection of AAVs into the anterior chamber allows vector transduction of a multitude of tissues, including the iris, corneal endothelium and the outflow tissues (Lai et al. 2002; Bogner et al. 2015). When injected directly into the AC, AAV2/2 and scAAV2/2 transduce the iris (Bogner et al. 2015; Lai et al. 2002). These have also been found to transduce corneal endothelial cells in human, rat and mouse (Bogner et al. 2015; Wang et al. 2017). AAV2/2 has been used to deliver sFLT-1 to the cornea of rats, which reduces angiogenesis in a rat model of corneal neovascularization (Lai et al. 2002). Early studies focusing on TM transduction by AAV found little to no TM transgene expression (Borrás et al. 2002). Treated cells contained AAV DNA but did not express the transgene RNA, and it was hypothesized the cause was a lack of conversion of AAV ssDNA to dsDNA (Borrás et al. 2006). To escape this step, scAAV2/2 was used and found to transfect human, rat and monkey TM (Borrás et al. 2006; Buie et al. 2010a). Interestingly, studies using scAAV2/2 have shown TM transduction in mice, but it remains extremely inefficient, indicating significant species differences in AAV transduction in the TM (Wang et al. 2017; Bogner et al. 2015). One group reported that the mutation of multiple tyrosine capsid residues to phenylalanine results in a large increase in AAV GFP expression in the mouse TM, presumably mediated by avoidance of proteasomal degradation (Bogner et al. 2015). Despite these species variations, scAAV2/2 has been used in to deliver IOP-lowering agents to the conventional outflow tissues (Borras et al. 2016; Borrás et al. 2015), including delivery of MMP-1 to a steroid induced ovine model of hypertension. This resulted in IOP reduction, close to that of baseline, which was consistent for at least four weeks (Borras et al. 2016). In summary, while not as far advanced as AAV therapies to the retina, there is substantial scope for AAV-mediated therapies that target the anterior chamber tissues.

Cytokines and glaucoma

In POAG, the environment in which the outflow tissue is exposed to has major effects on the properties of these cells. SC cells isolated from glaucomatous eyes were found to have increased subcortical stiffness, as measured by atomic force microscopy, which was inversely proportional to pore density and porosity. These cells also express some glaucoma related cytokines, such as TGF-β2, CTGF and PAI-1 to a greater extent than normal SC cells (Darryl R Overby et al. 2014). Human TM donor tissue has been shown to have higher stiffness, which is postulated to be from a dysregulation of ECM remodeling, and changes in the cytoskeleton (Last et al. 2011). The TM is composed of cells that are structurally supported by an elastic fibre network, these fibres are coated in a sheath composed of ECM proteins such collagen IV, laminin and fibrillan. The ECM sheath is thicker and its arrangement becomes more irregular in the glaucomatous eye (Tektas & Lütjen-Drecoll 2009). In both the SC and TM from glaucomatous patient tissues, phenotypes and expression profiles are altered. The composition of the AH, that supplies the outflow tissues with growth factors and a homeostatic environment in which to grow is key for their proper functioning. Of importance in glaucomatous AH, is the levels of inflammatory cytokines and growth factors. Numerous studies have looked at cytokine levels in the AH of POAG patients and some of those found to be increased were: IL-8, IL-12, IFN-γ, CXCL-9, MIP1-β, MCP-1, P-10, TGF-β1 and TGF-β2. Those that studies found reduced were: IL-6, IL-10, CCL-2, and VEGF (Agarwal et al. 2015; Engel et al. 2014; Takai et al. 2012; Chua et al. 2012; Kokubun et al. 2017). Changes in all these cytokine levels could have a myriad of effects, but of these TGF-β2 has been the most widely studied with relation to POAG.

TGFβ-2 pathways

TGF-β2 is the most abundant TGF-β isoform in the eye and is known to increase ECM protein synthesis while concurrently reducing ECM turnover. It signals through both canonical and non-canonical pathways. The signaling pathway activated is context dependent, and so cell type receptor expression and cofactor expression all have an effect on the downstream effects (Wordinger et al. 2014). The canonical pathway involves the TGF-β type I and type II receptors, TGFβ-2 binds the type II receptor leading to phosphorylation of the type II receptor. The

phosphorylation of the receptor complex activates the Smad protein pathway, leading to the nuclear localization of Smad2 and/or Smad3 to the nucleus leading to a changes to gene expression (Wordinger et al. 2014). Smad2/3 activation is linked to the expression of several pro-fibrotic genes including collagens, plasminogen activator-1 (PAI-1), proteoglycans, integrins, connective tissue growth factor (CTGF), and to the repression of MMP expression (Walton et al. 2017). PAI-1 is one of the most highly up-regulated TGF-β2 induced genes, it inhibits plasmin generation limiting ECM degradation, and is more highly expressed in glaucomatous SC cells (Darryl R Overby et al. 2014; Samarakoon et al. 2013). CTGF is highly expressed in the TM and AH; it is a mitogen for fibroblasts, induces ECM production and actin stress fibre formation (Junglas et al. 2012). Both PAI-1 and CTGF are also induced by mechanical stress on cells, and in response to cytoskeletal deformation (Samarakoon et al. 2010). In the non-canonical pathway TGF-β2 does not result in Smad translocation to the nucleus. The activated TGF-β receptors utilize MAP kinases such as extracellular signal-regulated kinases (ERK), p38 mitogen-activated protein kinases (p38MAPK), and c-Jun N-terminal kinases (JNK) proteins to effect transcription regulation (Wordinger et al. 2014). There is some added complexity in that the Smad proteins, which are usually regulated by TGF-β receptor mediated phosphorylation, can be phosphorylated by some kinases in the non-canonical pathway (Zhang 2009). TGF-β2 is known to increase ECM deposition in part through increased expression of PAI-1 and CTGF.

TGF-β2 in the TM and SC

TGF-β2 has been implicated with the pathology of glaucoma, generally it is linked to aberrant regulation of the ECM in trabecular tissues (Wordinger et al. 2014). A meta-analysis of TGF-β2 expression in glaucomatous human AH found that both total and active TGF-β2 protein levels were significantly associated with POAG. This study also indicated that age, gender and IOP had no correlation with AH TGF-β2 levels (Agarwal et al. 2015). In cultured TM cells exogenous TGF-β2 induces the expression of a number of ECM proteins including fibronectin, collagen, elastin and proteoglycans.

ECM degradation is retarded in TM cells treated with TGF-β2 by the increased expression of PAI-1 and tissue inhibitor of metalloproteinase-1 (TIMP-1)

(Fuchshofer & Tamm 2009). PAI-1 is associated with fibrosis, and increased levels are associated with age-related pathologic conditions such as diabetes, cardiovascular disease and atherosclerosis (Ghosh & Vaughan 2012). In perfused human eyes TGF-β2 caused a 27% decrease in facility and the build up of fibrillar material in the JCT region (Gottanka et al. 2004). Much of this ECM deposition is thought to be mediated by the up-regulation of CTGF and knock-down of CTGF expression in TM cells prevents TGF-β2-induced increase in fibronectin synthesis (Junglas et al. 2009). In addition to ECM deposition, TGF-β2 induces the expression of transglutaminase via the canonical pathway. Tissue transglutaminase is involved in irreversible cross-linking of TM fibronectin; it is expressed by the TM but is found in higher amounts in POAG TM tissue. Its effect reduces ECM turnover in the TM and also increases the stiffness of the tissue, which is linked to increased outflow resistance (Fuchshofer & Tamm 2012).

TGF-β2 is also involved in the regulation of the actin cytoskeleton of the TM. HTM cells treated with TGF-β2, show an increase in actin stress fibre formation and in focal adhesions. Concurrent with this is an increase in PAI-1 and α-smooth muscle actin (α-SMA) expression, that appears to be mediated by kinases on the non-canonical signaling pathway (Pattabiraman & Rao 2010; Han et al. 2011). In other cells types the presence of α-SMA in stress fibres increases cell stiffness, conferring a two-fold stronger contractile activity (Fuchshofer & Tamm 2012). Cellular contraction or relaxation is thought to modulate outflow resistance in the TM tissue, as agents that decrease TM contraction are known to increase outflow facility (Luna et al. 2012).

Very little work has been done on the effects of TGF-β2 on the SC endothelial cells. In *ex vivo* human eyes perfused with TGF-β2 there was a decrease in active filtration length of the SC, and a greater proportion of the SC inner wall was in contact with fibrillar material found within the JCT. The cells of the SC inner wall contained very few vacuoles and at points the cells bulged into the SC lumen, and in these regions the endothelial lining could not be defined by EM (Gottanka et al. 2004). Similar to TM cells, TGF-β2 treatment of human SC cells induces stress fibre formation and up-regulates expression of fibronectin, collagen I, and collagen IV. These cells are grown on a matrix and retain the SC marker expression of VE-cadherin and CD-31. However, on TGF-β2 treatment SC specific proteins are down-

regulated and the expression of the mesenchymal marker α-SMA is up-regulated (C. N. Dautriche et al. 2015). In mice treated with an adenovirus expressing TGF-β2 in the AC, the SC tissues display increased amounts of fibronectin, CTGF and PAI-1 (Swaminathan et al. 2014). Together these findings show that though there is currently little known on the effect of TGF-β2 or its downstream mediator PAI-1 on SC cells, this interaction may play a role in the pathogenesis of POAG.

In this study the effectiveness of six AAV pseudotypes (AAV-2/2, -2/5, -2/9, and scAAV-2/2, -2/5, -2/9) at transducing the tissues of the mouse AC was studied. Contrary to results in other species, very little eGFP expression was observed in the mouse outflow tissues using scAAV2/2, or any other pseudotype, in spite of the fact that all constructs were shown to be active following sub-retinal inoculation. However AAV2/9 strongly transduced the mouse corneal endothelium, with widespread eGFP expression. Data now published, in O'Callaghan, Crosbie et al. (2017), on the use of this system for controlled secretion of a MMP-3 into the AC to enhance AH outflow is appended to this chapter. Further studies resulted in the identification of PAI-1, a target induced by TGF-β2, that was up-regulated in the AH of POAG patients. PAI-1 is a known regulator of ECM deposition and is highly up-regulated in the conventional outflow tissues in response to TGF-β2 (Fuchshofer & Tamm 2012). Therefore, it was hypothesized that increased PAI-1 expression may have a role in POAG pathogenesis, and reduce AH outflow. PAI-1 was shown to increase resistance across SCEC monolayers, and increase SCEC contractility via restructuring of the actin cytoskeleton. AAV2/9 was used to introduce PAI-1 into the mouse corneal endothelium for secretion into the AH, whereby it could follow the natural flow of AH into the outflow tissues. Contrary to expectations, AAV2/9 delivery of PAI-1 to the mouse AC had no significant effect on mouse IOP or outflow facility over a 12-week period.

Results

AAV transduction of the AC tissues

AAV2/2, 2/5 and 2/9, both in single stranded and self-complementary forms, were used in these studies. All methods used in this chapter are outlined in **Chapter 5**. Virus preparations were commissioned from Vector Biolabs, with viral titres ranging from 2 x 10^{12} to 8.1 x 10^{13} GC/ml (**5.26**). All of the vectors expressed eGFP under the control of a CMV promoter. In order to demonstrate initial viability in a proven system, all six AAVs were injected sub-retinally in wild type mice (C57BL/6J) (2.0 x 10^{12} GC/ml in a volume of 1ul). After 4 weeks, retinal flatmounts were stained for eGFP and examined using Z-stack software, as shown in **Fig. 3.1**, qualitatively, all six viral preparations displayed extensive eGFP fluorescence in the retina. To test the transduction efficiency of the multiple AAV vectors in the AC, the six pseudotypes and a PBS control were intracamerally injected into the AC of C57BL/6J mice (**5.27**): AAV2/2, AAV2/5, AAV2/9, scAAV2/2, scAAV2/5, and scAAV2/9. Each serotype was injected into 3 different eyes at a concentration of 2.0×10^{12} GC/ml. After an incubation time of 3 weeks the eGFP expression in the eye tissues was examined by confocal microscopy. On investigation of the outflow tissues AAV2/9 did not display any fluorescence in these tissues. AAV 2/2 displayed eGFP expression in the limbal vasculature and scAAV 2/9 expressed in the cells surrounding the limbal vasculature, both of which was sparse. AAV 2/5, scAAV2/5 and scAAV 2/2 exhibited a sparse amount of eGFP expression in the TM. Enface flatmount images of outflow tissue treated with AAV displayed sparse expression of eGFP in all pseudotypes tested (**Fig. 3.2**).

Next, eGFP expression in the cornea was investigated. None of the following displayed eGFP expression in the sections: AAV2/2, scAAV2/2, and scAAV2/9. After intracameral injection of AAV2/5, scAAV2/5, and AAV2/9, displayed eGFP expression in the corneal endothelium, with expression especially strong in AAV2/9 treated eyes (**Fig. 3.3a**). On further investigation, with whole mouse anterior segments and AC flatmounts it was observed that AAV2/9 expression was widespread thoughout the corneal endothelium (**Fig. 3.3b**). Hence, AAV2/9 was chosen as a vector that could deliver recombinant secretory proteins to the AH and from there to the outflow tissues. A valuable aspect of any vector in target delivery is control of expression and so an AAV2/9-eGFP vector was made whereby the

eGFP transgene was under the control of a doxycycline inducible promoter (indAAV2/9-eGFP). Mice were injected with the indAAV2/9-eGFP vector and were administered with 0.2% doxyclycline eyedrops to activate expression, or with PBS eyedrops as a control. The doxycycline treated mice displayd eGFP expression in the corneal endothelium and the PBS treated animals showed no eGFP expression (**Fig. 3.3c**)**.** Previously, intravitreal injections have been used to deliver AAV vectors to the AC. This study injected AAV serotypes containing AAV2 genomes with eGFP under the control of a CMV promoter in various capsids (AAV1, 2, 5, 7, 8, 9) at 1 x 10^{10} GC/eye and found that AAV 2/7, 2/8 and 2/9 transduced some tissues at the outflow tract (Lebherz et al. 2008). Here, the difference of AAV transduction delivered intravitreally was examined in WT C57BL/6J mice (**5.28**). No eGFP expression was seen in the outflow tissues of any eye. Similarly to intracameral injection, both AAV2/9 and scAAV2/5 tranduced the corneal endothelium. scAAV-2/2 transduced the NPE of the CB and scAAV-2/9 transduced the iris (**Fig. 3.4**).

In summary, no AAV pseudotype tested here efficiently transduced the tissues of the mouse outflow pathway. However, AAV2/9 treatment resulted in widespread eGFP expression in the corneal endothelium. This could be used in the delivery of soluble compounds to the AH and hence to the AH outflow tissues. In addition, a system was verified whereby topical doxycycline eyedrops induced transgene expression. Both the constituitive and inducible versions of AAV2/9 were subsequently used to deliver MMP-3 to the mouse AH. This treatment resulted in increased AH outflow and decreased IOP. O'Callaghan, Crosbie et al., (2017) contains the published data outlining this work and is appended to this chapter.

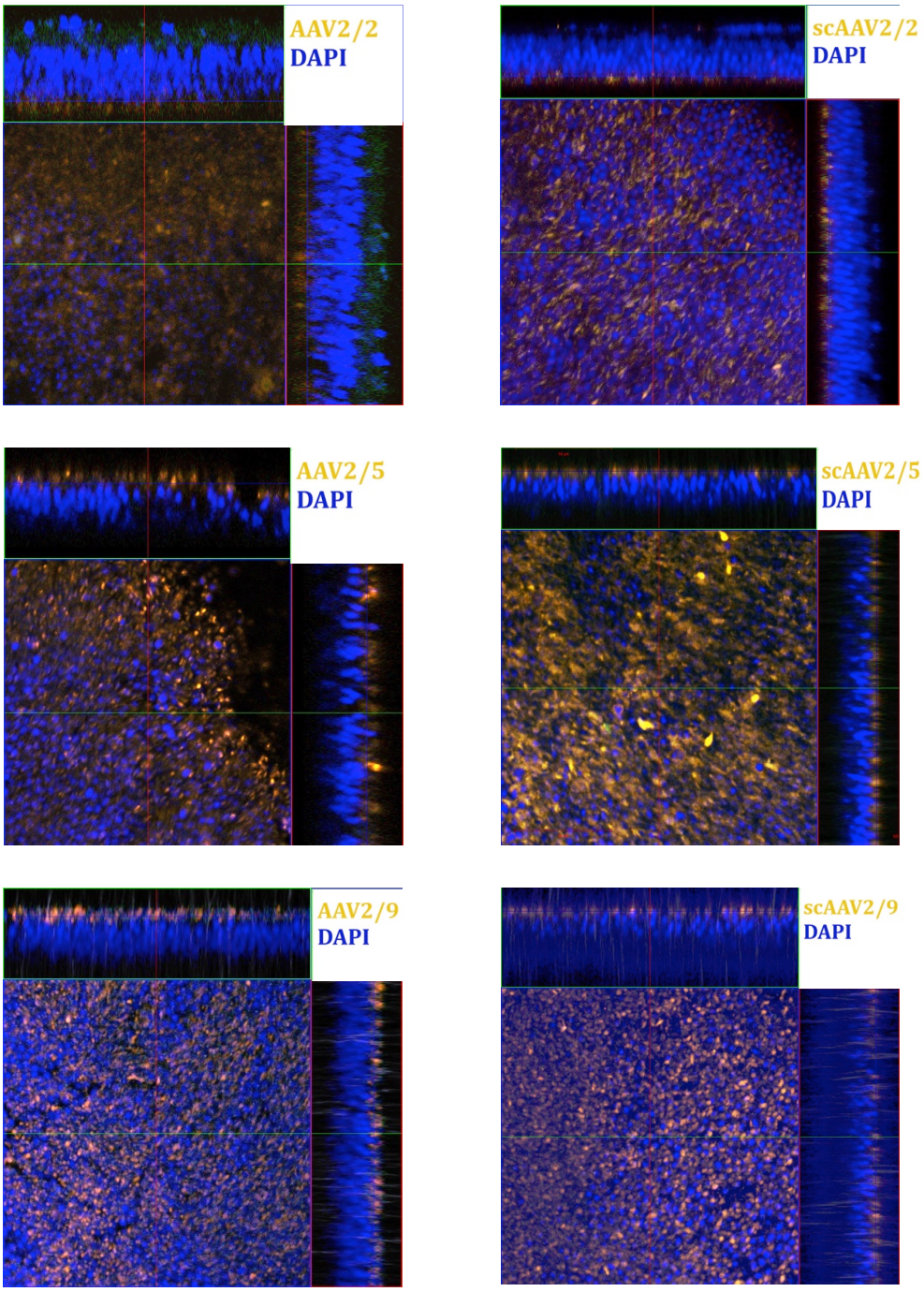

Fig. 3.1. eGFP expression in the murine retina following AAV injection. AAV2/2, 2/5, 2/9 and scAAV2/2. 2/5, 2/9 were sub-retinally injected into C57BL/6J mouse eyes. The figure displays enface and Z-stack images of retinal flatmounts from these animals, showing co-localisation of eGFP signal and Cy3 signal from eGPF antibody. Main image is an en face view of the retina with side panels representing retinal sections created from the Z-stack. Orange = colocalisation of eGFP (Green) and Cy3 (Red). Blue = DAPI nuclear stain.

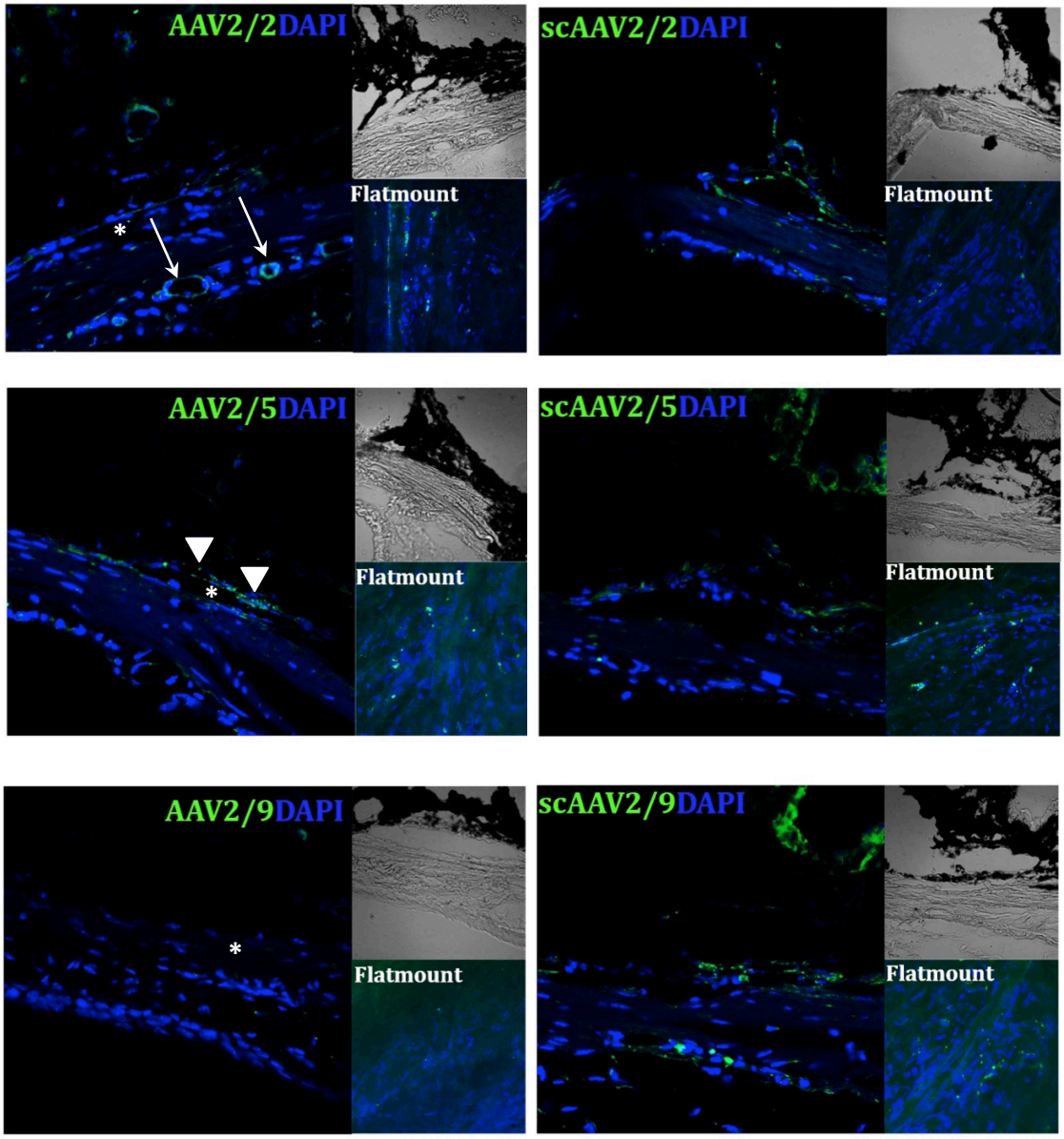

Fig. 3.2. AAV transduction of the mouse outflow pathways after intracameral injection.

Frozen sections of AAV treated mouse iridocorneal angles. AAV2/2 treated animals show eGFP expression around the episcleral blood vessels. In scAAV2/9 sections eGFP is expression is found in the tissues around the episcleral vessels. AAV2/5, scAAV2/5 and scAAV2/2 treated animals display eGFP expression at the TM. No eGFP expression was found in the AAV2/9 treated outflow tissues. For each pseudotype, confocal (main) and light images (top right) of treated AC sections and confocal images of flatmounted (bottom right) treated ACs are displayed.

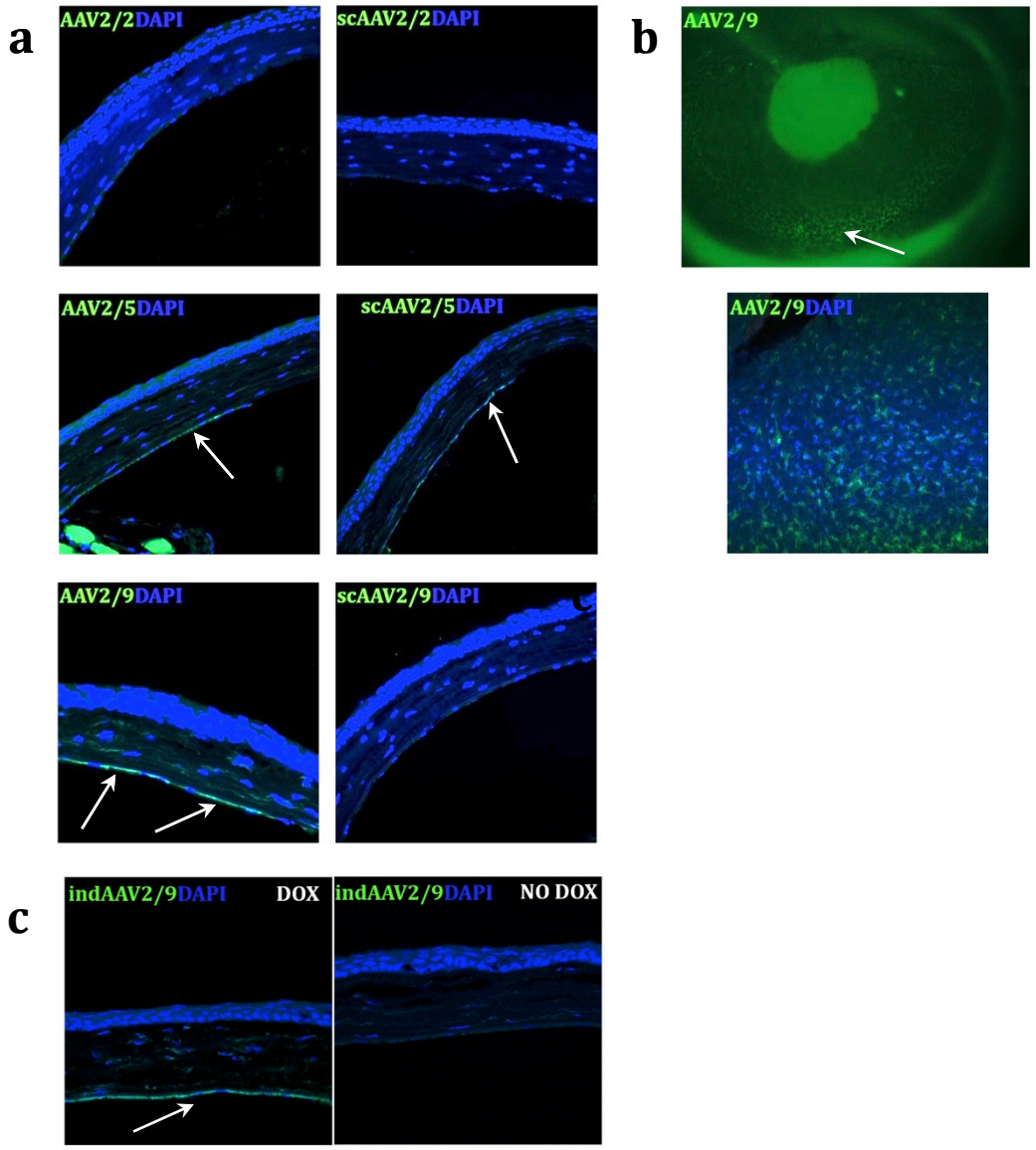

1

Fig. 3.3. AAV transduction of the mouse cornea after intracameral injection. **(a)** Frozen sections of AAV treated mouse corneas. No eGFP expression was seen in AAV2/2, scAAV2/2, and scAAV2/9 treated eyes. AAV2/5, scAAV2/5, and AAV2/9 displayed eGFP expression in the mouse cornea. **(b)** Fluorescent image of whole mouse anterior segment, and a confocal AC flatmount image after AAV2/9-eGFP treatment. **(c)** Confocal image of mouse cornea after treatment with AAV2/9 with eGFP under a doxycycline inducible promoter, with and without doxycycline treatment. White arrow = eGFP expression in the cornea endothelium; DOX = eyes administered with doxycycline eyedrops; NO DOX = eyes administered with PBS eyedrops.

2

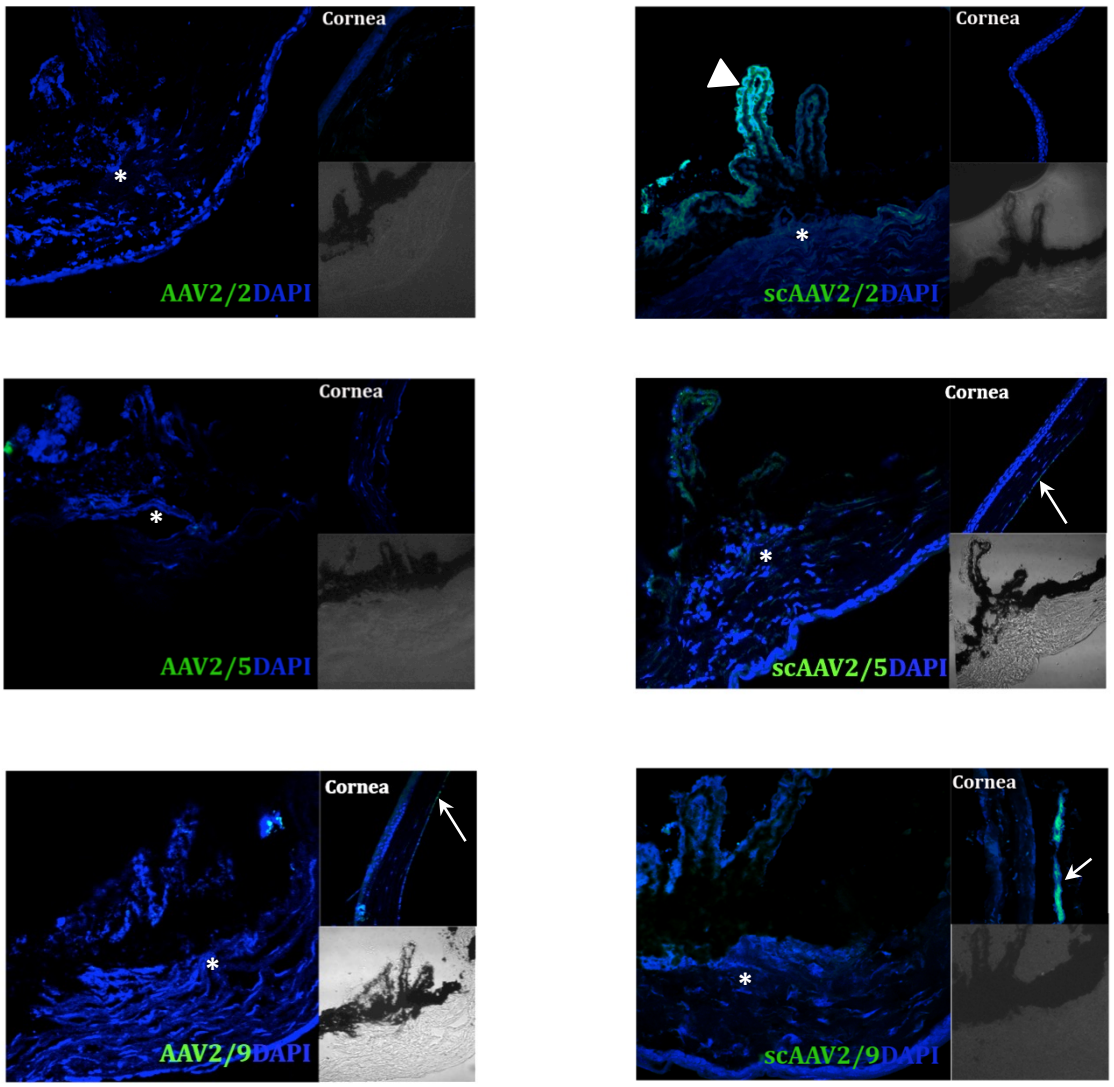

3

Fig. 3.4. AAV transduction of AC tissues after intravitreal injection.

Both AAV2/9 and scAAV2/5 treated eyes displayed eGFP expression in the corneal endothelium. scAAV2/2 treated eyes displayed eGFP expression in the non-pigmented endothelium of the CB. scAAV-2/9 treated eyes had eGFP expression in the iris. * = Schlemm's canal lumen. White arrow = eGFP expression in the corneal endothelium and iris. White arrowhead = eGFP expression in the epithelium of the ciliary body. Green = eGFP; blue = DAPI nuclear stain.

PAI-1 and TGF-β2 in POAG AH

The finding of highly efficient transduction of the corneal endothelium using AAV2/9 offered an opportunity to deliver soluble proteins to the outflow tissue, such as MMP-3. To identify suitable soluble targets that may regulate the outflow pathway, cytokine levels in the AH from human control cataract patients were compared with AH from both POAG and pseudoexfoliative glaucoma (PXG(G)) patients (**5.12**). In each case, 3 patient samples were pooled and equal volumes analysed using a human cytokine array profiler (**5.13**). Compared to cataract both PXF(G) and POAG samples had minor increases in levels of IL-13, MCP-1, and MIF; large increases were seen in soluble ICAM-1, and PAI-1 levels in both glaucoma groups relative to cataract samples. Only in POAG samples were there large increases in IL-1 receptor antagonist (IL-1ra). No Interferon-inducible T-cell alpha chemoatractant (I-TAC) was seen in cataract samples, with a small amount in PXF(G) samples, relative to this a large amount was found in POAG samples. PXF(G) samples showed a minor increase in the level of complement C5 (**Fig. 3.5a**). TGF-β2 has been linked to glaucoma (Fuchshofer & Tamm 2012), and is known to induce PAI-1 expression, which is increased in glaucomatous AH. Therefore, the levels of TGF-β2 in POAG AH relative to cataract AH were investigated by Western blot (**5.17**). Equal protein concentrations were loaded per lane as assayed by nanodrop, and no significant difference in TGF-β2 levels was found between cataract and POAG samples (CAT n = 4, POAG n = 6; p = 0.38) (**Fig. 3.5b**). There was a 76% increase in PAI-1 levels in the AH of POAG patients compared to that of cataract patients (p = 0.03, n = 4). Cataract AH had mean PAI-1 levels of 113.6 [27.44, 199.9] pg/ml compared to 200.1 [153.7, 245.4] pg/ml in POAG AH (**Fig. 3.5c**). The effect of AH from POAG, PXF(G) and cataract patients on SCEC permeability was assessed (**5.14**). The TEERs of confluent SCECs were compared at baseline (0 hr) and after 24 hr of treatment with POAG, PXF(G) and cataract AH. 24hr after POAG and PXF(G) treatment SCECs displayed an average TEER increase of 91.3% and 59.9% respectively, compared to the cataract control (-8%). The absolute increase was an average increase of POAG 17.67 [15.11, 20.23] $\Omega.cm^2$ (p = <0.0001, n = 12), PXF (G) 12.41 [2.867, 21.96] $\Omega.cm^2$ (p = 0.1541, n = 4) and cataract -1.680 [-6.419, 3.059] $\Omega.cm^2$ (p = 0.4039, n = 6) (**Fig. 3.5d**). AH from PXF(G) and POAG patients significantly decreased paracellular permeability across the SCEC monolayer (**5.15**).

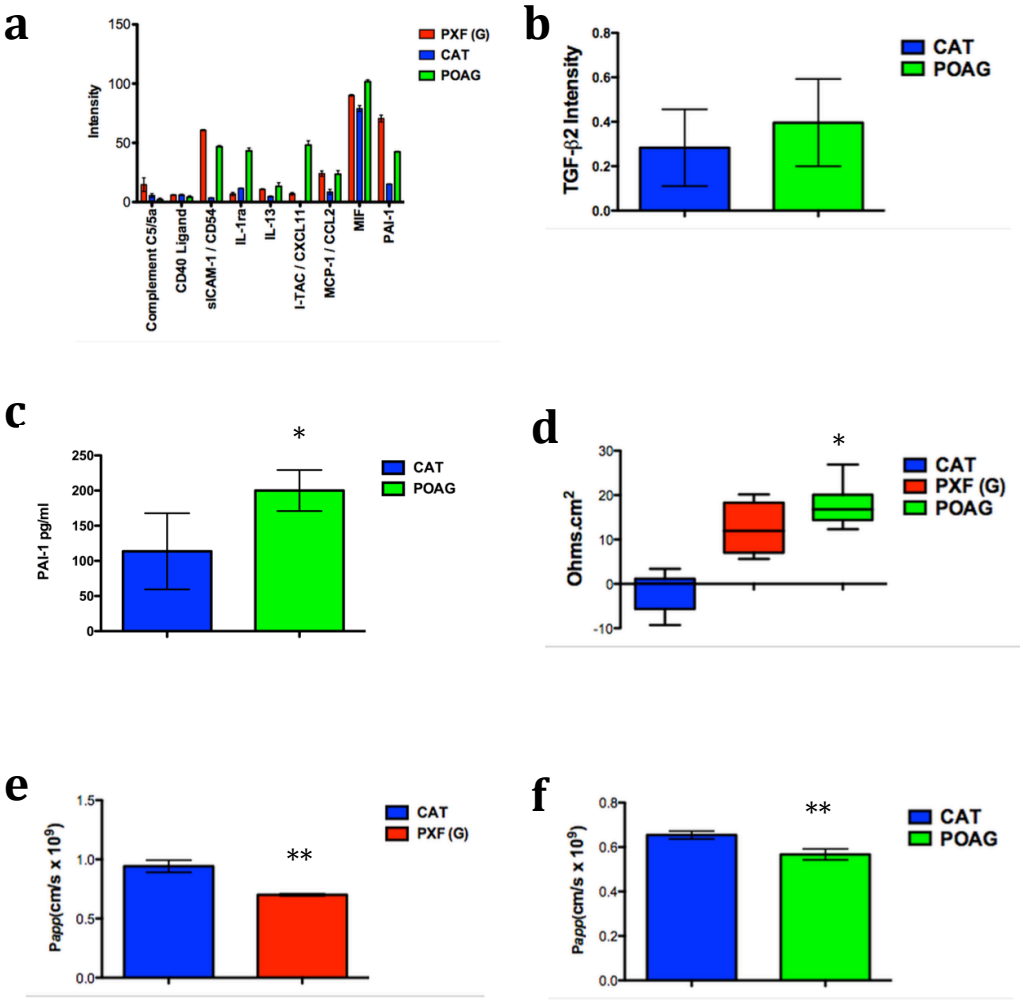

Fig. 3.5. Comparison human AH from glaucomatous and cataract source. **(a)** The cytokine profile of human AH was compared between POAG, PXF(G), and cataract (CAT) samples. 3 samples of each were pooled for the array, error bars are standard deviation from technical replicates. **(b)** Relative levels of TGF-β2 in cataract and POAG AH from Western blot analysis. **(c)** PAI-1 protein levels are increased in POAG AH. **(d)** Change in TEER from 0 hr baseline to 24 hr post treatment with AH on SCECs, POAG treatment resulted in an average change of 17.67Ω.cm^2, error bars denote maximum and minimum values. **(e-f)** PXF(G) and POAG AH treatment on SCECs resulted in a decrease in paracellular permeability to 70kDa dextran when compared to cataract control. All graphs excepting **(d)** denote mean values with standard deviations. **(d)** Graph denotes mean and whiskers display maximum and minimum values. CAT = cataract; PXF (G) = Pseudoexfoliative glaucoma; POAG = Primary open angle glaucoma. Symbols *, **, *** denote *p* values of <0.05, <0.01, and <0.001 respectively.

24 hr after PXF(G) treatment the mean difference of paracellular flux, as measured by permeability coefficient (P_{app}), to 70kDa FITC-dextran was -0.24 [-0.28, -0.20] cm/s x 10^{-9} (p = <0.0001, n = 9) (**Fig. 3.5e**). After POAG treatment the mean difference (P_{app}) across the SCEC monolayer was -0.09 [-0.11, -0.07] cm/s x 10^{-9}(p = <0.0001, n = 9) (**Fig. 3.5f**).

Effect of recombinant PAI-1 and TGF-β2 on SCEC and TM monolayers

As PAI-1 and TGF-β2 are increased in glaucomatous AH, the effect of recombinant PAI-1 and TGF-β2 on SCEC and TM cell monolayers was investigated. Recombinant PAI-1 increases the resistance across both SCEC and TM monolayers (**5.14**). SCECs were treated with both PAI-1 (10ng/ml) and it's upstream regulator TGF-β2 (20ng/ml) for 24 hr. Comparison of TEERs of SCECs at 0 hr and 24 hr demonstrated no significant increase (3.3%) in control samples, PAI-1 treatment resulted in an increase of 17.7%, and TGF-β2 treatment resulted in an increase of 29%. The absolute change for PAI-1 was 2.118 [1.103, 3.132] Ω.cm^2 (p = 0.0003, n = 8), and for TGF-β2 was 3.561 [2.629, 4.494] Ω.cm^2 (p = <0.0001, n = 8) (**Fig. 3.6a**). TEERs at 0 hr and 24 hr were compared in TM cells, all cells demonstrated an increase in TEER values, however the increases in PAI-1 and TGF-β2 cells were significantly higher than in control cells; control 29%, PAI-1 303% (p = <0.0001), and TGF-β2 262% (p = <0.0001). The absolute mean increase for each was: control 1.084 [0.5351, 1.633] Ω.cm^2 (p = 0.0019, n = 7), PAI-1 7.384 [6.512, 8.255] Ω.cm^2 (p = <0.0001, n = 8), and TGF-β2 5.899 [4.771, 7.026] Ω.cm^2 (p = <0.0001, n = 8) (**Fig. 3.6b**). Paracellular permeability (P_{app}) of SCECs was examined 24 hr after PAI-1 (10ng/ml) and TGF-β2 (20ng/ml) treatment and compared to control cells (**5.15**). Similar to the TEER results TGF-β2 treatment resulted a decrease in paracellular flux of 70kDa FITC-dextran by -0.455 [-0.552, -0.358] cm/s x 10^{-9} (p = <0.0001, n = 4), whereas PAI-1 treatment increased permeability by 0.170 [0.079, 0.261] cm/s x 10^{-9} (p = <0.01, n = 4) (**Fig. 3.6c**). In comparison to control cell permeability, TGF-β2 decreased paracellular flux across a TM monolayer. Whereas the effect of PAI-1 on the TM was concentration dependent, with 1ng/ml decreasing permeability but 10ng/ml decreasing permeability non-significantly. PAI-1 (1ng/ml) treatment decreased flux of 70kDa FITC-dextran by -0.23 [-0.37, -0.09] cm/s x 10^{-9} (p = <0.001, n = 4) and PAI-1 (10ng/ml) decreased P_{app} by -0.09

[-0.23, 0.05] cm/s x 10^{-9} (p = 0.14, n = 4). TGF-β2 treatment decreased flux across the TM monolayer by -0.39 [-0.53, -0.24] cm/s x 10^{-9} (p = <0.0001, n = 4) (**Fig. 3.6d**). To rule out any cytotoxic or proliferation effects that may affect cell permeability, an MTS assay was undertaken (**5.16**). Based on these results recombinant PAI-1 had no significant effects on SCEC and TM viability up to 2μg/ml (**Fig. 3.7a-b**)**.** For TGF-β2, SCECs treated with concentrations below 1.475μg/ml have an average cell viability for n = 3 exceeding 85% based on **Fig. 3.7c**. TM cells were more sensitive to TGF-β2 treatment, with an average viability of at least 85% for TGF-β2 concentrations up to 0.496μg/ml (n = 3) (**Fig. 3.7d**).

In summary, both PAI-1 and TGF-β2 increase resistance across SCEC and TM cell monolayers. TGF-β2 is found to decrease paracellular permeability in both SCEC and TM cells. PAI-1 decreases paracellular flux across TM cells, but interestingly, increases paracellular flux across the SCEC monolayer, seemingly in contradiction to the TEER results. However, these assays measure different forms of membrane transport and suggest that PAI-1 decreases ionic transport, and increases macromolecule transport across SCEC monolayers.

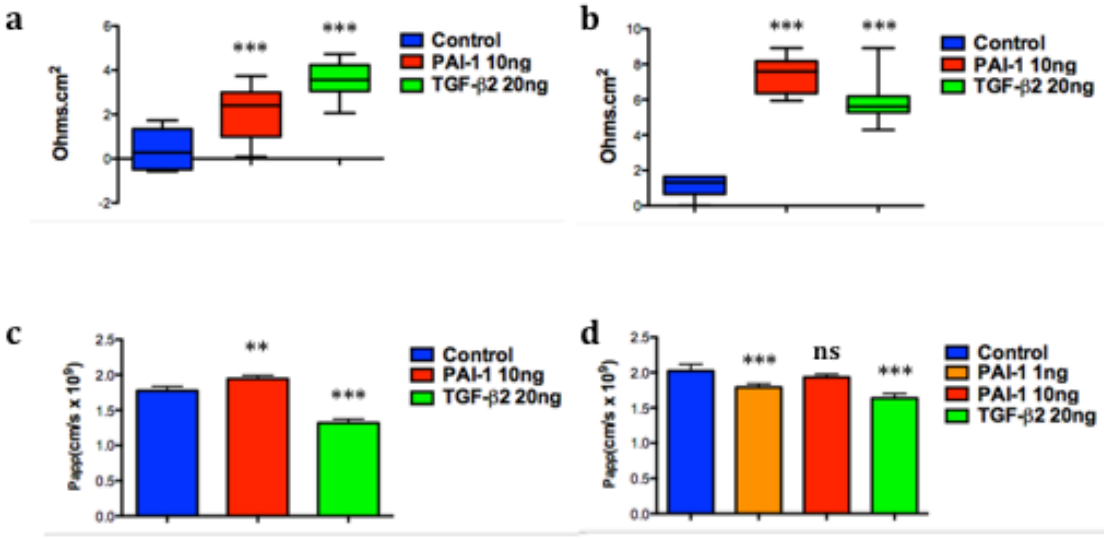

Fig. 3.6. The effect of PAI-1 and TGF-β2 on SCEC and TM cell permeability. **(a)** Treatment of SCECs with both PAI-1 and TGF-β2 significantly increased TEER after 24 hr compared to baseline. **(b)** TM TEERs increased in PAI-1 and TGF-β2 treatment significantly more after 24 hr in comparison to control TM cells. **(c)** 24 hr PAI-1 treatment increased SCEC paracellular permeability to 70kDa FITC-dextran (P_{app}) and TGF-β2 reduced P_{app} relative to control. **(d)** TM paracellular permeability was decreased after 24 hr by both PAI-1 1ng/ml and TGF-β2 treatment significantly; and was not significantly reduced after PAI-1 10ng/ml treatment relative to controls. **(a-b)** Graphs denote mean with whiskers displaying max and min values. **(c-d)** Graphs demonstrate means with SD. ns = non-significant. Symbols **, *** denote *p* values of <0.01, and <0.001 respectively.

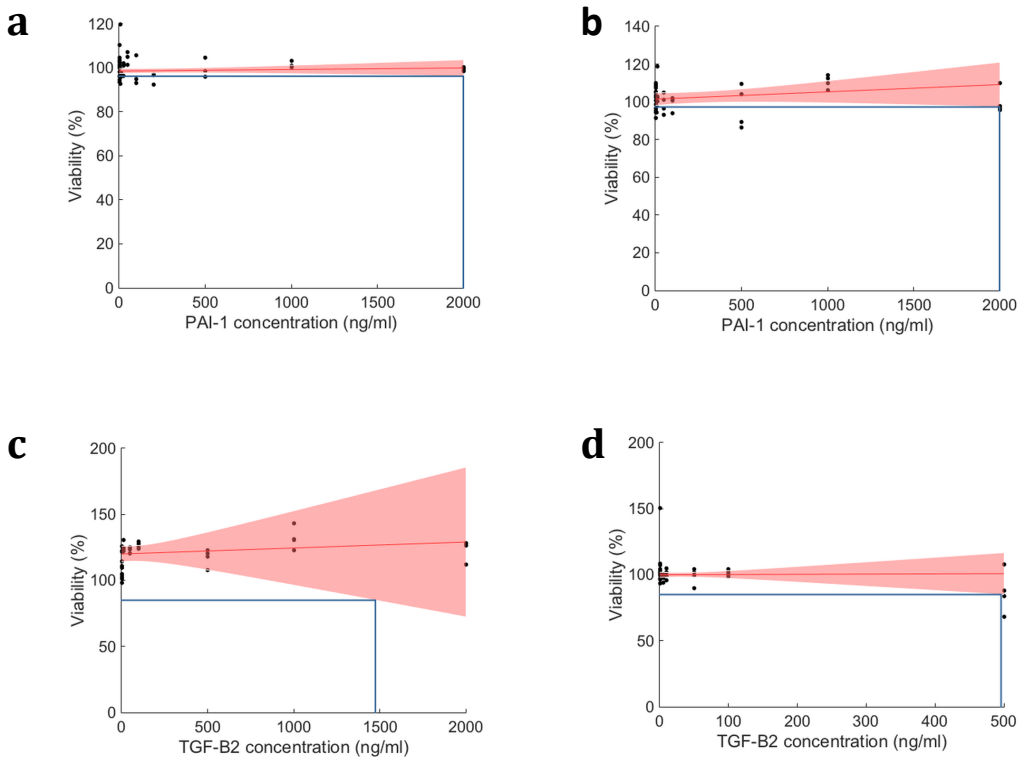

Fig. 3.7. The effect of PAI-1 and TGF-β2 on SCEC and TM cell viability. **(a-b)** Recombinant PAI-1 had no effect on SCEC or TM viability up to 2μg/ml after 24 hr. **(c)** An average viability of 85% was expected with TGF-β2 concentrations up to 1.475μg/ml in SCECs and in **(d)** up to 0.496μg/ml in TM cells. Data points on each graph denote value from a single well, with 3 replicates for each concentration. Red line is a best-fit line through the data. Pink area is 95% confidence interval on the best-fit line. Blue line indicates concentration at which cell viability decreases to below 85%.

Tight junction and ECM expression on PAI-1/TGF-β2 treatment

The effect of PAI-1 and TGF-β2 on SCEC tight junctions was assessed 48 hr after treatment, as these proteins play a role in changes in SCEC permeability (**5.21**). Tricellulin protein expression did not significantly increase with the addition of PAI-1 or TGF-β2. However the relative fold-change, in comparison to control, increased with increasing PAI-1 treatment with mean changes as follows; PAI-1 1ng/ml 1.238, PAI-1 10ng/ml 2.185, and PAI-1 50ng/ml 3.005 (p = ns, n = 5, for all concentrations). There was no obvious difference in tricellulin immunostaining between control and PAI-1 10ng/ml treated SCECs. TGF-β2 20ng/ml treatment caused a non-significant increase in tricellulin expression with an average fold change of 2.013 (p = ns, n = 5). Tricellulin stained SCECs that were treated with TGF-β2 had less cytoplasmic tricellulin around the nucleus and more tricellulin localized to the membrane. This was repeated twice and was apparent throughout the cell culture well, future work would include looking at tricellulin localization using varying concentrations (**Fig. 3.8a**). ZO-1 protein levels were unchanged after any treatment, with mean fold changes of PAI-1 1ng/ml 0.9631 [0.173, 2.552], PAI-1 10ng/ml 0.7726 [0.020, 3.501], PAI-1 50ng/ml 0.7692 [0.146, 1.991], TGF-β2 0.7014 [0.332, 1.197] (p = ns, n = 5 for all treatments). SCECs stained for ZO-1 demonstrated no differences between control and PAI-1 treated cells, TGF-β2 treated cells displayed more intense punctate ZO-1 staining, with ZO-1 in the control cell more diffuse in the cytoplasm (**Fig. 3.8b**)**.** TGF-β2 is known to affect ECM deposition, and so the ECM protein production in TM cells and SCECs was investigated 48 hr after treatment (**5.22**) (Gottanka et al. 2004). Fibronectin expression was significantly up-regulated by 1ng/ml PAI-1 treatment, with a mean fold change of 2.566 (p = 0.02, n = 3). Both PAI-1 10ng/ml and 50ng/ml treatments non-significantly increased fold change in fibronectin expression by 2.490 and 1.931 respectively (p = ns, n = 3). TGF-β2 treatment resulted in an increase in fibronectin expression of 3.879 relative to control expression (p = 0.0008, n = 4), as shown by Western blot and immunohistochemistry (**Fig. 3.9a**). Collagen protein expression was increased significantly after both PAI-1 and TGF-β2 treatment. PAI-1 treatment resulted in increased collagen expression stepwise with PAI-1 concentration, with a mean fold

change of; PAI-1 1ng/ml 1.308 (p = ns, n = 2), PAI-1 10ng/ml 1.848 (p = 0.025, n = 4), and PAI-1 50ng/ml 1.746 (p = 0.043, n = 4). Also, TGF-β2 treatment increased collagen expression in SCECs by 3.538 (p = 0.006, n = 4) relative to control, as shown by Western blot and immunohistochemistry (**Fig. 3.9b**). After PAI-1 treatment no significant change in laminin expression was seen, however there was a trend of increasing laminin with PAI-1 treatment. There was a fold increase of: 1ng/ml 2.451, 10ng/ml 2.317, and 50ng/ml 12.70 (p = ns, n = 3; for all treatments). Laminin was strongly induced in SCECs by TGF-β2, with a fold increase of 25.41 (p = 0.023, n = 3). In control cells laminin expression was clustered around the nucleus, in both PAI-1 and TGF-β2 treated SCECs laminin staining was more spread throughout the cells, with laminin most notably in TGF-β2 treated cells (**Fig. 3.9c**)**.** In TM cells no significant change in fibronectin expression was found with a fold change of 0.321 in PAI-1 1ng/ml, 0.4925 in PAI-1 10ng/ml, 1.620 in PAI-1 50ng/ml, and 1.502 in TGF-β2 treated cells (p = ns, n = 4) (**Fig. 3.10a**). Collagen expression was significantly induced with PAI-1 50ng/ml treated cells; fold change of 3.057 (p = 0.02, n = 3). For all other treatments collagen expression was non-significantly increased compared to control cells: PAI-1 1ng/ml 1.599, PAI-1 10ng/ml 2.814, and TGF-β2 2.291 (p = ns, n = 3; for all treatments) (**Fig. 3.10b**). No change in laminin expression in TM cells was found after all PAI-1 and TGF-β2 treatments (p = ns, n = 2) (**Fig. 3.10c**).

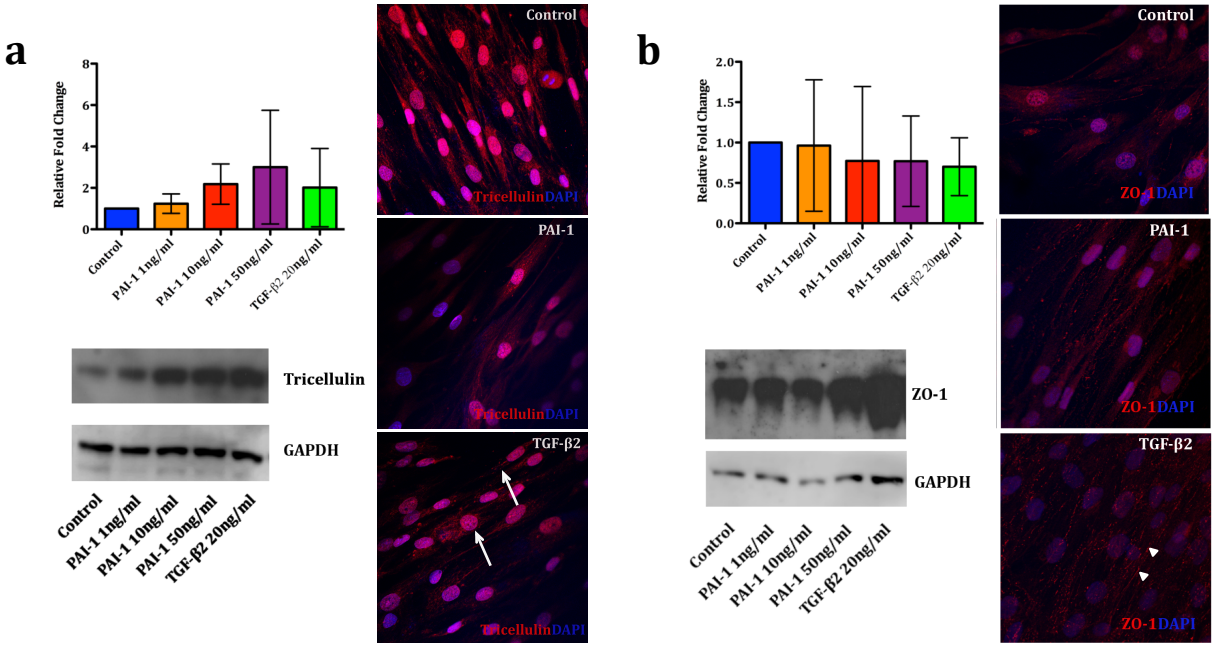

Fig. 3.8. Tight junction expression in SCECs after PAI-1 and TGF-β2 treatment. **(a)** No significant increases in tricellulin protein expression were seen in SCECs after PAI-1 and TGF-β2 treatment by Western blot analysis as seen by fold change and representative blot. SCECs stained for tricellulin have less cytoplasmic stained surrounding the nucleus in TGF-β2 treated cells. White arrows = membrane tricellulin staining. **(b)** ZO-1 expression did not change after PAI-1 or TGF-β2 treatment as shown by fold change and representative Western blot. TGF-β2 treated cells had strong punctate ZO-1 staining (white arrowheads) whereas the control cells had more diffuse ZO-1 cytoplasmic staining.

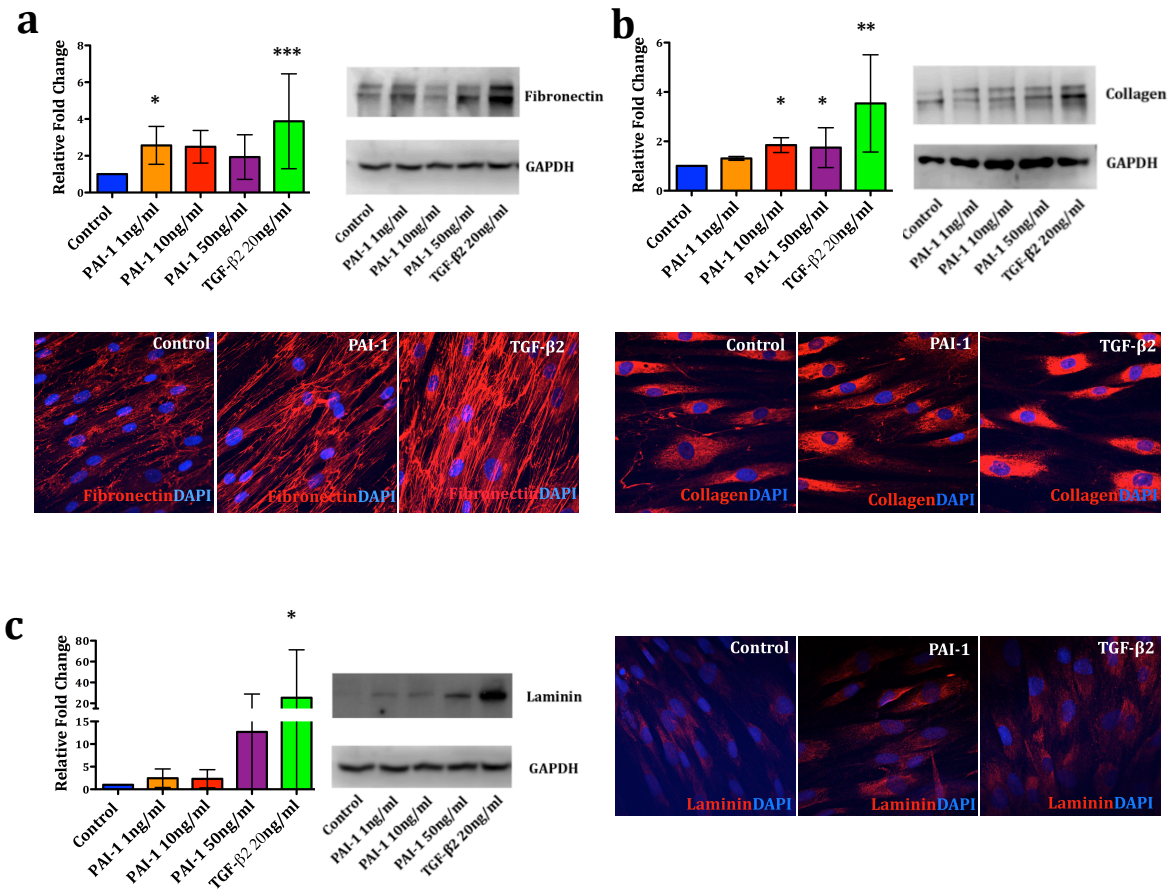

Fig. 3.9. Expression of ECM protein expression in SCECs after PAI-1 and TGF-β2 treatment.

(a) Fibronectin expression is upregulated by PAI-1 1ng/ml and TGF-β2. Fibronectin is present in a strand formation in stained cells, and staining is increased in both PAI-1 and TGF-β2. **(b)** Collagen expression is upregulated by both 10ng/ml, 50ng/ml PAI-1 and by TGF-β2. Collagen staining in SCECs is increased following both PAI-1 and TGF-β2 treatment **(c)** TGF-β2 treatment highly induces laminin expression. Laminin staining of SCEC cells show increased staining in SCEC cells treated with both PAI-1 10ng/ml and TGF-β2 20ng/ml. Fold change in protein expression is quantified by Western blot against untreated control and is represented graphically and by representative Western blot. Graphs show means with s.d. Symbols denote *p* values *, **, *** represent <0.05, <0.01, and <0.001 respectively. Blue = DAPI nuclear stain. Red = Cy3 stain.

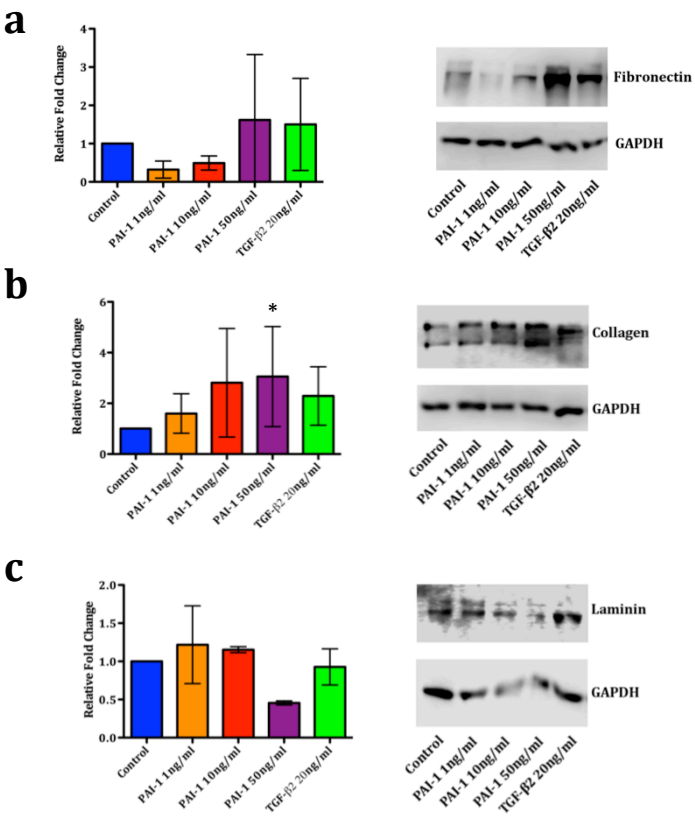

Fig. 3.10. Expression of ECM proteins in TM cells after PAI-1 and TGF-β2 treatment.

(a) No treatment induced a significant differences in fibronectin expression. **(b)** Collagen expression is increased in TM cells after all treatments with a significant difference in PAI-1 50ng/ml treated cells. **(c)** No significant differences in laminin expression between treatments was observed although laminin was decreased in PAI-1 50ng/ml treated cells. Fold change in protein expression is quantified by Western blot against untreated control and is represented graphically and by representative Western blot. *p* value, * = <0.05. Blue = DAPI nuclear stain. Red = Cy3 stain.

The effect of PAI-1/TGF-β2 on cytoskeletal structure

Increased SCEC contraction is associated with increased outflow resistance (Stamer et al. 2015), and so the contraction of SCECs treated with PAI-1 and TGF-β2 was investigated. In a collagen cell contraction assay both PAI-1 and TGF-β2 treatment significantly increased cell contractility at time points (60 – 180 mins) after matrix release (t = 0 min), TGF-β2 contraction was also significantly different at t = 30 min. TGF-β2 and PAI-1 treated cells contracted by 63.26 [61.47, 65.05] % and 48.29 [46.78, 51.08] % at t = 180 relative to baseline, compared with untreated control cells 42.29 [38.79, 45.79] % (n = 3)(**Fig. 3.11a**). Cytoskeletal structure affects cell contraction and so the expression of α-SMA was investigated by Western blot. All PAI-1 treatments resulted in a non-significant increase in α-SMA protein expression in SCECs. TGF-β2 treatment strongly induced α-SMA expression with a fold change of 34.94 relative to control expression (**Fig. 3.11b**). SCECs were double stained for α-SMA and F-actin (**5.19**). In control SCECs α-SMA staining localized to perinuclear areas in the cell. PAI-1 (10ng/ml) treatment caused the α-SMA to form cytoskeletal fibres along the long axis of the cell, these fibres align with F-actin staining as seen in the merged image (yellow). In TGF-β2 (20ng/ml) treated SCECs α-SMA stained more globally across the cell and formed strands at the cell tips to a lesser extent than PAI-1 treated cells. The F-actin strands in PAI-1 and TGF-β2 treated cells were thicker and more disorganized compared to control cells (**Fig. 3.11c**). In TM cells, α-SMA expression trended upwards in all treatments with significant increases in the PAI-1 50ng/ml and TGF-β2 treated cells. The mean fold change relative to control cells was 1.64 (p = 0.04, n = 3) and 2.33 (p = 0.002, n = 2) respectively, no obvious differences in α-SMA structure were observed between treatments (**Fig. 3.12a**). F-actin cross-linked actin networks (CLAN) structures have been shown to form in TM cells on TGF-β2 treatment and are associated with increased cell stiffness. Here the effect of PAI-1 treatment on CLAN formation was investigated (Bermudez et al. 2017). TM cells were treated with PAI-1 10ng/ml, TGF-β2 10ng/ml and left untreated, control. These were stained for F-actin and CLAN structures were counted relative to cell number, as counted by DAPI stained nuclei per image. CLAN structures were denoted as an F-actin structure with 5

hubs with 3 triangular arrangements of spokes. Examples of CLAN formations are shown in treated cells. PAI-1 and TGF-β2 treated cells both had increased CLAN formation with 2.797 [0.3296, 1.573] (p = 0.016, n = 19) CLANs/cell and 2.228 [1.204, 3.251] (p = 0.028, n = 19) CLANs/cell respectively, compared to 0.9515 [0.3206, 1.573] CLANs/cell in the control samples (**Fig. 3.12b**).

These data demonstrate that PAI-1 induces both ECM deposition and changes in the actin cytoskeleton of SCECs. This suggests that PAI-1 may have a role in increasing outflow resistance and is a promising candidate for AAV-mediated secretion into the AH, with the goal of effecting AH outflow facility and controlled elevation of IOP. This would offer an attractive POAG model that did not physically disturb the outflow tissues, such as in the microbead model, and would have reduced off-target effects, such as those in the steroid-induced model of glaucoma.

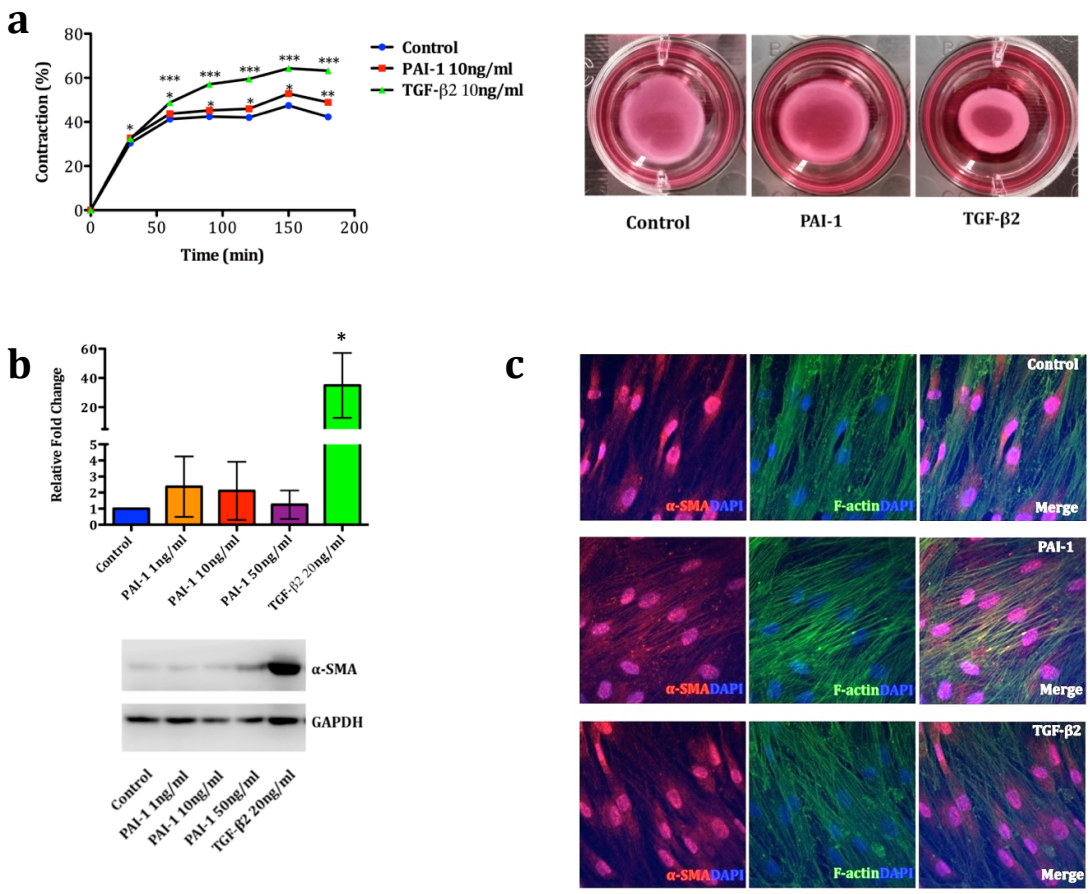

Fig. 3.11. Effect of PAI-1 and TGF-β2 on SCEC contractility.

(a) SCECs treated with TGF-β2 had a greater reduction of collagen matrix size after release compared with control untreated SCECs at all timepoints after T = 30 mins post matrix release. PAI-1 treated cells retracted faster at all points post T = 60 mins. Representative image of retracted collagen matrices at 180 mins post release (right). **(b)** SCEC α-SMA protein expression is increased in TGF-β2 treatments. Graphical depiction of mean fold change, with s.d. and representative Western blot. **(c)** α-SMA staining in SCEC cells; PAI-1 treatment results in the formation of α-SMA stress fibres, that colocalise with F-actin strands. TGF-β2 treated cells show more α-SMA staining throughout the cell. F-actin strands are thicker and more disorganised in both PAI-1 and TGF-β2 treated SCECs. Symbols denote *p* values *, **, *** represent <0.05, <0.01, and <0.001 respectively. Blue = DAPI nuclear stain. Red = Cy3 stain. Green = Alexa-488 conjugated phalloidan. Yellow = co-localised F-actin and α-SMA.

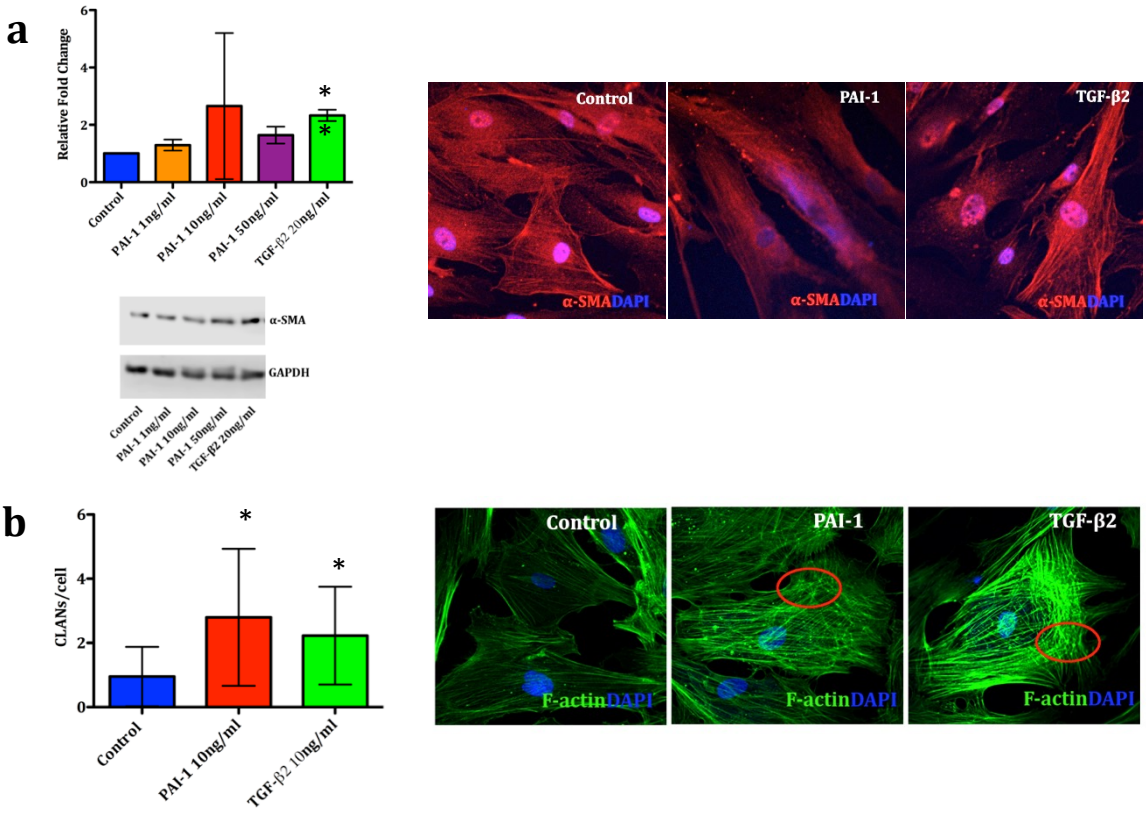

Fig. 3.12. Effect of PAI-1 and TGF-β2 treatment on the TM cytoskeleton.
(a) All treatments lead to an increase in α-SMA protein expression in TM cells**,** as shown graphically and by representative Western blot. Staining revealed no obvious differences in α-SMA structure between treatments. **(b)** Both PAI-1 and TGF-β2 treatment induced the formation of F-actin structures known as CLANs. The representative images of F-actin in TM cells treated with PAI-1 and TGF-β2 displaying the intense node staining typical of CLANs. Graphs display mean and s.d. Red ellipse = CLAN structures. Symbols denote *p* values *, **, represent <0.05, <0.01 repectively. Red = Cy3. Blue = DAPI nuclear stain. Green = Alexa-488 conjugated phalloidan.

AAV-mediated secretion of PAI-1 to the mouse AH

To test the effect of PAI-1 on outflow facility *in vivo* a mouse *PAI-1* cDNA transgene was placed under the control of a CMV promoter in AAV-2/9 (AAV-PAI-1) (**5.26**). This approach uses the corneal endothelium as a reservoir for PAI-1 secretion into the AH, and through the natural AH flow dynamics the secreted PAI-1 will be transported into the outflow tissues. 2µl of AAV-PAI-1 ($1x10^{11}$GC/eye) was intracamerally injected into C57BL/6J mouse ACs with the contralateral eye injected with 2µl of Null AAV-2/9 (AAV-Null) ($1x10^{11}$GC/eye) control vector (**5.27**). IOP was measured pre-injection and post-injection, from week 3, bi-weekly until week 11 post-injection (**5.30**). At no time points was there an increase in IOP in the AAV-PAI-1 treated eyes compared to baseline or compared to the contralateral control eyes (p = ns, n = 16 per group) (**Fig. 3.13a**). At week 12 post-injection the conventional outflow facility, or pressure dependent outflow, of the AAV injected eyes was measured using the *iPerfusion* system (**5.33**)(Sherwood et al. 2016). Eyes were enucleated and perfused in pairs over incrementing steps in applied pressure. The resulting facility data from this analysis showed that control eyes had an average facility of 6.873 ± 1.238 nl/min/mmHg with experimental eyes having an average facility of 6.710 ± 1.264 nl/min/mmHg (**Fig. 3.13b**). Therefore, there was no change in facility, with an average difference in facility of -2 [-26, 30] % in experimental eyes compared to contralateral control eyes (p = 0.862, n = 10 per group). (**Fig. 3.13c**). PAI-1 immunostaining of AAV treated sections demonstrate a lack of PAI-1 staining in the endothelium AAV-Null corneas and strong PAI-1 staining in the AAV-PAI-1 treated eyes (**Fig. 3.14a**). PAI-1 levels in AAV treated mouse AH were investigated by ELISA, AAV-Null treated eyes having mean PAI-1 levels of 415.3 [75.42, 755.1] pg/ml with AAV-PAI-1 treated eyes having mean PAI-1 levels of 528.9 [66.64, 991.1] pg/ml. This corresponds to an average increase of PAI-1 in experimental eyes of 113.6 [-285, -512.3] pg/ml, however this is non-significant due to the variable nature of PAI-1 levels in mouse AH (p = 0.497, n = 4 per group) (**Fig. 3.14b**). This marginal increase in the treated eyes may offer an explanation as to why no change in outflow facility or IOP was observed.

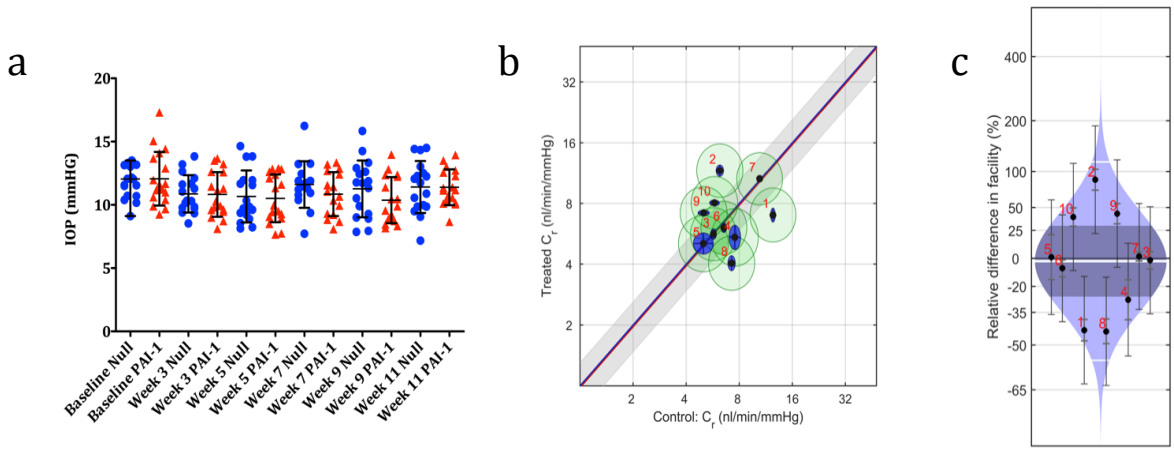

Fig. 3.13. Effect of AAV-2/9 PAI-1 on mouse outflow facility and IOP. **(a)** IOP never increased in AAV-PAI-1 treated mouse eyes over an 11 week period compared to baseline or compared to AAV-null treated contralateral control. Graph displays IOP median and range for each timepoint. **(b)** Paired outflow facility plot. Each inner point represents an eye pair, with log-transformed facilities of the control eye (AAV-Null) plotted on the x axis, and treated (AAV-PAI-1) eye on the y axis. Outer blue and green ellipses show uncertainties generated from fitting the data to a model, intra-individual and cannulation variability respectively. Average increase is denoted by the red line, enclosed by a grey 95% CI, indicating significantly increased facility (does not overlap the blue unity line). No change is seen between groups. **(c)** 'Cello' plot depicting individual % changes in outflow facility values for eyes at 8 mmHg (Cr) and statistical distribution of the percentage change. Each point represents a single eye with 95% CI. Log normal distribution is shown, with the central white band showing the geometric mean and the thinner white bands showing two geometric standard deviations from the mean. The shaded region represents the 95% CI on the mean.

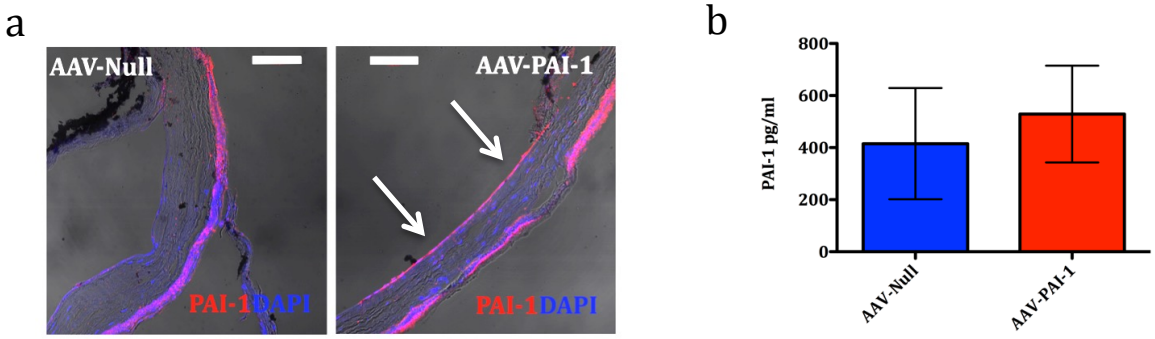

Fig. 3.14. AAV-mediated delivery of PAI-1 to the AH.

(a) PAI-1 staining in the mouse cornea. PAI-1 staining is found in the corneal endothelium of the AAV-PAI-1 treated eye and not in the contralateral control. **(b)** PAI-1 (pg/ml) levels in the AH of mice treated with AAV-Null and AAV-PAI-1 as measured by ELISA. Graph displays mean and sd. White scale bar = 100μm. White arrow = PAI-1 expression in the corneal endothelium. Blue = DAPI nuclear stain. Red = Cy3.

Discussion

In this study, the efficacy of AAV viruses at transducing the tissues of the AC was investigated, with the goal of delivering outflow modulating compounds to the TM and SC. Previously, adenoviruses have been used to deliver vectors to various tissues of the AC (Borrás et al. 2001; Junglas et al. 2012; Testa et al. 2013). However, these viruses are immunogenic and transgene expression is only transient (Shepard et al. 2010). AAVs however are less immunogenic, non-replicating and transduce tissues over long periods (Samulski et al. 2015). Other studies have previously focused on AAV transduction of the outflow tissues, the TM and SC. These studies found that the human TM does not express the delivered transgene, this is because the viral ssDNA does not get converted to dsDNA and so is not transcribed (Borrás et al. 2006). This dsDNA synthesis step can be avoided by the use of scAAVs, and in this regard it has been demonstrated that scAAV2/2 has an ability to transfect the TM in humans, monkeys, rats, and sheep (Buie et al. 2010a; Borras et al. 2016). Thus, scAAV has been used to deliver MMP-1 as well as a gene encoding a dominant negative RhoA mutant to sheep and rat TM respectively, with a resultant outflow-lowering effect (Borras et al. 2016; Borrás et al. 2015).

The study outlined here focused on the use of AAVs in the mouse AC, investigating 6 different AAV pseudotypes (AAV2/2, 2/5, 2/9, and scAAV2/2, 2/5, 2/9). It was found that scAAV2/2 along with AAV2/5 and scAAV2/5 did show eGFP expression in the mouse outflow tissues, however transgene expression was sparse as seen by AC flatmount and mouse AC sections. Other tissues transduced at the mouse AC angle were the endothelial cells of the episcleral vessels, by AAV2/2, and the tissues surrounding the episcleral veins by scAAV2/9. These results do not agree with the established view of AAV transduction in the TM, however some recent studies have had similar results using scAAV2/2 in the mouse AC (Bogner et al. 2015; Wang et al. 2017). These studies both show that scAAV2/2 shows weak transduction of the outflow tissues, with one using a mutated AAV capsid and another a hybrid AAV2 and AAV8 capsid to increase transduction of these tissues. Wang et al. found that TM cells, if treated at a high concentration, could be transduced by single stranded AAV, demonstrating that these cells do in fact have the capability of synthesizing dsDNA from viral ssDNA (Wang et al. 2017). This fits

with the data of this study, which demonstrates the transduction of the mouse TM using the single-stranded virus AAV2/5. However, different viral preparations of any of these pseudotypes may have varying tropisms than as seen here, due to either empty capsids in the preparations or mispackaged capsids, these cannot be ruled out as stock titre was not confirmed in house and vector genomes were not sequenced after production. In spite of these concerns, using the 6 pseudotypes in this study, the mouse outflow tissue is not a viable target for AAV-mediated therapy.

Previously, it has been reported that AAV2/2 and scAAV2/2 transduce the corneal endothelium to a small extent (Bogner et al. 2015; Lai et al. 2002); this was not evident in this study, which may be due to the injection method or differing viral preps. In the work outlined above, three of the pseudotypes transduced the cells of the corneal endothelium, AAV2/5, scAAV2/5, and AAV2/9. Of these, AAV2/9 treated corneas demonstrated the most consistent and strong eGFP expression. On flatmount analysis, transduction was found to be widespread throughout the cornea. The transduction of the corneal endothelium represents a reservoir in which to express soluble compounds for secretion into the AH, the natural flow of AH then carrying these compounds to the outflow tissues. Another advantage of using the corneal endothelium as a reservoir is that it can be accessed by topical eyedrops (Koizumi et al. 2014). Therefore any viral vector delivered to this tissue could be induced via eyedrop. To test this hypothesis a plasmid containing the eGFP transgene was placed under the control of a doxycycline inducible promoter, and delivered to the corneal endothelium by AAV2/9. This inducible promoter has previously been used in ocular studies, however the doxycycline was administered orally (Stieger et al. 2007). These data are the first to show that doxycycline topical eye-drops can be used to induce AAV mediated transgene expression in the eye. The next step in this study was the delivery of MMP-3 to the AH. To this end a paper (O'Callaghan, Crosbie et al 2017) appended to this Chapter describes the use of this delivery system to increase outflow facility in mice, expressing soluble MMP-3 from the corneal endothelium. Both the CMV driven MMP-3 and doxycycline induced MMP-3 treated eyes demonstrated an increase outflow facility, proving the viability of this system.

The next goal was to discover other targets that may modulate outflow resistance, if expressed from AAV-2/9 in the corneal endothelium. To this end, a cytokine array was used to find soluble proteins in the AH that are associated with glaucoma. Human AH samples were taken from cataract, primary open-angle glaucoma (POAG), and pseudoexfoliative glaucoma (PXF(G)) patients undergoing routine cataract surgery. This study shows that both POAG and PXF(G) increase the transendothelial electrical resistance (TEER) and decreased the paracellular flux across the SCEC monolayer. TEER is a measure of endothelial barrier integrity, and reflects the ionic conductance across the endothelial monolayers. Paracellular flux is measured by the transport of a non-electrolyte molecular tracer, in this case 70kDa FITC-dextran, across a monolayer. This reading reflects the paracellular water flux across an endothelial barrier, in addition to the pore size of the tight junction (Srinivasan et al. 2015). In the paracellular flux assay, plates cannot be directly compared across due to minor differences between runs and so the different Papp values in cataract treated plates does not indicate a difference of biological importance. In SCECs, IOP-lowering compounds decrease the TEER and increase permeability across the monolayer; here we see the opposite effect using the glaucomatous AH. The TEER effect was only significant in the POAG treated cells, however due to the scarcity of human AH there was low replicates for the PXG treated cells. These results indicate that there are soluble compounds in the AH that are linked to glaucoma and that these can increase outflow resistance in the tissues of the conventional pathway.

The array used tests for 36 separate human cytokines, chemokines, and acute phase proteins; 9 of these proteins were detected in the patient AH. Of these sICAM-1, MCP-1, and PAI-1 were greatly increased in PXF(G) compared to cataract; I-TAC/CXCL11 was also present in PXF(G) AH but not detected in CAT. PXF(G) is a late stage fibrillopathy with secondary glaucoma, which is linked with increased systemic inflammation and endothelial dysfunction (Garweg et al. 2017). In the POAG AH there was a similar increase in sICAM-1, MCP-1 and PAI-1 as in PXG; I-TAC/CXCL11 was even further increased in POAG relative to the PXF(G), and soluble IL-1ra was only increased in POAG. ICAM-1 is an immunoglobulin like cell adhesion molecule expressed by leukocytes and endothelial cells, the soluble form

is increased in the serum of patients with cardiovascular disease. ICAM-1 is involved in the transendothelial migration of leukocytes to sites of inflammation; the soluble version lacks the cytoplasmic tail and is produced by endothelial cells by as yet an unknown mechanism, and binds competitively to ligands of the membrane bound protein (Lawson & Wolf 2009; Derosa & Maffioli 2016). In the eye sICAM-1 levels in the vitreous have been linked to retinal vascular permeability and severity in diabetic macular edema (Zhu et al. 2014). MCP-1 is also involved in the innate immune response, has a potent ability to mediate macrophage recruitment and migration to sites of inflammation; it is produced by astrocytes, fibroblasts, endothelial cells and vascular smooth muscle cells (Semple et al. 2010). MCP-1 has been reported to be significantly increased in the plasma of NTG patients, and is hypothesized to be linked to vascular dysfunction and inflammation in NTG (Lee et al. 2012). I-TAC/CXCL11 is a chemokine that is also involved in leukocyte migration and is induced in corneal fibroblasts by IFN-γ and TNF-α (McInnis et al. 2005). The IL-1ra is a major mediator of inflammatory and immune reactions, along with IL-1β and IL-1α, with the ratio between these components key in the inflammatory response (Yan et al. 2016). Interestingly, IL-1α has been shown to increase MMP-3 expression in human TM cells and to increase outflow facility in perfused porcine anterior segment organ culture (Kelley et al. 2007). Hypothetically increased IL-1ra levels may result in reduced IL-1α-mediated MMP-3 in the outflow tissues and thus reduce ECM degradation in glaucomatous eyes.

Of all the proteins increased in this cytokine array PAI-1 was the most interesting. PAI-1 is a member of the serine protease inhibitor (serpin) family and is the principal physiological inhibitor of urokinase-type plasminogen activator (u-PA) and tissue-type plasminogen activator (t-PA), which convert plasminogen into plasmin by proteolytic cleavage. Plasmin is a serine protease that is involved in ECM degradation, especially of blood proteins such as fibrin (Diebold et al. 2008). One of PAI-1s targets, t-PA, has been shown to decrease steroid induced ocular hypertension in sheep after a single injection of recombinant protein (Gerometta et al. 2010; Candia et al. 2014). In the eye, PAI-1 expression is known to be induced by TGF-β2 in the outflow tissues, which is associated with increased outflow

resistance in perfused human anterior segments (Gottanka et al. 2004; Swaminathan et al. 2014).

TGF-β2 induces ECM build-up by increased ECM protein production and reduced ECM degradation in the TM, in addition to increasing TM cell stiffness (Fuchshofer & Tamm 2012; Bermudez et al. 2017). In this study the levels of TGF-β2 and PAI-1 in the AH of POAG patients were compared to cataract patient AH, there was an increase in POAG samples in both cases, however this was significant only in the case of PAI-1. Previously, a meta-analysis of combined studies found that both total and active TGF-β2 levels were significantly up-regulated in POAG (Agarwal et al. 2015). This difference may be because in this instance TGF-β2 levels were adjusted to total protein concentration and previous studies have found that there is an increase of total protein content in POAG AH, which would mask this increase (Tripathi et al. 1994; Schlötzer-Schrehardt et al. 2003). Both TGF-β2 and another of it's downstream regulators CTGF, have been used to create induced mouse models of POAG, that develop ocular hypertension and RGC death (Shepard et al. 2010; Junglas et al. 2012). As PAI-1, also a downstream regulator of TGF-β2, is increased in POAG AH, and is an inhibitor of a factor that relieves ocular hypertension, it was chosen for further study.

The effect TGF-β2 has on the outflow resistance has been well investigated; however most of the knowledge of TGF-β2 activity is related to the TM (Fuchshofer & Tamm 2012), with little known of it's effects on the cells of the SC (C. N. Dautriche et al. 2015). In this study the effects of both PAI-1 and TGF-β2 on SCECs and human TM cells were investigated with the focus on SCECs. Firstly, both PAI-1 and TGF-β2 increased the TEER values on SCEC and TM monolayers, implying an increase in barrier integrity. It seems these treatments had a far more extreme effect on the TM cells in comparison to the SCECs. Though the TEER values of TM cells were far lower, ~3-4 $\Omega.cm^2$ compared to ~12-14 $\Omega.cm^2$ for SCECs on average, the total increase in $\Omega.cm^2$ was greater for both treatments in the TM cells. Similarly, TGF-β2 treatment decreased paracellular flux across both the TM and SC monolayers, with this treatment reducing tracer flow between cells. Conversely, in SCECs, PAI-1 treatment actually increased paracellular permeability relative to untreated cells, which appears to contradict the later TEER results. In

fact these two assays are measures of separate phenomena, one is the measure of ionic conductance and the other a measure of the movement of a paracellular tracer across a barrier as previously mentioned. Hypothetically, this difference could be due do a change in tight junction complex formation that decreases permeability to ions but at the same time increases permeability to non-electrolyte tracers (Rosenthal et al. 2017). In TM cells PAI-1 appeared to have a dose dependent effect on permeability, with flux decreasing after 1ng/ml PAI-1 treatment but increasing with increasing PAI-1 concentration. The effects were also found to be independent of any change in viability, either of increased cell proliferation or increased cell death. These apparently confounding effects of PAI-1 on cell permeability mirror it's conflicting roles in other processes such as in angiogenesis and vascular remodeling. In the case of vascular remodeling PAI-1 both promotes and represses remodeling dependent on the vascular bed, the type of lesion or the experimental or clinical conditions (Diebold et al. 2008). With regard to angiogenesis, PAI-1 has been found to have a dose dependent effect on choroidal neovascularization being pro-angiogenic at low concentrations and anti-angiogenic at high concentrations (Lambert et al. 2003). PAI-1 both inhibits plasminogen activators and activates ERK signaling through the low density lipoprotein receptor-related protein 1 (LRP) (Balsara & Ploplis 2008). Thus, with increasing PAI-1 concentration it's inhibitory effect on the plasminogen activators could be offset by it's signaling through LRP-1 and result in increasing cell permeability. These results suggest that PAI-1 has multiple effects on the tissues of the outflow pathway, and so changes in protein expression with PAI-1 and TGF-β2 treatment was assessed in these cells.

During the study it was found that both PAI-1 and TGF-β2 appeared to induce the expression of the tight junction protein tricellulin, and to have little effect on ZO-1 expression. However, only in TGF-β2 treated cells was there a difference in tight junction protein localization, with increased tricellulin staining at the cell borders and ZO-1 staining more punctate and less diffuse through the cytoplasm. These findings would need to be corroborated with EM imaging as they are only initial studies of duplicated immunofluorescence, however this may indicate that TGF-β2 treatment causes cytoplasmic ZO-1 protein to migrate to the membrane junctions, therefore suggesting tight junction rearrangement may play

a role in changes in permeability. As previously discussed, eyes perfused with TGF-β2 have increased deposition of ECM at the outflow tissues, here both PAI-1 and TGF-β2 induced the production of ECM proteins in SCECs. Fibronectin, collagen and laminin expression were all increased in SCECs with both treatments. In TM cells, there appeared to be an increase in ECM production by PAI-1, however as TM is not the focus of this study there are not enough numbers to be positive on this account. ECM proteins levels are known to be up-regulated in the TM on TGF-β2 treatment and so it is possible that PAI-1 does indeed increase ECM deposition in the TM (Vranka, Kelley, et al. 2015). A rise in ECM deposition at the JCT-SC junction is a feature of POAG and is seen in eyes with elevated TGF-β2 (Fuchshofer & Tamm 2012; Vranka, Kelley, et al. 2015). As outlined in this work both TGF-β2 and PAI-1 induced increased ECM production in SCECs, which may play a role in TGF-β2 mediated pathogenesis.

All AH must pass through the inner wall of the SC and this continuous barrier has some unique features to deal with the pressure gradient across it, including pore and giant vacuole formation (Braakman et al. 2015b; Ryan M. Pedrigi et al. 2011). It has been found in SCECs from glaucomatous donors, that there is an increase in cell stiffness and this correlates with a decrease in pore density (Darryl R Overby et al. 2014). In addition after treatment with a Rho-kinase inhibitor, which reduces SC stiffness and cell contractility, there is an increase in giant vacuole formation in bovine eyes (Jin et al. 2005; Lu et al. 2008). Cell stiffness and contraction are governed by cytoskeletal structure and so the effect of PAI-1 and TGF-β2 on cell contraction and actin structures was investigated. Both TGF-β2 and PAI-1 treatment increased SCEC contraction, with TGF-β2 having a greater effect. Concurrent with this observation, both treatments increased F-actin staining, with the strands traversing the cell in a more disorganized manner in treated cells. α-SMA was greatly induced by TGF-β2 treatments in SCECs, and is organized into strands at the cell tips. Interestingly, even though PAI-1 does not induce α-SMA expression to the same extent, it does lead to the formation of α-SMA fibres throughout the cell that align with F-actin filaments. Similarly, α-SMA was increased in TM cells after both PAI-1 and TGF-β2 treatment. This increase in α-SMA in the outflow tissues occurs, along with an increase in other mesenchymal markers, in glaucomatous and aged eyes and is

associated with increased cell stiffness and outflow resistance (Park et al. 2014a; Liu et al. 2017). In addition, the PAI-1 TM cells displayed an increase in F-actin CLAN structures. These structures are TM-specific, have previously been observed in TGF-β2 treated and glaucomatous TM cells and are associated with an increase in sub-corticol cell stiffness (Bermudez et al. 2017). These studies demonstrate that PAI-1 has multiple effects on the tissues of the outflow pathways to modulate outflow resistance, including an increase in ECM deposition and cytoskeletal reorganization.

To test the effect of PAI-1 *in vivo,* the mouse PAI-1 transgene driven by a CMV promoter was placed into an AAV-2/9 vector and was injected into the mouse eye with AAV-null as a control in the contralateral eye. Over the course of 11 weeks post injection there was no increase in IOP in the treated eye. Outflow facility is a measure of pressure dependent outflow, the majority of which is ascribed to the conventional outflow pathway. At week 12, outflow facility was compared in these mice, with no difference apparent between the treated and control eyes. Despite this, immunohistochemistry of the AAV-PAI-1 treated eyes displayed PAI-1 production in the corneal endothelium, which was lacking in the control eyes. ELISA analysis of the AH from these mice showed an increase in PAI-1 level that was not significant. Due to the small amount of AH taken from the mouse AC, ~3µl, samples had to be pooled and so examined samples were low, in addition there was high variability in PAI-1 between samples. These factors contributed to the non-significance of the increase. However, taken in conjunction with the immunohistochemistry it is likely that the virus did produce PAI-1 that was secreted into the AH. Therefore, there are multiple factors that may play a role in the lack of effect on IOP and outflow facility in this instance.

Firstly, glaucoma is a chronic and complex disease and the effect of PAI-1 on the outflow tissue may require long-term exposure at elevated levels. Secondly, is there a species-specific difference in the action of PAI-1 on the outflow tissues? At the present time, study of the mouse outflow pathway is limited owing to its small size and difficulty in isolation, and so one must speculate. The murine PAI-1 protein has conserved domains compared with the human protein, including anti-fibrinolytic, LRP-1 binding and vitronectin binding domains (Xu et al. 2004). In

addition, PAI-1 is up-regulated in the murine outflow tissues by TGF-β2, and similarly to in humans this results in increased outflow resistance (Shepard et al. 2010; Junglas et al. 2012). Another aspect may be that there is not enough active PAI-1 reaching the outflow tissues to enact a measurable change in outflow. This could be due to the spontaneous inactivation of PAI-1 soon after production. PAI-1 is secreted in a labile form prone to conversion to it's latent form unless complexed with vitronectin, which is found in high amounts in ECMs and is produced by the TM (Ueda et al. 2002; Xu et al. 2004). In this regard, there are available methods of optimizing viral transduction and transgene efficiency that could be addressed in future studies. Firstly, a different viral prep may increase vector titre as well as reduce the risk of mis-packaged capsids by using the dual plasmid method of production for example (Grimm et al. 2003). Although with a titre of 5×10^{13} GC/ml, the current viral prep is already a high concentration. This titre was not assessed in house, rather by Vector Biolabs who isolate AAVs via CsCl gradient, giving a low amount of empty vector. Therefore, it may be more profitable to investigate methods of increasing transgene production. In this study the constitutive CMV promoter was used, as this is not isolated from a mammalian species its may not maximize transgene expression; a tissue specific promoter may increase corneal endothelial expression of PAI-1. Recently, the POU6FS promoter has been found to demonstrate high specificity for corneal endothelial expression and may be a good candidate (Yoshihara et al. 2017). Otherwise, codon optimization could be used to increase transgene stability and protein production, this method preferentially uses more codon variants corresponding to more abundant tRNAs to help translation efficiency (Mauro & Chappell 2014). This method has been used to increase stability and translation of an AAV delivered transgene in a therapy targeting X-linked Retinitis Pigmentosa and has shown retention of rods and cones two years after delivery of a codon optimized RPGR to a canine model of the disease (Beltran et al. 2017). In addition, PAI-1 has a latent confirmation and has a short half-life of 2h *in vivo*, and so use of a mutant showing more constitutive activity could be of benefit. The cys-mutated PAI-1 which has similar inhibitory activity to the wild-type protein with a half life increase of 2h to >700h would be a good candidate in this case (Chorostowska-Wynimko et al. 2003; Lindahl et al. 1989). Further, it must be considered that all quantitative

measures of PAI-1 concentration in the AC are through AH ELISA. However, due to the secondary protein pathway at the anterior iris base, the outflow tissues may experience a 5-fold increase in protein concentration observed in the AH (Freddo 2013; Bert et al. 2006). Added to this is the fact both the TM and SC produce PAI-1, further increasing the possible pool of active PAI-1 that reaches the conventional outflow tissues. The effect of PAI-1, *in vitro,* on cell monolayer is more apparent, and these are obviously more responsive and simple to manipulate than *in vivo* tissues. However, this *in vitro* data provides good evidence to illustrate the role of PAI-1 in POAG and TGF-β2-induced ocular hypertension. In conclusion, introduction of PAI-1 from the corneal endothelium using AAV2/9 has no effect on IOP or outflow resistance, likely due to a concentration deficit. Nonetheless recombinant PAI-1 increases human SCEC contractility via remodeling of the cytoskeletal structure, increases ECM deposition, and likely has a role in the increasing outflow resistance at the conventional outflow pathway.

Human Molecular Genetics, 2017, Vol. 26, No. 7 1230–1246

doi: 10.1093/hmg/ddx028
Advance Access Publication Date: 1 February 2017
Original Article

ORIGINAL ARTICLE

Therapeutic potential of AAV-mediated MMP-3 secretion from corneal endothelium in treating glaucoma

Jeffrey O'Callaghan[1,*], Darragh. E. Crosbie[1], Paul. S. Cassidy[1], Joseph M. Sherwood[2], Cassandra Flügel-Koch[3], Elke Lütjen-Drecoll[3], Marian M. Humphries[1], Ester Reina-Torres[1], Deborah Wallace[4], Anna-Sophia Kiang[1], Matthew Campbell[1], W. Daniel Stamer[5], Darryl R. Overby[2], Colm O'Brien[6], Lawrence C. S. Tam[1,*,†] and Peter Humphries[1,*,†]

[1]Ocular Genetics Unit, Smurfit Institute of Genetics, University of Dublin, Trinity College, Dublin, D2, Ireland, [2]Department of Bioengineering, Imperial College London, London, SW7 2BX, UK, [3]Department of Anatomy II, University of Erlangen-Nürnberg, D-91054 Erlangen, Germany, [4]Clinical Research Centre, UCD School of Medicine and Medical Science, University College Dublin, Belfield, Dublin 4, Ireland, [5]Departments of Ophthalmology and Biomedical Engineering, Duke University, Durham, NC, USA and [6]Department of Ophthalmology, Mater Misericordiae University Hospital, Dublin, D7, Ireland

*To whom correspondence should be addressed: Tel: 353 1 896 2164, 353 1 896 1547; Fax: 353 1 679 8558; E-mail: ocallaje@tcd.ie (J.O.), lawrenct@tcd.ie (L.C.S.T.), pete.humphries@tcd.ie (P.H.)

Abstract

Intraocular pressure (IOP) is maintained as a result of the balance between production of aqueous humour (AH) by the ciliary processes and hydrodynamic resistance to its outflow through the conventional outflow pathway comprising the trabecular meshwork (TM) and Schlemm's canal (SC). Elevated IOP, which can be caused by increased resistance to AH outflow, is a major risk factor for open-angle glaucoma. Matrix metalloproteinases (MMPs) contribute to conventional aqueous outflow homeostasis in their capacity to remodel extracellular matrices, which has a direct impact on aqueous outflow resistance and IOP. We observed decreased MMP-3 activity in human glaucomatous AH compared to age-matched normotensive control AH. Treatment with glaucomatous AH resulted in significantly increased transendothelial resistance of SC endothelial and TM cell monolayers and reduced monolayer permeability when compared to control AH, or supplemented treatment with exogenous MMP-3.

Intracameral inoculation of AAV-2/9 containing a CMV-driven MMP-3 gene (AAV-MMP-3) into wild type mice resulted in efficient transduction of corneal endothelium and an increase in aqueous concentration and activity of MMP-3. Most importantly, AAV-mediated expression of MMP-3 increased outflow facility and decreased IOP, and controlled expression using an inducible promoter activated by topical administration of doxycycline achieved the same effect. Ultrastructural analysis of MMP-3 treated matrices by transmission electron microscopy revealed remodelling and degradation of core extracellular

†These authors contributed equally to this work.

Received: December 9, 2016. **Revised:** January 17, 2017. **Accepted:** January 18, 2017

matrix components. These results indicate that periodic induction, via use of an eye drop, of AAV-mediated secretion of MMP-3 into AH could have therapeutic potential for those cases of glaucoma that are sub-optimally responsive to conventional pressure-reducing medications.

Introduction

The eye is pressurised by a balance in the production of aqueous humour (AH) by the ciliary processes and resistance to its drainage through the trabecular meshwork (TM) and Schlemm's canal (SC). Located at the apex of the iridocorneal angle, SC is a flattened circular vessel with an average meridional diameter of 233 μm in humans (1). AH exits the lumen of SC into collector channels and drains into the episcleral veins that are visible on the surface of the sclera. Precise regulation of aqueous inflow together with outflow resistance is critical in maintaining an average intraocular pressure (IOP) of approximately 16 mmHg in a normal functioning eye (2). In cases of primary open-angle glaucoma (POAG), so-called because the iridocorneal angle remains open without noticeable physical obstruction, resistance to AH drainage through the TM and SC is increased by mechanisms that have yet to be fully elucidated, resulting in elevated IOP (3). This, in turn, results in deformation of the lamina cribrosa—the tissue that structurally supports the optic nerve head—(often referred to as 'cupping' of the optic nerve head), damaging retinal ganglion cell axons, leading to ganglion cell degeneration and irreversible blindness.

Lowering IOP remains the only effective treatment for POAG. Topical pressure reducing medications either increase the rate of aqueous outflow through the conventional or unconventional pathway, or reduce aqueous production (3). The U.S. spends $1.9 billion per annum to treat glaucoma, 38–52% of such costs being related to topical pressure reducing medications (4). However, such medications often do not reduce IOP to the desired target pressure and may induce side effects in certain patients. Such patients may then undergo surgical interventions, which have associated risks and complications. Hence, there remains an unmet clinical need for improved methods of disease treatment.

Functional studies have provided evidence that the generation of aqueous outflow resistance is most significant in the juxtacanalicular tissue (JCT—the outer layer of the TM) and inner wall endothelium of SC (5,6). In particular, the extracellular matrix (ECM) composition in the JCT region has been shown to influence outflow patterns and resistance generation (6–11). Competitive disruption or inhibition of integrin-ECM linkages that attach the cell to the ECM, or inhibition of ECM receptors have been associated with increases in endothelial monolayer permeability and transendothelial transport (12–15). This implicates features that are relevant to SC endothelial cells (SCEC) and their supporting basement membrane, such as integrin-ECM interactions, along with other inter-endothelial junctions that govern cell shape, in the control of endothelial paracellular permeability (16). TM cells play an integral role in modulating the ECM of the JCT to preserve AH flow pathways via continual and signal-initiated ECM remodelling (17). The ECM in the JCT region is comprised of a heterogeneous group of fibrous and matrical materials including collagen type IV, proteoglycans, laminin and fibronectin, all of which provide tensile strength and support to surrounding cells. The cribriform plexus, a structure composed of elastic fibres, connects the inner wall endothelium and the ciliary muscle, allowing for JCT expansion in response to IOP elevation (18). ECM reconditioning of these matrix networks can thus induce changes in the actin cytoskeleton through integrin-ECM linkages, enabling F-actin or alpha-smooth muscle actin (α-SMA) to act as markers for active ECM remodelling (19–21). ECM turnover in the conventional outflow pathway is regulated by a family of zinc-dependent endopeptidases, the matrix metalloproteinases (MMPs). These secreted proteases are responsible for the degradation of ECM proteins and cell proliferation, and are thus key components in ECM remodelling and outflow tissue homeostasis (22). MMPs are secreted as inactive protein precursors and are activated when cleaved by extracellular proteinases and other MMPs (23). Levels of MMPs, along with TIMPs (Tissue Inhibitors of Metalloproteinases), have been shown to differ in glaucomatous AH and TM tissue as compared to those from normotensive individuals (24,25). Imbalance in MMP/TIMP ratios, and reduced MMP enzymatic activity, has been correlated with the accumulation of ECM materials in the TM that ultimately leads to an increase in outflow resistance (26,27). Therefore, reduction in ECM turnover within the TM and JCT region as a result of an imbalanced latent-to-activated MMP ratio can be a contributing factor to increased outflow resistance, as observed in glaucoma. It is therefore evident that increasing ECM turnover in outflow tissues may have therapeutic significance by reducing outflow resistance. Here, we set out to develop a gene-based therapy for the delivery of MMP targeting the conventional outflow tissues, with the primary aim of reducing both outflow resistance and IOP. Introduction of MMPs into the anterior chamber of the eye has previously been shown to increase outflow facility in organ-perfused cultures, indicating their therapeutic potential (28–31). Of the many classes of MMPs, MMP-3 (stromelysin-1) presents itself as an attractive candidate for targeting the ECM of outflow tissues. MMP-3 possesses a vast proteolytic target profile including type IV collagen, fibronectin, laminin, elastin, and proteoglycans, all of which are present in the meshwork and JCT regions of the outflow tissues, making this MMP of particular interest (32–36). In addition, MMP-3 can also activate other MMPs, including MMP-1 and MMP-9 (23,37–39), further assisting in the remodelling of ECM components (40–42).

Efficient gene delivery into the anterior segment of the eye is feasible through the use of adenoviral and adeno-associated viral (AAV) vectors. In particular, self-complementary AAV vectors have been shown to have such capability (43–46). Owing to the fact that MMP-3 is a secretory enzyme synthesised in the endoplasmic reticulum, transduction of tissues of the anterior segment with AAV expressing MMP-3 will result in the secretion of the protein into the AH. This will subsequently enable MMP-3 to be delivered into outflow tissues via conventional aqueous flow, potentially facilitating targeted degradation of ECM components and thus increasing aqueous outflow. In this regard, we observed highly efficient transduction of corneal endothelial cells following a single intracameral inoculation of AAV-2/9 expressing MMP-3, and both levels and activity of MMP-3 were significantly elevated in mouse AH following such inoculation. Importantly, AAV-mediated expression of MMP-3 in corneal endothelium, either from a CMV-, or doxycycline-inducible promoter, resulted in a marked increase in outflow facility and reduction in IOP. These observations correlated with structural alterations in the ECM of the outflow tissues, suggesting a mechanism of action for MMP-3 in modulating outflow resistance.

Results

Effects of glaucomatous aqueous humour on SC endothelial and TM cell monolayers

We treated cultured human SCEC monolayers with human glaucomatous (POAG) or control (cataract) AH for 24 h, and quantified levels of total secreted and activated MMP-3 in culture media. This was achieved by performing an ELISA and FRET assay, to monitor the degree of cleavage of an MMP-3 specific substrate, on cell media 24 h post-treatment. We did not observe a significant increase in the level of total (latent and active forms) secreted MMP-3 in culture media following treatment with POAG aqueous, with an increase of 0.15 [−0.35, 0.66] ng/ml (mean [95% confidence interval (CI)]) ($P = 0.45$, $n = 3$, Fig. 1A) over controls. However, activity assays indicated that the MMP-3 secreted in response to POAG aqueous had less enzymatic activity than that of cataract control AH, with an average change of −0.15 [−0.28, −0.02] mU/ml ($P = 0.024$, $n = 9$ cataract, $n = 7$ POAG, Fig. 1B). These observations corroborate results obtained involving other members of the MMP family in POAG aqueous (24) in that the amount of secreted MMP may remain relatively unchanged but its proteolytic activity is reduced.

Effects of glaucomatous AH on the permeability of SCEC and human TM (HTM) monolayers were determined by trans-endothelial electrical resistance (TEER) and FITC-dextran flux assays. Treatment of cultured SCEC monolayers with POAG AH resulted in increased TEER by an average of 102% after 24-h treatment compared to control AH (−7%), displaying an average absolute increase of 19.82 [15.82, 23.81] $\Omega.cm^2$ ($P < 0.0001$, $n = 6$ cataract, $n = 12$ POAG, Fig. 1C). Similarly, HTM responded with an increase of 9.79 [5.55, 14.05] $\Omega.cm^2$ in response to glaucomatous AH, ($P = 0.0002$, $n = 8$, Fig. 1D). Glaucomatous AH also reduced paracellular flux, as measured by permeability co-efficient (P_{app}), to dextran of 70 kDa as compared to cataract controls, with a mean difference of 0.14 [0.05, 0.22] cm/s $\times 10^{-8}$ ($P = 0.009$, $n = 3$ cataract, $n = 3$ POAG, Fig. 1E). A reduction in HTM permeability was also observed with a mean difference of 0.17 [0.09, 0.23] cm/s $\times 10^{-9}$ ($P = 0.005$, $n = 8$ cataract, $n = 7$ POAG, Fig. 1F).

Treatment of outflow cell monolayers with recombinant human MMP-3 increases permeability with concomitant reductions in TEER

In contrast to the negative effects of glaucomatous AH on SCEC and HTM permeability and resistance, we observed that treatment of cultured monolayers with 10 ng/ml of active recombinant human MMP-3 reduced TEER values on average by 5.62 [2.92, 8.32] $\Omega.cm^2$ greater than inactivated MMP-3 controls over the course of 24 h for SCEC ($P < 0.0001$, $n = 8$, Fig. 2A) and by 4.29 [0.11, 8.48] $\Omega.cm^2$ for HTM ($P = 0.0137$, $n = 8$, Fig. 2B) respectively. Permeability assays complemented these data as increases in paracellular flux of 70 kDa FITC-dextran by 0.14 [0.12, 0.18] cm/s $\times 10^{-9}$ ($P < 0.0001$, $n = 8$, Fig. 2C) were observed in SCEC, and 0.04 [0.01, 0.06] cm/s $\times 10^{-9}$ ($P < 0.01$, $n = 8$, Fig. 2D) in HTM monolayers when comparing treatments of MMP-3 to its inactivated counterpart control: TIMP-1 incubated with MMP-3. To rule out cytotoxicity as a reason for the observed changes in paracellular permeability, a cell viability assay was undertaken. Based on data shown in Figure 2E, for concentrations below 36 ng/ml MMP-3, the average SCEC cell viability for $n = 3$ will exceed 85%. Greater tolerability was observed in HTM cases, retaining an average viability of at least 85% for MMP-3 concentrations up to 151 ng/ml ($n = 3$, Fig. 2F).

Treatment of SCEC and HTM monolayers with active recombinant human MMP-3 induces remodelling and degradation of ECM components

In order to attribute increases in permeability to the ECM remodelling effects associated with MMP-3, SCEC and HTM monolayers were both treated as above with 10 mg/ml MMP-3 for 24 h. Following treatment, we observed changes in the staining pattern and intensity of a number of ECM proteins by immunocytochemistry. Specific collagen IV staining was localised to perinuclear areas and cytoplasm in both SCEC and HTM cells (Fig. 3A and B). In particular, we observed a decrease in the staining intensity around perinuclear areas in treated cells as compared to controls. A-SMA fibres facilitating cell-cell contacts in SCEC localised specifically to the cytoplasm and cytoskeleton, and MMP-3 treatment led to an attenuation of fibre bundles with thinning of intercellular connections (Fig. 3C). Fluorescent images of F-actin in HTM monolayers also revealed constricted actin bundles and a reduced tendency for bundle crossovers (Fig. 3D). Immunofluorescence staining of laminin in SCEC and HTM cells showed diminished cytoplasmic localisation and reduced network complexity and multiplicity in MMP-3 treated cells as compared to control staining intensity of laminin (Fig. 3E and F). To visualise fibronectin clearly without cellular interference, decellularisation was performed after MMP-3 treatment to isolate the ECM scaffold from the cell monolayer. Fluorescent images show significant perturbation of fibronectin network in treated cells as opposed to the linear cellular organisation observed in control cells (asterisk, Fig. 3G and H). To quantitatively demonstrate remodelling of these proteins, western blot analysis was performed on both cell lysate and media fractions of SC and HTM cell monolayers (Supplementary Material, Fig. S1). Specific bands were observed at 300 kDa for collagen IV, 42 kDa for α-SMA, 220 kDa for laminin and 290 kDa for fibronectin. A significant reduction of collagen IV ($P = 0.01$, $P = 0.01$) α-SMA ($P = 0.04$, $P = 0.04$) and laminin ($P = 0.04$, $P = 0.03$) were observed in SC and HTM whole cell lysate samples respectively ($n = 4$ for all cases). Collectively, these data clearly illustrate that MMP-3 mediates remodelling of ECM components in both SCEC and HTM cell monolayers.

Intracameral inoculation of AAV-2/9 expressing a CMV-driven MMP-3 gene efficiently transduces corneal endothelium and results in elevated levels of MMP-3 in aqueous humour

AAV-mediated transduction of corneal endothelium could, in principle, serve as an efficient means of expressing and secreting MMP-3 into AH. The advantage of such an approach is that the natural flow dynamics of AH will allow transportation of secreted MMP-3 towards the outflow tissues (Fig. 4A). We evaluated the efficiency of a number of AAV serotypes with either single stranded or self-complementary genomes to deliver MMP-3 to the outflow tissues. 2μl of viral particles (2×10^{12} vector genomes/ml) of each serotype, expressing a CMV-driven eGFP reporter gene (Fig. 4B) were intracamerally inoculated into wild type C57BL/6 mice and eyes examined via fluorescent microscopy at 3 weeks post-inoculation. Extensive expression of the reporter gene was observed in the corneal endothelium of eyes injected with non-self-complementary AAV-2/9 (Fig. 4C top), with no fluorescence being detectable in the outflow tissues themselves using this construct. Hence, the eGFP cDNA from AAV-2/9 was exchanged with murine MMP-3 cDNA to generate AAV-MMP-3, and similar inoculation resulted in MMP-3 expression that was prominently detected in the corneal

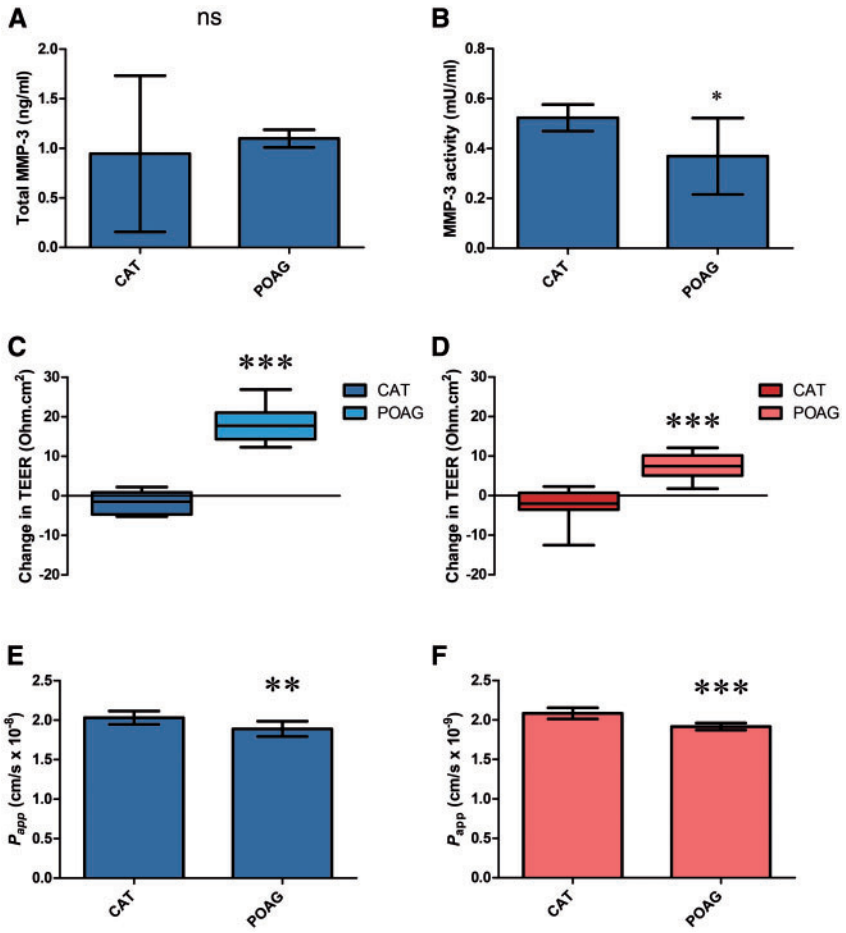

Figure 1. MMP-3 concentration in glaucomatous AH and the resulting effect on SCEC and HTM monolayers. (**A**) MMP-3 concentrations in the media of SCEC monolayers treated with either cataract (control) or POAG human AH showed no significant difference after 24 h. (**B**) POAG aqueous-treated SC media samples from (A) were found to have an average change in MMP-3 proteolytic activity of -0.15 [−0.28, −0.02] mU/ml compared to control media. (**C**) Addition of POAG aqueous humour onto SC monolayers resulted in an average increase in TEER of 102% compared to controls. (**D**) Treatment of HTM cells with human aqueous also increased TEER value. (**E,F**) SCEC and HTM subjected to AH were tested for cellular permeability using a FITC-Dextran flux assay respectively. Decreased permeability to a 70 kDa dextran was observed in response to POAG rather than cataract AH. Graphs show mean with 95% CI error bars. CAT = cataract, POAG = primary open-angle glaucoma. Figures A-F were analysed with a Student's *t*-test. NS = non-significant. Symbols *, ** and *** denote *P* values of < 0.05, < 0.01 and < 0.001, respectively.

endothelium and not in null controls (Fig. 4C, bottom). No significant difference in central corneal thickness was detected following AAV inoculation between treated (116.7 [112.5, 120.9] μm) and control eyes (116.4 [113.6, 119.1] μm) ($n = 4$, Supplementary Material, Fig. S2). Corneas also appeared clear with no signs of cataracts upon visual inspection.

The level of total MMP-3 in the AH of twelve inoculated animals was quantified using enzyme-linked immunosorbent assay (ELISA), and we observed a significant average increase in total MMP-3 protein of 56%, 1.37 [0.89, 1.84] ng/ml as compared to 0.87 [0.59, 1.12] ng/ml for control AAV ($P = 0.016$, $n = 12$, Fig. 4D). The activity of AAV-mediated production of MMP-3 was also assessed using FRET, and a significant increase in activity of 34 [6.86, 61.14] % was observed, on average, in AAV-MMP-3 treated eyes compared to contralateral controls ($P = 0.0164$, $n = 17$, Fig. 4E).

Intracameral inoculation of AAV-2/9 expressing an MMP-3 gene increases outflow facility and reduces IOP in murine eyes

In order to determine the effect of AAV-mediated expression of MMP-3 from the corneal endothelium on aqueous outflow, the conventional outflow facility was measured using the recently developed *iPerfusion* system designed specifically to measure conventional outflow facility in mice (47). Wild type mice were intracamerally injected with $1x10^{11}$ vector genomes of AAV-MMP-3, and contralateral eyes received the same quantity of AAV-Null. Four weeks post-inoculation, eyes were enucleated and perfused in pairs over incrementing steps in applied pressure. A representative flow-pressure plot provided in Supplementary Material, Figure S3A describes the relationship between flow rate (Q) at each pressure (P) step in both AAV-MMP-3 (red) and AAV-Null (blue) eyes. Furthermore, the relative percentage difference in facility within each data pair is depicted in Supplementary Material, Figure S3B (left). The resulting facility data presented in Figure 5A and B clearly illustrate that control eyes have an average facility of 8.44 [6.14, 11.60] nl/min/mmHg with treated eyes having an average facility of 11.73 [8.05, 17.08] nl/min/mmHg. There is, therefore, an average increase in outflow facility of 39 [19, 63] % in pairs, between treated eyes and their contralateral controls ($P = 0.002$, $n = 8$ pairs).

As the major pathology in POAG is IOP elevation, and an increased outflow facility was observed, tonometric IOP

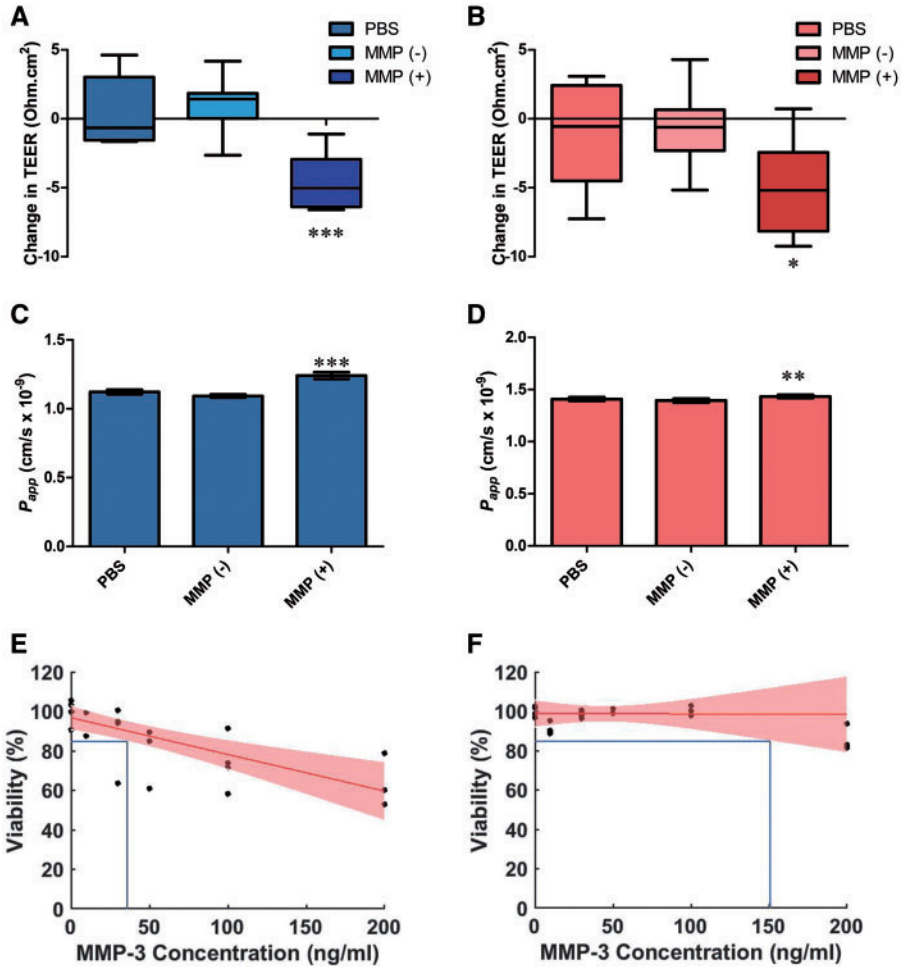

Figure 2. Effect of recombinant human MMP-3 on paracellular permeability in HTM and SCEC cell monolayers. SCEC and HTM cells were treated with 10 ng/ml recombinant MMP-3 for 24 h, using PBS and inactivated MMP-3 (incubation with TIMP-1, MMP(−)) as vehicle and negative controls respectively. (**A**) SCEC and (**B**) HTM both show reductions in TEER values after treatment of 4.6 [2.9, 6.2] and 5 [2.2, 7.8] Ohms.cm^2 respectively. Permeability to a 70 kDa dextran was increased in treated cells (MMP (+)) in both (**C**) SCEC and (**D**) HTM. (**E**) An average viability of 85% was expected for SCEC with MMP-3 concentrations up to 36 ng/ml. (**F**) 85% viability is retained on average in HTM cells at concentrations up to 151 ng/ml MMP-3. A, C and E in blue represent SCEC data, whereas B, D and F in red represent HTM data.

measurements were taken both immediately before (pre), and four weeks after (post) intracameral injection of AAV-2/9 expressing MMP-3 or a null vector in the case of the control. Differences between pre- and post-injection IOP were calculated using the non-parametric Wilcoxon matched-pairs signed rank test. Eyes treated with AAV-Null had no significant change in IOP -0.5 ± 2.9 mmHg (median ± median absolute deviation (MAD), $P = 0.61$, $n = 7$, Wilcoxon signed-rank test with a theoretical median IOP change of 0) after treatment. In comparison, when treated with AAV-MMP-3, median IOP significantly decreased by 3.0 ± 2.9 mmHg ($P = 0.022$, $n = 7$, Fig. 5C). The IOP difference in AAV-MMP-3 treated eyes was significantly greater than the IOP difference in the contralateral AAV-Null treated eyes by 2.5 ± 0.7 mmHg ($P = 0.034$, $n = 7$, Fig. 5C).

Controlled periodic activation of MMP-3

To incorporate a control mechanism for the secretion of MMP-3 from corneal endothelium, we first introduced AAV-2/9 expressing eGFP under the control of a tetracycline-inducible promoter into the anterior chambers of both eyes of wild type mice. After 3 weeks, mice were treated with a regime of one drop of 0.2% doxycycline (a tetracycline derivative) two times per day (approx. 8 h between each application) for 10–16 days in one eye only. PBS was administered onto the contralateral eye as a control. As illustrated in Supplementary Material, Figure S4, extensive expression of the reporter gene was observed only in the corneal endothelium, and no expression was observed in the contralateral control. Following this, we replaced the reporter cDNA with murine MMP-3 cDNA and the resulting AAV (Induc. AAV-MMP-3) was injected into the anterior chambers of animals at 1x10^{11} viral genomes per eye. Using the inducible eGFP virus (Induc. AAV-eGFP) as a contralateral control, expression was induced by administering doxycycline (as above) to both eyes. Contralateral eyes were perfused as above, the control group exhibiting an average facility of 8.30 [5.75, 11.26] nl/min/mmHg and the MMP-3 treatment group resulting in a facility of 14.01 [11.09, 17.72] nl/min/mmHg. Paired, these eyes exhibit an average increase in outflow facility of 68 [24, 128] % ($P = 0.004$, $n = 11$, Fig. 5D and E). The relative difference in facility within individual pairs is presented in Supplementary Material, Figure S3B (right). This observation strongly supports the concept that MMP-3 expression could be induced in a controlled and reversible manner, with periodic IOP measurements utilised to guide the induction of expression.

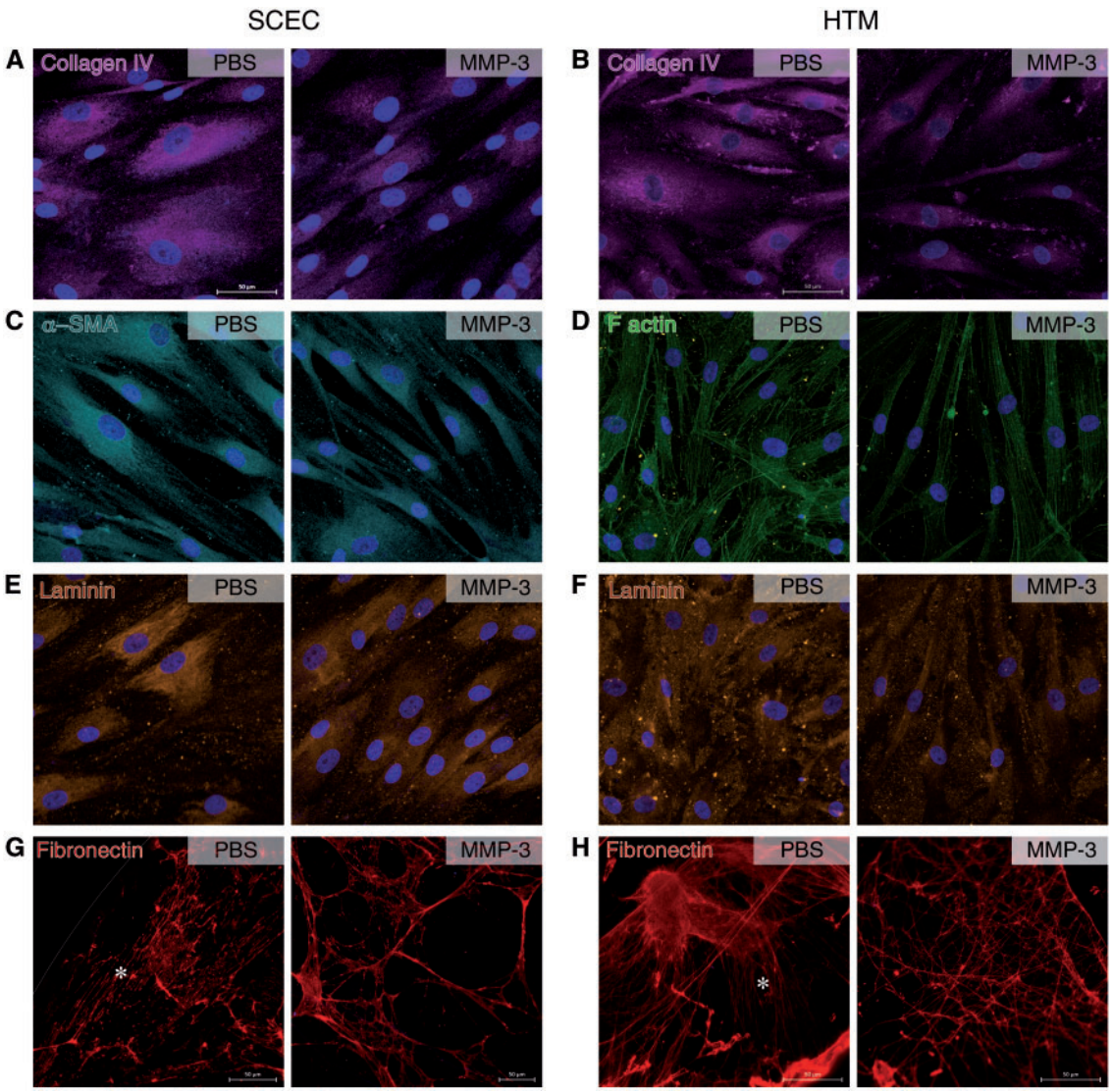

Figure 3. Remodelling of ECM components in SCEC and HTM cell monolayers. Immunocytochemistry shows various remodelling artefacts on core ECM components in SCEC and HTM cells in response to MMP-3 treatment. (**A,B**) Collagen IV appears to have reduced intensity in both cell types after treatment. Collagen IV is concentrated around cells in controls but shows reduced spread after treatment, fibrils barely protruding past the cell nuclei. (**C**) Alpha smooth muscle fibres extend the width of the cell towards a neighbouring cell. Treated samples show that these fibre bundles have constricted, leading to multiple thin connections between cells. (**D**) HTM F-actin staining depicts a slight thinning of filament bundles and a reduction of filament branching post MMP-3 treatment. (**E,F**) Laminin expression exhibits a modest reduction in staining intensity in both cell types, and a reduction in network complexity in TM cells. (**G,H**) Fibronectin was visualised after decellularisation, depicting linear and organised strands in PBS controls, as denoted by an asterisk. Treatment groups lacked a linear network, and instead showed a disjointed, porous network. Scale bars represent 50 μm. Left column pairs = SCEC, right column pairs = HTM.

Ultrastructural analysis of AAV-MMP-3 treated eyes

In order to evaluate whether the AAV-MMP-3 treatment affects the morphology of the eye and the TM including the inner wall of SC, ultrastructural investigation was performed in four pairs of mouse eyes. Corneas appeared translucent and healthy on visual inspection during enucleation. Semi-thin sections clearly demonstrated that there were no signs of an inflammatory reaction, either in the TM or in the cornea, uvea or retina (Fig. 6A and B). Ultrastructural analysis of control eyes revealed normal outflow structural morphology, cell-matrix attachments and cell-cell connections between the SC and TM. The inner wall endothelial cells formed foot-like connections with subendothelial TM cells, as well as connections to underlying elastic fibres and discontinuous basement membrane (Fig. 6C). However, in some regions of treated eyes, especially those with a prominent SC lumen and scleral spur-like structure typical of the nasal quadrant (48), there appeared to be more optically empty space directly underlying the inner wall endothelium of SC, compared to AAV-Null controls (Fig. 6D). In these optically empty spaces, foot-like extensions of the inner wall to the sub-endothelial layer were absent or disconnected from the subendothelial cells or elastic fibres (Fig. 6D and E). Occasionally, we observed an accumulation of ECM clumps beneath the inner wall that were not observed within the controls (Fig. 6F) and may represent remnants of digested material.

We quantified the optically empty length directly underlying the inner wall of SC. In control eyes, the percent optically empty length in any one region ranged from 19 to 49% with an average of 37%. In the treated eyes, the equivalent range was

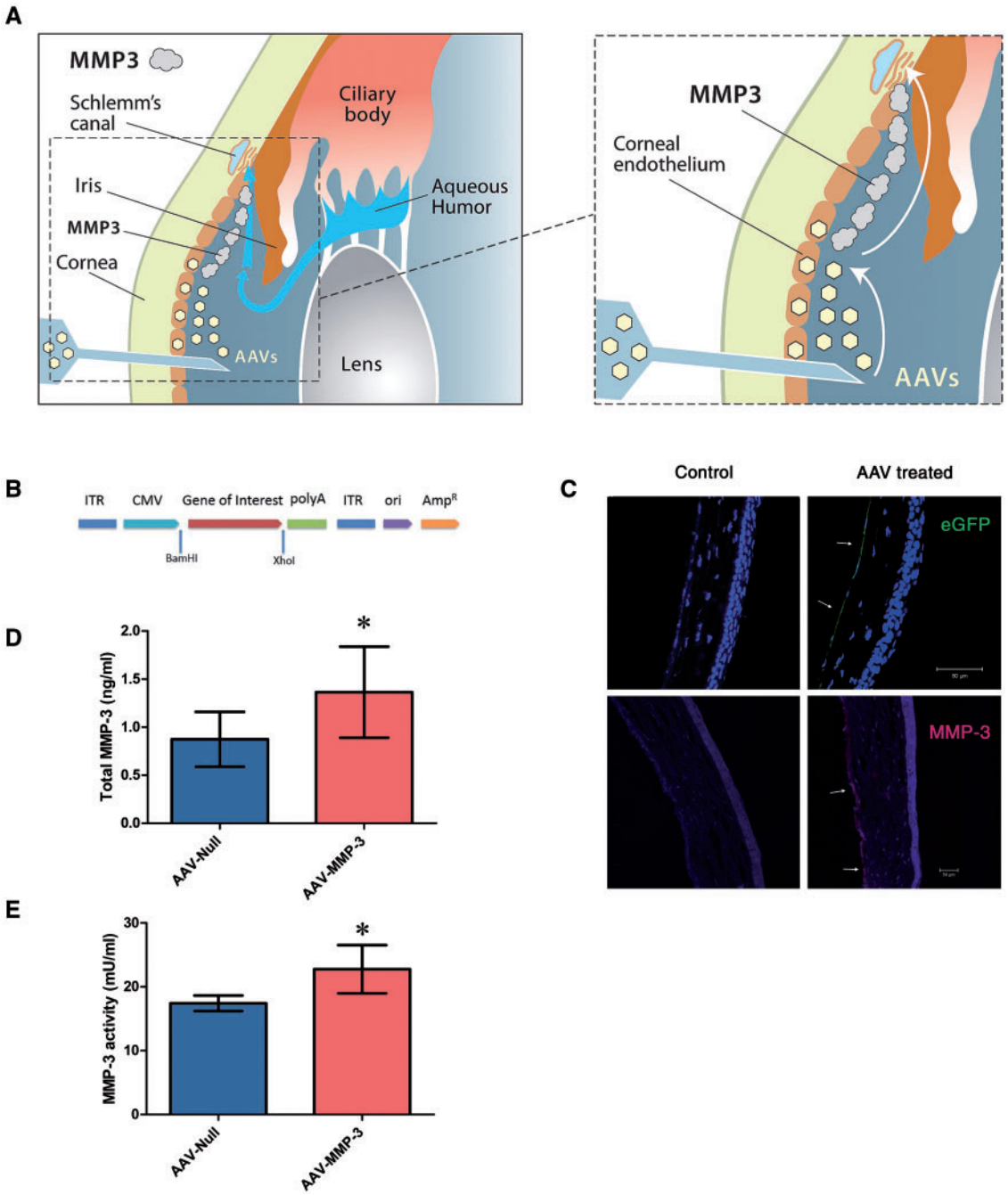

Figure 4. AAV-2/9 mediated MMP-3 expression in the corneal endothelium. (**A**) Diagrams illustrating the therapeutic concept addressed in this study. AAV-2/9 transduces the corneal endothelium upon intracameral inoculation (left). MMP-3 molecules are secreted into the AH from this location and are transported toward the outflow tissue by the natural flow of the aqueous (right). (**B**) A schematic diagram of the AAV-2/9 vector used for the expression of either eGFP or MMP-3. Murine MMP-3 cDNA was sub-cloned into the pAAV-MCS plasmid and constitutively driven by a CMV promoter (AAV-MMP-3). (**C**) Immunohistochemistry images of corneas from WT murine eyes intracamerally inoculated with AAV-2/9 expressing eGFP. AAV virus containing a CMV promoter demonstrates transduction and expression at the corneal endothelium (marked with arrows). Using the AAV-MMP-3 virus, MMP-3 was detected at the corneal endothelium in treated eyes only, denoted by arrows. (**D**) ELISA was performed on murine AH 4 weeks post-injection of virus. MMP-3 concentrations had increased by an average of 0.49 [0.11, 0.87] ng/ml in AAV-MMP-3 treated eyes (paired Student's *t*-test). (**E**) Aqueous MMP-3 activity was significantly increased by an average of 5.34 [1.12, 9.57] mU in AAV-MMP-3 treated eyes. Scale bars represent 50 μm. Asterisk symbol denotes a *P* value of < 0.05.

39–76% with an average of 59% (Fig. 6G). The differences between control and experimental eyes for each pair ranged from 16 to 26%, which corresponded to a statistically significant increase in the proportion of open space underlying the inner wall with AAV-MMP-3 relative to AAV-Null ($P = 0.002$, $n = 4$; paired Student's *t*-test). These data indicate that reduced ECM material in the TM and along the inner wall of SC is associated with AAV-MMP-3 treatment and may explain the enhanced outflow facility and IOP reduction. Furthermore, these morphological changes, because they were absent from controls, could not be attributed to an inflammatory or lytic response to AAV alone.

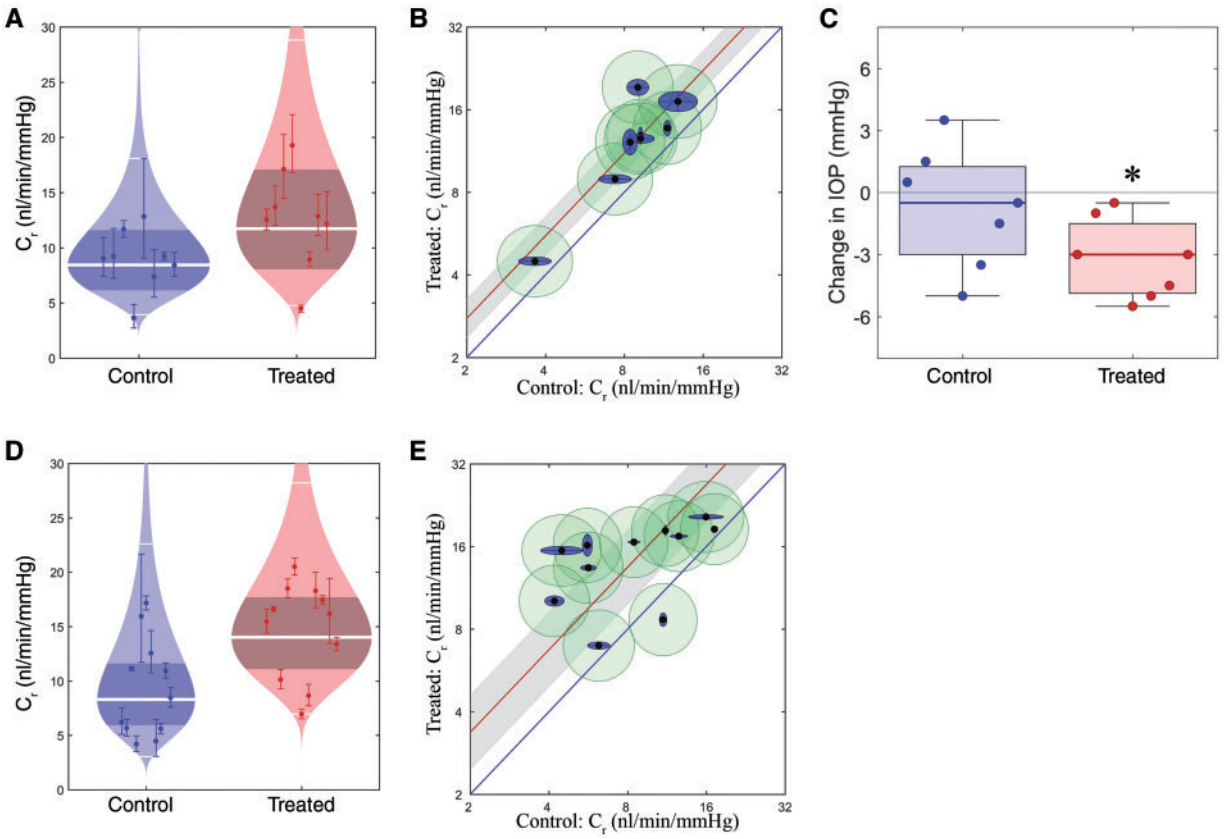

Figure 5. Effect of ECM remodelling on outflow facility and IOP. (**A**) 'Cello' plot depicting individual outflow facility values for eyes at 8 mmHg (Cr) and statistical distribution of both control (AAV-Null) and experimental (AAV-MMP-3) groups. Each point represents a single eye with 95% CI on C_r. Log normal distribution is shown, with the central white band showing the geometric mean and the thinner white bands showing two geometric standard deviations from the mean. The shaded region represents the 95% CI on the mean. (**B**) Paired outflow facility plot. Each inner point represents an eye pair, with log-transformed facilities of the control eye plotted on the x axis, and treated eye on the y axis. Outer blue and green ellipses show uncertainties generated from fitting the data to a model, intra-individual and cannulation variability respectively. Average increase is denoted by the red line, enclosed by a grey 95% CI, indicating significantly increased facility (does not overlap the blue unity line). (**C**) Box plots showing the change in IOP in treated and control eyes. Boxes show interquartile range and error bars represent the 5th and 95th percentiles. A significant reduction in IOP is observed in AAV-MMP-3 treated eyes (Wilcoxon signed-rank test). (**D-E**) Cello and paired facility plots for inducible AAV data sets.

Discussion

Matrix metalloproteinases are key regulators in the remodelling of extracellular matrices in the JCT region of the TM. Dysregulation of MMP expression and loss of MMP/TIMP homeostasis in glaucomatous AH have been associated with abnormal fibrillary ECM accumulation in the JCT region of POAG eyes (49–53). Furthermore, perfusion of anterior segments with purified MMPs increased outflow facility, while the use of metalloproteinase inhibitors (TIMP, minocycline) reduced outflow rates (30). Consistent with these findings, upregulation of MMPs following clinical laser treatment has been associated with the ocular hypotensive effect of trabeculoplasty (54,55). It is therefore apparent that the reduction in ECM turnover within the outflow tissues contributes to increased outflow resistance, and strategies specifically targeting outflow ECM may be effective in reducing outflow resistance. In this study, we focused on the development of a gene-based therapy for the delivery of MMP-3 into outflow tissues to facilitate aqueous outflow and reduce IOP.

It has been reported that the activity of a range of regulatory cytokines and growth factors found in AH directly impacts permeability in the outflow tissue, and many of these are known to be dysregulated in POAG AH (56,57). In particular, cytokines such as IL-1, TGF and TNF are known to influence the expression and secretion of ECM modulators, including MMPs in outflow tissues (58–60). It was therefore of interest to assess how POAG AH may affect the MMP-3 secretion and their relative activity in outflow cell culture systems.

We performed permeability assays with AH-treated SCEC and HTM monolayers to demonstrate that dysregulated MMP's in POAG AH influence monolayer permeability via modified ECM remodelling. (12,61). SCEC monolayers showed decreased permeability *in vitro* in response to glaucomatous AH, and this decrease was associated with a reduction in extracellular MMP-3 activity. HTM cells exhibited similar reductions in permeability. In contrast, treatment of cell monolayers exclusively with recombinant MMP-3 elevated monolayer permeability in comparison to controls, suggesting that MMP-3 could correct the permeability lowering effects of POAG aqueous. Because MMP-3 has previously been associated with apoptotic behaviour in Chinese hamster ovary cells and osteoclasts (62,63), we evaluated the effect of a wide concentration range of MMP-3 on SCEC and HTM viability. This way, we confirm that increases in paracellular permeability were not related to an MMP-3 cytotoxic effect, but rather its proteolytic activities, which these data support. More importantly, even lower concentrations of MMP-3 were detected *in vivo* in murine AH after AAV-mediated MMP-3 secretion (1.37 [0.89, 1.84] ng/ml, Fig. 4D) than those used in *in vitro* experiments. Collectively, these results indicate that a

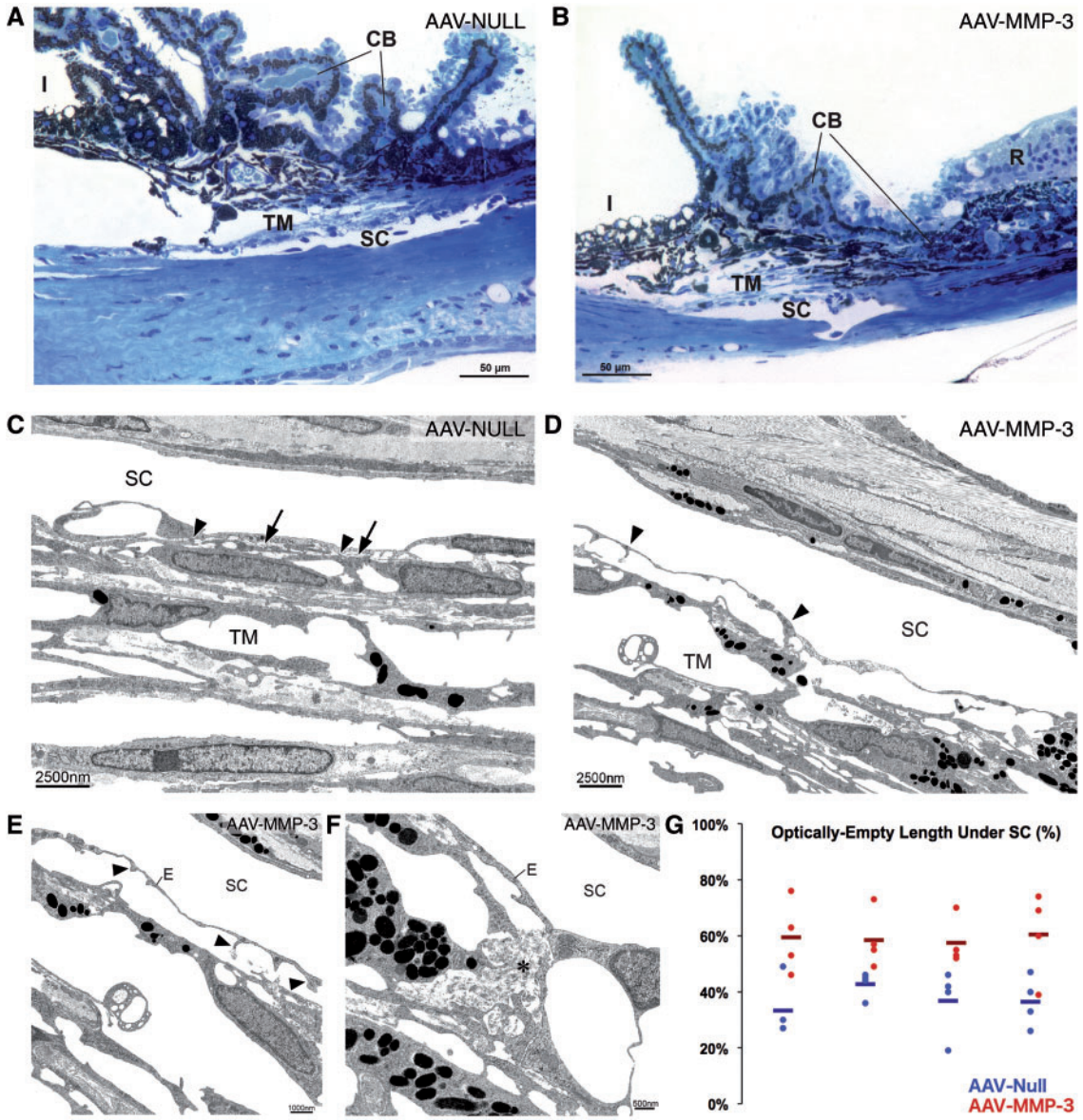

Figure 6. Transmission electron microscopy (TEM) analysis of ECM remodelling in outflow tissues. Semi-thin sections of the iridocorneal angle in mouse eyes treated with either (**A**) AAV-Null or (**B**) AAV-MMP-3. AAV-MMP-3 treated eyes show greater inter-trabecular spaces in outer trabecular meshwork (TM) than controls. Scale bar denotes 50 μm. (**C,D**) Transmission electron micrograph of the inner wall of Schlemm's Canal (SC) and the outer TM. (C) Control eye illustrating normal attachment between foot-like extensions of the inner wall endothelium and subendothelial cells (arrowheads), as well as with the discontinuous basement-membrane material underlying the inner wall endothelium (arrows). (D) Representative TEM image of an MMP-3 treated eye showing a disconnection of the inner wall endothelium from the subendothelial cells and the ECM (arrowheads). The widened subendothelial region lacks basement-membrane material and other ECM components. (**E,F**) Higher magnification of the inner wall of a treated eye. (E) Foot-like extensions of the inner wall endothelium (E) have disconnected from the subendothelial cells and the ECM (arrowheads), and the lack of ECM in this region is shown. (F) In other regions of treated eyes, clumps of presumably degraded ECM-material are localised underneath the inner wall of SC (asterisk). Such clumps of ECM are not present in controls. Scale bars are denoted on each image. CB = ciliary body, I = iris, R = retina. (**G**). Morphometric measurements of the optically empty space immediately underlying SC from four regions of contralateral eyes treated with AAV-MMP-3 (red data points) or AAV-Null (blue data points). Bars indicate average values for each eye. Contralateral eyes are presented immediately next to one another.

plausible target for MMP-3 activity is likely to be the ECM of TM and the inner wall endothelium of SC. This further contributes to the body of evidence demonstrating that the molecular pathological effects of glaucomatous AH are due, in part, to dysregulations of MMP-mediated remodelling and that induced elevations in MMP-3 expression in outflow tissues will have an enhancing effect on increasing aqueous outflow.

Previously, perfusion of explants of human anterior segments with a mixture of MMP-3, -2, -9 has been shown to result in an increase in outflow facility to 160% of baseline level (30). It has also been demonstrated that increases in IOP lead to an up-regulation of MMP-2, -3 and -14 through mechanical stretching of the TM and a reduction in TIMP2 (31,64–68). Such observations support the concept that controlled expression of MMPs within the anterior chamber holds therapeutic potential in regard to facilitating aqueous outflow. The inner wall endothelium of SC along with its basement membrane and JCT modulate the resistance to outflow. The interconnections between all components responsible for the outflow resistance generation is essential to maintain the homeostasis of outflow

drainage (11). Thus, targeting the ECM for remodelling in the JCT region using MMPs may effectively increase permeability of surrounding cells, thus increasing AH outflow rate and lowering IOP.

Owing to the fact that MMP-3 is a secretory enzyme, transduction of the corneal endothelium with AAV-MMP-3 will result in the secretion and delivery of the protein to the outflow tissues by following the natural flow of AH in the anterior chamber. *Ex vivo* studies in human corneas or corneal fibroblasts have demonstrated the potential and efficiency of delivering AAV to this tissue type (69,70). Successful transfection of different layers in the rabbit cornea by recombinant AAV further supports the potential of recombinant/exogenous protein delivery from corneal cells (71). Thus, it is likely that secreted MMP-3, expressed by corneal endothelia, will be directed toward the outflow tissue and activated with the aid of existing endogenous MMP-3 after which it will then be available for remodelling a range of ECM components. Attaining exclusive AAV expression in the cornea was obtained by using a single stranded AAV-2/9, as although single stranded AAV may enter other cells such as the TM, self-complementary viruses are required for sufficient DNA replication, and hence transduction of these cells (72).

The current data provide a direct proof of concept that AAV-mediated expression of MMP-3 from corneal endothelium decreases IOP with a concomitant increase in the rate of AH outflow through the drainage channels *ex vivo*. A number of parameters will require further refinement in order to address the translational feasibility of this approach. Although significant elevations in transient MMP-3 were found in murine AH post-treatment with AAV-MMP-3, these were well within tolerable limits as defined by our *in vitro* experiments (Fig. 2E and F). These MMP-3 elevations in AH (Fig. 4D), along with visually translucent corneas of normal thickness (Supplementary Material, Fig. S2), suggests that MMP-3 is preferentially secreted apically into the AH. MMP-3 expressed in the corneal endothelial cell layer is in the inactive form, which requires secretion for cleavage-induced activation, and is therefore unlikely to induce remodelling or damage to the endothelium itself. Activation is likely to occur in the AH after secretion, or extracellularly within the outflow tissues in the presence of other proteases. The observed elevation in aqueous MMP-3 activity indicates that activation at least begins in the AH (Fig. 4E). However, sustained expression of MMP-3, as would occur following permanent transfection of cells of the anterior chamber, could result in off-target proteolysis over time. A potentially more effective approach will be to employ an inducible promoter to drive MMP-3 expression on a periodic basis once the virus has been introduced into the anterior segment tissues of the eye. It is of note that the use of glucocorticoid-inducible promoters has been explored in this regard in adenoviral and AAV delivery systems to express MMP-1 in tissues of the TM (46). However, the use of a steroid response promoter may not be ideally suited from a therapeutic standpoint in humans, as activation of the promoter would require continuous exposure to steroid components, which can lead to abnormal IOP elevation (73–75). Glucocorticoids have also been shown to influence gene expression, which may play a pathogenic role in developing hypertension (76). Hence, we explored the effectiveness of a tetracycline-inducible system to express MMP-3 from the corneal endothelia, which allows for controllable and reversible activation by topically applied eye drops. We noted that activation of AAV for over 10 days was sufficient to significantly increase outflow facility *ex vivo* in mice and suggest that incorporation of other tetracycline derivatives may further enhance the effectiveness of the promoter and hence MMP-3 production. Our observed increase in facility of 68 [24, 128] % rivals that of conventional prostaglandin analogues which are in current use to treat glaucoma, noted to have an increase of 56 [−4, 154] % in the case of PDA205, also using the iPerfusion system (47).

To date, in studies utilising MMPs for increasing outflow or reducing IOP little emphasis has been given to the mechanism of action. Here, we show that MMP-3-mediated remodelling of specific ECM components is likely responsible for increased outflow, and hence, decreased IOP. Reductions in intensity and distribution of core ECM materials including collagen IV and laminin were observed *in vitro*, along with the disorganisation of the fibronectin meshwork and constrictions in the actin skeleton. These modifications suggest the development of a porous nature within the ECM of these monolayers. Semi-quantitation via western blot analysis coincides with these results, showing significant reductions in collagen IV, α-SMA and laminin proteins in the cell lysate fraction, where ECM proteins are likely to reside as no significant changes were displayed in media samples. It is reasonable to assume that these extracellular changes contribute to the observed alterations in electrical resistance and paracellular flux. Ultrastructural analysis of AAV-MMP-3 treated mouse eyes also showed reductions in ECM material at the sub-endothelial/JCT region, including areas of degraded ECM and widened inter-trabecular spaces. Upon quantification, these areas optically lacking ECM material were found to be consistently increased in response to MMP-3 both between regions of the anterior chamber and between treated eyes. Tight junctions remained intact after incubation with AAV-MMP-3 (Supplementary Material, Fig. S5), contrary to previous studies which have shown tight junction degradation by MMPs (77,78); validating that MMP-3 may primarily augment cell monolayer permeability via other mechanisms such as alteration of ECM components. These data indicate that a reduction in ECM material in the TM and inner wall of SC is responsible for the enhancement of outflow facility and consequently lowering of IOP in the treated eyes. The data also show that the reduction in ECM is not due to an inflammatory response that secondarily induces lytic enzymes in the treated eyes but most likely to the induction of MMP-3 through the treatment directly.

We show here for the first time that a topical eye drop regime can control the expression of a gene therapy vector utilised to reduce outflow resistance and IOP through ECM remodelling. The current approach may hold substantial potential as an effective human therapy should long-term safety and efficacy prove successful in non-human primates.

Materials and Methods

Cell culture

Human SCEC were isolated, cultured and fully characterised according to previous protocols (79–81). Briefly, cells were isolated from the SC lumen of human donor eyes using a cannulation technique. Isolated cells were tested for positive expression of VE-cadherin and fibulin-2, but absence of myocilin induction upon treatment with 100 nM dexamethasone for 5 days. Confluent cells displayed a characteristic linear fusiform morphology, were contact inhibited and generated a net transendothelial electrical resistance (TEER) greater than 10 $\Omega.cm^2$. TEER values were confirmed again prior to MMP-3 treatments. SCEC strains used were SC82 and SC83 between passages 2 and 7. Dulbecco's modified eagle medium (Gibco, Life Sciences) 1%

Pen/Strep/glutamine (Gibco, Life Sciences) and 10% foetal bovine serum (FBS) performance plus (Gibco, Life Sciences) was used as culture media in a 5% CO_2 incubator at 37 °C. Cells were passaged with trypsin-EDTA (Gibco-BRL) and seeded into 12 well or 24 well transwell plates (Costar, Corning). Human trabecular meshwork (HTM) cells were isolated and fully characterised according to the procedures described in (82–85). TM tissue is removed from human donor eyes using a blunt dissection technique, and TM cells are dissociated from the tissue using a collagenase digestion protocol as previously described (82). Isolated cells are characterised by their dramatic induction of myocilin protein following treatment with dexamethasone (100 nM) for 5 days as detailed before (79). HTM123 and HTM134 cells were cultured similar to SCEC's and matured for one week in 1% FBS media prior to treatment.

Human AH samples (detailed below) were added 1:10 to fresh media for cellular treatment for use with TEER and permeability assays as described below.

Recombinant human active MMP-3 (ab96555, Abcam) was added to cell media at a concentration of 10 ng/ml for TEER, permeability assays, western blotting and immunocytochemistry as described below. Inactivated MMP-3 controls were achieved by incubating active MMP-3 (10 ng/ml) with recombinant human active TIMP-1 (100 ng/ml, ab82104, Abcam) in cell media for 1 h prior to treatment.

Animals

Animals and procedures used in this study were carried out in accordance with regulations set out by The Health Products Regulatory Authority (HPRA), responsible for the correct implementation of EU directive 2010/63/EU. 8–11-week-old male and female C57BL/6 mice were used in all experimentation outlined in this study. Animals were bred and housed in specific-pathogen-free environments in the University of Dublin, Trinity College and all injections and IOP measurements complied with the HPRA project authorisation number AE19136/P017.

Patient aqueous humour samples

Human aqueous was obtained from the Mater Misericordiae Hospital, Dublin, Ireland. Upon informed consent, AH samples were collected from both POAG and control patients undergoing routine cataract surgery. The criteria for POAG was defined as the presence of glaucomatous optic disc cupping with associated visual field loss in an eye with a gonioscopically open anterior drainage channel, with an intraocular pressure $>$ 21 mmHg (86). The samples were taken immediately prior to corneal incision at the start of the procedure using a method described previously (87). Human AH collection conformed to the WMA Declaration of Helsinki and was approved by the Mater Misericordiae University Hospital Research Ethics Committee.

TEER measurement

Electrical resistance values were used as a representative of the integrity of the endothelial cell-cell junctions. Cells grown on Costar transwell-polyester membrane inserts with a pore size of 0.4 μm were treated with 10 ng/ml MMP-3 as described above. TEER readings were measured before and 24 h after treatment. An electrical probe (Millicell ERS-2 Voltohmmeter, Millipore) was placed into both the apical and basal chambers of the transwells and a current was passed through the monolayers, reported as a resistance in $\Omega.cm^2$. A correction was applied for the surface area of the membrane (0.33 cm^2) and for the electrical resistance of the membrane (blank transwell).

Permeability assessment by FITC-dextran flux

The extent of monolayer permeability was assessed by the basal to apical movement of a tracer molecule through the monolayer. Measures of permeability were taken 24h after treatment immediately after TEER values, keeping experimental set-up identical to that of TEER readings. The permeability protocol was repeated as described in (88). A 70 kDa fluorescein isothiocyanate (FITC)-conjugated dextran (Sigma) was added to the basal compartment of the transwell. Fresh medium was applied to the apical chamber and aliquots of 100 μl were taken every 15 min for a total of 120 min, replacing with fresh media. Sample aliquots were analysed for FITC fluorescence (FLUOstar OPTIMA, BMG Labtech) at an excitation wavelength of 492 nm and emission wavelength of 520 nm. Relative fluorescent units (RFU) were converted to their corresponding concentrations by interpolating from a known standard curve. Corrections were made for background fluorescence and the serial dilutions generated over the experiments time course. P_{app} values were calculated representing the apparent permeability coefficient for control (PBS) and treatment (10 ng/ml MMP-3). This was achieved via the following equation:

$$P_{app}(cm/s) = (dM/dT)/(A \times C_0),$$

Where dM/dT is the rate of appearance of FITC-dextran (FD) (μg/s) in the apical chamber from 0 to 120 min after the introduction of FD into the basal chamber. A is the effective surface area of the insert (cm^2) and C_0 is the initial concentration of FD in the basal chamber.

Cell viability

Cultured cells were treated with increasing concentrations of recombinant human MMP-3 (ab96555, Abcam) from 0 to 200 ng/ml. Cell viability was assessed 24 h post-treatment with MMP-3 using a CellTitre 96® AQueous One Solution Cell Proliferation Assay (Promega). Cell media was aspirated and a 1 in 6 dilution of the supplied reagent in media was added to the cell surface. Cells were incubated at 37 °C for 1 h and the media/reagent was transferred to a 96-well plate for reading by spectrophotometry (Multiskan FC, Thermo Scientific) at 450 nm. Standard *in vitro* viability calculations fail to consider sample size and the biological significance of the data. Hence, a modified approach was taken to determine at which concentration SCEC's show a reduced tolerability to MMP-3. This was defined at an average of 85% viability over three cell samples. This conservative value ensures that a cell population would remain viable and still be able to proliferate. Anything lower should be regarded as MMP-3 intolerability i.e. reduced cell proliferation or cell death. Control samples (0 ng/ml MMP-3) were normalised to 100% viability and a linear model fitted to the normalised data. The MMP-3 concentration at which cells had an average of 85% viability was interpolated from the lower 95% confidence bound from this linear model. This value represents the concentration of MMP-3 at which the average of three cell samples would have a 97.5% chance of retaining a greater to or equal than 85% viability.

Immunocytochemistry (cell monolayers)

Immunocytochemistry was performed to visualise changes in ECM composition in response to MMP-3. Human SCEC and HTM were grown on chamber slides (Lab-Tek II) and fixed in 4% paraformaldehyde (pH 7.4) for 20 min at room temperature and then washed with PBS for 15 min. Cell monolayers were blocked in PBS containing 5% normal goat serum (10658654, Fischer Scientific) and 0.1% Triton X-100 (T8787, Sigma) at room temperature for 30 min. Primary antibodies of collagen IV (ab6586, Abcam), α-SMA (ab5694, Abcam), laminin (ab11575, Abcam) and F-actin (A12379, ThermoFisher Scientific) were diluted at 1:100 in blocking buffer and incubated overnight at 4 °C. Secondary antibodies (ab6939, Abcam) were diluted at 1:500 in blocking buffer and then incubated for 2 h at room temperature. Following incubation, chamber slides were mounted with aqua-polymount (Polyscience) after nuclei-counterstaining with DAPI. Fluorescent images of SCEC monolayers were captured using a confocal microscope (Zeiss LSM 710), and processed using imaging software ZEN 2012.

For clear fibronectin (ab23750, Abcam) staining, cells were grown on cover slips and subsequently decellularised, leaving only the ECM material. Round cover slips (15 mm Diameter, Sparks Lab Supplies) were silanised before cell seeding to enhance binding to ECM products. This was achieved by initially immersing slips in 1% acid alcohol (1% concentrated HCL, 70% ethanol, 29% dH_2O) for 30 mins. Slips were washed in running water for 5 min, immersed in dH_2O twice for 5 min, immersed in 95% ethanol twice for 5 min and let air dry for 15 min. Cover slips were then immersed in 2% APES (3-aminopropyl triethoxysilane (A3648, Sigma) in acetone (Fisher Chemical)) for 1 min. Slips were again washed twice in dH_2O for 1 min and dried overnight at 37 °C. Cells were grown to confluency on these cover slips and, following treatment, were decellularised. This was achieved by consecutive washes in Hank's Balanced Salt Solution (HBSS), 20 mM ammonium hydroxide (Sigma) with 0.05% Triton X-100, and finally HBSS again. Matrices were fixed and stained as described above with chamber slides.

Western blotting

Cells were treated with 10 ng/ml MMP-3 for 24 h in serum-free media. Media supernatants were aspirated and mixed 1:6 with StrataClean resin (Agilent). After centrifugation, the supernatant was removed and the pellet was resuspended in NP-40 lysis buffer containing 50 mM Tris pH 7.5, 150 mM NaCL, 1% NP-40, 10% SDS, 1X protease inhibitor (Roche). Cells were lysed using NP-40 lysis buffer for protein collection. Samples were centrifuged at 10,000 rpm for 15 min (IEC Micromax microcentrifuge) and supernatant was retained. Protein samples were loaded onto a 10% SDS-PAGE gel at 30–50μg per well. Proteins were separated by electrophoresis over the course of 150 min at constant voltage (120 V) under reducing conditions and subsequently electro-transferred onto methanol-activated PVDF membranes at constant voltage (12 V). Gels intended for use with Collagen IV antibodies were run under native conditions. Membranes were blocked for 1 h at room temperature in 5% non-fat dry milk and incubated overnight at 4 °C with a rabbit primary antibodies to collagen IV, α-SMA, laminin and fibronectin as previously stated at concentrations of 1 in 1000 but 1 in 500 for laminin. Membrane blots were washed 3x5 min in TBS and incubated at room temperature for 2 h with horse radish peroxidase-conjugated anti-rabbit secondary antibody (Abcam). Blots were again washed and treated with a chemiluminescent substrate (WesternBright ECL, Advansta) and developed on a blot scanner (C-DiGit, LI-COR). The membranes containing cell lysate samples were re-probed with GAPDH antibody (ab9485, Abcam) for loading control normalisation. Media samples were normalised against their total protein concentration as determined by a spectrophotometer (ND-1000, NanoDrop). A total of four replicate blots were quantified for each cell lysate sample antibody, and 2–3 replicates for a media sample. Band images were quantified using Image J software. Fold change in band intensity was represented in comparison to vehicle control treatments of PBS.

AAV

AAV-2/9 containing the enhanced green fluorescent protein (eGFP) reporter gene (Vector Biolabs) was initially used to assess viral transduction and expression in the anterior chambers of wild type mice (C57/BL6). Murine MMP-3 cDNA was incorporated into Bam HI/Xhol sites of the pAAV-MCS vector (Cell Biolabs Inc) for constitutive expression of MMP-3. A null virus was used as contralateral control using the same capsid and vector. The inducible vector was designed by cloning MMP-3 cDNA into a pSingle-tTS (Clontech) vector. This vector was then digested with BsrBI and BsrGI and the fragment containing the inducible system and MMP-3 cDNA was ligated into the Not1 site of expression vector pAAV-MCS, to incorporate left and right AAV inverted terminal repeats (L-IRT and R-ITR). AAV-2/9 was generated using a triple transfection system in a stable HEK-293 cell line (Vector Biolabs). For animals injected with the inducible virus, after a 3-week incubation period, 0.2% doxycycline (D9891, Sigma) in PBS was administered twice daily to the eye for 10–16 days to induce viral expression. A similar inducible virus expressing eGFP was used as a control in the inducible study.

Intracameral injection

Animals were anaesthetised by intra-peritoneal injection of ketamine (Vetalar V, Zoetis) and domitor (SedaStart, Animalcare) (66.6 and 0.66 mg/kg, respectively). Pupils were dilated using one drop of tropicamide and phenylephrine (Bausch & Lomb) on each eye. 2 μl of virus at a stock titre of $5x10^{13}$ vector genomes per ml was initially back-filled into a glass needle (ID1.0 mm, WPI) attached via tubing (ID-1.02 mm, OD-1.98 mm, Smiths) to a syringe pump (PHD Ultra, Harvard Apparatus). An additional 1 μl of air was then withdrawn into the needle. Animals were injected intracamerally just above the limbus. Viral solution was infused at a rate of 1.5 μl/min for a total of 3 μl to include the air bubble. Contralateral eyes received an equal volume and titre of either AAV-MMP-3 or AAV-Null. The air bubble prevented the reflux of virus/aqueous back through the injection site when the needle was removed. Fucidic gel (Fucithalmic Vet, Dechra) was applied topically following injection as an antibiotic agent. To counter anaesthetic, Antisedan (atipamezole hydrochloride, SedaStop, Animalcare) was intra-peritoneally injected (8.33 mg/kg) and a carbomer based moisturising gel (Vidisic, Bausch & Lomb) was applied during recovery to prevent corneal dehydration.

Immunohistochemistry (mouse eyes)

Eyes were enucleated 4 weeks post-injection of virus and fixed in 4% paraformaldehyde overnight at 4 °C. The posterior

segment was removed by dissection and anterior segments were washed in PBS and placed in a sucrose gradient of incrementing sucrose concentrations containing 10%, 20% and finally 30% sucrose in PBS. Anterior segments were frozen in O.C.T compound (VWR Chemicals) in an isopropanol bath immersed in liquid nitrogen and cryosectioned (CM 1900, Leica Microsystems) at 12 μm thick sections. Sections were gathered onto charged Polysine® slides (Menzel-Gläser) and blocked for 1 h with 5% normal goat serum (10658654, Fischer Scientific) and 0.1% Triton X-100 in PBS. Slides were incubated overnight at 4 °C in a humidity chamber with a 1:100 dilution of primary antibody. Antibodies used were MMP-3 (ab52915, Abcam) and GFP (Cell Signalling). Sections were washed three times in PBS for 5 min and incubated with a Cy-3 conjugated anti-rabbit IgG antibody (ab6936, Abcam) at a 1:500 dilution for 2 h at 37 °C in a humidity chamber. Slides were washed as before and counter stained with DAPI for 30 s. Slides were mounted using Aquamount (Hs-106, National Diagnostics) with coverslips (Deckgläser) and visualised using a confocal microscope (Zeiss LSM 710).

Total MMP-3 quantification

MMP-3 concentration was quantified using enzyme-linked immunosorbent assay (ELISA) kits for both human SC monolayers (DMP300, R&D Systems) and murine aqueous (RAB0368-1KT, Sigma) according to the manufacturer's protocol. SC monolayers were cultured and treated with a 1 in 10 dilution of human cataract and POAG AH, a method previously described (87). Media was taken from the monolayers 24 h post-treatment and assayed for total MMP-3.

To measure the secretion of MMP-3 by AAV-2/9 into the AH, animals were inoculated with virus as described previously via intracameral injection. Four weeks post-injection, the animals were sacrificed and AH was collected. This was achieved by the cannulation of the cornea with a pulled glass needle (1B100-6, WPI) and gentle pressing of the eye until it was deflated. Aqueous was expelled from the needle (approximately 5 μl) by the attachment of a 25ml syringe connected via barb fitting and tubing (Smiths Medical) and a gradual push of the syringe plunger. Aqueous was assayed using the previously mentioned ELISA kit.

MMP-3 activity assay (FRET)

Enzymatic activity of secreted MMP-3 was quantified using fluorescence resonance energy transfer (FRET). A fluorescent peptide consisting of a donor/acceptor pair remains quenched in its intact state. This peptide contains binding sites specific to MMP-3. Once cleavage occurs through MMP-3 mediated proteolysis, fluorescence is recovered by the transfer of energy from the donor to the acceptor, resulting in an increase in the acceptor's emission intensity. Cleavage of substrate, and therefore fluorescence, was monitored on a FLUOstar OPTIMA (BMG Labtech) over the course of 2.5 h at 37 °C, to allow ample time for substrate cleavage. Media samples were collected from treated SC monolayers and combined with a 1:100 dilution of an MMP-3 specific substrate (ab112148, Abcam). Levels of active MMP-3 were interpolated from a standard curve defined by ELISA. For murine aqueous MMP-3 activity, aqueous was retrieved four weeks post-injection of AAV-MMP-3 or AAV-Null as described above. Aqueous samples were processed through an activity kit (abe3730, Source Bioscience), selected for its high sensitivity and specificity, according to the manufacturer's protocol.

Enzymatic activity was calculated as described in MMP-3 activity Assay Kit's (ab118972, Abcam) protocol:

$$\text{MMP}-3\ \text{Activity}\ (\text{nmol/min/ml}) = \frac{B\ \times\ \textit{Dilution Factor}}{(T2-T1)\ \times\ V},$$

Where B is the level of MMP-3 interpolated from the standard curve, T1 is the time (min) of the initial reading, T2 is the time (min) of the second reading and V is the sample volume (ml) added to the reaction well. The units 'nmol/min/ml' are equivalent to 'mU/ml'.

Measurement of outflow facility

Animals were sacrificed for outflow facility measurement 4 weeks after injection of virus. Eyes were enucleated for *ex vivo* perfusion using the *iPerfusion*™ system as described in (47). Contralateral eyes were perfused simultaneously using two independent but identical iPerfusion systems. Each system comprises an automated pressure reservoir, a thermal flow sensor (SLG64-0075, Sensiron) and a wet-wet differential pressure transducer (PX409, Omegadyne), in order to apply a desired pressure, measure flow rate out of the system and measure the intraocular pressure respectively. Enucleated eyes were secured to a pedestal using a small amount of cyanoacrylate glue in a PBS bath regulated at 35 °C. Perfusate was prepared (PBS including divalent cations and 5.5mM glucose) and filtered (0.2 μm, GVS Filter Technology) before use. Eyes were cannulated using a bevelled needle (NF33BV NanoFil™, World Precision Instruments) with the aid of a stereomicroscope and micromanipulator (World Precision Instruments). Eyes were perfused for 30 min at a pressure of ~8 mmHg in order to acclimatise to the environment. Incrementing pressure steps were applied from 4.5 to 21 mmHg, while recording flow rate and pressure. Flow (Q) and pressure (P) were averaged over 4 min of steady data, and a power law model of the form

$$Q = C_r\left(\frac{P}{P_r}\right)^{\beta} P$$

was fit to the data using weighted power law regression, yielding values of C_r, the reference facility at reference pressure $P_r = 8$ mmHg (corresponding to the physiological pressure drop across the outflow pathway), and β, a nonlinearity parameter characterising the pressure-dependent increase in facility observed in mouse eyes (47).

IOP

IOP measurements were performed by rebound tonometry (TonoLab, Icare) both prior to intracameral injection and 4 weeks post-injection. Readings, which were the average IOP values after five tonometric events, were taken 10 min after the intraperitoneal administration of mild general anaesthetic (53.28 mg/kg ketamine and 0.528 mg/kg domitor). Two readings were taken for one eye, then the other. This was repeated for a total of four readings per eye. Due to a minimum reading of 7 mmHg by the tonometer, a non-parametric approach was taken in the analysis of the readings. The median IOP was

calculated for each eye, and MAD (median absolute deviation) values were used as a measure of dispersion. For comparing median values in a paired population, the Wilcoxon matched-pairs signed-rank test was employed to test for changes in IOP pre- and post-injection, and also for changes between contralateral eyes.

Analysis of central corneal thickness

Enucleated mouse eyes transduced with AAV-MMP-3 or its contralateral control, AAV-Null, were fixed overnight in 4% PFA and washed in PBS. Posterior segments were removed by dissection under the microscope and anterior segments were embedded in medium (Tissue-Tek OCT Compound). Serial sectioning was performed on each eye and five frozen sections (12 μm) were transferred to a Polysine slide (Thermo Scientific) for staining with DAPI and mounted with aqua-polymount (Polyscience). Corneal sections were judged to be central by qualitatively taking the same distance from both iridocorneal angles. For quantitation, we measured the corneal thickness of sections on five consecutive slides by light and confocal microscopy (Zeiss LSM 710). A total of 25 measurements were taken from each eye to represent mean central corneal thickness (μm) using the NIH ImageJ software.

Transmission electron microscopy

Ultrastructural investigation was performed by transmission electron microscopy (TEM) in four pairs of mouse eyes. One eye of each pair was injected with AAV-Null, the other with AAV-MMP-3, as described above. Four weeks after injection, the eyes were enucleated and immersion fixed in Karnovsky's fixative (2.5% PFA, 0.1M cacodylate, 2.25% glutaraldehyde and dH_2O) for 1 h. Eyes were then removed from fixative and the cornea pierced using a 30-gauge needle (BD Microlance 3, Becton Dickinson). Eyes were placed back into fixative overnight at 4 °C, washed 3x10 min, stored in 0.1M cacodylate and sent to Erlangen.

Here the eyes were cut meridionally through the centre of the pupil, the lens carefully removed, and the two halves of each eye embedded in Epon. Semi-thin sagittal and then ultrathin sections of Schlemm's canal (SC) and trabecular meshwork (TM) were cut from one end of each half, and then the other approximately 0.2–0.3 mm deeper. The location of the superficial and deeper cut ends was alternated for the second half of the eye such that all four regions examined were at least 0.2–0.3 mm distant from one another. The ultrathin sections contained the entire anterior posterior length of the inner wall and the TM.

In four regions of each eye, we measured the length of optically empty space immediately underlying the inner wall endothelium of SC (Supplementary Material, Fig. S6). We also measured the inner wall length in contact with ECM, including basement membrane material, elastic fibres, or amorphous material. The optically empty length divided by the total length (optically empty + ECM lengths) was calculated and defined as the percentage of optically empty length for that region. All measurements were performed at 10,000x magnification, with each region including approximately 100 individual lengths of ECM or optically empty space. The measurements were performed by the two authors: ELD and CFK.

Statistical analysis

For TEER values, activity units (mU/ml) and concentrations (ng/ml), statistical differences were analysed by using unpaired two-tailed Student's *t*-tests. Differences in P_{app} values (cm/s) were determined by a one way ANOVA with Tukey's correction for multiple comparisons, where appropriate. ELISA standard curve concentrations were log-transformed and absorbance values were fitted to a sigmoidal dose response curve with variable slope for interpolation. Fold change of western blot data was log-transformed and investigated for significance using a one-sample *t*-test against a theoretical mean of 0. To measure MMP-3 concentration and activity in the AH of wild type (WT) mice, a paired two-tailed *t*-test was carried out for contralateral samples. Outflow facility was analysed using a weighted paired *t*-test performed in MATLAB as described in (47), incorporating both system and biological uncertainties. For IOP data, median values were obtained to reflect the non-parametric nature of the tonometer, and the Wilcoxon matched-pairs signed rank test was used to compare changes in paired populations. For morphology, the distribution of values representing the percent optically empty length was first examined using a Shapiro-Wilk and Anderson-Darling tests to detect for deviations from a normal distribution. The percent optically empty length between contralateral eyes was then analysed using a paired Student's *t*-test. Statistical significance was inferred when $P < 0.05$ in all experimentation. Results were depicted as 'mean, [95% Confidence Intervals]' unless otherwise stated in the results section.

Supplementary Material

Supplementary Material is available at *HMG* online.

Acknowledgements

We wish to acknowledge Caroline Woods and Charles Murray for animal husbandry. We would also like to thank Elke Kretzschmar, Britta Bäckermann and Andrea Eichnorn for preparing the semi-and ultrathin sections and Marco Gößwein for his assistance in finalizing the TEM images for publication.

Conflict of Interest statement. None declared.

Funding

Research at the Ocular Genetics Unit at the University of Dublin, Trinity College was supported by the European Research Council [ERC-2012-AdG 322656-Oculus]. We also acknowledge an equipment grant from Science Foundation Ireland in support of this project [12/ERC/B2539]. Research at Imperial College London was supported by the US National Institutes of Health (EY022359 and EY019696), the UK Engineering and Physical Sciences Research Council (EP/J010499/1), and Fight for Sight UK (Ref 1385). Work at Duke University was also supported by the US National Institutes of Health (EY022359). Funding to pay the Open Access publication charges for this article was provided by the European Research Council.

References

1. Yan, X., Li, M., Chen, Z., Zhu, Y., Song, Y. and Zhang, H. (2016) Schlemm's Canal and Trabecular Meshwork in Eyes with Primary Open Angle Glaucoma: A Comparative Study Using High-Frequency Ultrasound Biomicroscopy. *PLoS One*, **11**, e0145824.

2. Lanza, M., Iaccarino, S., Mele, L., Carnevale, U.A., Irregolare, C., Lanza, A., Femiano, F. and Bifani, M. (2016) Intraocular pressure evaluation in healthy eyes and diseased ones using contact and non contact devices. *Cont. Lens. Anterior. Eye*, **39**, 154–159.
3. Grant, W.M. (1951) Clinical measurements of aqueous outflow. *Am. J. Ophthalmol.*, **34**, 1603–1605.
4. Rylander, N.R. and Vold, S.D. (2008) Cost analysis of glaucoma medications. *Am. J. Ophthalmol.*, **145**, 106–113.
5. Hamanaka, T. and Bill, A. (1988) Effects of alpha-chymotrypsin on the outflow routes for aqueous humor. *Exp. Eye Res.*, **46**, 323–341.
6. Johnson, M. (2006) 'What controls aqueous humour outflow resistance?' *Exp. Eye Res.*, **82**, 545–557.
7. Tanihara, H., Inatani, M., Koga, T., Yano, T. and Kimura, A. (2002) Proteoglycans in the eye. *Cornea*, **21**, 62–69.
8. Floyd, B.B., Cleveland, P.H. and Worthen, D.M. (1985) Fibronectin in human trabecular drainage channels. *Invest. Ophthalmol. Vis. Sci.*, **26**, 797–804.
9. Keller, K.E., Bradley, J.M., Vranka, J.A. and Acott, T.S. (2011) Segmental versican expression in the trabecular meshwork and involvement in outflow facility. *Invest. Ophthalmol. Vis. Sci.*, **52**, 5049–5057.
10. Swaminathan, S.S., Oh, D.J., Kang, M.H., Ren, R., Jin, R., Gong, H. and Rhee, D.J. (2013) Secreted protein acidic and rich in cysteine (SPARC)-null mice exhibit more uniform outflow. *Invest. Ophthalmol. Vis. Sci.*, **54**, 2035–2047.
11. Overby, D.R., Stamer, W.D. and Johnson, M. (2009) The changing paradigm of outflow resistance generation: towards synergistic models of the JCT and inner wall endothelium. *Exp. Eye Res.*, **88**, 656–670.
12. Curtis, T.M., McKeown-Longo, P.J., Vincent, P.A., Homan, S.M., Wheatley, E.M. and Saba, T.M. (1995) Fibronectin attenuates increased endothelial monolayer permeability after RGD peptide, anti-alpha 5 beta 1, or TNF-alpha exposure. *Am. J. Physiol.*, **269**, 248–260.
13. Stickel, S.K. and Wang, Y.L. (1988) Synthetic peptide GRGDS induces dissociation of alpha-actinin and vinculin from the sites of focal contacts. *J. Cell Biol.*, **107**, 1231–1239.
14. Lampugnani, M.G., Resnati, M., Dejana, E. and Marchisio, P.C. (1991) The role of integrins in the maintenance of endothelial monolayer integrity. *J. Cell Biol.*, **112**, 479–490.
15. Wu, M.H., Ustinova, E. and Granger, H.J. (2001) Integrin binding to fibronectin and vitronectin maintains the barrier function of isolated porcine coronary venules. *J. Physiol.*, **532**, 785–791.
16. Mehta, D. and Malik, A.B. (2006) Signaling mechanisms regulating endothelial permeability. *Physiol. Rev.*, **86**, 279–367.
17. Keller, K.E. and Acott, T.S. (2013) The Juxtacanalicular Region of Ocular Trabecular Meshwork: A Tissue with a Unique Extracellular Matrix and Specialized Function. *J. Ocul. Biol. Dis. Infor.*, **1**, 3.
18. Rohen, J.W., Futa, R. and Lutjen-Drecoll, E. (1981) The fine structure of the cribriform meshwork in normal and glaucomatous eyes as seen in tangential sections. *Invest. Ophthalmol. Vis. Sci.*, **21**, 574–585.
19. Faralli, J.A., Schwinn, M.K., Gonzalez, J.M., Jr., Filla, M.S. and Peters, D.M. (2009) Functional properties of fibronectin in the trabecular meshwork. *Exp. Eye Res.*, **88**, 689–693.
20. Tamm, E.R., Siegner, A., Baur, A. and Lutjen-Drecoll, E. (1996) Transforming growth factor-beta 1 induces alpha-smooth muscle-actin expression in cultured human and monkey trabecular meshwork. *Exp. Eye Res.*, **62**, 389–397.
21. Schlunck, G., Han, H., Wecker, T., Kampik, D., Meyer-ter-Vehn, T. and Grehn, F. (2008) Substrate rigidity modulates cell matrix interactions and protein expression in human trabecular meshwork cells. *Invest. Ophthalmol. Vis. Sci.*, **49**, 262–269.
22. Acott, T.S., Kelley, M.J., Keller, K.E., Vranka, J.A., Abu-Hassan, D.W., Li, X., Aga, M. and Bradley, J.M. (2014) Intraocular pressure homeostasis: maintaining balance in a high-pressure environment. *J. Ocul. Pharmacol. Ther.*, **30**, 94–101.
23. Nagase, H., Suzuki, K., Enghild, J.J. and Salvesen, G. (1991) Stepwise activation mechanisms of the precursors of matrix metalloproteinases 1 (tissue collagenase) and 3 (stromelysin). *Biomed. Biochim. Acta*, **50**, 749–754.
24. Schlotzer-Schrehardt, U., Lommatzsch, J., Kuchle, M., Konstas, A.G. and Naumann, G.O. (2003) Matrix metalloproteinases and their inhibitors in aqueous humor of patients with pseudoexfoliation syndrome/glaucoma and primary open-angle glaucoma. *Invest. Ophthalmol. Vis. Sci.*, **44**, 1117–1125.
25. Ronkko, S., Rekonen, P., Kaarniranta, K., Puustjarvi, T., Terasvirta, M. and Uusitalo, H. (2007) Matrix metalloproteinases and their inhibitors in the chamber angle of normal eyes and patients with primary open-angle glaucoma and exfoliation glaucoma. *Graefes Arch. Clin. Exp. Ophthalmol.*, **245**, 697–704.
26. Tektas, O.Y. and Lutjen-Drecoll, E. (2009) Structural changes of the trabecular meshwork in different kinds of glaucoma. *Exp. Eye Res.*, **88**, 769–775.
27. Overby, D.R., Bertrand, J., Tektas, O.Y., Boussommier-Calleja, A., Schicht, M., Ethier, C.R., Woodward, D.F., Stamer, W.D. and Lutjen-Drecoll, E. (2014) Ultrastructural changes associated with dexamethasone-induced ocular hypertension in mice. *Invest. Ophthalmol. Vis. Sci.*, **55**, 4922–4933.
28. Pang, I.H., Fleenor, D.L., Hellberg, P.E., Stropki, K., McCartney, M.D. and Clark, A.F. (2003) Aqueous outflow-enhancing effect of tert-butylhydroquinone: involvement of AP-1 activation and MMP-3 expression. *Invest. Ophthalmol. Vis. Sci.*, **44**, 3502–3510.
29. Webb, J.G., Husain, S., Yates, P.W. and Crosson, C.E. (2006) Kinin modulation of conventional outflow facility in the bovine eye. *J. Ocul. Pharmacol. Ther.*, **22**, 310–316.
30. Bradley, J.M., Vranka, J., Colvis, C.M., Conger, D.M., Alexander, J.P., Fisk, A.S., Samples, J.R. and Acott, T.S. (1998) Effect of matrix metalloproteinases activity on outflow in perfused human organ culture. *Invest. Ophthalmol. Vis. Sci.*, **39**, 2649–2658.
31. De Groef, L., Van Hove, I., Dekeyster, E., Stalmans, I. and Moons, L. (2013) MMPs in the trabecular meshwork: promising targets for future glaucoma therapies?. *Invest. Ophthalmol. Vis. Sci.*, **54**, 7756–7763.
32. Rehnberg, M., Ammitzboll, T. and Tengroth, B. (1987) Collagen distribution in the lamina cribrosa and the trabecular meshwork of the human eye. *Br. J. Ophthalmol.*, **71**, 886–892.
33. Medina-Ortiz, W.E., Belmares, R., Neubauer, S., Wordinger, R.J. and Clark, A.F. (2013) Cellular fibronectin expression in human trabecular meshwork and induction by transforming growth factor-beta2. *Invest. Ophthalmol. Vis. Sci.*, **54**, 6779–6788.
34. Hann, C.R., Springett, M.J., Wang, X. and Johnson, D.H. (2001) Ultrastructural localization of collagen IV, fibronectin, and laminin in the trabecular meshwork of normal and glaucomatous eyes. *Ophthalmic Res.*, **33**, 314–324.

35. Umihira, J., Nagata, S., Nohara, M., Hanai, T., Usuda, N. and Segawa, K. (1994) Localization of elastin in the normal and glaucomatous human trabecular meshwork. *Invest. Ophthalmol. Vis. Sci.*, **35**, 486–494.
36. Wirtz, M.K., Bradley, J.M., Xu, H., Domreis, J., Nobis, C.A., Truesdale, A.T., Samples, J.R., Van Buskirk, E.M. and Acott, T.S. (1997) Proteoglycan expression by human trabecular meshworks. *Curr. Eye Res.*, **16**, 412–421.
37. Murphy, G., Cockett, M.I., Stephens, P.E., Smith, B.J. and Docherty, A.J. (1987) Stromelysin is an activator of procollagenase. A study with natural and recombinant enzymes. *Biochem. J.*, **248**, 265–268.
38. Lijnen, H.R., Silence, J., Van Hoef, B. and Collen, D. (1998) Stromelysin-1 (MMP-3)-independent gelatinase expression and activation in mice. *Blood*, **91**, 2045–2053.
39. Ogata, Y., Enghild, J.J. and Nagase, H. (1992) Matrix metalloproteinase 3 (stromelysin) activates the precursor for the human matrix metalloproteinase 9. *J. Biol. Chem.*, **267**, 3581–3584.
40. Yang, Y., Estrada, E.Y., Thompson, J.F., Liu, W. and Rosenberg, G.A. (2007) Matrix metalloproteinase-mediated disruption of tight junction proteins in cerebral vessels is reversed by synthetic matrix metalloproteinase inhibitor in focal ischemia in rat. *J. Cereb. Blood Flow Metab.*, **27**, 697–709.
41. Yamada, H., Yoneda, M., Inaguma, S., Watanabe, D., Banno, S., Yoshikawa, K., Mizutani, K., Iwaki, M. and Zako, M. (2013) Infliximab counteracts tumor necrosis factor-alpha-enhanced induction of matrix metalloproteinases that degrade claudin and occludin in non-pigmented ciliary epithelium. *Biochem. Pharmacol.*, **85**, 1770–1782.
42. Rajashekhar, G., Shivanna, M., Kompella, U.B., Wang, Y. and Srinivas, S.P. (2014) Role of MMP-9 in the breakdown of barrier integrity of the corneal endothelium in response to TNF-alpha. *Exp. Eye Res.*, **122**, 77–85.
43. Buie, L.K., Rasmussen, C.A., Porterfield, E.C., Ramgolam, V.S., Choi, V.W., Markovic-Plese, S., Samulski, R.J., Kaufman, P.L. and Borras, T. (2010) Self-complementary AAV virus (scAAV) safe and long-term gene transfer in the trabecular meshwork of living rats and monkeys. *Invest. Ophthalmol. Vis. Sci.*, **51**, 236–248.
44. Bogner, B., Boye, S.L., Min, S.H., Peterson, J.J., Ruan, Q., Zhang, Z., Reitsamer, H.A., Hauswirth, W.W. and Boye, S.E. (2015) Capsid Mutated Adeno-Associated Virus Delivered to the Anterior Chamber Results in Efficient Transduction of Trabecular Meshwork in Mouse and Rat. *PLoS One*, **10**, e0128759.
45. Gerometta, R., Spiga, M.G., Borras, T. and Candia, O.A. (2010) Treatment of sheep steroid-induced ocular hypertension with a glucocorticoid-inducible MMP1 gene therapy virus. *Invest. Ophthalmol. Vis. Sci.*, **51**, 3042–3048.
46. Borras, T., Buie, L.K. and Spiga, M.G. (2016) Inducible scAAV2.GRE.MMP1 lowers IOP long-term in a large animal model for steroid-induced glaucoma gene therapy. *Gene Ther.*, **23**, 438–449.
47. Sherwood, J.M., Reina-Torres, E., Bertrand, J.A., Rowe, B. and Overby, D.R. (2016) Measurement of Outflow Facility Using iPerfusion. *PLoS One*, **11**, e0150694.
48. Overby, D.R., Bertrand, J., Schicht, M., Paulsen, F., Stamer, W.D. and Lutjen-Drecoll, E. (2014) The structure of the trabecular meshwork, its connections to the ciliary muscle, and the effect of pilocarpine on outflow facility in mice. *Invest. Ophthalmol. Vis. Sci.*, **55**, 3727–3736.
49. Nga, A.D., Yap, S.L., Samsudin, A., Abdul-Rahman, P.S., Hashim, O.H. and Mimiwati, Z. (2014) Matrix metalloproteinases and tissue inhibitors of metalloproteinases in the aqueous humour of patients with primary angle closure glaucoma - a quantitative study. *BMC Ophthalmol.*, **14**, 33.
50. Ashworth Briggs, E.L., Toh, T., Eri, R., Hewitt, A.W. and Cook, A.L. (2015) TIMP1, TIMP2, and TIMP4 are increased in aqueous humor from primary open angle glaucoma patients. *Mol. Vis.*, **21**, 1162–1172.
51. Badier-Commander, C., Verbeuren, T., Lebard, C., Michel, J.B. and Jacob, M.P. (2000) Increased TIMP/MMP ratio in varicose veins: a possible explanation for extracellular matrix accumulation. *J. Pathol.*, **192**, 105–112.
52. Lutjen-Drecoll, E., Shimizu, T., Rohrbach, M. and Rohen, J.W. (1986) Quantitative analysis of 'plaque material' between ciliary muscle tips in normal- and glaucomatous eyes. *Exp. Eye Res.*, **42**, 457–465.
53. Rohen, J.W., Lutjen-Drecoll, E., Flugel, C., Meyer, M. and Grierson, I. (1993) Ultrastructure of the trabecular meshwork in untreated cases of primary open-angle glaucoma (POAG). *Exp. Eye Res.*, **56**, 683–692.
54. Parshley, D.E., Bradley, J.M., Samples, J.R., Van Buskirk, E.M. and Acott, T.S. (1995) Early changes in matrix metalloproteinases and inhibitors after in vitro laser treatment to the trabecular meshwork. *Curr. Eye Res.*, **14**, 537–544.
55. Parshley, D.E., Bradley, J.M., Fisk, A., Hadaegh, A., Samples, J.R., Van Buskirk, E.M. and Acott, T.S. (1996) Laser trabeculoplasty induces stromelysin expression by trabecular juxtacanalicular cells. *Invest. Ophthalmol. Vis. Sci.*, **37**, 795–804.
56. Takai, Y., Tanito, M. and Ohira, A. (2012) Multiplex cytokine analysis of aqueous humor in eyes with primary open-angle glaucoma, exfoliation glaucoma, and cataract. *Invest. Ophthalmol. Vis. Sci.*, **53**, 241–247.
57. Chua, J., Vania, M., Cheung, C.M., Ang, M., Chee, S.P., Yang, H., Li, J. and Wong, T.T. (2012) Expression profile of inflammatory cytokines in aqueous from glaucomatous eyes. *Mol. Vis.*, **18**, 431–438.
58. Kelley, M.J., Rose, A.Y., Song, K., Chen, Y., Bradley, J.M., Rookhuizen, D. and Acott, T.S. (2007) Synergism of TNF and IL-1 in the induction of matrix metalloproteinase-3 in trabecular meshwork. *Invest. Ophthalmol. Vis. Sci.*, **48**, 2634–2643.
59. Bradley, J.M., Anderssohn, A.M., Colvis, C.M., Parshley, D.E., Zhu, X.H., Ruddat, M.S., Samples, J.R. and Acott, T.S. (2000) Mediation of laser trabeculoplasty-induced matrix metalloproteinase expression by IL-1beta and TNFalpha. *Invest. Ophthalmol. Vis. Sci.*, **41**, 422–430.
60. Alexander, J.P., Samples, J.R. and Acott, T.S. (1998) Growth factor and cytokine modulation of trabecular meshwork matrix metalloproteinase and TIMP expression. *Curr. Eye Res.*, **17**, 276–285.
61. Partridge, C.A., Jeffrey, J.J. and Malik, A.B. (1993) A 96-kDa gelatinase induced by TNF-alpha contributes to increased microvascular endothelial permeability. *Am. J. Physiol.*, **265**, 438–447.
62. Si-Tayeb, K., Monvoisin, A., Mazzocco, C., Lepreux, S., Decossas, M., Cubel, G., Taras, D., Blanc, J.F., Robinson, D.R. and Rosenbaum, J. (2006) Matrix metalloproteinase 3 is present in the cell nucleus and is involved in apoptosis. *Am. J. Pathol.*, **169**, 1390–1401.
63. Garcia, A.J., Tom, C., Guemes, M., Polanco, G., Mayorga, M.E., Wend, K., Miranda-Carboni, G.A. and Krum, S.A. (2013) ERalpha signaling regulates MMP3 expression to induce FasL cleavage and osteoclast apoptosis. *J. Bone Miner. Res.*, **28**, 283–290.

64. Bradley, J.M., Kelley, M.J., Rose, A. and Acott, T.S. (2003) Signaling pathways used in trabecular matrix metalloproteinase response to mechanical stretch. *Invest. Ophthalmol. Vis. Sci.*, **44**, 5174–5181.
65. Bradley, J.M., Kelley, M.J., Zhu, X., Anderssohn, A.M., Alexander, J.P. and Acott, T.S. (2001) Effects of mechanical stretching on trabecular matrix metalloproteinases. *Invest. Ophthalmol. Vis. Sci.*, **42**, 1505–1513.
66. Gonzalez, P., Epstein, D.L. and Borras, T. (2000) Genes upregulated in the human trabecular meshwork in response to elevated intraocular pressure. *Invest. Ophthalmol. Vis. Sci.*, **41**, 352–361.
67. Luna, C., Li, G., Liton, P.B., Epstein, D.L. and Gonzalez, P. (2009) Alterations in gene expression induced by cyclic mechanical stress in trabecular meshwork cells. *Mol. Vis.*, **15**, 534–544.
68. Vittitow, J. and Borras, T. (2004) Genes expressed in the human trabecular meshwork during pressure-induced homeostatic response. *J. Cell. Physiol.*, **201**, 126–137.
69. Lai, L., Lin, K., Foulks, G., Ma, L., Xiao, X. and Chen, K. (2005) Highly efficient ex vivo gene delivery into human corneal endothelial cells by recombinant adeno-associated virus. *Curr. Eye Res.*, **30**, 213–219.
70. Sharma, A., Ghosh, A., Hansen, E.T., Newman, J.M. and Mohan, R.R. (2010) Transduction efficiency of AAV 2/6, 2/8 and 2/9 vectors for delivering genes in human corneal fibroblasts. *Brain Res. Bull.*, **81**, 273–278.
71. Liu, J., Saghizadeh, M., Tuli, S.S., Kramerov, A.A., Lewin, A.S., Bloom, D.C., Hauswirth, W.W., Castro, M.G., Schultz, G.S. and Ljubimov, A.V. (2008) Different tropism of adenoviruses and adeno-associated viruses to corneal cells: implications for corneal gene therapy. *Mol. Vis.*, **14**, 2087–2096.
72. Borras, T., Xue, W., Choi, V.W., Bartlett, J.S., Li, G., Samulski, R.J. and Chisolm, S.S. (2006) Mechanisms of AAV transduction in glaucoma-associated human trabecular meshwork cells. *J. Gene Med.*, **8**, 589–602.
73. Herschler, J. (1976) Increased intraocular pressure induced by repository corticosteroids. *Am. J. Ophthalmol.*, **82**, 90–93.
74. Mandapati, J.S. and Metta, A.K. (2011) Intraocular pressure variation in patients on long-term corticosteroids. *Indian Dermatol. Online J.*, **2**, 67–69.
75. Pleyer, U., Ursell, P.G. and Rama, P. (2013) Intraocular pressure effects of common topical steroids for post-cataract inflammation: are they all the same? *Opthalmol. Ther.*, **2**, 55–72.
76. Clark, A.F., Steely, H.T., Dickerson, J.E., Jr., English-Wright, S., Stropki, K., McCartney, M.D., Jacobson, N., Shepard, A.R., Clark, J.I., Matsushima, H., *et al.* (2001) Glucocorticoid induction of the glaucoma gene MYOC in human and monkey trabecular meshwork cells and tissues. *Invest. Ophthalmol. Vis. Sci.*, **42**, 1769–1780.
77. Gurney, K.J., Estrada, E.Y. and Rosenberg, G.A. (2006) Blood-brain barrier disruption by stromelysin-1 facilitates neutrophil infiltration in neuroinflammation. *Neurobiol. Dis.*, **23**, 87–96.
78. Vermeer, P.D., Denker, J., Estin, M., Moninger, T.O., Keshavjee, S., Karp, P., Kline, J.N. and Zabner, J. (2009) MMP9 modulates tight junction integrity and cell viability in human airway epithelia. *Am. J. Physiol. Lung Cell Mol. Physiol.*, **296**, 751–762.
79. Stamer, W.D., Roberts, B.C., Howell, D.N. and Epstein, D.L. (1998) Isolation, culture, and characterization of endothelial cells from Schlemm's canal. *Invest. Ophthalmol. Vis. Sci.*, **39**, 1804–1812.
80. Perkumas, K.M. and Stamer, W.D. (2012) Protein markers and differentiation in culture for Schlemm's canal endothelial cells. *Exp. Eye Res.*, **96**, 82–87.
81. Heimark, R.L., Kaochar, S. and Stamer, W.D. (2002) Human Schlemm's canal cells express the endothelial adherens proteins, VE-cadherin and PECAM-1. *Curr. Eye Res.*, **25**, 299–308.
82. Stamer, W.D., Seftor, R.E., Williams, S.K., Samaha, H.A. and Snyder, R.W. (1995) Isolation and culture of human trabecular meshwork cells by extracellular matrix digestion. *Curr. Eye Res.*, **14**, 611–617.
83. Stamer, W.D., Seftor, R.E., Snyder, R.W. and Regan, J.W. (1995) Cultured human trabecular meshwork cells express aquaporin-1 water channels. *Curr. Eye Res.*, **14**, 1095–1100.
84. Stamer, W.D., Huang, Y., Seftor, R.E., Svensson, S.S., Snyder, R.W. and Regan, J.W. (1996) Cultured human trabecular meshwork cells express functional alpha 2A adrenergic receptors. *Invest. Ophthalmol. Vis. Sci.*, **37**, 2426–2433.
85. Stamer, W.D. and Clark, A.F. (2016) The many faces of the trabecular meshwork cell. *Exp. Eye Res*, in press.
86. Siah, W.F., Loughman, J. and O'Brien, C. (2015) Lower Macular Pigment Optical Density in Foveal-Involved Glaucoma. *Ophthalmology*, **122**, 2029–2037.
87. Wallace, D.M., Clark, A.F., Lipson, K.E., Andrews, D., Crean, J.K. and O'Brien, C.J. (2013) Anti-connective tissue growth factor antibody treatment reduces extracellular matrix production in trabecular meshwork and lamina cribrosa cells. *Invest. Ophthalmol. Vis. Sci.*, **54**, 7836–7848.
88. Keaney, J., Walsh, D.M., O'Malley, T., Hudson, N., Crosbie, D.E., Loftus, T., Sheehan, F., McDaid, J., Humphries, M.M., Callanan, J.J., *et al.* (2015) Autoregulated paracellular clearance of amyloid-beta across the blood-brain barrier. *Sci. Adv.*, **1**, e1500472.

Statement of collaboration

Paul Kenna performed AAV subretinal injections. Marian Humphries constructed AAV plasmids. Lawrence Tam conducted AH TEER and flux studies on SCECs and collaborated on TM CLAN counts. Colm O'Brien supplied patient aqueous humour.

Chapter 4

Detection of age-related changes in eye morphology and aqueous humour flow dynamics in DBA/2J mice using contrast-enhanced ocular MRI

Chapter 4: Detection of age-related changes in eye morphology and aqueous humour dynamics in DBA/2J mice using contrast-enhanced ocular MRI

Introduction

Summary

Intraocular hypertension is the major risk factor in glaucoma and IOP reduction is the main mode of treatment. IOP is homeostatically regulated by rate of AH production and its drainage from the AC, and this highly regulated process breaks down in glaucoma (Bonomi et al. 1998). Assessment of AH dynamics offers a crucial opportunity in furthering our understanding of the pathogenesis of glaucoma, in the living eye. Initially the difficulty *in vivo* arises due to the small volume of the AH in the AC, and the isolation of the AH from the systemic circulation. MRI is a powerful biological imaging tool that provides non-invasive, high-resolution 3-D images with excellent soft tissue contrast and no depth limitations.

The purpose of this study was to further investigate the utility gadolinium-enhanced magnetic resonance imaging (Gd-MRI) to identify age-related changes in eye morphology and aqueous humor flow dynamics in the DBA/2J mouse model of pigmentary glaucoma. A rodent-specific 7T MRI was used to assess eye anatomy and aqueous humor flow dynamics (via intravenous administration of Gd-DTPA contrast agent) in C57BL/6 and DBA/2J mice at 3 and 9 months of age. Topical latanoprost treatment in C57BL/6 mice reduced initial signal intensity increase in the anterior chamber. Age-related increases in AC area, AC depth and eye size were observed in DBA/2J mice compared to C57BL/6 mice. The rate of Gd-DTPA accumulation and peak Gd-DTPA intensity was lowest in 9-month old DBA/2J mice compared to 3-month old DBA/2J mice and C57BL/6 mice at both ages. Leakage of Gd-DTPA posteriorly into the VB was also observed in 9-month old DBA/2J mice. In conclusion**,** these studies indicate that age-related changes in aqueous humor flow may be a contributing factor to raised intraocular pressure (IOP) in the DBA/2J model of pigmentary glaucoma. Gd-DTPA MRI may allow for better understanding of mechanisms and dynamics of aqueous humor circulation in

normal and glaucomatous mouse eyes or following topical administration of medicines to reduce IOP.

Methods of AH flow measurements in vivo.

Early studies of AH dynamics measured the diffusion of macromolecules, such as radioactive tracers or fluorescein, from the blood after systemic injection or injection directly into the AC (O'Rourke 1970; Becker 1962; McLaren 2009). These studies measured the differences in diffusion of these tracers, tracking changes after treatment with glaucoma medications, thus demonstrating a correlation with AH flow (Becker 1962; O'Rourke 1970). In more contemporary methods fluorescein is instilled into the cunjunctival cul-de-sac and left to permeate through the cornea into the AH. Once the fluorescein is uniformly distributed in the AH the fluorescein concentration is measured as it is washed out of the AC (McLaren 2009), thus acting as a measure of the total outflow. Schiøtz tonography estimates the outflow facility *in vivo* by determining fluid volume leaving the eye in response to a known pressure elevation. IOP is elevated by application of a known weight to the cornea over the course of 2-4 minutes, thus increasing pressure dependent flow. The change in IOP measured at the beginning and end of tonography is used to estimate the volume of AH lost over this time period (Kazemi et al. 2017). Using these techniques the AH flow in humans has been calculated to be in the range of 2.2-3.1 µl/min (McLaren 2009), with AH flow slowing with age by ~4% per decade, concurrent with a decrease of AC volume of 2.4 µl/year on average (Toris et al. 2002; Toris et al. 1999). Differences in AH outflow have been demonstrated between ocular hypertensive and normotensive patients (Toris et al. 2002), although contrary to expectation mean AH outflow is independent of mean IOP (McLaren 2009), indicating that these methods of measuring AH flow have inherent inaccuracies. Fluorescein measurement depends on the assumption that all of the fluorescein in the AC is removed via the outflow pathways, and on the accurate measurement of the mass of fluorescein in the AC, both of which have the capacity to introduce error (McLaren 2009). In addition, Schiøtz tonography measurement which is based on the indentation of the cornea made by the probe, can be biased by age-related increase of corneal rigidity which reduces the apparent outflow facility value (Gaasterland et al. 1978). Thus a consistent and reliable method to assess AH flow in the *in vivo* eye is required.

Magnetic Resonance Imaging (MRI)

MRI is a powerful imaging tool that offers non-invasive structural and functional biological readings which is based on nuclear magnetic resonance, and nuclear spin. MRI uses a strong magnetic field to align the nuclear spin of the protons in a subject. The alignment of these protons is flipped using a radio frequency; the 'relaxation' of the proton spin to the original alignment after the application of the radio frequency produces a measurable signal. Therefore, molecules in the subject with a high number of proton such as water or fat give a higher signal (Armstrong & Keevil 1991). There are two types of scan often used to measure tissue structures, these are T_1- and T_2-weighted scans. T_1-weighted scans take advantage of the differences in the 'relaxation' time for protons to realign with the main magnetic field after the radio frequency pulse. Each tissue has differing T_1 relaxation times, which generates a high-contrast tissue gradient on the image. In the eye the lens has a relatively long relaxation time and appears darker in comparison to the aqueous and vitreous humors. T_2-weighted scans are then based on the differences in the time taken for protons to decay from their alignment. T_2-weighted scans have longer relaxation times and often have opposite tissue contrasts in comparison to T_1 images (Brown et al. 2016).

The contrast of these images can be enhanced with the use of so-called contrast agents such as manganese ions (Mn^{2+}) and gadolinium ions, generally in the form gadolinium-diethylenetriamine pentaacetate (Gd-DTPA). These paramagnetic ions decrease the T_1 relaxation time and to some extent the T_2 relaxation time of water and any tissue in which they accumulate (Carr et al. 1984; Massaad & Pautler 2011). Another type of MRI scan exists to detect water diffusion in tissues (Diffusion MRI); in biological tissues diffusion of water molecules is predominantly in one direction. As protons move through a magnetic field they lose transverse magnetization, which is used to create diffusion maps. This can be used in tracking the nerve fibres, such as in the optic tract (Fiedorowicz et al. 2011). Functional-MRI (fMRI) is a standard for inferring neuronal activity in human subjects and is based off the Blood Oxygenation Level Dependent (BOLD) signal. Increases in neuronal activity are accompanied by a change in blood oxygenation, which can be measured as changes in this BOLD signal. The BOLD

effect occurs due to two reasons. Firstly, local concentrations of deoxyhemoglobin generate magnetic field gradients along the blood vessels that reduces MR signal and secondly corresponding drops in deoxyhemoglobin with neuronal activity are seen as an increase in MR signal (Duncan et al. 2007).

MRI in the eye

The naturally clear pathway in the eye has given rise to multiple imaging modalities for visualizing optical structures, for example, scanning laser polarimetry, confocal scanning laser ophthalmology, and optical coherence tomography (OCT) (Townsend et al. 2008). However, in comparison to these methods, MRI offers some advantages: it has a large field of view, no depth limitations, is not obscured by ocular abnormalities, and offers functional in addition to structural insights (Duong & Muir 2009). Anatomical structures are generally visualized in the greatest detail using T_1-weighted imaging because of the high signal-to-noise ratio, although the short T_1 constant of fat can lead to over-saturated images. The surface of the inner globe is best imaged using T_2-weighting, due to the contrast offered by the bright vitreous signal; this method is more subject to motion artifacts and has a lower signal-to-noise ratio (Townsend et al. 2008). MRI is also used to image morphology of pathological changes such as retinal detachment. In an induced rat model of retinal inflammation retinal detachments as small as $0.1mm^2$ could be observed (Townsend et al. 2008). The vessels of the retinal and choroidal vasculature are sealed by tight junctions and do not allow Gd-DTPA diffusion into the vitreous. Therefore, contrast enhanced MRI is useful in examining the integrity of the BRB (Campbell et al. 2010; Duong & Muir 2009). In addition, Gd-DTPA MRI can be used to visualize retinal layers; differentiating the ganglion cell layer, both the inner and outer photoreceptor layer, and the choroid (Shen et al. 2006). In fact this technique was used to detect loss of the outer nuclear layer and photoreceptors during disease progression in a rat model of retinitis pigmentosa (Cheng et al. 2006). Manganese enhanced-MRI increases contrast, in the measurement of retinal layer thickness, but is also used in measurement of changes in ion conductance and transport along the optic nerve (Eter 2010). Retinal vessel autoregulation is a major pathology observed in diabetic retinopathy and fMRI can be used to assess the oxygen concentration

across the entire retina, with abnormal BOLD signals, in response to hyperoxic provocation, having been shown to precede retinal lesions (Duong & Muir 2009; Eter 2010). Practically, MRI has been used in glaucoma patients to assess drug distribution to the retina following different delivery methods. Gd-DTPA was administered both subconjunctively and via intrascleral injection, to test their efficacy in targeting the retina for therapy. Very little Gd-DTPA reached the posterior chamber after subconjunctival delivery whereas intrascleral delivery resulted in increased vitreous contrast (Eter 2010). Going forward the use of eye specific coils or the use of more powerful 7 Tesla machines for MRI capture could potentially increase resolution and reduce artifacts, allowing the identification of optic disc drusen or other abnormalities associated with retinal degenerations. However at present for the retina, MRI readouts are generally limited to layer-specific anatomy, blood-flow, and functionality.

MRI in glaucoma

Glaucoma is a disease with specific visual field defects and RGC degeneration originating from axon damage at the optic nerve head (Weinreb et al. 2014). MRI has been used to observe changes in the optic nerve head in papilledema. In patients with papilledema MRI was used to visualize optic nerve sheath enlargement and tortuosity of the ON (Degnan & Levy 2013). Both increased intracranial pressure and deformation of the optic nerve head are associated with glaucoma (Promelle et al. 2016; Wong et al. 2017). In both POAG and NTG, studies using MRI have shown that patients have reduced optic nerve head diameter and smaller optic chiasm heights compared to healthy controls (Brown et al. 2016). In a rat model of ocular hypertension, a reduction of 10% in axonal density after development of increased IOP was shown using diffusion tensor MRI (Hui et al. 2007). Similarly, in glaucoma patients, changes in diffusivity in the ON axons correlated with severity of glaucomatous optic neuropathy (Garaci et al. 2009). In glaucoma, nerve damage has been described as far up the central visual pathway as the LGN and visual cortex (Harris & Wirostko 2013). Cerebral T_1 MR images have displayed a significant reduction in LGN size in glaucoma patients relative to controls. Similarly, activity changes in the visual cortex of glaucomatous patients have been measured in response to a scotoma-mapping stimulus using fMRI. The

spatial pattern of the visual cortex activity change was found to correspond to the pattern of visual field loss assessed using standard automated perimetry (Duncan et al. 2007). The DBA/2J mouse model of pigmentary glaucoma shows progressive loss of RGCs with age. MRI assessment of this model using the arterial spin labeling has shown that there is reduced choroidal and retinal blood flow in aged animals (Lavery et al. 2012). These aged mice also were found to have age-related differences in ion regulation at the inner retina as demonstrated by manganese enhanced-MRI (Calkins et al. 2008). In addition, MRI has been used to image the positioning and the functionality of AH shunts after surgery, as well as the drainage of AH into the sub-scleral bleb after Ahmed implantation (Ferreira et al. 2015; De Feo et al. 2009).

AH predominantly consists of water, with only 1% of the total protein of plasma, and so gives a short T_1 relaxation time that can be further shortened with Gd-DTPA contrast agent (Freddo 2001). The use of Gd-DTPA has previously been used as a blood tracer and as a solute tracer to assess various barriers *in vivo*; it has previously been used to trace passive permeability through the BRB in diabetic rats and in our own lab it has been used to demonstrate opening of the iBRB using siRNA targeting claudin-5 (Campbell et al. 2010; Berkowitz et al. 2004). Gd-DTPA can cross the BAB and enter AC enhancing AH signal, and is separated from the vitreous body with no signal enhancement seen in the posterior chamber (Kolodny et al. 1996). Gadolinium enhanced MRI (Gd-MRI) has been used to demonstrate a breakdown in BAB integrity in a rabbit model of uveitis and in patients with end-stage renal disease (Kolodny et al. 2002; Kanamalla & Boyko 2002). In addition, Gd-MRI has been used to validate the anterior protein pathway in rabbits and humans, clearly demonstrating signal enhancement beginning at the AC angle and diffusing throughout the AC thereafter, with no signal enhancement in the posterior chamber (Kolodny et al. 1996; Bert et al. 2006). These results have helped to explain the mechanism behind pilocarpine-associated flare, which was thought of as a pathological breakdown of the BAB, but is in fact simply a result of reduced AH in-flow (Freddo et al. 2006; Freddo et al. 2013). Using this knowledge, studies on AH dynamics in an induced rat model of glaucoma have shown that increased Gd-DTPA accumulation in the AC of the glaucomatous eye and was decreased after treatment with IOP-lowering medications (Chan et al. 2008; Ho et

al. 2014), thus demonstrating a novel spatio-temporal method of measuring AH dynamics *in vivo* using Gd-MRI.

Overview

Pigment dispersion syndrome is characterized by shedding and dispersion of iris pigment throughout the anterior (AC) and posterior chambers of the eye (Niyadurupola & Broadway 2008). It is associated with elevated IOP that can lead to damage of the optic nerve and pigmentary glaucoma, a form of secondary open-angle glaucoma that tends to affect younger people (Siddiqui et al. 2003). The DBA/2J mouse strain recapitulates many facets of human pigmentary glaucoma such as pigment dispersion, iris atrophy, iris transillumination and elevated IOP (Zhou et al. 2005; Libby et al. 2005), though unlike the human condition, angle closure is a feature of this strain due to the development of anterior synechias (attachment of the anterior iris to the trabecular meshwork) (John et al. 1998). Elevated IOP presents at 2-6 months in DBA/2J mice, reaching a peak at 9-11 months; resulting in retinal ganglion cell loss and optic nerve cupping(Saleh et al. 2007; Inman et al. 2006; Jakobs et al. 2005; Schuettauf et al. 2002).

Regulation of AH secretion and drainage are integral to maintaining physiological IOP and data show that age-related IOP increases in glaucomatous eyes stem from disruption of AH outflow pathways (Goel et al. 2010). In the case of the DBA/2J mouse model, mutations in the *Tyrp1* and *Gpnmb* genes induce iris atrophy and pigment dispersion (Chang et al. 1999; Anderson et al. 2002), processes which are thought to affect AH outflow at the trabecular meshwork. However, the dynamics of AH secretion and drainage in normal and glaucomatous mouse eyes are still unresolved and little is known about aqueous humor flow changes in pigmentary glaucoma.

MRI using contrast agents such as Gd-DTPA or manganese (Mn^{2+}) have been used to assess ocular anatomy (Cheng et al. 2006), retinal blood flow (Lavery et al. 2012), blood-retina barrier permeability (Campbell et al. 2010), and AH flow in rodents, monkeys and humans, among other species (Ho et al. 2014; Bert et al. 2006). Gd-DTPA is a water-soluble passive tracer (938 Da) that under homeostatic conditions can cross the blood-aqueous barrier following systemic administration but has not been reported to cross the BRB under normal conditions (Bert et al.

2006; Ho et al. 2014). Clearance of Gd-DTPA from the AC occurs via the conventional outflow pathway consisting of the trabecular meshwork and Schlemm's canal (SC) and via the unconventional pathway between the ciliary muscle fibres (often referred to as the uveoscleral route).

In the present study, Gd-DTPA-enhanced MRI was used to assess total rates of AH flow and ocular permeability in the mouse eye following topical administration of latanoprost, a prostaglandin $F_{2\alpha}$-receptor analogue that alters AH outflow. Though a commonly used treatment for ocular hypertension latanoprost's pathway has yet to be fully elucidated, traditionally its effects have been ascribed to an increase in drainage through the ciliary muscle in humans, however it has been shown to also increase outflow through the trabecular meshwork (Weinreb et al. 2002; Bahler et al. 2008). In contrast in mice, latanoprost increases outflow facility through the conventional pathway but has less effect on the unconventional pathway and has been shown to increase lymphatic drainage (Cameron Millar et al. 2011; Tam et al. 2013). Having established the utility of Gd-DTPA-enhanced MRI in the detection of flow changes through the AC, this was followed by assessment of AH flow dynamics at different ages in the DBA/2J mouse model of pigmentary glaucoma with age-matched C57BL/6 mice as controls. These data indicate that BAB breakdown accompanies changes in AH flow dynamics with age in the DBA/2J mouse, and may contribute to elevated IOP in this model.

Results

Gd-MRI in the mouse AC

C57BL/6J mice were anaesthetized and placed in a 7T rodent MRI scanner and 25 sequential T_1 coronal scans were taken of the C57BL/6J eyes before the administration of Gd-DTPA contrast agent (**5.34**). In the pre-Gd images the lens tissue had a long relaxation time and had low signal while both the vitreous and aqueous humors, had short relaxation times with higher signal. The generalized signal over the eye is due to the use of hydrating gel (**Fig. 4.1a-b**). After intravenous administration of Gd-DTPA (post-Gd) the relaxation time of the AH was reduced thus increasing the signal. No signal enhancement was seen in the vitreous. The vitreous appeared darker in post-Gd scans as the MRI software adjusted the contrast from the pre-Gd scan to account for the greater signal from the AH (**Fig. 4.1a**).

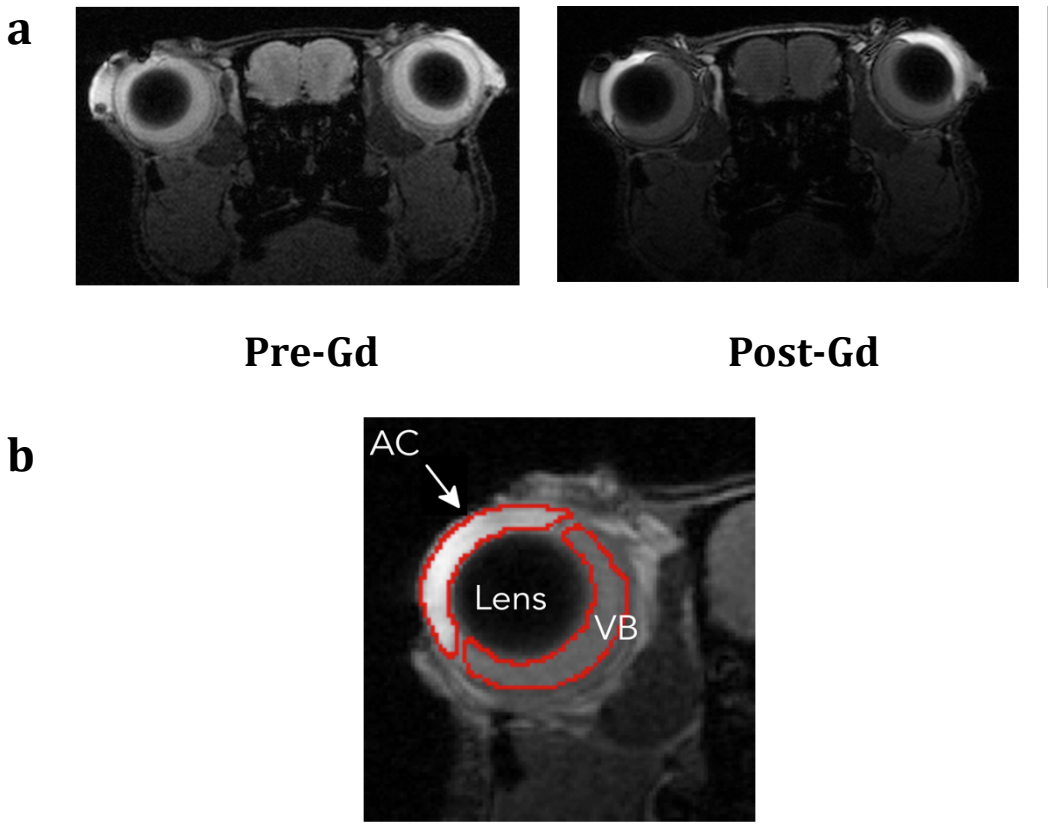

Fig. 4.1. Representative images of C57BL/6J ocular MRI scans.
(a) Representative images of C57Bl/6J mouse MRI scan prior to Gd-DTPA administration (pre-Gd), and post Gd-DTPA administration (post-Gd), note the signal enhancement of the AH. **(b)** Post-Gd image displaying relevant anatomy. AC = anterior chamber; VB = vitreous body. Red lines outline respective areas.

Next the dynamics of Gd-DTPA diffusion into the AH was examined (**5.37**). 3M C57BL/6J mice were intravenously injected with Gd-DTPA (Time = 0 min) and immediately after these animals were examined with MRI taking a scan every minute. In rabbit and human Gd-DTPA enters via the anterior protein pathway at the iris root (Kolodny et al. 1996; Bert et al. 2006). Similarly, in this study signal enhancement was first seen at the AC angle. 3-D rendered images of the T_1 scan were pseudo-coloured based on pixel intensity to more easily demonstrate differences in T_1 signal. In these images the signal enhancement of the AH by Gd-DTPA was first seen as a ring at the iridocorneal angle at T = 1 min. Over the course of the next 6 mins the contrast agent was seen to diffuse throughout the AC reaching a homogenous state (**Fig. 4.2a**). In the coronal 2-d versions of the T_1 scan there was bright signal enhancement at the iridocorneal angle immediately prior to Gd-DTPA administration, T = 0 min, with the centre of the AC displaying less signal. Over the course of 10 mins again the contrast agent was seen to diffuse to the AC centre (**Fig. 4.2b**). The mean signal intensity of the AC angle, AC centre and VB were measured and compared over time. The VB displayed no significant increase in signal over 30 mins with no evidence of Gd-DTPA entry (n = 4). The signal at the AC angle was immediately higher at T = 0 min and reached a max at T = 3 min before plateauing (n = 4). In the AC centre the signal was similar to the VB at T = 0 min before increasing and reaching a similar max as seen in the AC angle at T = 20, from where it plateaued for the remaining scan time (n = 4) (**Fig. 4.2c**). The ocular areas where signal intensity was measured are shown in (**Fig. 4.2d**). These results demonstrate that Gd-DTPA enters the mouse AH at the iridocorneal angle and not at the CB.

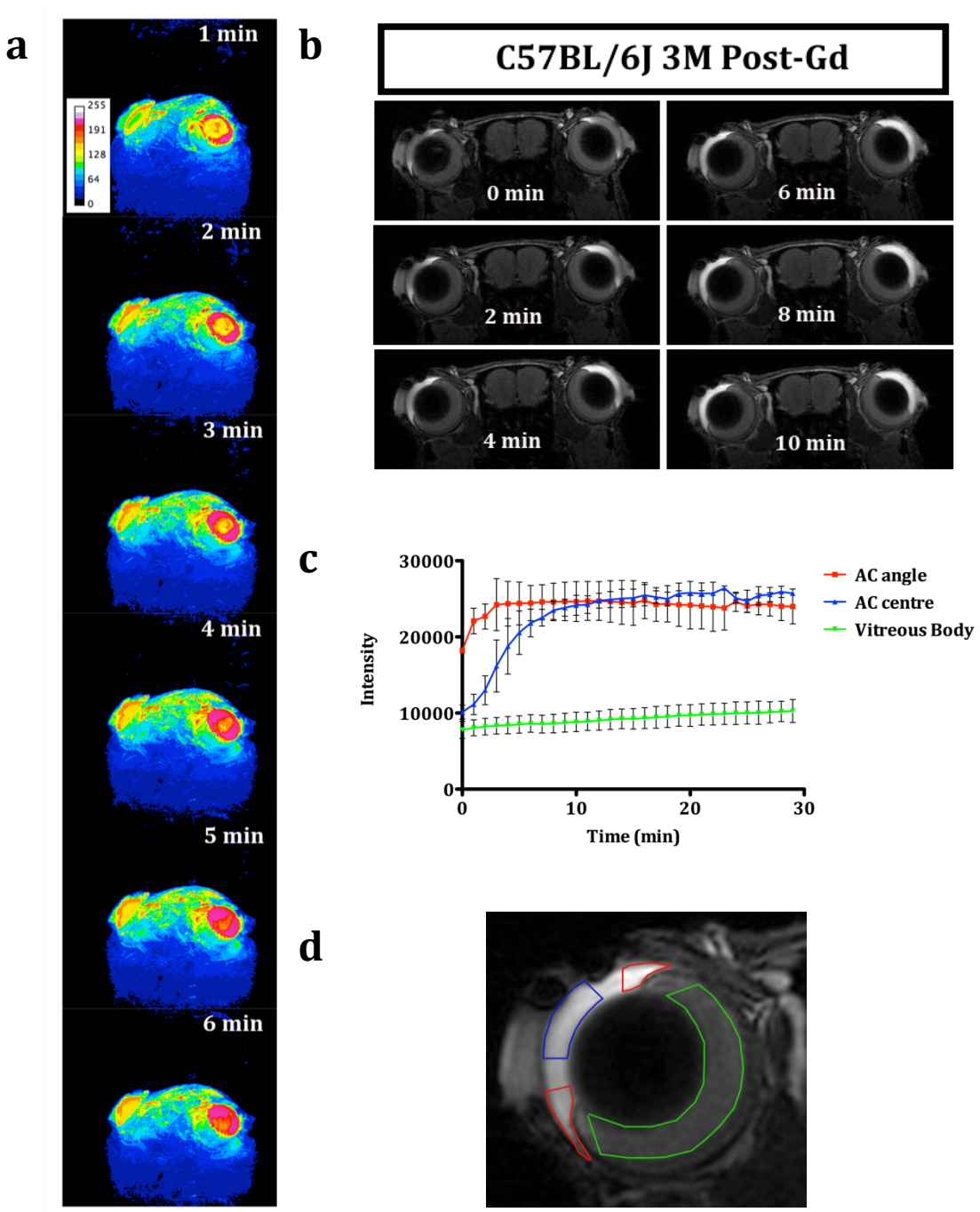

Fig. 4.2. Entry of Gd-DTPA into the AC via the anterior protein pathway.

(a) 3-d rendered image of Gd-DTPA entry into the AC over time, image is pseudo-coloured to represent pixel intensity with attached intensity scale in image = 1 min. **(b)** Representative image of T_1 MRI scan of a 3M C57BL/6J mouse demonstrating Gd-DTPA entry over time. **(c)** Pixel intensity in the AC angle, AC centre and VB over time after Gd-DTPA injection. **(d)** Representation of areas used for pixel intensity measurement. Red = AC angle; Blue = AC centre; Green = Vitreous body. In all figures Time = time after Gd-DTPA injection with injection at 0 min.

Gd-MRI used to assess AH dynamics

The use of Gd-MRI to track changes in mouse AH flow dynamics as previously demonstrated in rats (Ho et al. 2014) was assessed. Gadolinium tracer enters at the iridocorneal angle but increases in AH flow will result in more tracer drainage and a reduction in signal enhancement. For this study the prostaglandin latanoprost was used to increase AH drainage (Tam et al. 2013). Each animal had one eye pre-treated with latanoprost eye-drops, whereas the contralateral control eye received saline eye-drops. The gadolinium tracer gadobenate dimeglumine (Gd-BOPTA) was used for this study, due to a lack of Gd-DTPA at this time. However, this contrast agent retains similar properties; it only enhances the AH signal (though not as strongly as Gd-DTPA) and also enters via the anterior pathway, as is demonstrated in (**Fig. 4.3a**). Signal enhancement was seen to begin at the iridocorneal angle T = 1 min and diffuse throughout the AC over the course of 10 mins. The percentage change in intensity, from T = 0 min, was compared between the latanoprost treated and control eyes. Signal enhancement reached a max at 10 min after contrast agent administration, and so the rate of signal enhancement was measured over the initial 10 min in the AC centre. The peak intensity reached over 60 min of scanning was also measured. Eyes treated with latanoprost had significantly lower AH signal enhancement with an average rate of signal increase of 0.33 [-0.23, 0.89] %/min compared to 1.60 [0.47, 2.74] %/min in saline treated eyes (n = 4, p = 0.018) (**Fig. 4.3b**). The average peak intensity was also reduced in the latanoprost treated eyes with a mean increase in signal enhancement of 17.23 [-2.672, 37.13] % and 31.21 [1.536, 60.88] % in the latanoprost and control treated eyes respectively (n = 4, p = 0.26) (**Fig. 4.3c**). Over the course of an hour of scanning post Gd-BOPTA administration the latanoprost eyes displayed a slower increase in AH signal enhancement, which was consistently lower throughout. At ~T = 30 min the signal in both groups began to decrease until T = 60 min where the latanoprost signal reached baseline compared to the control eyes, which still showed contrast enhancement (**Fig. 4.3d**). This demonstrated that Gd-MRI can be used to detect changes in AH flow caused by the glaucoma medication latanoprost.

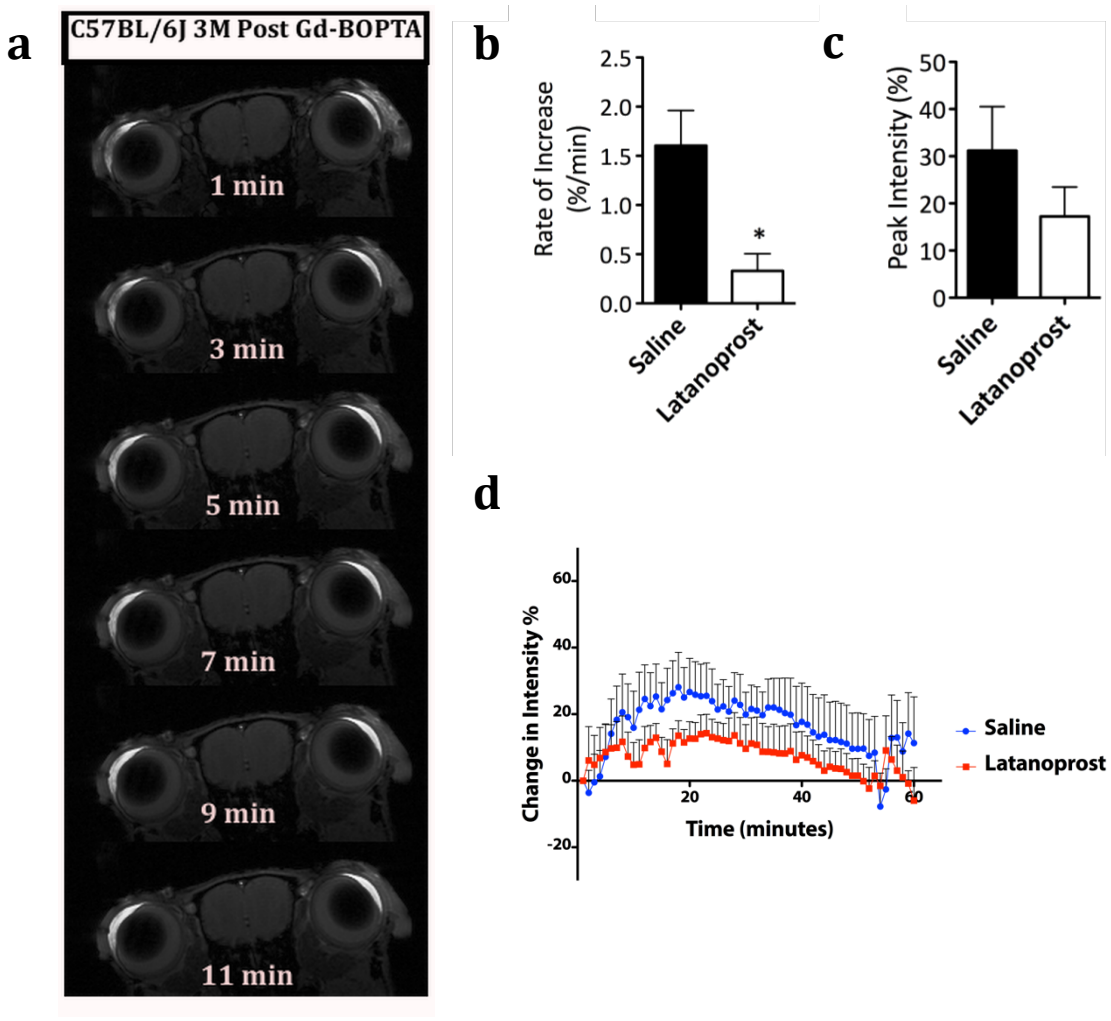

Fig. 4.3. Latanoprosts effect on Gd-BOPTA accumulation in the mouse AC. **(a)** T_1 MRI scan of C57BL/6J 3M mice after Gd-BOPTA administration T = 0 min. Left eye treated with latanoprost, right eye saline. **(b)** Mean rate of signal enhancement over the first 10 min post Gd-BOPTA administration in latanoprost treated contralateral control eyes. Relative AH signal enhancement is calculated with T = 0 min as baseline. **(c)** Mean AH peak signal enhancement reached over the course of 60 min in latanoprost treated and contralateral control eyes. **(d)** Averaged change in AH signal enhancement plotted over the course of 60 min. All times are relative to T = 0 min for Gd-BOPTA administration. Error bars display s.e.m. * = $p < 0.05$.

Age-related changes in the DBA/2J mouse

Next, age-related changes in morphology and AH dynamics in the DBA/2J mouse model of glaucoma were analysed using Gd-MRI. 3M, 6M, and 9M DBA/2J animals were compared with age-matched C57BL/6J controls. **Fig. 4.4a** displays representative T_1 images of these animals. The morphological aspects of the eyes of each animal were measured from the T_1 images using ImageJ. There were age-related increases in AC area, AC depth, AC signal intensity and eye size in DBA/2J mice as compared to age-matched C57BL/6 mice. Signal intensity, pre-contrast enhancement, of the AC and overall eye size was significantly increased in DBA/2J at 9M in comparison to age-matched C57BL/6 controls (AC signal intensity: 44. 1% increase (n = 3, p = <0. 001); eye size: 9. 0% increase (n = 3, *p* = <0. 001). Quantification of AC area, and AC depth showed increases that were significant at 6M in DBA/2J mice when compared to age-matched C57BL/6 mice. Mean increases were as follows, AC area: 12. 9% increase (n = 3, *p* = <0.05); AC depth: 24. 3% increase, (n = 3, *p* = <0. 01). These differences were even more pronounced at 9M when compared to age-matched C57BL/6 mice. The mean differences were as follows: AC area: 17. 8% increase (n = 3, *p* = <0. 001); AC depth: 49. 6% increase (n = 3, *p* = <0. 001). Measurements of other ocular components – VB area, VB signal intensity, VB depth and lens size – showed no significant differences with age or between DBA/2J and C57BL/6 strains (**Fig. 4.4b**). These data clearly demonstrated that the AC of the DBA/2J animals increased in size with age, thus the 3D volume of the ACs were assessed. The mean volume for 3M C57BL/6J AC of 1.79 [1.48, 2.10] mm^3 did not significantly change with age. The mean 3M DBA/2J AC volume (2.04 [1.54, 2.54] mm^3) was not significantly different from WT control, however by 9M the DBA/2J AC volume was significantly increased compared to control, with a mean difference in AC volume of 98.6% (n = 6, *p* = <0.001) and a mean volume of 3.05 [2.012, 4.094] mm^3 (**Fig. 4.4c**).

DBA/2J animals have age-related increases in IOP which are mirrored by decreases in outflow facility. C57BL/6J animals had no age related increases in IOP with average IOPs of 13.13 [11.46, 14.79] mmHg, 14.83 [13.57, 16.10] mmHg, and 10.67 [9.874, 11.46] mmHg; at 3M, 6M, and 9M respectively. In comparison DBA/2J mice had IOP similar to C57BL/6J at 3M with increases at 6M of 80.27% (n = 8, *p* = <0.05) and at 9M of 39.02% (n = 6, *p* = <0.001) relative to young DBA/2J

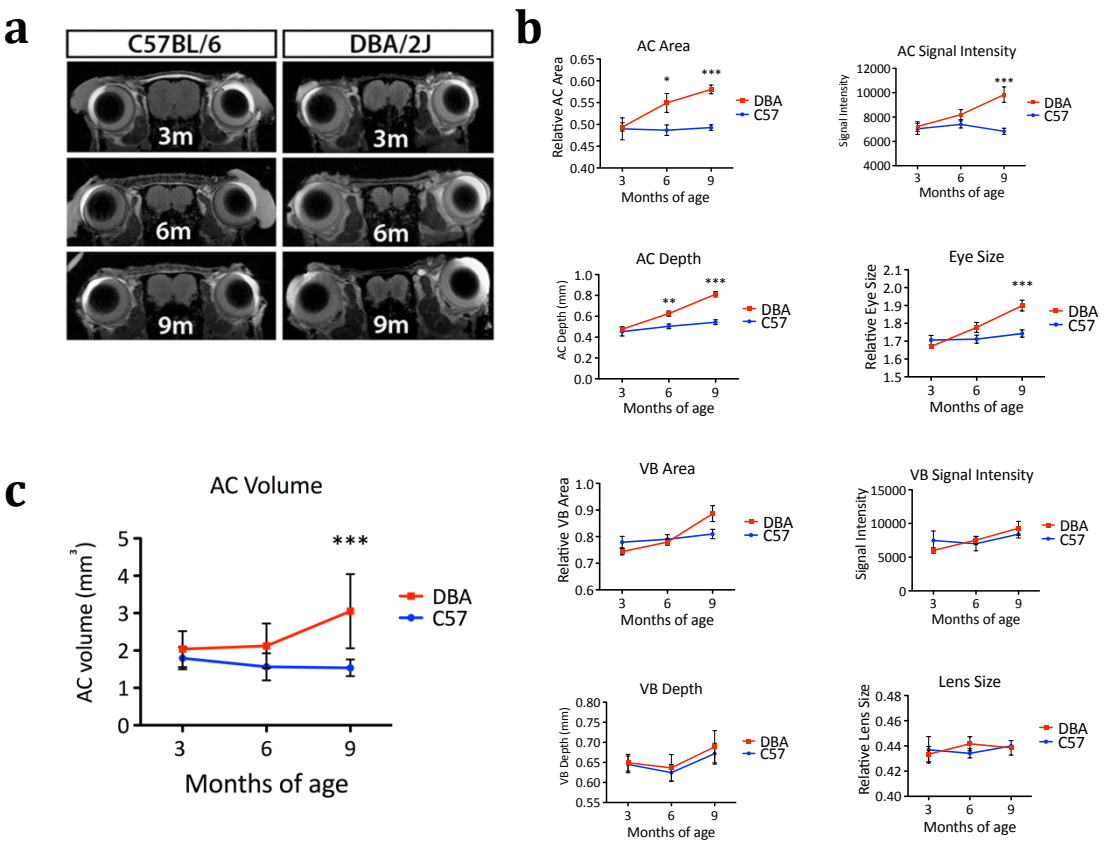

Fig. 4.4. Morphological analysis of eye anatomy in C57BL/6J and DBA/2J mice using T1-weighted MRI.

(a) Representative MR images of eye morphology in C57BL/6J and DBA/2J mice at 3, 6 and 9 months of age. **(b)** Quantification of area, depth and signal intensity of AC and VB, along with lens and eye size in C57BL/6J and DBA/2J mice at various ages. Age-related increases in AC area, AC signal intensity, AC depth and eye size were observed in DBA/2J mice. **(c)** Quantification of AC volume in C57BL/6J and DBA/2J mice at various ages. One-way ANOVA followed by Bonferroni's post hoc test for multiple comparisons was used to test significance, with 95% confidence interval, n = 3-5 separate animals per age and strain. Symbols *, **, ***, denote *p*-values of <0.05, <0.01, and <0.001 respectively. Data are means ± s. e. m.

mice. Mean IOPs of 11.25 [10.48, 12.02] mmHg , 20.28 [16.97, 23.59] mmHg, and 15.64 [13.76, 17.51] mmHg were measured at 3M, 6M, and 9M respectively (**Fig. 4.5a**). Next the facility, or pressure dependent AH outflow, was compared between 9M and 3M DBA/2J animals. Eyes were enucleated and perfused in pairs over incrementing steps in applied pressure, this was plotted and the facility at 8 mmHg interpolated. Aged animals had significantly lower facility with a decrease of -46 [-67, -12] % compared to young DBA/2J animals (3M n = 7; 9M n = 6, $p = 0.019$). Young 3M DBA/2J animals had an average facility of 11.228 ± 2.521 nl/mmHg/min, whereas aged 9M animals had an average facility of 6.072 ± 1.974 nl/mmHg/min (**Fig. 4.5b**). Following Gd-DTPA administration, T1-weighted MRI showed a reduced signal enhancement of the AC in 9M DBA/2J mice compared to age-matched C57BL/6 animals: sample images are shown in **Fig. 4.6a**. Relative change in signal intensity, compared to T = 0 min baseline, in the first 10 mins post-Gd-DTPA injection showed that signal enhancement was lowest in 6M and 9M DBA/2J mice (**Fig. 4.6b**). The extent of AC signal enhancement in 3 month-old DBA/2J animals was comparable to 3M and 9M C57BL/6 mice. Mean rates of C57BL/6J 3M 10.62 [-1.97, 23.22] %/min, 9M 14.02 [4.427, 23.62] %/min, and DBA/2J 3M 9.58 [-6.85, 26.01] %/min. Furthermore, **Fig. 4.6c** illustrates that the rate of Gd-DTPA accumulation in the AC over the initial 10 minutes was significantly lower in the DBA/2J 9M ($p = 0.003$) and DBA/2J 6M ($p = 0.018$) eyes, mean rate: 3.69 [2.19, 5.19] %/min, and 3.271 [0.16, 6.38] %/min, respectively, relative to C57BL/6J 9M controls 14.02 [4.427, 23.62] %/min (C57 n = 5; DBA 6M n = 5; DBA 9M n = 8, whereas no significant difference was seen between the 3M DBA/2J and age matched C57BL/6J mice or between 3M and 9M DBA/2J mice. Similarly the peak percentage intensity in Gd-DTPA signal enhancement over the course of 60 min was lowest in 6M and 9M DBA/2J mice, although statistical significance was not reached (**Fig. 4.6d**).

Interestingly, T_1-weighted imaging following Gd-DTPA administration also revealed significant leakage of Gd-DTPA into the VB of 9M DBA/2J mice but not age-matched C57BL/6 animals (**Fig. 4.7a**). At early stages post-Gd-DTPA injection, the contrast agent appeared to be emanating from the ciliary body and diffusing toward the posterior VB, indicating a breakdown in blood-aqueous barrier integrity in the non-pigmented epithelium of the ciliary body. Analysis of

percentage change in Gd-DTPA intensity using a region of interest in the VB showed prolonged leakage of Gd-DTPA in the VB for as long as 60 mins post-Gd-DTPA injection (**Fig. 4.7b**). All methods used in this study are outlined in **Chapter 5**.

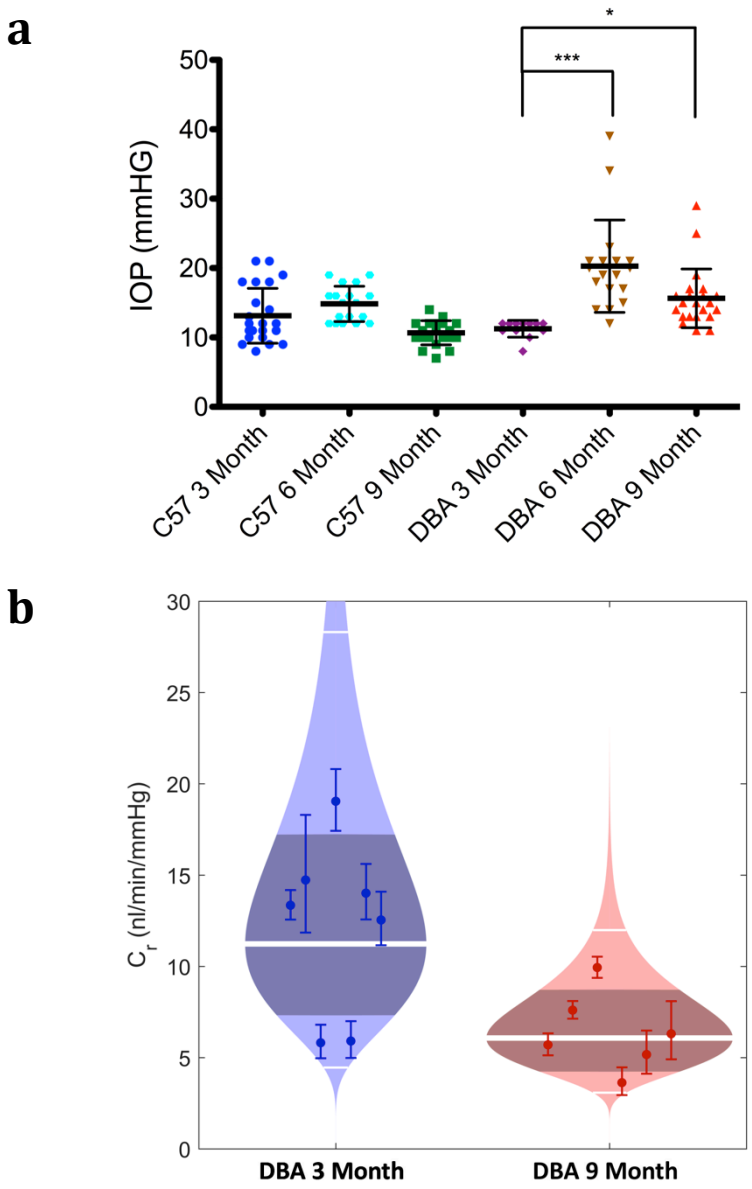

Fig. 4.5. Age-related changes in IOP and facility in the DBA/2J mouse.

(a) Averaged IOPs of C57BL/6J and DBA/2J animals at 3, 6, and 9 months of age. Each individual point is an IOP reading for an eye. Graph displays means with 95% confidence intervals. **(b)** 'Cello' plot depicting individual outflow facility values for eyes at 8 mmHg (C_r) and statistical distribution of both DBA/2J 3M and DBA/2J 9M groups. Each point represents a single eye with 95% CI on C_r. Log normal distribution is shown, with the central white band showing the geometric mean and the thinner white bands showing two geometric standard deviations from the mean. The shaded region represents the 95% CI on the mean. IOPs are compared using non-parametric One-way ANOVA with Dunn's multiple comparison test. Symbols *, and *** represent *p*-values of <0.05, and <0.001 respectively.

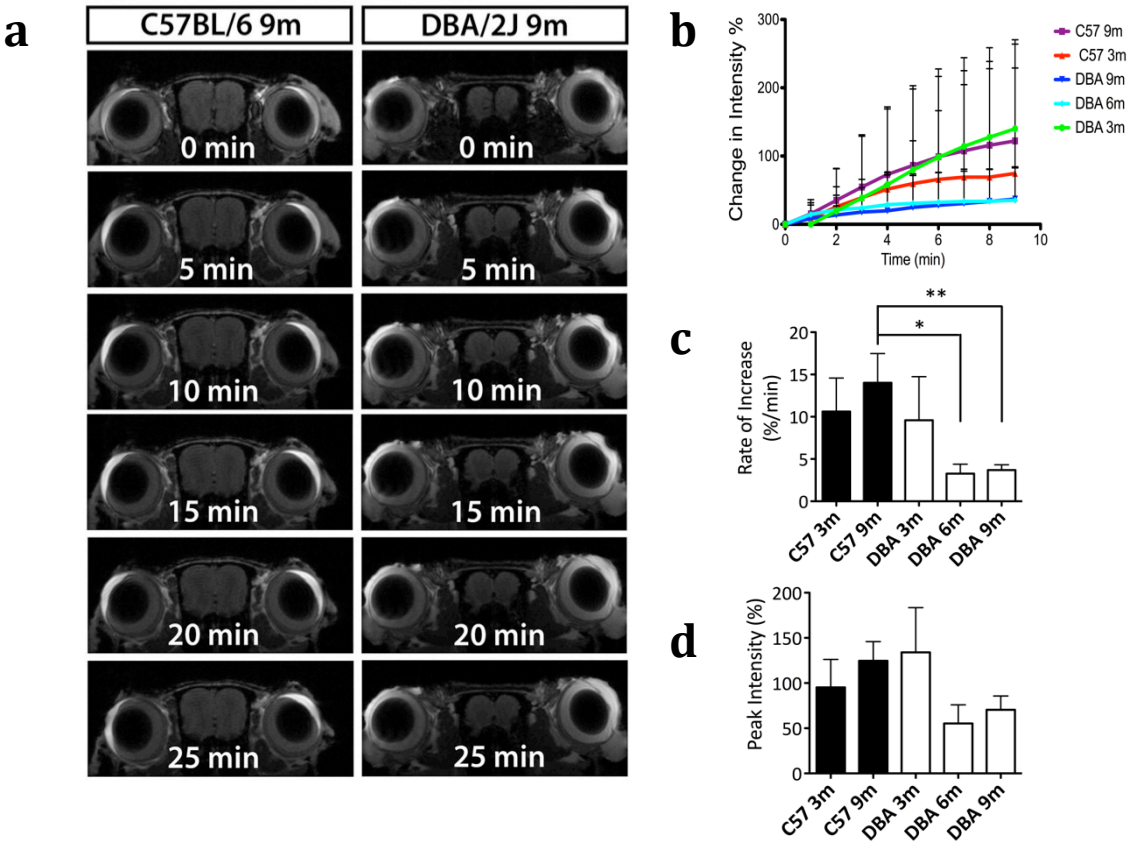

Fig. 4.6. Assessing aqueous solute flow dynamics with age in the DBA/2J model of pigmentary glaucoma using T1-weighted Gd-DTPA MRI.
(a) Representative serial T1-weighted MR images of Gd-DTPA enhancement in C57BL/6 and DBA/2J mouse eyes at 9 months of age. **(b)** Average percentage change in intensity of AC in the first 10 mins post-Gd-DTPA injection. All change is relative to T = 0 min. Decreased levels of Gd-DTPA signal enhancement in the AC were observed in 6M and 9M DBA/2J mice compared to 3M DBA/2J mice and C57BL/6 mice at all ages. **(c)** The rate of Gd-DTPA signal increase over the initial 10 minutes was lowest in 6M and 9M DBA/2J mice compared to 3M DBA/2J mice and C57BL/6 mice at all ages. **(d)** Peak Gd-DTPA signal enhancement in the AC was lowest in 6M and 9M DBA/2J mice. All graphs display mean and s.e.m. Symbols *, and ** denote *p*-valiues of <0.05, and <0.01 respectively.

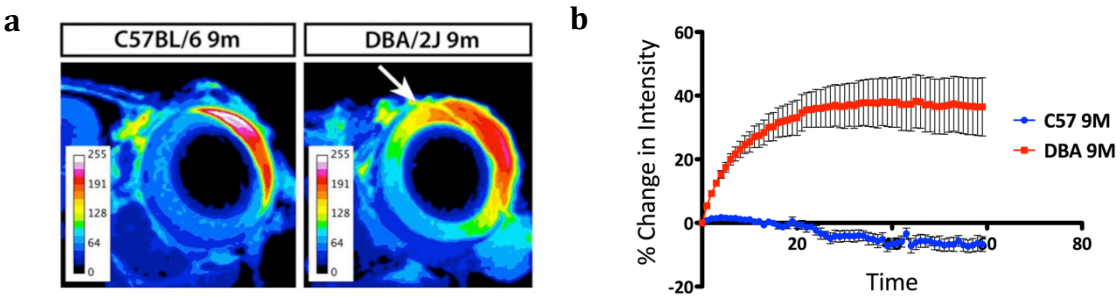

Fig. 4.7. Leakage of Gd-DTPA into the vitreous body in aged DBA/2J mice. **(a)** Pseudo-colored T1-weighted Gd-DTPA-enhanced MR images of single eyes from 9M C57BL/6 and DBA/2J mice demonstrating leakage of Gd-DTPA into the vitreous body of DBA/2J eyes (white arrow). **(b)** Average percentage change in intensity in a region of interest in the vitreous body of 9M DBA/2J and 9M C57BL/6J mouse eyes. Increased Gd-DTPA enhancement in the vitreous body of 9M DBA/2J mice indicates reduced AC penetration and leakage back into the vitreous body. Graph displays means and s.e.m.

Discussion

In this study, dynamic contrast-enhanced MRI was used to investigate aqueous humor flow dynamics and blood-aqueous barrier permeability in the DBA/2J mouse model of pigmentary glaucoma and to identify age-related changes in these phenotypes. The MR images were taken using a rodent specific 7 Tesla MRI machine, the small head coil and high power allowed very high-resolution images to be taken in a small timeframe. Coronal scans comprising of 25-slices were taken over 1 minute, allowing high resolution imaging of temporal changes and allowing minute by minute tracking of Gd-DTPA entry into the AC. Gd-DTPA enhancement was first seen at the iridocorneal angle gradually migrating toward the AC centre, with Gd-DTPA enhancement consistent throughout the AC at 10 min post administration. This is a demonstration of a separate anterior solute pathway to the AH for mice. Previously Gd-MRI has been used to support the presence of an anterior diffusional pathway for solutes in both rabbit and human eyes (Kolodny et al. 1996; Bert et al. 2006). No direct comparisons can be made between this current study and those mentioned due to variance in MRI machine, T_1 relaxation times and contrast agents used. However, in the rabbit, the time taken for consistent signal enhancement throughout the AC was far longer than seen in this study, around 30 minutes relative to 10 minutes seen in the mouse. As most mammals have similar AH turnover rates, this may be due to AH mixing differences between species mediated by the reduced AC volume (Aihara et al. 2003; Modarreszadeh et al. 2014). This demonstration of an anterior pathway for gadolinium contrast agent entry allows for assessment of AH dynamics.

The anterior protein pathway is not intrinsically linked to AH production, this can be seen in the daily cyclical changes in AH protein levels in both nocturnal and diurnal species. AH protein concentration levels are highest at times when AH secretion is low, usually during sleep (Freddo 2013; Zhou & Liu 2006). Similarly, use of the glaucoma drug timolol, reduces AH production from the CB and was found to increase AH protein concentration in glaucoma patients (Stur et al. 1986). Therefore, it was hypothesized that using a treatment that increased AH outflow the gadolinium contrast enhancement in the AC would be decreased. Here, Gd-MRI was used to assess differences in AH tracer accumulation in the AC of mouse eyes treated with latanoporst, which increases AH outflow. Gd-DTPA and Gd-BOPTA

were both found to cause consistent signal enhancement in the AC centre in the first 10 minutes post administration in control WT animals. Therefore, the rate of signal enhancement over the first 10 minutes was compared between treated and contralateral control eyes. Topical application of latanoprost in C57BL/6 mice resulted in reduced rates of Gd-BOPTA signal enhancement and decreased peak Gd-BOPTA intensity in the AC, indicative of a change of Gd-accumulation in the AC, indicative of a change of Gd-accumulation in the ACs of latanoprost-treated eyes. This clearance of Gd-BOPTA from the AC in latanoprost-treated eyes in the first 10 mins after Gd-BOPTA injection also demonstrates the effect of IOP-lowering agents on solute entry into the AH. This demonstrates the capability of Gd-MRI to assess differences in AH dynamics between experimental and control contralateral eyes.

Iris atrophy and pigment dispersion have previously been associated with elevated IOP and degeneration of retinal ganglion cells in the DBA/2J glaucoma mouse model (John et al. 1998; Saleh et al. 2007; Inman et al. 2006; Jakobs et al. 2005; Schuettauf et al. 2002). In this study the 6 month IOP group is non-significantly elevated relative to the 9 month group, this is most likely due to the high variation of IOP between eyes in these mice and the low numbers in this study. Previous work profiling the change of IOP in DBA/2J mice with age examined 68 and 169 eyes in the 6 month and 9 month groups respectively, compared with 6 and 10 eyes in those groups in this study (Libby et al. 2005). Manganese-enhanced MRI has previously shown impaired intraretinal uptake of manganese in aged DBA/2J mice (Calkins et al. 2008). In the present study, age-relate changes in morphology and AH dynamics were measured and compared between the DBA/2J mouse and age-matched C57BL/6J controls. Analysis of Gd-MR images demonstrated that AC depth and volume increased substantially with age in DBA/2J animals. This finding is in agreement with previous reports of age-associated increases in AC depth measured using ultrasound (John et al. 1998), slit-lamp (Libby et al. 2005) and whole-eye optical coherence tomography (Chou et al. 2011). Indeed, this clear “bulging” of the AC observed in the MR images correlated with increased AC area, AC volume, AC signal intensity and eye size in DBA/2J mice. It was observed that Gd-accumulation is altered in the AC of the aged DBA/2J mouse compared to age matched C57BL/6 mice. Reduced AC signal enhancement was observed in aged DBA/2J mice at 6-9M, in addition to lower

rates of Gd-DTPA increase and lower Gd-DTPA peak intensities compared to age-matched controls and young DBA/2J mice. However, a reduction in Gd-DTPA signal enhancement is unexpected as the DBA/2J mouse has age-related increase in IOP, and outflow facility is decreased in aged animals compared to young DBA/2J mice, leading to the assumption that the aged animals would have increased Gd-DTPA enhancement in the AH. The observed result may be partially due to the increased AC volume in the aged DBA/2J mice, which would further dilute the incoming Gd-DTPA. This would not account for the large difference observed, and in fact these aged mice were found to have another pathology apart from decreased AH flow, breakdown of the BAB. The posterior chamber of these animals displayed signal enhancement emanating from the ciliary body. This was not present in the C57L/6J animals and supports previous findings that Gd-DTPA does not enter the posterior chamber unless in the case of iBRB disruption (Campbell et al. 2010). In the aged DBA/2J this is not the case with signal enhancement increasing until 20 minutes post Gd-DTPA administration in the VB. This Gd-DTPA leakage into the posterior chamber offers an explanation to the reduced rate of signal enhancement in the DBA/2J anterior chamber and also demonstrates disruption of the BAB allowing diffusion of a 938 Da tracer. It should be pointed out that this observation is not in conflict with the reduction in outflow facility observed in aged DBA/2J mice. Gd-MRI tracks AH flow dynamics as it enters the AC, whereas outflow facility is calculated in *ex vivo* eyes with perfusate entering via AC cannula. Therefore, changes in BAB integrity do not affect outflow facility measured using the iPerfusion system.

The use of dynamic contrast-enhanced MRI to assess flow dynamics of Gd-DTPA from systemic circulation to the AC could show utility in advancing the development of novel IOP-lowering compounds for the treatment of POAG and pseudoexfoliation glaucoma, allowing *in vivo* assessment of AH dynamics with the use of a contralateral eye as control. The dynamic AH flow changes observed in this study in both C57BL/6 and DBA/2J mice may provide important information to determine the effectiveness of long-term surgical treatments. Recently, the use of glaucoma drainage devices for both primary and refractory glaucoma such as the Baerveldt, the Ahmed or more recently the Alxon EX-PRESS miniature glaucoma shunt has dramatically increased. These surgical implants can have

serious complications, including hypotony or tube obstruction that can lead to subconjunctival fibrosis and tube failure (Giovingo 2014). As any intervention requires surgery, Gd-DTPA MRI offers a method to directly monitor an implant's effect on AH dynamics allowing diagnosis of tube obstruction or tube damage prior to any further surgical intervention. This technique may also have a role in the evaluation of novel surgical implants such as the EX-PRESS, which has been recently approved for use in patients with uncontrolled glaucoma, allowing for a comparison of this technique's effect on AH dynamics with more traditional trabeculectomies (Chan & Netland 2015). In addition, Gd-enhanced MRI may be used to track dynamic changes in glaucomatous eyes and provide a better understanding of the mechanisms involved in systemic delivery of drugs into the AC.

Statement of collaboration

Christian Kerskens made the MRI scan protocols. Lawrence Tam and James Keaney assisted in mouse preparation and tail vein cannulation. James Keaney collaborated with the assessment of DBA/2J morphology.

Chapter 5
Materials and Methods

Chapter 5: Materials and Methods

5.1 Cell Culture

Human SCEC were isolated, cultured and fully characterized according to previous protocols.(Stamer et al. 1998; Perkumas & Stamer 2012; Heimark et al. 2002) Briefly, cells were isolated from the SC lumen of human donor eyes using a cannulation technique. Isolated cells were tested for positive expression of VE-cadherin and fibulin-2, but absence of myocilin induction upon treatment with 100 nM dexamethasone for 5 days. Confluent cells displayed a characteristic linear fusiform morphology, were contact inhibited and generated a net transendothelial electrical resistance greater than 10 $\Omega.cm^2$. SCEC strains used were SC82 and SC83 between passages 2 and 7. Dulbecco's modified eagle medium (Gibco, Life Sciences) 1% Pen/Strep/glutamine (Gibco, Life Sciences) and 10% fetal bovine serum (FBS) performance plus (Gibco, Life Sciences) was used as culture media in a 5% CO_2 incubator at 37°C. Cells were transferred to a media containing only 1% FBS a week prior to protein treatment. Cells were passaged with trypsin-EDTA (Gibco-BRL) and seeded into 12 well or 24 well transwell plates (Costar, Corning). Human trabecular meshwork (HTM) cells were isolated and fully characterized according to the procedures described in.(Stamer et al. 1995; Stamer et al. 1996; Stamer & Clark 2017) TM tissue is removed from human donor eyes using a blunt dissection technique, and TM cells are dissociated from the tissue using a collagenase digestion protocol as previously described.(Stamer et al. 1995) Isolated cells are characterized by their dramatic induction of myocilin protein following treatment with dexamethasone (100 nM) for 5 days as detailed before.(Stamer et al. 1998)

5.2 Animals

Animals and procedures used in this study were carried out in accordance with regulations set out by The Health Products Regulatory Authority (HPRA), responsible for the correct implementation of EU directive 2010/63/EU. Wild-type C57BL/6 mice were sourced from Jackson Laboratories and bred on-site in the Smurfit Institute of Genetics in Trinity College Dublin (TCD). DBA/2J mice were

obtained from Harlan. Animals were housed under a 12-hour light–dark cycle and were provided unrestricted access to food and water. Animals were bred and housed in specific-pathogen-free environments in University of Dublin, Trinity College and all injections and IOP measurements complied with the HPRA project authorisation number AE19136/P017.

5.3 Human tight junction PCR array

The human TJ RT^2 Profiler PCR array (PAHS-143ZA, Qiagen) was used to profile the expression of 84 key genes encoding proteins that form selective barriers between epithelial and endothelial cells to regulate size selectivity, polarity, proliferation and differentiation. Total RNA was extracted from four different human SC cell strains (SC65, 68, 76 and 77) at passages 3 to 5 using RNEasy Mini Kit (Qiagen) according to manufacturer's protocol. Genomic DNA contamination was eliminated by DNase treatment. Total RNA was reverse-transcribed into cDNA using RT^2 First Strand Kit (Qiagen). The Threshold cycle (Ct) values of different passage numbers from each SCEC strain were determined and averaged using ABI Prism 7700 Sequence Detector. The mean normalized expression ($2^{-\Delta Ct}$) of genes encoding claudin and adhesion junctional proteins was determined and analyzed using the online Qiagen RT^2 Profiler PCR Array Data Analysis software. Normalized gene expression was calculated by using the equation: $2^{-\Delta Ct} = 2^{-[Ct(\text{gene of interest})-Ct(\text{Housekeeping genes})]}$. Normalization was carried out with five housekeeping genes (*ACTB, B2M, GAPDH, HPRT1 and RPLP0*) included in the PCR array. For the comparison of junctional proteins between healthy and glaucomatous SCEC, total RNA was extracted from 3 different healthy (SC68, 76 and 77 at passage 3) and 2 glaucomatous (SC57g and SC 63g/64g at passage 3) SCEC strains, and profiled using the human TJ RT^2 PCR Profiler PCR array. The $2^{-\Delta\Delta CT} = 2^{-\Delta Ct\ \text{treated}} / 2^{-\Delta Ct\ \text{control}}$ method was used to calculate fold changes for each gene as difference in gene expression. A positive value indicates gene up-regulation and a negative value indicates gene down-regulation.

5.4 Mouse tight junction PCR array

Under microscopic view, the anterior segments from wild type mice were isolated by making an incision at the limbus, circumferential cuts were then made anterior

of the limbus removing the lens and posterior segment. The cornea was then removed by cutting circumferentially anterior to the ciliary body. The outflow tissue was then isolated using a small surgical blade to cut along the pigmented line of the scleral spur below the TM. Forceps were used to hold the TM and pull it free along Schwalbe's line. The outflow tissue was placed in RNA*later*® solution prior to RNA extraction. Total RNA was extracted from mouse outflow tissues using RNEasy Mini Kit (Qiagen) according to manufacturer's protocol. Genomic DNA contamination was eliminated by DNase treatment Total RNA was reverse-transcribed into cDNA by RT^2 First Strand Kit (Qiagen). Mouse TJ RT^2 Profiler PCR Array expression profile was used to analyse TJ transcripts (PAMM-143ZA, Qiagen). PCR was performed on ABI Prism 7700 Sequence Detector. The threshold cycle (C_t) of each gene was determined and analysed by RT^2 Profiler PCR Array Data Analysis software provided by Qiagen. Normalised gene expression was calculated by using the equation: $2^{\Delta Ct} = 2^{-[Ct(\text{gene of interest})-Ct(\text{Housekeeping genes})]}$. Normalisation was carried out with five housekeeping genes included in the PCR array.

5.5 siRNAs

The following *in vivo* predesigned siRNAs used in this study were synthesized by Ambion and reconstituted as per manufacturer's protocol, with siRNA identification numbers are as follows: human claudin-11 siRNA (ID number: s9925) sense, 5'- GUCAUUUACUUGUACGAGAtt and antisense, 5'- UCUCGUACAAGUAAAUGACct; human ZO-1 siRNA (ID number: s14156) sense, 5'- CGAUCUCAUAAACUUCGUAtt and antisense 5'- UACGAAGUUUAUGAGAUCGct; human MARVELD2 siRNA (ID number: s45794) sense 5'- ACGAGAGAAUUUCAAGAAUtt and antisense 5'- AUUCUUGAAAUUCUCUCGUtt.

In the DBA/2J study siRNA sequences and in vivo siRNA administration Claudin-5 and occludin siRNAs were obtained from Dharmacon, and the sequences used were as follows: claudin-5 siRNA sense, 5′-CGUUGGAAAUUCUGGGUCUUU-3′, and antisense, 5′-AGACCCAGAAUUUCCAACGUU-3′; occludin siRNA sense, 5′-GAUAUUACUUGAUCGUGAUUU-3′, and antisense, 5′-AUCACGAUCAAGUAAUAUCUU-3′. Nontargeting negative control siRNA (Silencer) were obtained from Ambion. Preparation and administration of siRNA in vivo were

performed as described previously (Nitta et al. 2003). Briefly, 20 mg of siRNA was combined with 6.4 ml of in vivo-jetPEI (Polyplus Transfection) in a 10% glucose solution. The solution was mixed and incubated for 15 min at room temperature to allow the siRNA–in vivo-jetPEI complexes to form. A final volume of 400 ml was slowly injected into the mouse tail vein.

5.6 Retinal dissection

To compare Aβ(1-40) levels and tight junction protein levels in siRNA treated 9M DBA/2J mice the retina was dissected. Mice were sacrificed by cervical dislocation and the eyes enucleated. Immediately post enucleation the eye was dissected along the limbus and he anterior section was discarded. The neural retina was then removed using blunt forceps and then placed in RIPA protein lysis buffer for Western analysis, or cold TBS for Aβ (1-40) ELISA analysis.

5.7 Western Blotting: Retinal lysates

Enucleated retinas were placed in RIPA buffer containing (10mM Tris-Cl, 1mM EDTA, 1% Triton X-100, 0.1% sodium deoxycholate, 0.1% SDS, 140mM NaCl and 1X protease inhibitor cocktail (Roche)). The homogenate was centrifuged at 10,000 r.p.m. (IEC Micromax microcentrifuge, 851 rotor) at 4°C for 20 min and the supernatant was stored at −80°C. . Protein samples were separated by electrophoresis on 10% SDS–PAGE under reducing conditions and electro-transferred to PVDF membranes. After blocking with 5% blotting grade blocker non-fat dry milk in TBS for 1 h at room temperature, membranes were incubated overnight at 4^{o}C with the following Rabbit polyclonal primary antibodies: claudin-5 (1:500; 34-1600, Invitrogen) and occludin (1:500; 71-1500, Invitrogen). Blots were washed with TBS and incubated with horse radish peroxidase-conjugated polyclonal rabbit IgG secondary antibody (1:4000; A6154, Sigma). The blots were developed using enhanced chemiluminescent kit (Pierce Chemical Co.) and exposed to Fuji X-ray films in a dark-room facility. Each blot was stripped with Restore Western Blot Stripping Buffer (Pierce) and probed with rabbit polyclonal to β-actin (1:2000; ab8227, Abcam) for loading normalisation. Fold change in band intensity was represented in comparison to vehicle control treatments of PBS.

5.8 Immunohistochemistry: retina

Eyes were enucleated from 9M DBA/2J and C57BL/6J mice and placed in 4% paraformaldehyde (pH 7.4) overnight at 4°C on a rotating device. These were washed in PBS 3 times for 15 mins and then dissected. The eye was dissected along the limbus and the anterior segment discarded, the posterior section washed in PBS for 15 min and sequentially submerged in 10, 20 and 30% sucrose. Dissected posterior segments were then suspended in specimen blocks with OCT solution (Tissue-Tek) and frozen in a bath of isopropanol submerged in liquid nitrogen. Frozen posterior segments were sectioned using a cryostat (Leica CM 1900) to 12 µm thickness. Sections were collected on Polysine® slides (Menzel-Glazer). To detect Aβ, sections were blocked for 20 min at room temperature in PBS containing 5% goat serum and 0.1% Triton-X, and incubated with the primary antibody polyclonal rabbit anti-amyloid-β AW7 (1:1000) diluted in blocking buffer at 4°C in a humidity chamber overnight. Sections were then washed three times in PBS and incubated with Cy-3 labelled anti-rabbit IgG antibody at 1:500 (Abcam) for 1 h at 37°C in a humidity chamber. Following incubation, sections were washed with PBS and mounted with aqua-polymount (Polyscience) after nuclei-counterstaining with DAPI (0.2 µg/ml, in PBS). Anterior segments were visualized using a confocal microscope (Zeiss LSM 710).

5.9 Plasma/brain tissue isolation and ELISA

Blood was collected from the tail veins of 9M DBA/2J mice
with a 30-gauge needle and transferred to cold EDTA-coated tubes. Sampleswere centrifuged at 1500 rpmfor 10 min at 4°C, and the plasma phase was stored at −80°C. The mouse retina was homogenized in ice-cold TBS and centrifuged at 16,000g for 30 min at 4°C. Supernatants were collected for analysis of soluble Ab(1–40) levels, and pellets were resuspended in ice-cold guanidine buffer (5 M guanidine hydrochloride/50mMtris-Cl, pH 8.0) for analysis of insoluble Aβ (1–42) levels. Plasma and brain Aβ (1–40) levels were quantified using the Human Ab40 ELISA kit (Invitrogen). Absorbances were read at 450 nm on a spectrophotometer (Rosys 2010, Anthos), and Aβ (1-40) concentrations were determined from the Ab peptide standard curves after correcting for background absorbance and dilution factors. ELISA preparation and analysis were performed blind to treatment. The

ratio of retina Aβ (1-40) to plasma Aβ (1-40) were compared to NT-siRNA treated and claudin-5/occludin-siRNA treated 9M DBA/2J mice.

5.10 Immunohistochemistry: AC flatmount (PECAM-1)

For visualising the SC in mouse AC flatmounts, C57BL/6J mouse eyes were enucleated and placed in 4% paraformaldehyde (pH 7.4) overnight at 4°C on a rotating device. These were washed in PBS 3 times for 15 mins and then dissected. The eye was dissected along the limbus and the posterior chamber discarded. Using a micro-scissors the CB and iris are removed from the AC and four cuts are placed towards the centre to flatmount the anterior segment. This was then blocked in 5% Normal goat serum and 0.4% Triton X-100 for two hours at 4°C. These were washed with PBS and then incubated with primary polyclonal PECAM-1 rabbit primary antibody (1:50; ab28364, Abcam) diluted in blocking buffer overnight at 4°C. ACs were then washed three times in PBS and incubated with Cy-3 labelled anti-rabbit IgG antibody at 1:500 (Abcam) for overnight at 4°C. Following incubation, sections were washed with PBS and mounted with aqua-polymount (Polyscience) after nuclei-counterstaining with DAPI (0.2 µg/ml, in PBS). ACs were visualized using a confocal microscope (Zeiss LSM 710).

5.11 Mouse AC dissociation and FACS analysis

In an attempt to isolate the mouse SC inner wall cells mouse ACs were dissociated. C57BL/6J mouse eyes were enucleated and placed in PBS on ice. The eye was immediately dissected along the limbus and the posterior chamber discarded. The anterior chamber was then placed in a gentleMACS C tube (130-093-237, Miltenyi Biotec) containing DMEM containing 3 mg/ml collagenase I. These were incubated with gentle agitation on the MACS mix (Miltenyi Biotec) at 37°C. Every 30 mins the C tube was run on a dissociation program on gentleMACS dissociator (Miltenyi Biotec) which agitates the ACs to assist in dissociation. After 2 hours 0.5 ml of 0.25% trypsin-EDTA (T4049, Sigma) is added to the dissociation mix, the previous protocol was followed for a further 2 hours. The C tube is then centrifuged briefly and the supernatant is filtered through a 70 µm filter, which is washed with HBSS. The filtrate was centrifuged at 300 xG for 10 minutes at room temperature. The pellet was re-suspended in HBSS buffer with 2% Annexin binding buffer. 10% of

the sample is taken for the unstained sample. The remainder was incubated with VEGFR-3 conjugated to Alexa-Fluor 488 (FAB743G, R&D Systems) and PECAM-1 conjugated to Alexa-Fluor 647 (A14716, Life Technologies Biosciences) in the dark at room temperature for 30 mins. These samples were then analysed using FACSAria Fusion (BD Biosciences). The sample was stained with propidium iodide to detect dead cells. Cell clumps were excluded using a FSC-width vs FSC-area gate, granular material such as cell debris were excluded using a SSC-area vs SSC-width gate, and dead cells were excluded using a propidium iodide (PI) stain vs FSC-area gate. From the remaining population cells were separated into a double positive population, that had increased fluorescence at both 647 nm and 488 nm wavelength, and a double negative control population that had little fluorescence at these wavelengths.

5.12 Patient aqueous humour samples

Human aqueous was obtained from the Mater Misericordiae Hospital, Dublin, Ireland. Upon informed consent, AH samples were collected from PXG, POAG and control patients undergoing routine cataract surgery. The criteria for POAG was defined as the presence of glaucomatous optic disc cupping with associated visual field loss in an eye with a gonioscopically open anterior drainage channel, with an intraocular pressure > 21 mmHg.(Siah et al. 2015) The diagnosis of PXG was defined by the presence of characteristic pseudoexfoliative material on the iris or lens capsule and evidence of glaucoma.(Dervan et al. 2010) The samples were taken immediately prior to corneal incision at the start of the procedure using a method described previously.(Wallace et al. 2013) Human AH collection conformed to the WMA Declaration of Helsinki and was approved by the Mater Misericordiae University Hospital Research Ethics Committee. Human AH samples were added 1:10 to fresh media for cellular treatment for use with TEER and permeability assays as described below.

5.13 Cytokine array of AH samples

Aqueous humour samples were run on the Proteome Profiler™ Array (R&D Systems). Briefly, the samples were incubated with the detection media containing biotinylated antibodies to 36 different substrates. This solution was then

incubated with a nitrocellulose membrane containing the 36 capture antibodies. These were then washed before application of Streptavidin-HRP and then chemi-luminescent reagents. The membranes were exposed to RX-N medical X-ray film (Fujifilm) which were then scanned, the resultant images underwent densitometry analysis using ImageJ.

5.14 Transendothelial Electrical Resistance (TEER) measurement

Electrical resistance values were used as a representative of the integrity of the endothelial cell-cell junctions. Cells grown on Costar transwell-polyester membrane inserts with pore size of 0.4μm were treated with 10ng/ml human recombinant PAI-1 (and 20ng/ml human recombinant TGF-β2. Briefly, the basal well received fresh cell culture media and the apical layer received 100μl of treatment in fresh cell culture medium. TEER readings were measured before and 24 hours after treatment. An electrical probe was placed into both the apical and basal chambers of the transwells and a current was passed through the monolayers, reported as a resistance in $\Omega.cm^2$. A correction was applied for the surface area of the membrane (0.33 cm^2) and for the electrical resistance of the membrane (blank transwell).

5.15 Permeability assessment by FITC-Dextran flux

The extent of monolayer permeability was assessed by the basal to apical movement of a tracer molecule through the monolayer. Measures of permeability were taken 24h after treatment immediately after TEER values, keeping experimental set-up identical to that of TEER readings. The permeability protocol was repeated as described in.(Keaney et al. 2015) A 70 kDa fluorescein isothiocyanate (FITC)-conjugated dextran (Sigma) was added to the basal compartment of the transwell. Fresh media was applied to the apical chamber and aliquots of 100 μl were taken every 15 minutes for a total of 120 minutes, replacing with fresh media. Sample aliquots were analysed for FITC fluorescence (FLUOstar OPTIMA, BMG Labtech) at an excitation wavelength of 492 nm and emission wavelength of 520 nm. Relative fluorescent units (RFU) were converted to their corresponding concentrations by interpolating from a known standard curve. Corrections were made for background fluorescence and the serial dilutions

generated over the experiments time course. P_{app} values were calculated representing the apparent permeability coefficient for control (PBS) and treatment (10 ng/ml MMP-3). This was achieved via the following equation:

$$P_{app}(cm/s) = (dM/dT)/(A\ x\ C_0),$$

Where dM/dT is the rate of appearance of FITC-dextran (FD) (µg/s) in the apical chamber from 0 to 120 minutes after introduction of FD into the basal chamber. A is the effective surface area of the insert (cm^2) and C_0 is the initial concentration of FD in the basal chamber.

5.16 Cell Viability

Cells cultured in a 96-well plate were treated with increasing concentrations of recombinant human PAI-1 and TGF-β2 from 0-2000 ng/ml. Cell viability was assessed 24 hours post treatment using a CellTitre 96® AQueous One Solution Cell Proliferation Assay (Promega). Cell media was aspirated and a 1 in 6 dilution of the supplied reagent in media was added to the cell surface. Cells were incubated at 37°C for 1 hour and the media was analysed by spectrophotometry (Multiskan FC, Thermo Scientific) at 450 nm. Standard *in vitro* viability calculations fail to consider sample size and the biological significance of the data. Hence, a modified approach was taken to determine at which concentration SCEC's and TM cells show a reduced tolerability to PAI-1 and TGF-β2. This was defined at an average of 85% viability over 3 cell samples. This conservative value ensures that a cell population would remain viable and still be able to proliferate. Anything lower should be regarded as MMP-3 intolerability i.e. reduced cell proliferation or cell death. Control samples (0 ng/ml MMP-3) were normalised to 100% viability and a linear model fitted to the normalised data. The PAI-1/TGF-β2 concentration at which cells had an average of 85% viability was interpolated from the lower 95% confidence bound from this linear model. This value represents the concentration of PAI-1/TGF-β2 at which the average of three cell samples would have a 97.5% chance of retaining a greater to or equal than 85% viability.

5.17 Total PAI-1 quantification

PAI-1 concentration was quantified using enzyme-linked immunosorbent assay (ELISA) kits for both human AH (KHC3071, Invitrogen) and murine AH (Dy3228-05, R&D systems) according to the manufacturer's protocol. Human POAG and CAT AH was diluted 2 in 7 in reagent diluent buffer, and then run as per the manufacturers protocols. The sample concentrations were calculated from a standard curve that was fitted to a four parameter logistics curve using the 4PL program in MATLAB.

To measure the secretion of PAI-1 by AAV-2/9 into the AH, animals were inoculated with virus as described via intracameral injection. 12-weeks post-injection, animals were anaesthetised using isoflurane and AH was collected. This was achieved by the cannulation of the cornea with a pulled glass needle (1B100-6, WPI) and AH collected in the needle under IOP of the eye. Aqueous was expelled from the needle (approximately 3 µl) by the attachment of a 25 ml syringe connected via barb fitting and tubing (Smiths Medical) and a gradual push of the syringe plunger. 3 samples were pooled and 10 µl total murine AH was diluted in reagent buffer, AH was assayed using the previously mentioned ELISA kit.

5.18 Western blotting of AH levels of TGF-β2

Human AH samples from cataract and POAG patients was taken and the total protein content was analysed by measuring absorbance at 280 nm using a nanodrop spectrophotometer. The AH samples were then loaded, normalised to the total protein concentration. Protein samples were separated by electrophoresis on 10% SDS–PAGE under reducing conditions and electro-transferred to PVDF membranes. After blocking with 5% blotting grade blocker non-fat dry milk in TBS for 1 h at room temperature, membranes were incubated overnight at 4^{o}C with the following Rabbit polyclonal primary antibody: rabbit polyclonal TGF-β2 (1:500; ab66045, Abcam) diluted in blocking buffer. Blots were developed as previously described.

5.19 Immunocytochemistry ECM components

Immunocytochemistry was performed to visualise changes in ECM composition in response to PAI-1 and TGF-β2. Human SCEC and HTM were grown on PET-G

coverslips (Sarstedt) in a 24-well plate, and fixed in 4% paraformaldehyde (pH 7.4) for 20 min at room temperature and then washed with PBS for 15 min. Cell monolayers were blocked in PBS containing 5% normal goat serum (10658654, Fischer Scientific) and 0.1% Triton X-100 (T8787, Sigma) at room temperature for 30 min. Primary antibodies of collagen IV (ab6586, Abcam), α-SMA (ab5694, Abcam), laminin (ab11575, Abcam), and fibronectin (ab23750, Abcam) were diluted at 1:400, 1:100, 1:100, and 1:40 respectively in blocking buffer and incubated overnight at 4°C. Anti-rabbit Cy3 conjugated secondary antibody (ab6939, Abcam) were diluted at 1:500 in blocking buffer and then incubated for 2 hr at room temperature. Cells were then washed and counterstained with Phalloidan-488 (A12379), that binds F-actin filaments, diluted 1:40 in blocking buffer for 30 minutes at room temperature. Following incubation, coverslips were mounted on microscope slides with aqua-polymount (Polyscience) after nuclei-counterstaining with DAPI. Fluorescent images of SCEC monolayers were captured using a confocal microscope (Zeiss LSM 710), and processed using imaging software ZEN 2012.

5.20 Immunocytochemistry tight junction proteins

Human SCEC were grown on Lab-Tek II chamber slides and fixed in 4% paraformaldehyde (pH 7.4) for 15 min at room temperature and then washed with PBS for 15 min. Cell monolayers were blocked in PBS containing 5% normal goat serum and 0.1% Triton X-100 at room temperature for 15 min. Primary antibodies claudin-11 (ab53041, Abcam), ZO-1 (61-7300, Invitrogen), tricellulin (48-8400, Invitrogen) were diluted at 1:100 in blocking buffer and incubated overnight at 4°C. Anti-rabbit Cy3 conjugated secondary antibody (ab6939, Abcam) were diluted 1:500 in blocking buffer were then incubated for 1 hr at 37°C. Coverslips were placed on slides and images processes as previously described.

5.21 Western Blotting: tight junctions

Protein lysates were isolated from cultured cells in protein lysis buffer containing 1M Tris pH 7.5, 1M NaCl, 1% NP-40, 10% SDS, 1X protease inhibitor cocktail (Roche). The homogenate was centrifuged at 10,000 r.p.m. (IEC Micromax microcentrifuge, 851 rotor) at 4°C for 20 min and the supernatant was stored at

−80°C. Protein concentration was determined by BCA Protein assay kit (Pierce, IL, USA) with bovine serum albumin (BSA) at 2 mg/ml as standards on 96-well plates according to the manufacturer's protocol. 30-50 µg of total protein was loaded in each lane. Protein samples were separated by electrophoresis on 7.5-10% SDS–PAGE under reducing conditions and electro-transferred to PVDF membranes. Westerns were carried out as previously described usingth following rabbit polyclonal primary antibodies: anti-oligodendrocyte specific protein antibody (1:500; ab53041, Abcam); anti-ZO-1 antibody (1:250; 61-7300, Invitrogen), anti-tricellulin C-terminal antibody (1:125; 48-8400, Invitrogen), anti-occludin antibody (1:500; 71-1500, Invitrogen) and anti-VE-cadherin antibody (1:1000; ab33168, Abcam). Each blot was stripped with Restore Western Blot Stripping Buffer (Pierce) and probed with rabbit polyclonal to β-actin (1:2000; ab8227, Abcam) or GAPDH (1:2000; ab9485, Abcam) as loading controls. Protein band intensities were quantified by scanning with a HP Scanjet Professional 10000 Mobile Scanner and analyzed using *Image J* (Version 1.50c). The percentage reduction in band intensity was calculated relative to the control non-targeting siRNA, which was standardized to represent 100% and normalized against β-actin or GAPDH. GAPDH was used as loading control in PAI-1 and TGF-β2 treatments as these affect cytoskeletal protein production. In these treatments cells were treated as described in *Western Blotting: ECM components* and probed for ZO-1 and tricellulin expression. African green monkey (*Chlorocebus Sabeus*) outflow tissue was obtained from St. Kitts Biomedical Research Foundation. This was lysed in NP-40 buffer and processed as previously decribed, claudin-5 was probed using the polyclonal claudin-5 rabbit antibody (1:500; 34-1600, Invitrogen).

5.22 Western Blotting: ECM components

Cells were treated with either 1, 10, 50 ng/ml PAI-1 or 20 ng/ml TGF-β2 for 48 hours in fresh media. Cells were lysed using NP-40 lysis buffer, containing 50 mM Tris pH 7.5, 150 mM NaCL, 1% NP-40, 10% SDS, 1X protease inhibitor (Roche), for protein collection. Samples were centrifuged at 10,000 rpm for 15 minutes (IEC Micromax microcentrifuge) and supernatant was retained. Protein samples were loaded onto a 10% SDS-PAGE gel at 30-50µg per well. Proteins were separated by electrophoresis over the course of 150 minutes at constant voltage (120 V) under

reducing conditions and subsequently electro-transferred onto methanol-activated PVDF membranes at constant voltage (12 V). Gels intended for use with collagen IV antibodies (1:1000; ab6586, Abcam) were run under native conditions. Membranes were blocked for one hour at room temperature in 5% non-fat dry milk and incubated overnight at 4°C with a rabbit primary antibodies to collagen IV, α-SMA (1:500; ab5694, Abcam), laminin (1:500; ab11575, Abcam) and fibronectin (1:1000; ab23750, Abcam) diluted in 3% BSA in TBS. Membrane blots were washed 3x5 min in TBS and incubated at room temperature for 2 hours with horse radish peroxidase-conjugated anti-rabbit secondary antibody (1:4000; A6154, Sigma). Blots were again washed and treated with a chemiluminescent substrate (WesternBright ECL, Advansta) and developed on a blot scanner (C-DiGit, LI-COR). Membranes were re-probed with GAPDH antibody (1:2000; ab9485, Abcam) for loading control normalisation. A total of 4 replicate blots were quantified for each cell lysate sample antibody, and 2-3 replicates for a media sample. Band images were quantified using Image J software. Fold change in band intensity was represented in comparison to vehicle control treatments of PBS.

5.23 Immunohistochemistry for frozen sections: AC and Schlemm's canal

Enucleated mouse eyes were fixed in 4% paraformaldehyde (pH 7.4) overnight at 4°C on a rotating device. Posterior segments of the eye were removed and anterior segments were then washed with PBS for 15 min and sequentially submerged in 10, 20 and 30% sucrose. Dissected anterior segments were then suspended in specimen blocks with OCT solution (Tissue-Tek) and frozen in a bath of isopropanol submerged in liquid nitrogen. Frozen anterior segments were sectioned using a cryostat (Leica CM 1900) to 12 μm thickness. Sections were collected on Polysine® slides (Menzel-Glazer). To detect TJ proteins, sections were blocked for 20 min at room temperature in PBS containing 5% goat serum and 0.1% Triton-X, and incubated with the primary antibodies ZO-1 (1:100; 61-7300, Invitrogen), tricellulin (1:100; 48-8400, Invitrogen), occludin (1:100; 71-1500, Invitrogen), claudin-4 (1:100; 36-4800, Invotrogen), claudin-1 (1:100; 51900, Invitrogen), JAM-3 (1:100; 81331, Abcam), claudin-7 (1:100; 34-9100, Invitrogen), claudin-11 (1:100; ab53041, Abcam), claudin-10 (1:100; 388400, Invitrogen) diluted in blocking buffer at 4°C in a humidity chamber. All sections were then

washed three times in PBS and incubated with Cy-3 labelled anti-rabbit IgG antibody at 1:500 (Abcam) for 1 h at 37°C in a humidity chamber. Following incubation, sections were washed with PBS and mounted with aqua-polymount (Polyscience) after nuclei-counterstaining with DAPI (0.2 µg/ml, in PBS). To detect VEGFR-3 and PECAM-1 sections were incubated with VEGFR-3 conjugated to Alexa-Fluor 488 (FAB743G, R&D Systems) and PECAM-1 conjugated to Alexa-Fluor 647 (A14716, Life Technologies Biosciences) and then processed as discussed without the addition of secondary antibody. Anterior segments were visualized using a confocal microscope (Zeiss LSM 710).

5.24 Immunohistochemistry for paraffin embedded sections

Paraffin sections of African green monkey (*Chlorocebus Sabeus*) anterior segments were rehydrated by immersion in the following solutions: twice for 2 min each in Histoclear solution; 100% ethanol for 1 min; 95% ethanol for 1 min; 70% ethanol for 1 min; deionized water for 1 min; washing twice for 5 min in PBS. For antigen retrieval, paraffin sections were heated to 95°C for 10 min in citrate buffer (Sodium citrate, pH 6). Paraffin sections were then blocked and stained as described above.

5.25 Immunohistochemistry AAV treated mouse AC

Eyes were enucleated 4-weeks post injection of virus and fixed in 4% paraformaldehyde overnight at 4°C. The posterior segment was removed by dissection and anterior segments were washed in PBS and placed in a sucrose gradient of incrementing sucrose concentrations containing 10%, 20% and finally 30% sucrose in PBS. Anterior segments were frozen in O.C.T compound (VWR Chemicals) in an isopropanol bath immersed in liquid nitrogen and cryosectioned (CM 1900, Leica Microsystems) at 12 µm thick sections. To visualise eGFP expression sections were gathered onto charged Polysine® slides (Menzel-Gläser) and blocked for 1 hour with 5% normal goat serum (10658654, Fischer Scientific) and 0.1% Triton X-100 in PBS. Slides were stained with DAPI nuclear stain. Slides were mounted using Aquamount (Hs-106, National Diagnostics) with coverslips (Deckgläser) and visualised using a confocal microscope (Zeiss LSM 710). For AAV-PAI-1 treated tissue, eyes were enucleated 12-weeks post injection of virus. Eyes

were processed as previously mentioned. After the blocking step sections were incubated overnight in PAI-1 (1:100;). Sections were washed three times in PBS for 5 minutes and incubated with a Cy-3 conjugated anti-rabbit IgG antibody (ab6936, Abcam) at a 1:500 dilution for two hours at 37°C in a humidity chamber. Slides were washed as before and counter stained with DAPI for thirty seconds. Slides were mounted using Aquamount (Hs-106, National Diagnostics) with coverslips (Deckgläser) and visualised using a confocal microscope (Zeiss LSM 710).

5.26 AAVs

AAV-2/2, -2/5, -2/9, and scAAV-2/2, -2/5, -2/9 in PBS were obtained from Vector Biolabs, where they were prepared via the triple transfection method in HEK-293 cells. In vector biolabs the AAV was purified from the lysate using a CsCl gradient and dialysis, the resulting viral stocks were titred using qPCR against a standard curve (Samulski et al. 2015). These viruses were at the following stock concentrations; AAV-2/2 2 x 10^{12} Genome copies/ml, AAV-2/5 5.3 x 10^{13} GC/ml, AAV-2/9 8.1 x 10^{13} GC/ml, scAAV-2/2 3.1 x 10^{12} GC/ml, scAAV-2/5 2.2 x 10^{13}, scAAC-2/9 3.3 x 10^{13}. All of the ssDNA AAVs have eGFP under the control of a CMV promoter in with AAV-2 ITRs, with the various pseudotyped capsids (AAV-2, -5, -9). The scAAV pseudotypes have the double-stranded eGFP transgene with the AAV-2/2 ITRs, with the various pseudotyped capsids (AAV-2, -5, -9). For animals injected with the inducible virus, after a 3 week incubation period, 0.2% doxycycline (D9891, Sigma) in PBS was administered twice daily to the eye for 10-16 days to induce viral expression. Murine PAI-1 cDNA was incorporated into the pAAV-MCS vector (Cell Biolabs Inc) for constitutive expression of PAI-1. AAV-2/9 was generated using a triple transfection system in a stable HEK-293 cell line (Vector Biolabs). A null virus was used as contralateral control using the same capsid and vector but lacking a transgene. Schematic illustration of the virus is shown in **Fig. 5.1**.

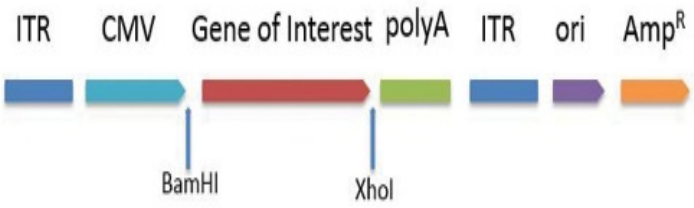

Fig. 5.1 Schematic representation of AAV vector plasmid.
This AAV viral vector was used to express both eGFP or PAI-1. Both under the control of a constitutive CMV promoter.

5.27 Intracameral Injection

Animals were anaesthetised by intra-peritoneal injection of ketamine (Vetalar V, Zoetis) and domitor (SedaStart, Animalcare) (66.6 and 0.66 mg/kg respectively). Pupils were dilated using one drop of tropicamide and phenylephrine (Bausch & Lomb) on each eye. AAV-PAI-1 and AAV-Null were all obtained from Vector Biolabs, PA USA. These viruses were produced by the triple transfection method, isolated using CsCl gradient and dialysis, the final preparation was titred using qPCR and a standard curve (Samulski et al. 2015). 2 µl of AAV-PAI-1 virus at a stock titre of $5x10^{13}$ vector genomes per ml was initially back-filled into a glass needle (ID1.0mm, WPI) attached via tubing (ID-1.02mm, OD-1.98mm, Smiths) to a syringe pump (PHD Ultra, Harvard Apparatus). An additional 1 µl of air was then withdrawn into the needle. Animals were injected intracamerally just above the limbus. Viral solution was infused at a rate of 1.5 µl/min for a total of 3 µl to include the air bubble. Contralateral eyes received an equal volume and titre of either AAV-MMP-3 or AAV-Null. The air bubble prevented the reflux of virus/aqueous back through the injection site when the needle was removed. Fucidic gel (Fucithalmic Vet, Dechra) was applied topically following injection as an antibiotic agent. To counter anaesthetic, Antisedan (atipamezole hydrochloride, SedaStop, Animalcare) was intra-peritoneally injected (8.33 mg/kg) and a

carbomer based moisturising gel (Vidisic, Bausch & Lomb) was applied during recovery to prevent corneal dehydration.

5.28 Intravitreal injections

Animals were anaesthetised by intra-peritoneal injection of ketamine (Vetalar V, Zoetis) and domitor (SedaStart, Animalcare) (66.6 and 0.66 mg/kg respectively). Pupils were dilated using one drop of tropicamide and phenylephrine (Bausch & Lomb) on each eye. 3 µl of virus at a stock titre of $2x10^{12}$ GC/ml was initially back-filled into a 33g blunt Hamilton syringe. A rubber ring was placed around the eye to reduce movement and a moisturising gel (Vidisic, Bausch & Lomb) applied. To allow visualisation of the posterior chamber a piece of glass coverslip was placed over the eye. Using a 30g needle a puncture hole was made at the limbus, with care taken to avoid causing a bleed. The blunt Hamilton needle was then inserted into the puncture wound and the virus injected into the vitreous humour. Proper injection of virus was noted on the blurring of the vitreous humour. To counter anaesthetic, Antisedan (atipamezole hydrochloride, SedaStop, Animalcare) was intra-peritoneally injected (8.33 mg/kg) and a carbomer based moisturising gel (Vidisic, Bausch & Lomb) was applied during recovery to prevent corneal dehydration.

5.29 Sub-retinal injections and retinal flatmount

C57BL/6J mice were anesthetized by intra-peritoneal injection of ketamine (Vetalar V, Zoetis) and domitor (SedaStart, Animalcare) (66.6 and 0.66 mg/kg respectively). A small puncture was made in the sclera. A 34-gage blunt-ended microneedle attached to a 10-µl syringe (Hamilton) was inserted through the puncture, 2×10^{12} GC/ml of AAV in 2 µl PBS was administered to the subretinal space. Eyes were encleated 4-weeks post-injection and placed in 4% PFA. Briefly the eye was dissected along the limbus and the anterior chamber was discarded. The neural retina was then removed from the posterior chamber cup with a pair of forceps, and was cut at the optic nerve head with a microscissors. This was flatmounted by placing four cuts directed toward the centre of the retina. This was blocked and permeabilised for 2 hours in PBS containing 0.4 % Triton X-100, 5 % Normal Goat Serum. After this was incubated overnight at 4°C with a Cy3

conjugated eGFP primary rabbit antibody (1:100). The retinas were washed and counterstained with DAPI nuclear stain for 5 minutes and then mounted on microscope slides using Aquamount (Hs-106, National Diagnostics), with coverslips (Deckgläser) and visualised using a confocal microscope (Zeiss LSM 710).

5.30 IOP measurements: AAV-PAI-1

IOP measurements were performed by rebound tonometry (TonoLab, Icare) both prior to intracameral injection and repeatedly until 11 weeks post injection under general anaesthesia with isoflurane (3% + 1 l/min oxygen). All IOP measurements were done between 10 am and 1 pm to avoid circadian changes. Under general anaesthesia, the spontaneous IOP declines steadily and so IOP values should be compared at an equivalent time point relative to the onset of anaesthesia. In order to account for this effect and improve the accuracy of IOP measurements, the following protocol was developed. For each animal, IOP was measured in one eye approximately 3 min after the flow of isoflurane commenced. The contralateral eye was measured 2 min later, and this was repeated three times yielding three IOP measurements, 4 min apart for each eye. In order to optimize accuracy, 3 IOP measurements (each involving 5 rebound events) were acquired at each time point. The TonoLab has a minimum measureable pressure of 7 mmHg, below which 7 mmHg is still output by the device. Hence, it was necessary to use a non-parametric approach to the analysis. The median of the 5 IOP measurements at each time point was calculated and a straight line was fit to the median values at the three time points. The IOP 5 min after onset of anaesthesia was then estimated by interpolation. The non-parametric Wilcoxon signed-rank test was used to investigate whether the IOP changed between pre- and post-injection measurements in each eye.

5.31 IOP: DBA/2J-siRNA

For DBA/2J animals treated with claudin-5 and occludin siRNA IOP measurements were performed by rebound tonometry (TonoLab, Icare) both prior to siRNA injection and 48hrs post injection. Readings, which were the average IOP values after 5 tonometric events, were taken 10 minutes after the intra-peritoneal

administration of mild general anaesthetic (53.28 mg/kg ketamine and 0.528 mg/kg domitor). One reading was taken for one eye, then the other. This was repeated for a total of five readings per eye. The mean IOP was calculated for each eye, and standard deviation values were used as a measure of dispersion. As the tonometer has a minimum reading of 7 mmHg a non-parametric comparison was used. The non-parametric Wilcoxon signed-rank test was used to investigate significant IOP change between pre- and post-injection measurements in each eye.

5.32 IOP: prior to MRI

For DBA/2J and C57BL/6J animals prior to MRI scanning IOP measurement were performed by rebound tonometry (TonoLab, Icare). These animals were anaesthetised using inhalation anaesthetic, isoflurane (3% + 1 l/min oxygen). 5 mins post anaesthesia induction IOP readings were taken. One reading is the average IOP value after 5 tonometric events. One reading was taken for one eye, then the other. This was repeated for a total of three readings per eye. The mean IOP was calculated for each eye, and standard deviation values were used as a measure of dispersion. As the tonometer has a minimum reading of 7 mmHg a non-parametric comparison was used, samples were compared using Oneway ANOVA and Dunn's multiple comparison post-test.

5.33 Measurement of Outflow Facility: AAV-PAI-1

Animals were sacrificed for outflow facility measurement 12-weeks after injection of virus. Eyes were enucleated for *ex vivo* perfusion using the *iPerfusion™* system as described in Sherwood et al. 2016, example of setup (**Fig. 5.2a**). Contralateral eyes were perfused simultaneously using two independent but identical iPerfusion systems. Each system comprises an automated pressure reservoir, a thermal flow sensor (SLG64-0075, Sensiron) and a wet-wet differential pressure transducer (PX409, Omegadyne), in order to apply a desired pressure, measure flow rate out of the system and measure the intraocular pressure respectively. Prior to eye perfusion the system is equilibrated using a micro-capillary with similar resistance to a mouse eye (**Fig. 5.2b**). Enucleated eyes were secured to a pedestal using a small amount of cyanoacrylate glue in a PBS bath regulated at 35°C. Perfusate was prepared (PBS including divalent cations and 5.5mM glucose) and filtered (0.2 μm,

GVS Filter Technology) before use. Eyes were cannulated using a bevelled needle (NF33BV NanoFil™, World Precision Instruments) with the aid of a stereomicroscope and micromanipulator (World Precision Instruments). Eyes were perfused for 30 minutes at a pressure of ~8 mmHg in order to acclimatise to the environment. Incrementing pressure steps were applied from 4.5 to 21 mmHg, while recording flow rate and pressure, example in (**Fig. 5.3**). Flow (Q) and pressure (P) were averaged over 4 minutes of steady data, and a power law model of the form

$$Q = C_r \left(\frac{P}{P_r}\right)^{\beta} P$$

was fit to the data using weighted power law regression, yielding values of C_r, the reference facility at reference pressure P_r = 8 mmHg (corresponding to the physiological pressure drop across the outflow pathway), and $\beta\beta$, a nonlinearity parameter characterising the pressure-dependent increase in facility observed in mouse eyes (Sherwood et al. 2016).

a

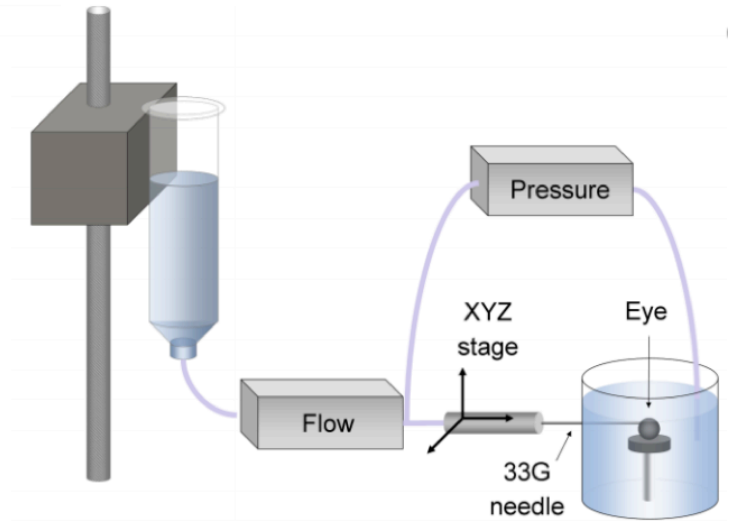

b

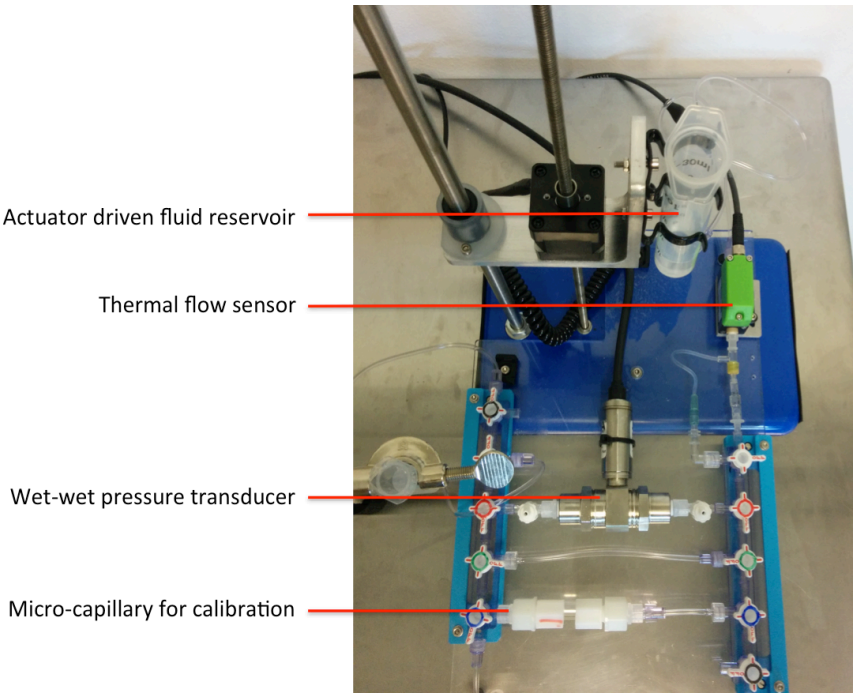

Fig. 5.2. Examples of iPerfusion setup.

(a) Schematic of the experimental setup including the reservoir, flow meter, pressure transducer, and eye in a heated bath. **(b)** Photographic example of experimental setup with the actuator driven fluid reservoir to control applied pressure, thermal flow sensor to measure flow at varying pressure steps, wet-wet pressure transducer to live-trace measured pressure, and micro-capillary for system calibration.

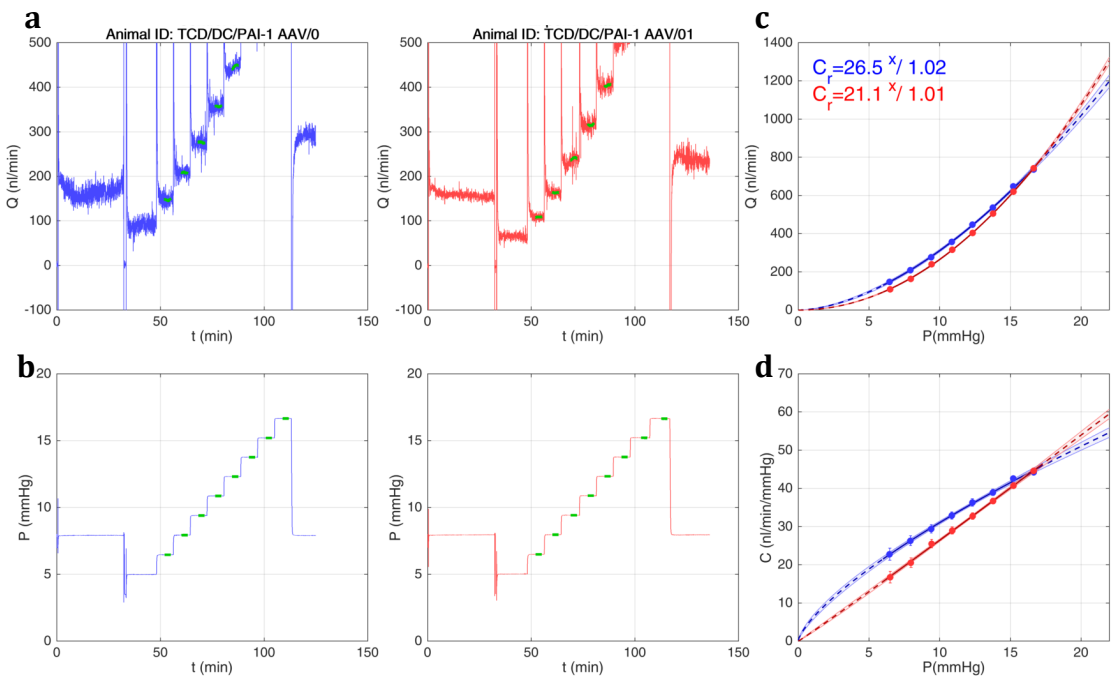

Fig. 5.3. Example of iPerfusion trace of perfused mouse eyes over various pressure steps.

Control (blue) and experimental (red) contralateral eyes are perfused over various pressure (P) in mmHg. **(a)** Example of flow perfusate flow rates at various pressure steps in both control and experimental eyes. **(b)** Example of pressure readings over time of perfusion time on x-axis is related to time in flow graph. **(c)** Averaged flow from **(a)** is plotted against averaged pressure from **(b)** and a power law model is fitted to the data with a power law regression to create facility values (C_r). **(d)** Facility values C_r are plotted against P and the reference C_r is taken from P = 8 mmHg.

5.34 MRI: mouse preparation

Aqueous humor flow was assessed using a dedicated small rodent 7T MRI system (Bruker BioSpec) at TCD. Tetracaine hydrochloride (1% w/v, Bausch and Lomb) was applied to both eyes to minimize eye movement and visidic eye gel (0. 2% w/w, Bausch and Lomb) was used to prevent corneal dryness. For latanoprost administration, each mouse received three doses of 50 mg/ml latanoprost eye-drops (Monopost Unidose, Thea Laboratories) at 24 hours, 12 hours and 3 hours prior to MRI imaging. The contralateral eye was dosed with saline eye-drops simultaneously as a control. Mice were anaesthetized with 5 % isoflurane and placed on an MRI-compatible support cradle. This cradle has an in-built system for maintaining the animal's body temperature at 37°C and a probe underneath the animal allows it to be physiologically monitored (electrocardiogram, respiration and temperature). The mouse tail vein was then cannulated with a 30g needle attached to medical tubing to allow Gd-DTPA administration as the animal was in the MRI scanner.

5.35 MRI scan protocol

To ensure accurate positioning of the animal, an initial rapid pilot image was recorded and used to ensure correct geometry for all subsequent scans. Blood-aqueous barrier integrity and aqueous humor flow were then visualized in high-resolution T1-weighted MR images before (pre-scan) and after (post-scan) intravenous (tail vein) administration of 200 µl of a 1:3 dilution of Gd-DTPA (Gadolinium diethylene-triamine penta-acetic acid, Magnevist, 0. 5 mmol/ml stock solution, Bayer), which was monitored over a period of 60 mins post-injection. MR images specifications were as follows: resolution: 63 x 63 μm^2; field of view: 16 x 16 mm^2; in-plane resolution: 256 x 256 pixels; slice thickness: 0. 25mm; repetition time/echo time: 409/7 ms; flip angle: 30°; number of averages: 1; acquisition time: 1 min, 10 sec; repetitions: pre-scan – 4, post-scan – 60. MR image analysis was performed using *ImageJ* and *MIPAV* software and all data was analyzed blind to treatment. For change in intensity analysis the baseline was taken from Time (0 min) after Gd-DTPA injection and rate of increase was calculated from a linear fit

over the initial 10 min period. For the latanoprost study the contrast agent Gd-BOPTA was used (Gadbentate dimeglumine, Mulithance, 529mg/ml stock, Bracco Diagnostics). Gd-BOPTA was used at the same molar concentration as the working concentration of Gd-DTPA.

5.36 MRI: Ocular anatomy

The following structures and measurements were recorded using the pre-Gd-DTPA MRI scans and *ImageJ* software – AC area, AC signal intensity, AC depth, VB area, VB signal intensity, VB depth, lens size and eye size. Analysis was performed by two lab members and was blind to subject age and strain.

5.37 Assessment of T1-weighted Gd-DTPA enhancement

AC signal intensity post-Gd-DTPA administration was calculated using *ImageJ* software**.** Briefly, in slices that transected the midpoint of the eye signal intensity was measured in the central AC over timepoints: T = 0 to T = 60. Thus tracking signal enhancement in the AC minute by minute. All measurements were normalised relative to baseline (T = 0), and shown as percentage increase in signal intensity. The rate of signal increase was calculated over the initial 10 min of the scan, used as a measure of Gd-DTPA clearance. The peak percentage of signal increase was taken from the entire hour of scanning relative to baseline.

5.38 Statistical Analysis

In the MRI analysis for each data set, the mean (μ), standard deviation (s.d.) and standard error of the mean (s.e.m.) were calculated. A two-tailed unpaired Student's t-test was used to evaluate the significance of differences between each data set. Differences were considered statistically significant when P values were ≤ 0.05. For multiple comparisons across groups, one-way ANOVA followed by Bonferroni's post hoc tests was used with $P \leq 0.05$ representing significance.
For TEER values, activity units (mU/ml) and concentrations (ng/ml), statistical differences were analysed by using unpaired two-tailed Student's *t*-tests. Differences in P_{app} values (cm/s) were determined by a one way ANOVA with Tukey's correction for multiple comparisons, where appropriate. ELISA standard curve concentrations were fitted to a 4 parameter logistical curve using MATLAB.

Concentrations relative to absorbance values were calculated from this curve. Normalised Western blot data was investigated for significance using two-tailed Student *t*-test. Outflow facility was analysed using a weighted paired *t*-test performed in MATLAB as described in (Sherwood et al. 2016), incorporating both system and biological uncertainties. For IOP data the Wilcoxon matched-pairs signed rank test was used to compare changes in paired populations. Statistical significance was inferred when $P < 0.05$ in all experimentation. Results were depicted as 'mean, [95% Confidence Intervals]' unless otherwise stated in the results section.

Concluding remarks and future studies

Concluding remarks and future studies

The ultimate goal of these studies was the development of novel glaucoma therapies targeting the conventional aqueous humor (AH) outflow pathway. The endothelia of Schlemm's canal joined by tight junctions are the final barrier to AH in the conventional pathway. AH flows through both transcellular pores that traverse SC endothelial cells and through paracellular gaps between the cells (Overby et al. 2009). Chapter 2 outlines the characterization of the tight junctions associated with the SC inner wall cells of humans, primates, and mice, with the view to targeting these with siRNA. Addressing the hypothesis that such down-regulation would result in widened gaps between the endothelial cells, thus enhancing AH outflow through the canal. The junctional proteins ZO-1, claudin-11, JAM-3, and tricellulin were all expressed at relatively high levels in primary human SC endothelial cells (SCEC). Interestingly, SCECs expressed low levels of claudin-5 and occludin, which are major components of the inner blood-retina barrier vasculature. The tight junction proteins ZO-1 and tricellulin were also identified in the murine SC inner wall using immunohistochemistry, while claudin-11 was absent. In humans SCECs and in monkey tissue, claudin-11, tricellulin and ZO-1 were identified as potential targets for siRNA-mediated down-regulation. In mice, ZO-1 and tricellulin were targeted for co-suppression in Tam et al. (2017) using siRNA, resulting in increased paracellular gaps between SC endothelial cells and a concomitant increase in AH outflow facility (see **Appendix I**). In translational terms, ongoing work will require safety, tolerability and efficacy studies to be undertaken in primates. In addition, while periodic intracameral inoculation for therapeutic purposes may be an option, it is of note that the episcleral delivery device, which has recently been developed by Retroject Inc (NC), would be ideal for use in this regard. The Retroject device would allow for retrograde delivery through the episcleral veins directly into SC (a diagrammatic representation of the Retroject device is illustrated in **Fig. C.1**). Alternatively, if an AAV capable of transfecting the SC inner wall cells can be identified, shRNA genes could in principle be periodically induced as indicated by IOP.

Systemic delivery of siRNAs targeting select tight junctions of the iBRB microvasculature have been previously reported from this laboratory (Campbell et

al. 2011; Campbell et al. 2012). These studies facilitate increased permeability of the iBRB to compounds of up to 1kDa in size via siRNA-mediated downregulation of claudin-5 demonstrating an increase in delivery of low-molecular weight drugs to the retina. An improved method targeting both claudin-5 and occludin in the blood-brain barrier (BBB) vasculature was developed, and improved permeability of 3kDa dextran across the endothelia of the BBB (Keaney et al. 2015). This method increased paracellular clearance of souble amyloid-β1-40 from the brain into the peripheral circulation, resulting in superior cognitive function. Enhanced removal of soluble amyloid-β from the retina could potentially have a neuroprotective effect in the glaucomatous eye. In Chapter 2, claudin-5 and occludin were targeted for co-supression in the iBRB vasculature of the DBA/2J mouse eye, resulting in a reduction in amyloid-β1-40 in treated mice. This preliminary study offers a novel method of retinal neuroprotection that warrants further investigation in a more suitable model of glaucoma. The DBA/2J model is associated with numerous difficulties; including variable onset of disease progression, asymmetric disease progression in contralateral eyes and an additional immune component in disease pathology that is not fully elucidated (Turner et al. 2017; Mo et al. 2003). To this end we are currently breeding a colony of transgenic *MYOC* mutant mice; these mice develop glaucoma phenotypes (i.e., elevated IOP, retinal ganglion cell death, and axonal degeneration) (Zode et al. 2011). If these animals demonstrate amyloid-β in their retinas with age, periodic co-suppression of claudin-5 and occludin to enhance soluble amyloid-β into the circulation, could hypothetically lead to a reduction in retinal ganglion cell death.

AAVs are promising vectors for therapeutic delivery as they have relatively low immunogenicity, are non-replicating, and transduce tissues over prolonged periods (Samulski et al. 2015). These vectors offer an attractive mode of therapeutic-delivery to the conventional outflow pathway. Previously, scAAV2/2 has been shown to efficiently transduce the trabecular meshwork in humans and rats (Buie et al. 2010; Borrás et al. 2006). In Chapter 3, transfection efficacy of six AAV pseudotypes was tested in mouse outflow tissues; no treatment resulted in widespread outflow tissue transduction with minimal eGFP expression seen in the TM of scAAV2/2 treated eyes. Similar results have been reported in the mouse eye,

with scAAV2/2 treatment resulting in minimal transduction of murine outflow tissues (Bogner et al. 2015; Wang et al. 2017). However, AAV2/9 demonstrated widespread transduction of the mouse corneal endothelium, offering a reservoir from which to express soluble compounds for secretion into the AC, the natural flow of AH carrying these compounds to the conventional outflow tissues. Next, doxycycline eye-drops were used to induce eGFP expression in the corneal endothelium of AAV2/9 treated animals, allowing for controlled delivery of compounds to the AH. In O'Callaghan, Crosbie et al. (2017), both the constitutive and inducible system were used in the delivery of MMP-3 to the AH, resulting in increased outflow facility and reduced IOP in treated eyes.

In addition, levels of PAI-1 were found to be elevated in POAG patient AH. PAI-1 is a downstream mediator of TGF-β2 in the conventional outflow pathway, and PAI-1 treatment of SCECs and TM cells resulted in an increase in endothelial resistance. Further, treatment of these SCECs with PAI-1 resulted in increased ECM deposition and cell contractility, in conjunction with actin cytoskeleton reorganization. Expression of PAI-1 from the corneal endothelium using AAV2/9 did not result in a glaucomatous phenotype as seen in the TGF-β2 mouse model, which may be due to minimal increases in AH PAI-1 protein levels (Shepard et al. 2010). However, the TGF-β2 model uses a viral vector expressing from the outflow tissues themselves. Therefore, an AAV with efficient transduction of the outflow pathway expressing PAI-1 may induce decreased AH outflow. Recent research in AAV transduction of the AC tissues using a triple mutated viral capsid have had success in targeting the TM (Bogner et al. 2015). Further, increased transgene efficiency could enhance PAI-1 expression from either the corneal reservoir or the outflow tissues enhancing this effect. Some methods of use here would include the following. Tissue-specific promoters, POU6FS has just recently been identified as a corneal endothelial specific promoter using transcriptome profiling (Yoshihara et al. 2017). Codon optimization of the PAI-1 transgene, this technique takes advantage of the differing frequencies of tRNAs in human cells to preferentially use codons in the transgenes that correspond to more abundant tRNA populations, thus increasing expression. Finally, the PAI-1 protein spontaneously inactivates *in vivo* and more of an effect on outflow could be seen using a mutant with an increased half-life, such as the cys-mutated PAI-1 which has been found to have

similar inhibitory activity to the wild-type protein with a half life increase of 2h to >700h (Chorostowska-Wynimko et al. 2003; Lindahl et al. 1989). It would be of interest to utilize these various techniques in the AAV2/9 or in another virus targeting the outflow tissues to investigate PAI-1's effect in the *in vivo* eye.

Assessment of AH dynamics *in vivo* is difficult owing to the small volume of the AH in the AC and the isolation of AH from the systemic circulation (McLaren 2009). MRI offers non-invasive and high-resolution 3-D tissue images, with excellent soft tissue definition and no depth limitations (Eter 2010). Use of gadolinium contrast agent as a tracer has demonstrated an anterior solute pathway in humans and has revealed differences in AH dynamics in glaucomatous rat eyes (Ho et al. 2014; Chan et al. 2008). In Chapter 3, a study investigating the use of Gd-MRI on the assessment of mouse AH dynamics is outlined. Gd-MRI demonstrated an anterior pathway for gadolinium into the mouse AH via the iridocorneal angle, bypassing the posterior chamber. In addition, treatment with the glaucoma medication latanoprost resulted in decreased gadolinium accumulation in the mouse AC. Despite reduced outflow facility in the aged DBA/2J mouse, gadolinium accumulation also decreased, compared to age-matched control. This was primarily due to the breakdown of the BAB at the ciliary body, as visualized using Gd-MRI. It would be of great interest in the future to use Gd-MRI to assess AH dynamics in a model of glaucoma with an intact BAB, such as the *MYOC* mutant mouse, in conjunction with a therapy targeting the conventional outflow pathway.

POAG is a multifactorial disease that affects a large amount of people. Going forward, what are some of the avenues to be explored with regards to both clinical and research aspects of glaucoma? Clinically, there is a movement toward self-assessment for glaucoma patients, especially with IOP measurements. IOP is constantly fluctuating on a diurnal cycle and vigilant monitoring of patient IOP levels throughout the day can demonstrate pressure peaks; when patients are at most risk. This system has the potential to lead to personalized dosing regimens that give peak IOP-lowering effects. To this end, implantable wireless IOP sensors are being developed to allow patient monitoring of IOP, some of which have already been tested in humans and others that allow IOP measuring using simply a

smartphone camera (Araci et al. 2014; Melki et al. 2014; Lee et al. 2017). These technologies could allow for more controlled dosage of glaucoma medications and could be used in conjunction with the inducible viral system detailed in this thesis.

With regards to research, there are some questions that have yet to be thoroughly examined such as: what are the changes that occur to glaucomatous outflow tissues? Is there any signaling between the tissues controlling AH production and AH drainage and if so how do they communicate? Glaucomatous SC cells display different phenotypes compared with their normal counterparts, such as increased subcortical stiffness and reduced transcellular pore formation (Overby et al. 2014). These cells retain these properties despite various passages in the same media as non-glaucomatous cell lines. This suggests that there are epigenetic changes in diseased cells, whether due to chronic exposure to a glaucomatous environment, i.e. IOP and glaucomatous AH. Greater knowledge of these changes is necessary to develop more therapies that target the conventional outflow tissues.

Finally, there is still a gap in the understanding of some of the basic biological processes involved in AH turnover. How does the AH outflow regulate inflow? AH outflow is a pressure-dependent phenomenon and so greater inflow increases pressure, leading to a higher rate of outflow and vice versa. However, this simple understanding does not illustrate some of the complicated biological processes involved such as the turnover of ECM, changes in cellular stiffness and formation of giant vacuoles in the SC endothelium, to name but a few. Are these processes all pressure dependent, or does signaling occur via exosomes or soluble proteins, through the anterior solute route? Also, very little is known on the regulation of AH production. Can the amount of AH production also be affected by pressure, and if so where does it occur? Could the outflow tissues signal back to the ciliary body through the unconventional outflow pathway and affect AH production? These are complicated biological processes involving different tissue types in separate microenvironments and there is no easy way to address these questions. However, as POAG is regarded fundamentally as a disease caused by dysregulated AH turnover it is important that these questions are addressed in the future.

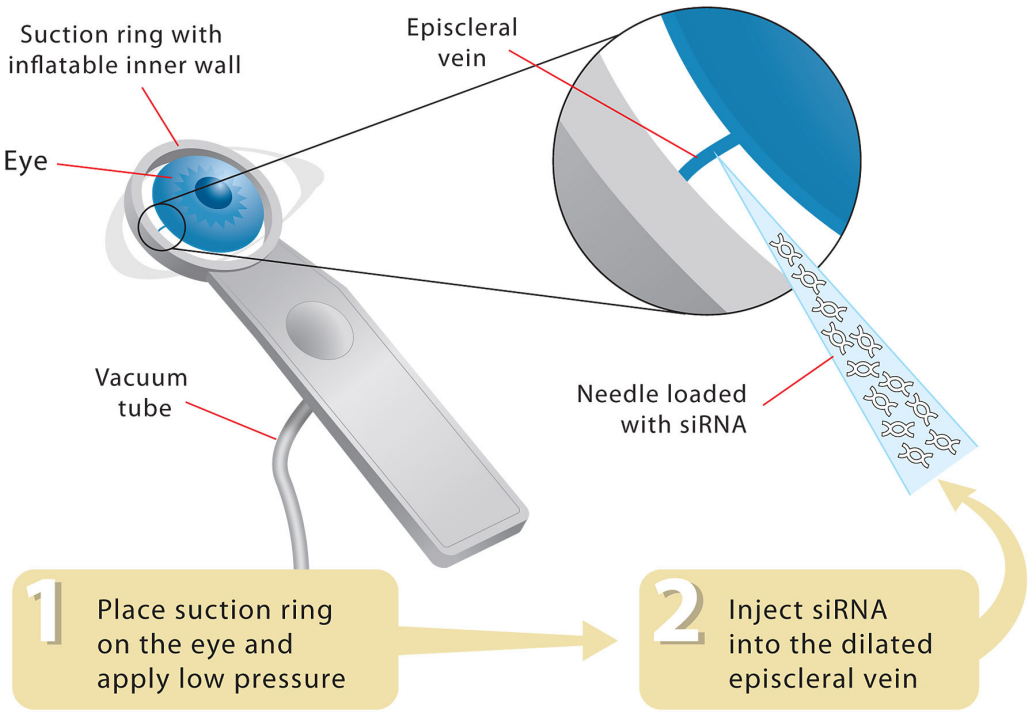

Fig. C.1. Diagrammatic representation of the Retroject device.
The Retroject device allows for retrograde delivery of siRNA to the outflow tissues via episcleral vein injection. This device has a suction ring to apply low pressure around the limbal vessels, thus dilating them. This allows episcleral vein cannulation and injection.

References

Abe, R.Y. et al., 2015. Lamina Cribrosa in Glaucoma: Diagnosis and Monitoring. *Current Ophthalmology Reports*, 3(2), pp.74–84.

Abu-amero, K., Kondkar, A.A. & Chalam, K. V, 2015. An Updated Review on the Genetics of Primary Open Angle Glaucoma. , (October), pp.28886–28911.

Acott, T.S. & Kelley, M.J., 2009. Extracellular Matrix in the Trabecular Meshwork. *Science*, 86(4), pp.543–561.

Agarwal, P., Daher, A.M. & Agarwal, R., 2015. Aqueous humor TGF-β2 levels in patients with open-angle glaucoma: A meta-analysis. *Molecular vision*, 21(February), pp.612–20.

Aihara, M., Lindsey, J.D. & Weinreb, R.N., 2003. Aqueous Humor Dynamics in Mice. *Investigative Ophthalmology and Visual Science*, 44(12), pp.5168–5173.

Allocca, M. et al., 2007. Novel Adeno-Associated Virus Serotypes Efficiently Transduce Murine Photoreceptors . , 81(20), pp.11372–11380.

Alm, A. & Nilsson, S.F.E., 2009. Uveoscleral outflow--a review. *Experimental eye research*, 88(4), pp.760–8.

Alvarado, J.A. et al., 2004. Endothelia of Schlemm's canal and trabecular meshwork: distinct molecular, functional, and anatomic features. *American journal of physiology. Cell physiology*, 286(3), pp.C621–C634.

Alvarado, J.A. et al., 2010. Monocyte modulation of aqueous outflow and recruitment to the trabecular meshwork following selective laser trabeculoplasty. *Archives of ophthalmology (Chicago, Ill. : 1960)*, 128(6), pp.731–7.

Anderson, M.G. et al., 2006. Genetic context determines susceptibility to intraocular pressure elevation in a mouse pigmentary glaucoma. *BMC biology*, 4, p.20.

Anderson, M.G. et al., 2008. GpnmbR150X allele must be present in bone marrow derived cells to mediate DBA/2J glaucoma. *BMC genetics*, 9, p.30.

Anderson, M.G. et al., 2002. Mutations in genes encoding melanosomal proteins cause pigmentary glaucoma in DBA/2J mice. *Nature genetics*, 30(january), pp.81–85.

Andrés-Guerrero, V., García-Feijoo, J. & Konstas, A.G., 2017. Targeting Schlemm's

Canal in the Medical Therapy of Glaucoma: Current and Future Considerations. *Advances in Therapy*, 34(5), pp.1049–1069.

Araci, I.E. et al., 2014. An implantable microfluidic device for self-monitoring of intraocular pressure. *Nature medicine*, 20(9), pp.1074–8.

Ariani, F. et al., 2006. Optineurin gene is not involved in the common high-tension form of primary open-angle glaucoma. *Graefe's Archive for Clinical and Experimental Ophthalmology*, 244(9), pp.1077–1082.

Armstrong, P. & Keevil, S.F., 1991. Magnetic-Resonance-Imaging .1. Basic Principles of Image Production. *British Medical Journal*, 303(6793), pp.35–40.

Asuri, P. et al., 2012. Directed Evolution of Adeno-associated Virus for Enhanced Gene Delivery and Gene Targeting in Human Pluripotent Stem Cells. *Molecular Therapy*, 20(2), pp.329–338.

ATCHISON, R.W., CASTO, B.C. & HAMMON, W.M., 1965. ADENOVIRUS-ASSOCIATED DEFECTIVE VIRUS PARTICLES. *Science (New York, N.Y.)*, 149(3685), pp.754–6.

Aung, T. et al., 2005. Clinical features and course of patients with glaucoma with the E50K mutation in the optineurin gene. *Investigative Ophthalmology and Visual Science*, 46(8), pp.2816–2822.

Auricchio, A. et al., 2001. Exchange of surface proteins impacts on viral vector cellular specificity and transduction characteristics: the retina as a model. *Human molecular genetics*, 10(26), pp.3075–81.

Bahler, C.K. et al., 2008. Prostaglandins Increase Trabecular Meshwork Outflow Facility in Cultured Human Anterior Segments. *American Journal of Ophthalmology*, 145(1), pp.114–119.

Bailey, J.N.C. et al., 2016. Genome-wide association analysis identifies TXNRD2, ATXN2 and FOXC1 as susceptibility loci for primary open-angle glaucoma. *Nature Genetics*, 48(2), pp.189–194.

Balsara, R.D. & Ploplis, V.A., 2008. Plasminogen activator inhibitor-1: the double-edged sword in apoptosis. *Thrombosis and haemostasis*, 100(6), pp.1029–36.

BARANY, E.H. & SCOTCHBROOK, S., 1954. Influence of testicular hyaluronidase on the resistance to flow through the angle of the anterior chamber. *Acta physiologica Scandinavica*, 30(2–3), pp.240–8.

BECKER, B., 1962. The measurement of rate of aqueous flow with iodide. *Investigative ophthalmology*, 1, pp.52–8.

Beltran, W.A. et al., 2017. Optimization of Retinal Gene Therapy for X-Linked Retinitis Pigmentosa Due to RPGR Mutations. *Molecular Therapy*, 25(8), pp.1866–1880.

Bentley, M.D., Hann, C.R. & Fautsch, M.P., 2016. Anatomical variation of human collector channel orifices. *Investigative Ophthalmology and Visual Science*, 57(3), pp.1153–1159.

Berkowitz, B.A. et al., 2004. Dynamic contrast-enhanced MRI measurements of passive permeability through blood retinal barrier in diabetic rats. *Investigative ophthalmology & visual science*, 45(7), pp.2391–8.

Bermudez, J.Y. et al., 2017. Cross-linked actin networks (CLANs) in glaucoma. *Experimental Eye Research*, 159, pp.16–22.

Bert, R.J. et al., 2006. Demonstration of an anterior diffusional pathway for solutes in the normal human eye with high spatial resolution contrast-enhanced dynamic MR imaging. *Investigative Ophthalmology & Visual Science*, 47(12), pp.5153–5162.

Bill, A. & Svedbergh, B., 1972. Scanning electron microscopic studies of the trabecular meshwork and the canal of Schlemm--an attempt to localize the main resistance to outflow of aqueous humor in man. *Acta ophthalmologica*, 50(3), pp.295–320.

Bogner, B. et al., 2015. Capsid Mutated Adeno-Associated Virus Delivered to the Anterior Chamber Results in Efficient Transduction of Trabecular Meshwork in Mouse and Rat. *Plos One*, 10(6), p.e0128759.

Bonomi, L. et al., 1998. Prevalence of glaucoma and intraocular pressure distribution in a defined population. The Egna-Neumarkt Study. *Ophthalmology*, 105(2), pp.209–15.

Borrás, T. et al., 2002. Gene therapy for glaucoma: treating a multifaceted, chronic disease. *Investigative ophthalmology & visual science*, 43(8), pp.2513–8.

Borrás, T. et al., 2006. Mechanisms of AAV transduction in glaucoma-associated human trabecular meshwork cells. *Journal of Gene Medicine*, 8(5), pp.589–602.

Borrás, T. et al., 2001. Non-invasive observation of repeated adenoviral GFP gene delivery to the anterior segment of the monkey eye in vivo. *The journal of gene medicine*, 3(5), pp.437–49.

Borrás, T. et al., 2015. Prevention of Nocturnal Elevation of Intraocular Pressure by

Gene Transfer of Dominant-Negative RhoA in Rats. *JAMA Ophthalmology*, 133(2), p.182.

Borras, T., Buie, L.K. & Spiga, M.G., 2016. Inducible scAAV2.GRE.MMP1 lowers IOP long-term in a large animal model for steroid-induced glaucoma gene therapy. *Gene therapy*, (November 2015), pp.438–449.

Bourne, R.R.A. et al., 2013. Causes of vision loss worldwide, 1990-2010: A systematic analysis. *The Lancet Global Health*, 1(6), pp.339–349.

Bourne, R.R.A. et al., 2016. Number of people blind or visually impaired by glaucoma worldwide and in world regions 1990 - 2010: A meta-analysis. *PLoS ONE*, 11(10), pp.1–16.

Bowles, D.E. et al., 2012. Phase 1 Gene Therapy for Duchenne Muscular Dystrophy Using a Translational Optimized AAV Vector. *Molecular Therapy*, 20(2), pp.443–455.

Bowles, D.E., Rabinowitz, J.E. & Samulski, R.J., 2003. Marker rescue of adeno-associated virus (AAV) capsid mutants: a novel approach for chimeric AAV production. *Journal of virology*, 77(1), pp.423–432.

Braakman, S.T. et al., 2014. Biomechanical strain as a trigger for pore formation in Schlemm's canal endothelial cells. *Experimental Eye Research*, 127(1–2), pp.224–235.

Braakman, S.T. et al., 2015a. Colocalization of outflow segmentation and pores along the inner wall of Schlemm's canal. *Experimental eye research*, 130, pp.87–96.

Braakman, S.T. et al., 2015b. Colocalization of outflow segmentation and pores along the inner wall of Schlemm's canal. *Experimental eye research*, 130, pp.87–96.

Braunger, B.M., Fuchshofer, R. & Tamm, E.R., 2015. The aqueous humor outflow pathways in glaucoma: A unifying concept of disease mechanisms and causative treatment. *European Journal of Pharmaceutics and Biopharmaceutics*, 95, pp.173–181.

Brooks, A.M. & Gillies, W.E., 1992. Ocular beta-blockers in glaucoma management. Clinical pharmacological aspects. *Drugs & aging*, 2(3), pp.208–21.

Brown, H.D.H. et al., 2016. Using magnetic resonance imaging to assess visual deficits: a review. *Ophthalmic & physiological optics : the journal of the British*

College of Ophthalmic Opticians (Optometrists), 36(3), pp.240–65.

Buckingham, B.P. et al., 2008. Progressive ganglion cell degeneration precedes neuronal loss in a mouse model of glaucoma. *J Neurosci*, 28(11), pp.2735–2744.

Buie, L.K. et al., 2010a. Self-complementary AAV virus (scAAV) safe and long-term gene transfer in the trabecular meshwork of living rats and monkeys. *Investigative Ophthalmology and Visual Science*, 51(1), pp.236–248.

Buie, L.K. et al., 2010b. Self-complementary AAV virus (scAAV) safe and long-term gene transfer in the trabecular meshwork of living rats and monkeys. *Investigative ophthalmology & visual science*, 51(1), pp.236–48.

Van Buskirk, E.M., 1977. Trabeculotomy in the immature, enucleated human eye. *Investigative ophthalmology & visual science*, 16(1), pp.63–6.

Calkins, D.J. et al., 2008. Manganese-enhanced MRI of the DBA/2J mouse model of hereditary glaucoma. *Investigative Ophthalmology and Visual Science*, 49(11), pp.5083–5088.

Cameron Millar, J., Clark, A.F. & Pang, I.H., 2011. Assessment of aqueous humor dynamics in the mouse by a novel method of constant-flow infusion. *Investigative Ophthalmology and Visual Science*, 52(2), pp.685–694.

Campbell, M. et al., 2009. An experimental platform for systemic drug delivery to the retina. *Proceedings of the National Academy of Sciences of the United States of America*, 106(42), pp.17817–22.

Campbell, M. et al., 2010. Reversible and size-selective opening of the inner Blood-Retina barrier: a novel therapeutic strategy. *Advances in experimental medicine and biology*, 664, pp.301–8.

Campbell, M. et al., 2008. RNAi-mediated reversible opening of the blood-brain barrier. *The journal of gene medicine*, 10(8), pp.930–47.

Campbell, M. et al., 2011. Systemic low-molecular weight drug delivery to pre-selected neuronal regions. *EMBO Molecular Medicine*, 3(4), pp.235–245.

Campbell, M. et al., 2012. Targeted suppression of claudin-5 decreases cerebral oedema and improves cognitive outcome following traumatic brain injury. *Nature communications*, 3(May), p.849.

Campochiaro, P.A., 2000. Retinal and choroidal neovascularization. *J Cell Physiol*, 184(3), pp.301–310.

Candia, O.A., Gerometta, R.M. & Danias, J., 2014. Tissue plasminogen activator reduces the elevated intraocular pressure induced by prednisolone in sheep. *Experimental Eye Research*, 128(4), pp.114–116.

Carlson, E.C. et al., 2003. Altered KSPG expression by keratocytes following corneal injury. *Molecular vision*, 9(September), pp.615–623.

Carr, D.H. et al., 1984. Gadolinium-DTPA as a contrast agent in MRI: initial clinical experience in 20 patients. *AJR. American journal of roentgenology*, 143(2), pp.215–24.

Carreon, T.A. et al., 2017. Segmental outflow of aqueous humor in mouse and human. *Experimental Eye Research*, 158, pp.59–66.

Cavet, M.E. et al., 2014. Nitric Oxide (NO): An Emerging Target for the Treatment of Glaucoma. *Investigative Ophthalmology & Visual Science*, 55(8), pp.5005–5015.

Cavet, M.E. et al., 2015. Regulation of Endothelin-1-Induced Trabecular Meshwork Cell Contractility by Latanoprostene Bunod. *Investigative ophthalmology & visual science*, 56(6), pp.4108–16.

Celkova, L., Doyle, S. & Campbell, M., 2015. NLRP3 Inflammasome and Pathobiology in AMD. *Journal of Clinical Medicine*, 4(1), pp.172–192.

Cha, E.D.K. et al., 2016. Variations in active outflow along the trabecular outflow pathway. *Experimental Eye Research*, 146, pp.354–360.

Chan, J.E. & Netland, P.A., 2015. EX-PRESS Glaucoma Filtration Device: efficacy, safety, and predictability. *Medical devices (Auckland, N.Z.)*, 8, pp.381–8.

Chan, K.C. et al., 2008. GD-DTPA enhanced MRI of ocular transport in a rat model of chronic glaucoma. *Experimental Eye Research*, 87(4), pp.334–341.

Chang, B. et al., 1999. Interacting loci cause severe iris atrophy and glaucoma in DBA/2J mice. *Nature genetics*, 21(april), pp.405–409.

Cheng, H. et al., 2006. Structural and functional MRI reveals multiple retinal layers. *Proceedings of the National Academy of Sciences of the United States of America*, 103(46), pp.17525–17530.

Child, A. et al., 2002. Adult-Onset Primary Open-Angle Glaucoma Caused by Mutations in Optineurin — Supplemental Data. , 295(March 2016), pp.1077–1079.

Chorostowska-Wynimko, J. et al., 2003. A novel form of the plasminogen activator inhibitor created by cysteine mutations extends its half-life: relevance to

cancer and angiogenesis. *Molecular cancer therapeutics*, 2(1), pp.19–28.

Chou, T.-H. et al., 2011. Postnatal elongation of eye size in DBA/2J mice compared with C57BL/6J mice: in vivo analysis with whole-eye OCT. *Investigative ophthalmology & visual science*, 52(6), pp.3604–12.

Chou, T.H., Tomarev, S. & Porciatti, V., 2014. Transgenic mice expressing mutated Tyr437His human myocilin develop progressive loss of retinal ganglion cell electrical responsiveness and axonopathy with normal IOP. *Investigative Ophthalmology and Visual Science*, 55(9), pp.5602–5609.

Chua, J. et al., 2012. Expression profile of inflammatory cytokines in aqueous from glaucomatous eyes. *Molecular vision*, 18(February), pp.431–8.

Chung, M. et al., 2017. Wet-AMD on a Chip: Modeling Outer Blood-Retinal Barrier In Vitro. *Advanced Healthcare Materials*, 1700028, pp.1–7.

Civan, M.M. & Macknight, A.D.C., 2004. The ins and outs of aqueous humour secretion. *Experimental Eye Research*, 78(3), pp.625–631.

Collignon-Brach, J., 1992. Long-term effect of ophthalmic beta-adrenoceptor antagonists on intraocular pressure and retinal sensitivity in primary open-angle glaucoma. *Current eye research*, 11(1), pp.1–3.

Congdon, N.G., 2003. Important Causes of Visual Impairment in the World Today. *JAMA*, 290(15), p.2057.

Constable, I.J. et al., 2016. EBioMedicine Phase 2a Randomized Clinical Trial : Safety and Post Hoc Analysis of Subretinal rAAV . sFLT-1 for Wet Age-related Macular Degeneration. *EBIOM*, 14, pp.168–175.

Da Costa, R. et al., 2016. A novel method combining vitreous aspiration and intravitreal AAV2/8 injection results in retina-wide transduction in adult mice. *Investigative Ophthalmology and Visual Science*, 57(13), pp.5326–5334.

Cracknell, K.P.B. & Grierson, I., 2009. Prostaglandin analogues in the anterior eye: their pressure lowering action and side effects. *Experimental eye research*, 88(4), pp.786–91.

Cunha-Vaz, J., Bernardes, R. & Lobo, C., 2011. Blood-retinal barrier. *European journal of ophthalmology*, 21 Suppl 6, pp.S3-9.

Cvekl, A. & Tamm, E.R., 2004. Anterior eye development and ocular mesenchyme: new insights from mouse models and human diseases. *BioEssays : news and reviews in molecular, cellular and developmental biology*, 26(4), pp.374–86.

Cwerman-Thibault, H. et al., 2017. Neuroglobin Can Prevent or Reverse Glaucomatous Progression in DBA/2J Mice. *Molecular Therapy - Methods and Clinical Development*, 5(June), pp.200–220.

Danias, J. et al., 2003. Quantitative Analysis of Retinal Ganglion Cell (RGC) Loss in Aging DBA/2NNia Glaucomatous Mice: Comparison with RGC Loss in Aging C57/BL6 Mice. *Investigative Ophthalmology and Visual Science*, 44(12), pp.5151–5162.

Daniel Stamer, W. et al., 2011. eNOS, a pressure-dependent regulator of intraocular pressure. *Investigative Ophthalmology and Visual Science*, 52(13), pp.9438–9444.

Dautriche, C. et al., 2015. A Closer Look at Schlemm's Canal Cell Physiology: Implications for Biomimetics. *Journal of Functional Biomaterials*, 6(3), pp.963–985.

Dautriche, C.N. et al., 2015. A biomimetic Schlemm's canal inner wall: A model to study outflow physiology, glaucoma pathology and high-throughput drug screening. *Biomaterials*, 65, pp.86–92.

Daya, S. & Berns, K.I., 2008. Gene therapy using adeno-associated virus vectors. *Clinical microbiology reviews*, 21(4), pp.583–93.

Degnan, A.J. & Levy, L.M., 2013. REVIEW ARTICLE MR Imaging of Papilledema and Visual Pathways : Effects of Increased Intracranial Pressure and. , (May), pp.1–6.

Denninger, A.R. et al., 2015. Claudin-11 Tight Junctions in Myelin Are a Barrier to Diffusion and Lack Strong Adhesive Properties. *Biophysical Journal*, 109(7), pp.1387–1397.

Derosa, G. & Maffioli, P., 2016. A review about biomarkers for the investigation of vascular function and impairment in diabetes mellitus. *Vascular Health and Risk Management*, 12, pp.415–419.

Dervan, E.W. et al., 2010. Protein Macroarray Profiling of Serum Autoantibodies in Pseudoexfoliation Glaucoma. *Investigative Opthalmology & Visual Science*, 51(6), p.2968.

Devaux, J. & Gow, A., 2008. Tight junctions potentiate the insulative properties of small CNS myelinated axons. *The Journal of Cell Biology*, 183(5), pp.909–921.

Diebold, I. et al., 2008. The "PAI-1 paradox" in vascular remodeling. *Thrombosis*

and haemostasis, 100(6), pp.984–91.

Duncan, R.O. et al., 2007. Retinotopic organization of primary visual cortex in glaucoma: Comparing fMRI measurements of cortical function with visual field loss. *Progress in Retinal and Eye Research*, 26(1), pp.38–56.

Duong, T.Q. & Muir, E.R., 2009. Magnetic resonance imaging of the retina. *Japanese Journal of Ophthalmology*, 53(4), pp.352–367.

Elliott, M.H. et al., 2016. Caveolin-1 modulates intraocular pressure: implications for caveolae mechanoprotection in glaucoma. *Scientific Reports*, 6(1), p.37127.

Engel, L.A. et al., 2014. The effect of previous surgery and topical eye drops for primary open-angle glaucoma on cytokine expression in aqueous humor. *Graefe's Archive for Clinical and Experimental Ophthalmology*, 252(5), pp.791–799.

Epstein, D.L. & Rohen, J.W., 1991. Morphology of the trabecular meshwork and inner-wall endothelium after cationized ferritin perfusion in the monkey eye. *Investigative Ophthalmology and Visual Science*, 32(1), pp.160–171.

Eshaq, R.S. et al., 2017. Diabetic retinopathy : Breaking the barrier. *Pathophysiology*, pp.1–13.

Eter, N., 2010. Molecular imaging in the eye. *The British journal of ophthalmology*, 94(11), pp.1420–6.

Ethier, C.R. et al., 1986. Calculation of flow resistance in the juxtacanalicular meshwork. ARVO Abstracts. *Investigative Ophthalmology and Visual Science*, 24(3), p.135.

Fanning, A.S. & Anderson, J.M., 2009. Zonula occludens-1 and -2 are cytosolic scaffolds that regulate the assembly of cellular junctions. *Annals of the New York Academy of Sciences*, 1165, pp.113–120.

De Feo, F. et al., 2009. Magnetic Resonance Imaging in Patients Implanted with Ex-PRESS Stainless Steel Glaucoma Drainage Microdevice. *American Journal of Ophthalmology*, 147(5), p.907–911.e1.

Fernandes, K.A. et al., 2015. Using genetic mouse models to gain insight into glaucoma: Past results and future possibilities. *Experimental Eye Research*, 141, pp.42–56.

Ferrari, F.K. et al., 1996. Second-strand synthesis is a rate-limiting step for efficient transduction by recombinant adeno-associated virus vectors. *Journal of*

Virology, 70(5), pp.3227–34.

Ferreira, J. et al., 2015. Magnetic Resonance Imaging Study on Blebs Morphology of Ahmed Valves. *Journal of current glaucoma practice*, 9(1), pp.1–5.

Fiedorowicz, M. et al., 2011. Magnetic resonance in studies of glaucoma. *Med Sci Monit*, 17(10), p.RA227-32.

Fingert, J.H., 2011. Primary open-angle glaucoma genes. *Eye*, 25(5), pp.587–595.

Fingert, J.H. et al., 2016. Transgenic TBK1 mice have features of normal tension glaucoma. *Human molecular genetics*, 26(1), p.ddw372.

Fletcher, D.A. & Mullins, R.D., 2010. Cell mechanics and the cytoskeleton. *Nature*, 463(7280), pp.485–492.

Floyd, B.B., Cleveland, P.H. & Worthen, D.M., 1985. Fibronectin in human trabecular drainage channels. *Investigative Ophthalmology and Visual Science*, 26(6), pp.797–804.

Forrester, J. V, 2004. Shedding light on a new eye protein. *British Journal of Ophthalmology*, 88(5), pp.602–603.

Foster, P.J. et al., 2002. The definition and classification of glaucoma in prevalence surveys. *British Journal of Ophthalmology*, 86(2), pp.238–242.

Freddo, T.F., 2013. A contemporary concept of the blood–aqueous barrier. *Progress in Retinal and Eye Research*, 32, pp.181–195.

Freddo, T.F., 1987. Intercellular junctions of the ciliary epithelium in anterior uveitis. *Investigative Ophthalmology and Visual Science*, 28(2), pp.320–329.

Freddo, T.F., 2001. Shifting the Paradigm of the Blood ± Aqueous Barrier. , pp.581–592.

Freddo, T.F., Neville, N. & Gong, H., 2013. Pilocarpine-induced flare is physiological rather than pathological. *Experimental Eye Research*, 107, pp.37–43.

Freddo, T.F., Patz, S. & Arshanskiy, Y., 2006. Pilocarpine's effects on the blood-aqueous barrier of the human eye as assessed by high-resolution, contrast magnetic resonance imaging. *Experimental Eye Research*, 82(3), pp.458–464.

Fuchshofer, R. et al., 2006. Biochemical and morphological analysis of basement membrane component expression in corneoscleral and cribriform human trabecular meshwork cells. *Investigative Ophthalmology and Visual Science*, 47(3), pp.794–801.

Fuchshofer, R. & Tamm, E.R., 2009. Modulation of extracellular matrix turnover in

the trabecular meshwork. *Experimental eye research*, 88(4), pp.683–8.

Fuchshofer, R. & Tamm, E.R., 2012. The role of TGF-β in the pathogenesis of primary open-angle glaucoma. *Cell and Tissue Research*, 347(1), pp.279–290.

Fudemberg, S.J., Batiste, C. & Katz, L.J., 2008. Efficacy, safety, and current applications of brimonidine. *Expert Opinion on Drug Safety*, 7(August), pp.795–799.

Fujimoto, K., 1995. Freeze-fracture replica electron microscopy combined with SDS digestion for cytochemical labeling of integral membrane proteins. Application to the immunogold labeling of intercellular junctional complexes. *Journal of cell science*, 108 (Pt 1(1–2), pp.3443–9.

Fukata, Y. et al., 2001. Rho-Rho-kinase pathway in smooth muscle contraction and cytoskeletal reorganization of non-muscle cells. *Trends in Pharmacological Sciences*, 22(1), pp.32–39.

Furuse, M. et al., 1998. Claudin-1 and -2: Novel integral membrane proteins localizing at tight junctions with no sequence similarity to occludin. *Journal of Cell Biology*, 141(7), pp.1539–1550.

Furuse, M. et al., 1993. Occludin: a novel integral membrane protein localizing at tight junctions. *The Journal of cell biology*, 123(6 Pt 2), pp.1777–88.

Gaasterland, D. et al., 1978. Studies of aqueous humour dynamics in man VI. Effect of age upon parameters of intraocular pressure in normal human eyes. *Experimental Eye Research*, 26(6), pp.651–656.

Garaci, F.G. et al., 2009. Optic nerve and optic radiation neurodegeneration in patients with glaucoma: in vivo analysis with 3-T diffusion-tensor MR imaging. *Radiology*, 252(2), pp.496–501.

Garnock-Jones, K.P., 2014. Ripasudil: first global approval. *Drugs*, 74(18), pp.2211–5.

Garweg, J.G. et al., 2017. Comparison of cytokine profiles in the aqueous humor of eyes with pseudoexfoliation syndrome and glaucoma. *PLoS ONE*, 12(8), pp.1–13.

George, L.A. et al., 2017. Hemophilia B Gene Therapy with a High-Specific-Activity Factor IX Variant. *The New England journal of medicine*, 377(23), pp.2215–2227.

Gerometta, R. et al., 2010. Treatment of sheep steroid-induced ocular hypertension

with a glucocorticoid-inducible MMP1 gene therapy virus. *Investigative ophthalmology & visual science*, 51(6), pp.3042–8.

Ghosh, A.K. & Vaughan, D.E., 2012. PAI-1 in tissue fibrosis. *Journal of cellular physiology*, 227(2), pp.493–507.

Giovingo, M., 2014. Complications of Glaucoma Drainage Device Surgery: A Review. *Seminars in Ophthalmology*, 29(5–6), pp.397–402.

Gloster, J. & Perkins, E.S., 1955. Effect of a Carbonic Anhydrase Inhibitor (Diamox) on Intra-Ocular Pressure of Rabbits and Cats. *British Journal of Ophthalmology*, 39(11), pp.647–658.

Goel, M. et al., 2010. Aqueous humor dynamics: a review. *The open ophthalmology journal*, 4, pp.52–9.

Goldblum, D. et al., 2007. Distribution of amyloid precursor protein and amyloid-?? immunoreactivity in DBA/2J glaucomatous mouse retinas. *Investigative Ophthalmology and Visual Science*, 48(11), pp.5085–5090.

Gonçalves, A., Ambrósio, A.F. & Fernandes, R., 2013. Regulation of claudins in blood-tissue barriers under physiological and pathological states. *Tissue barriers*, 1(3), p.e24782.

Gong, H. et al., 2002. A new view of the human trabecular meshwork using quick-freeze, deep-etch electron microscopy. *Experimental Eye Research*, 75(3), pp.347–358.

Gong, H., Tripathi, R.C. & Tripathi, B.J., 1996. Morphology of the aqueous outflow pathway. *Microscopy research and technique*, 33(4), pp.336–67.

Gottanka, J. et al., 2004. Effects of TGF-β2 in Perfused Human Eyes. *Investigative Ophthalmology and Visual Science*, 45(1), pp.153–158.

Gould, D.B. et al., 2006. Mutant Myocilin Nonsecretion In Vivo Is Not Sufficient To Cause Glaucoma. *Molecular and Cellular Biology*, 26(22), pp.8427–8436.

Gow, a et al., 1999. CNS myelin and sertoli cell tight junction strands are absent in Osp/claudin-11 null mice. *Cell*, 99(6), pp.649–659.

GRANT, W., 1963. Experimental aqueous perfusion in enucleated human eyes. *Archives of Ophthalmology*, 69(6), pp.783–801.

Grimm, D., Kay, M.A. & Kleinschmidt, J.A., 2003. Helper virus-free, optically controllable, and two-plasmid-based production of adeno-associated virus vectors of serotypes 1 to 6. *Molecular therapy : the journal of the American*

Society of Gene Therapy, 7(6), pp.839–50.

Gu, X. et al., 2017. Caveolins and caveolae in ocular physiology and pathophysiology. *Progress in retinal and eye research*, 56, pp.84–106.

Günzel, D. & Yu, A.S.L., 2013. Claudins and the modulation of tight junction permeability. *Physiological reviews*, 93(2), pp.525–69.

Gupta, D. & Chen, P.P., 2016. Glaucoma. *American Family Physician*, 93(8), pp.668–674.

Haddadin, R.I. et al., 2017. SPARC-null Mice Exhibit Lower Intraocular Pressures AND. , 50(8).

Hajjar, R.J. et al., 2008. Design of a Phase 1/2 Trial of Intracoronary Administration of AAV1/SERCA2a in Patients With Heart Failure. *Journal of Cardiac Failure*, 14(5), pp.355–367.

Hamanaka, T. & Bill, A., 1987. Morphological and functional effects of Na2EDTA on the outflow routes for aqueous humor in monkeys. *Experimental eye research*, 44(2), pp.171–90.

Han, H. et al., 2011. Elasticity-dependent modulation of TGF-β responses in human trabecular meshwork cells. *Investigative Ophthalmology and Visual Science*, 52(6), pp.2889–2896.

Hann, C.R., Bahler, C.K. & Johnson, D.H., 2005. Cationic ferritin and segmental flow through the trabecular meshwork. *Investigative ophthalmology & visual science*, 46(1), pp.1–7.

Hann, C.R. & Fautsch, M.P., 2009. Preferential fluid flow in the human trabecular meshwork near collector channels. *Investigative Ophthalmology and Visual Science*, 50(4), pp.1692–1697.

Harasymowycz, P. et al., 2016. Medical Management of Glaucoma in the 21st Century from a Canadian Perspective. *Journal of Ophthalmology*, 2016.

Harris, A. & Wirostko, B., 2013. Cerebral Blood Flow in Glaucoma Patients. *Journal of Glaucoma*, 22(10), pp.S46–S48.

Heijl, A., 2002. Reduction of Intraocular Pressure and Glaucoma Progression. *Archives of Ophthalmology*, 120(10), p.1268.

Heimark, R.L., Kaochar, S. & Stamer, W.D., 2002. Human Schlemm's canal cells express the endothelial adherens proteins, VE-cadherin and PECAM-1. *Current eye research*, 25(5), pp.299–308.

High, K.A. & Anguela, X.M., 2016. Adeno-associated viral vectors for the treatment of hemophilia. *Human molecular genetics*, 25(R1), pp.R36-41.

Hines-Beard, J. et al., 2016. Virus-mediated EpoR76E gene therapy preserves vision in a glaucoma model by modulating neuroinflammation and decreasing oxidative stress. *Journal of neuroinflammation*, 13(1), p.39.

Hippert, C. et al., 2012. Corneal transduction by intra-stromal injection of AAV vectors in vivo in the mouse and Ex vivo in human explants. *PLoS ONE*, 7(4).

Hirt, J. & Liton, P.B., 2017. Autophagy and mechanotransduction in outflow pathway cells. *Experimental Eye Research*, 158, pp.146–153.

Ho, L.C. et al., 2014. In vivo assessment of aqueous humor dynamics upon chronic ocular hypertension and hypotensive drug treatment using gadolinium-enhanced MRI. *Investigative Ophthalmology and Visual Science*, 55(6), pp.3747–3757.

Hoffman, E.A. et al., 2009. Regulation of myocilin-associated exosome release from human trabecular meshwork cells. *Invest Ophthalmol Vis Sci*, 50(3), pp.1313–1318.

Hollands, H. et al., 2013. Do Findings on Routine Examination Identify Patients at Risk for Primary Open-Angle Glaucoma? *JAMA*, 309(19), p.2035.

Huang, P. et al., 2017. MicroRNA Expression Patterns Involved in Amyloid Beta – Induced Retinal Degeneration.

Hui, E.S. et al., 2007. Diffusion tensor MR study of optic nerve degeneration in glaucoma. *Annual International Conference of the IEEE Engineering in Medicine and Biology - Proceedings*, (852), pp.4312–4315.

Ikenouchi, J. et al., 2005. Tricellulin constitutes a novel barrier at tricellular contacts of epithelial cells. *Journal of Cell Biology*, 171(6), pp.939–945.

Inagaki, E. et al., 2013. Expression and distribution of claudin subtypes in human corneal endothelium. *Investigative ophthalmology & visual science*, 54(12), pp.7258–65.

Inazaki, H. et al., 2017. One-year efficacy of adjunctive use of Ripasudil, a rho-kinase inhibitor, in patients with glaucoma inadequately controlled with maximum medical therapy. *Graefe's Archive for Clinical and Experimental Ophthalmology*, (Table 1).

Inman, D.M. et al., 2006. Quantitative correlation of optic nerve pathology with

ocular pressure and corneal thickness in the DBA/2 mouse model of glaucoma. *Investigative ophthalmology & visual science*, 47(3), pp.986–96.

Inoue, T. & Tanihara, H., 2013. Rho-associated kinase inhibitors: a novel glaucoma therapy. *Progress in retinal and eye research*, 37, pp.1–12.

Ishikawa, M. et al., 2015. Experimentally Induced Mammalian Models of Glaucoma. *BioMed Research International*, 2015.

Itakura, T., Peters, D.M. & Fini, M.E., 2015. Glaucomatous MYOC mutations activate the IL-1/NF-κB inflammatory stress response and the glaucoma marker SELE in trabecular meshwork cells. *Molecular vision*, 21(September), pp.1071–84.

Van Itallie, C.M. & Anderson, J.M., 2014. Architecture of tight junctions and principles of molecular composition. *Seminars in Cell & Developmental Biology*, 36, pp.157–165.

Van Itallie, C.M. & Anderson, J.M., 2013. Claudin interactions in and out of the tight junction. *Tissue Barriers*, 1(3), p.e25247.

Ito, Y. et al., 2012. Induction of amyloid-β(1-42) in the retina and optic nerve head of chronic ocular hypertensive monkeys. *Molecular vision*, 18, pp.2647–57.

Jacobson, N. et al., 2001. Non-secretion of mutant proteins of the glaucoma gene myocilin in cultured trabecular meshwork cells and in aqueous humor. *Human molecular genetics*, 10(2), pp.117–25.

Jakobs, T.C. et al., 2005. Retinal ganglion cell degeneration is topological but not cell type specific in DBA/2J mice. *The Journal of cell biology*, 171(2), pp.313–25.

Jang, J.H. et al., 2011. An evolved adeno-associated viral variant enhances gene delivery and gene targeting in neural stem cells. *Molecular Therapy*, 19(4), pp.667–675.

Janson, C. et al., 2002. Clinical protocol. Gene therapy of Canavan disease: AAV-2 vector for neurosurgical delivery of aspartoacylase gene (ASPA) to the human brain. *Human gene therapy*, 13(11), pp.1391–412.

Jin, M. et al., 2005. Rpe65 is the retinoid isomerase in bovine retinal pigment epithelium. *Cell*, 122(3), pp.449–59.

John, S.W. et al., 1998. Essential iris atrophy, pigment dispersion, and glaucoma in DBA/2J mice. *Investigative ophthalmology & visual science*, 39(6), pp.951–62.

Johnson, M. et al., 2002. The pore density in the inner wall endothelium of

Schlemm's canal of glaucomatous eyes. *Investigative ophthalmology & visual science*, 43(9), pp.2950–5.

Johnson, M., 2006. What controls aqueous humour outflow resistance? *Experimental Eye Research*, 82(4), pp.545–557.

Johnson, M., McLaren, J.W. & Overby, D.R., 2017. Unconventional aqueous humor outflow: A review. *Experimental Eye Research*, 158, pp.94–111.

Johnstone, M.A. & Grant, W.G., 1973. Pressure-dependent changes in structures of the aqueous outflow system of human and monkey eyes. *American journal of ophthalmology*, 75(3), pp.365–83.

Junglas, B. et al., 2012. Connective tissue growth factor causes glaucoma by modifying the actin cytoskeleton of the trabecular meshwork. *American Journal of Pathology*, 180(6), pp.2386–2403.

Junglas, B. et al., 2009. Connective tissue growth factor induces extracellular matrix deposition in human trabecular meshwork cells. *Experimental Eye Research*, 88(6), pp.1065–1075.

Kagan, D.B., Gorfinkel, N.S. & Hutnik, C.M., 2014. Mechanisms of selective laser trabeculoplasty: A review. *Clinical and Experimental Ophthalmology*, 42(7), pp.675–681.

Kahloun, R. et al., 2016. Anterior chamber aqueous flare , pseudoexfoliation syndrome , and glaucoma. *International Ophthalmology*, 36(5), pp.671–674.

Kameda, T. et al., 2012. The effect of Rho-associated protein kinase inhibitor on monkey Schlemm's canal endothelial cells. *Investigative ophthalmology & visual science*, 53(6), pp.3092–103.

Kanamalla, U.S. & Boyko, O.B., 2002. Gadolinium Diffusion into Orbital Vitreous and Aqueous Humor, Perivascular Space, and Ventricles in Patients with Chronic Renal Disease. *American Journal of Roentgenology*, 179(5), pp.1350–1352.

Kaneko, Y. et al., 2016. Effects of K-115 (Ripasudil), a novel ROCK inhibitor, on trabecular meshwork and Schlemm's canal endothelial cells. *Scientific reports*, 6(January), p.19640.

Karim, M.J. et al., 2011. Comparison of tight junction protein expression in the ciliary epithelia of mouse, rabbit, cat and human eyes. *Biotechnic & histochemistry : official publication of the Biological Stain Commission*, 86(3), pp.161–7.

Kasetti, R.B. et al., 2016. Expression of mutant myocilin induces abnormal intracellular accumulation of selected extracellular matrix proteins in the trabecular meshwork. *Investigative Ophthalmology and Visual Science*, 57(14), pp.6058–6069.

Kass, M.A. et al., 2002. The Ocular Hypertension Treatment Study: a randomized trial determines that topical ocular hypotensive medication delays or prevents the onset of primary open-angle glaucoma. *Archives of ophthalmology (Chicago, Ill. : 1960)*, 120(6), pp.701-13-30.

Kaufman, P.L., 2017. Latanoprostene bunod ophthalmic solution 0.024% for IOP lowering in glaucoma and ocular hypertension. *Expert opinion on pharmacotherapy*, 18(4), pp.433–444.

Kazemi, A. et al., 2017. Comparison of Aqueous Outflow Facility Measurement by Pneumatonography and Digital Schiøtz Tonography. *Investigative Opthalmology & Visual Science*, 58(1), p.204.

Keaney, J. et al., 2015. Autoregulated paracellular clearance of amyloid-β across the blood-brain barrier. *Sci Adv.*, 1(8), pp.1–24.

Keller, K.E. et al., 2008. Effects of modifiers of glycosaminoglycan biosynthesis on outflow facility in perfusion culture. *Investigative Ophthalmology and Visual Science*, 49(6), pp.2495–2505.

Keller, K.E. et al., 2011. Segmental versican expression in the trabecular meshwork and involvement in outflow facility. *Investigative Ophthalmology and Visual Science*, 52(8), pp.5049–5057.

Keller, K.E. & Acott, T.S., 2013. The Juxtacanalicular Region of Ocular Trabecular Meshwork: A Tissue with a Unique Extracellular Matrix and Specialized Function. *Journal of ocular biology*, 1(1), p.3.

Kelley, M.J. et al., 2007. Synergism of TNF and IL-1 in the induction of matrix metalloproteinase-3 in trabecular meshwork. *Investigative ophthalmology & visual science*, 48(6), pp.2634–43.

Kiel, J.W. et al., 2011. Ciliary blood flow and aqueous humor production. *Progress in retinal and eye research*, 30(1), pp.1–17.

Kim, B.S. et al., 2001. Targeted Disruption of the Myocilin Gene (Myoc) Suggests that Human Glaucoma-Causing Mutations Are Gain of Function. *Molecular and cellular biology*, 21(22), pp.7707–13.

Kipfer-Kauer, A. et al., 2010. Distribution of amyloid precursor protein and amyloid-beta in ocular hypertensive C57BL/6 mouse eyes. *Current eye research*, 35(9), pp.828–34.

Kitajiri, S.-I. et al., 2014. Deafness in occludin-deficient mice with dislocation of tricellulin and progressive apoptosis of the hair cells. *Biology open*, 3(8), pp.759–66.

Kizhatil, K. et al., 2014. Schlemm's canal is a unique vessel with a combination of blood vascular and lymphatic phenotypes that forms by a novel developmental process. *PLoS biology*, 12(7), p.e1001912.

Klaassen, I. et al., 2009. Altered expression of genes related to blood-retina barrier disruption in streptozotocin-induced diabetes. *Experimental eye research*, 89(1), pp.4–15.

Koizumi, N. et al., 2014. New Therapeutic Modality for Corneal Endothelial Disease Using Rho-Associated Kinase Inhibitor Eye Drops. *Cornea*, 33, pp.S25–S31.

Kokubun, T. et al., 2017. Characteristic Profiles of Inflammatory Cytokines in the Aqueous Humor of Glaucomatous Eyes. *Ocular Immunology and Inflammation*, 0(0), pp.1–12.

Kolodny, N.H. et al., 1996. Contrast-enhanced magnetic resonance imaging confirmation of an anterior protein pathway in normal rabbit eyes. *Investigative Ophthalmology and Visual Science*, 37(8), pp.1602–1607.

Kolodny, N.H. et al., 2002. Evaluation of Therapeutic Effectiveness Using MR Imaging in a Rabbit Model of Anterior Uveitis. *Experimental Eye Research*, 74(4), pp.483–491.

Kotterman, M.A. & Schaffer, D. V, 2014. Engineering adeno-associated viruses for clinical gene therapy. *Nature Reviews Genetics*, 15(7), pp.445–451.

Kowluru, R.A. & Odenbach, S., 2004. Role of interleukin-1beta in the pathogenesis of diabetic retinopathy. *The British journal of ophthalmology*, 88(10), pp.1343–7.

Kramer, T.R. & Noecker, R.J., 2001. Comparison of the morphologic changes after selective laser trabeculoplasty and argon laser trabeculoplasty in human eye bank eyes. *Ophthalmology*, 108(4), pp.773–779.

Ku, C.A. & Pennesi, M.E., 2015. Retinal Gene Therapy: Current Progress and Future Prospects. *Expert review of ophthalmology*, 10(3), pp.281–299.

Lai, Y.K.Y. et al., 2002. Potential long-term inhibition of ocular neovascularisation by recombinant adeno-associated virus-mediated secretion gene therapy. *Gene therapy*, 9(12), pp.804–813.

Lambert, V. et al., 2003. Dose-dependent modulation of choroidal neovascularization by plasminogen activator inhibitor type I: implications for clinical trials. *Investigative ophthalmology & visual science*, 44(6), pp.2791–7.

Last, J.A. et al., 2011. Elastic modulus determination of normal and glaucomatous human trabecular meshwork. *Investigative Ophthalmology and Visual Science*, 52(5), pp.2147–2152.

Laties, A. et al., 2016. A Randomized Phase 1 Dose Escalation Study to Evaluate Safety, Tolerability, and Pharmacokinetics of Trabodenoson in Healthy Adult Volunteers. *Journal of ocular pharmacology and therapeutics*, 0(0), pp.1–8.

Lavery, W.J. et al., 2012. Magnetic resonance imaging indicates decreased choroidal and retinal blood flow in the DBA/2J mouse model of glaucoma. *Investigative Ophthalmology and Visual Science*, 53(2), pp.560–564.

Lawson, C. & Wolf, S., 2009. ICAM-1 signaling in endothelial cells. *Pharmacological reports : PR*, 61(1), pp.22–32.

Lebherz, C. et al., 2008. Novel AAV serotypes for improved ocular gene transfer. *The Journal of Gene Medicine*, 10(4), pp.375–382.

Lee, J.O. et al., 2017. A microscale optical implant for continuous in vivo monitoring of intraocular pressure. *Microsystems & Nanoengineering*, 3(April), p.17057.

Lee, N.Y. et al., 2012. Analysis of systemic endothelin-1, matrix metalloproteinase-9, macrophage chemoattractant protein-1, and high-sensitivity C-reactive protein in normal-tension glaucoma. *Current eye research*, 37(12), pp.1121–1126.

Lei, C. et al., 2017. Amelioration of Amyloid β induced retinal inflammatory responses by a LXR agonist TO901317 is associated with inhibiting of the NF-κB signaling and NLRP3 Inflammasome. *Neuroscience*, 360, pp.48–60.

Lei, Y. et al., 2011. Outflow physiology of the mouse eye: Pressure dependence and washout. *Investigative Ophthalmology and Visual Science*, 52(3), pp.1865–1871.

Lertkiatmongkol, P. et al., 2016. Endothelial functions of platelet/endothelial cell adhesion molecule-1 (CD31). *Current opinion in hematology*, 23(3), pp.253–9.

Leske, M.C., 2007. Open-angle glaucoma -- an epidemiologic overview. *Ophthalmic epidemiology*, 14(4), pp.166–72.

Li, A. et al., 2011. Sustained elevation of extracellular ATP in aqueous humor from humans with primary chronic angle-closure glaucoma. *Experimental eye research*, 93(4), pp.528–33.

Li, G. et al., 2013. Optimizing gene transfer to conventional outflow cells in living mouse eyes. *Experimental Eye Research*, 109, pp.8–16.

Li, G. et al., 2016. Visualization of conventional outflow tissue responses to netarsudil in living mouse eyes. *European Journal of Pharmacology*, 787, pp.20–31.

Li, J.J. et al., 2014. Soluble beta-amyloid peptides, but not insoluble fibrils, have specific effect on neuronal MicroRNA expression. *PLoS ONE*, 9(3).

Li, T. et al., 2016. Comparative Effectiveness of First-Line Medications for Primary Open-Angle Glaucoma: A Systematic Review and Network Meta-analysis. *Ophthalmology*, 123(1), pp.129–40.

Li, W. et al., 2008. Engineering and Selection of Shuffled AAV Genomes: A New Strategy for Producing Targeted Biological Nanoparticles. *Molecular Therapy*, 16(7), pp.1252–1260.

Libby, R.T. et al., 2005. Inherited glaucoma in DBA/2J mice: pertinent disease features for studying the neurodegeneration. *Visual neuroscience*, 22, pp.637–648.

Lindahl, T.L., Sigurdardottir, O. & Wiman, B., 1989. Stability of plasminogen activator inhibitor 1 (PAI-1). *Thrombosis and haemostasis*, 62(2), pp.748–51.

Liu, B. et al., 2017. Aging and ocular tissue stiffness in glaucoma. *Survey of Ophthalmology*, pp.1–19.

Liu, M.M., Tuo, J. & Chan, C.-C., 2011. Gene therapy for ocular diseases. *The British journal of ophthalmology*, 95(5), pp.604–612.

Liu, Y. & Allingham, R.R., 2017. Major review: Molecular genetics of primary open-angle glaucoma. *Experimental Eye Research*, 160(2), pp.62–84.

Llobet, A., Gasull, X. & Gual, A., 2003. Understanding Trabecular Meshwork Physiology: A Key to the Control of Intraocular Pressure? *Physiology*, 18(5), pp.205–209.

Lourenço, S. V et al., 2007. Human salivary gland branching morphogenesis:

morphological localization of claudins and its parallel relation with developmental stages revealed by expression of cytoskeleton and secretion markers. *Histochemistry and cell biology*, 128(4), pp.361–9.

Lu, L.J., Tsai, J.C. & Liu, J., 2017. Novel pharmacologic candidates for treatment of primary open-angle glaucoma. *Yale Journal of Biology and Medicine*, 90(1), pp.111–118.

Lu, Z. et al., 2008. The mechanism of increasing outflow facility by rho-kinase inhibition with Y-27632 in bovine eyes. *Experimental eye research*, 86(2), pp.271–81.

Luna, C. et al., 2012. Regulation of trabecular meshwork cell contraction and intraocular pressure by miR-200c. *PloS one*, 7(12), p.e51688.

Mabuchi, F. et al., 2003. Optic Nerve Damage in Experimental Mouse Ocular Hypertension. *Investigative Opthalmology & Visual Science*, 44(10), p.4321.

Maclachlan, T.K. et al., 2011. Preclinical Safety Evaluation of AAV2-sFLT01 — A Gene Therapy for Age-related Macular Degeneration. *Molecular Therapy*, 19(2), pp.326–334.

Mäepea, O. & Bill, A., 1992. Pressures in the juxtacanalicular tissue and Schlemm's canal in monkeys. *Experimental eye research*, 54(6), pp.879–83.

Mäepea, O. & Bill, A., 1989. The pressures in the episcleral veins, Schlemm's canal and the trabecular meshwork in monkeys: effects of changes in intraocular pressure. *Experimental eye research*, 49(4), pp.645–63.

Maheshri, N. et al., 2006. Directed evolution of adeno-associated virus yields enhanced gene delivery vectors. *Nature Biotechnology*, 24(2), pp.198–204.

Manasses, D.T. & Au, L., 2016. The New Era of Glaucoma Micro-stent Surgery. *Ophthalmology and therapy*, 5(2), pp.135–146.

Mariano, C. et al., 2011. A look at tricellulin and its role in tight junction formation and maintenance. *European Journal of Cell Biology*, 90(10), pp.787–796.

Marquis, R.E. & Whitson, J.T., 2005. Management of glaucoma: Focus on pharmacological therapy. *Drugs and Aging*, 22(1), pp.1–21.

Marrazzo, J.M. et al., 2015. Tenofovir-based preexposure prophylaxis for HIV infection among African women. *The New England journal of medicine*, 372(6), pp.509–18.

Massaad, C.A. & Pautler, R.G., 2011. Manganese-Enhanced Magnetic Resonance

Imaging (MEMRI). In M. Modo & J. W. M. Bulte, eds. Methods in Molecular Biology. Totowa, NJ: Humana Press, pp. 145–174.

Mauro, V.P. & Chappell, S.A., 2014. A critical analysis of codon optimization in human therapeutics. *Trends in Molecular Medicine*, 20(11), pp.604–613.

McCabe, M.J. et al., 2016. Claudin-11 and occludin are major contributors to Sertoli cell tight junction function, in vitro. *Asian journal of andrology*, 18(4), pp.620–6.

McCarty, D.M., 2008. Self-complementary AAV vectors; advances and applications. *Mol Ther*, 16(10), pp.1648–1656.

McCarty, D.M., Monahan, P.E. & Samulski, R.J., 2001. Self-complementary recombinant adeno-associated virus (scAAV) vectors promote efficient transduction independently of DNA synthesis. *Gene therapy*, 8(16), pp.1248–1254.

McCarty, D.M., Young, S.M. & Samulski, R.J., 2004. Integration of adeno-associated virus (AAV) and recombinant AAV vectors. *Annual review of genetics*, 38, pp.819–45.

McEWEN, W.K., 1958. Application of Poiseuille's law to aqueous outflow. *A.M.A. archives of ophthalmology*, 60(2), pp.290–4.

McInnis, K.A. et al., 2005. Synthesis of alpha-chemokines IP-10, I-TAC, and MIG are differentially regulated in human corneal keratocytes. *Investigative ophthalmology & visual science*, 46(5), pp.1668–74.

McKay, B.S. et al., 2013. A Role for Myocilin in Receptor-Mediated Endocytosis T. S. Acott, ed. *PLoS ONE*, 8(12), p.e82301.

McKinnon, S.J., Schlamp, C.L. & Nickells, R.W., 2009. Mouse models of retinal ganglion cell death and glaucoma. *Experimental Eye Research*, 88(4), pp.816–824.

McLaren, J.W., 2009. Measurement of aqueous humor flow. *Experimental eye research*, 88(4), pp.641–7.

Melki, S., Todani, A. & Cherfan, G., 2014. An implantable intraocular pressure transducer: initial safety outcomes. *JAMA ophthalmology*, 132(10), pp.1221–5.

Menaa, F. et al., 2011. Keeping an eye on myocilin: A complex molecule associated with primary open-angle glaucoma susceptibility. *Molecules*, 16(7), pp.5402–5421.

Messmer, C., Flammer, J. & Stümpfig, D., 1991. Influence of betaxolol and timolol on the visual fields of patients with glaucoma. *American journal of ophthalmology*, 112(6), pp.678–81.

Minegishi, Y. et al., 2013. Enhancedoptineurin E50k-TBK1 interaction evokes protein insolubility and initiates familial primary open-angle glaucoma. *Human Molecular Genetics*, 22(17), pp.3559–3567.

Mingozzi, F. et al., 2007. CD8 + T-cell responses to adeno- associated virus capsid in humans. *Nature Medicine*, 13(4), pp.419–422.

Mo, J.-S. et al., 2003. By altering ocular immune privilege, bone marrow-derived cells pathogenically contribute to DBA/2J pigmentary glaucoma. *The Journal of experimental medicine*, 197(10), pp.1335–1344.

Modarreszadeh, S.A. et al., 2014. Physiology of aqueous humor dynamic in the anterior chamber due to rapid eye movement. *Physiology and Behavior*, 135, pp.112–118.

Mohan, R.R. et al., 2003. Gene transfer into rabbit keratocytes using AAV and lipid-mediated plasmid DNA vectors with a lamellar flap for stromal access. *Experimental Eye Research*, 76(3), pp.373–383.

Mohan, R.R. et al., 2010. Vector delivery technique affects gene transfer in the cornea in vivo. *Molecular vision*, 16(October), pp.2494–501.

Morgan, J.E. & Tribble, J.R., 2015. Microbead models in glaucoma. *Experimental eye research*, 141, pp.9–14.

Morrison, J.C. et al., 2012. Nerve Damage : Insights From Rodent Models of. , 93(2), pp.156–164.

Murphy, C.G., Johnson, M. & Alvarado, J.A., 1992. Juxtacanalicular tissue in pigmentary and primary open angle glaucoma. The hydrodynamic role of pigment and other constituents. *Archives of ophthalmology (Chicago, Ill. : 1960)*, 110(12), pp.1779–85.

Myers, J.S. et al., 2016. A Dose-Escalation Study to Evaluate the Safety, Tolerability, Pharmacokinetics, and Efficacy of 2 and 4 Weeks of Twice-Daily Ocular Trabodenoson in Adults with Ocular Hypertension or Primary Open-Angle Glaucoma. *Journal of ocular pharmacology and therapeutics : the official journal of the Association for Ocular Pharmacology and Therapeutics*, 32(8), pp.555–562.

Nair, K.S. et al., 2014. Determining immune components necessary for progression of pigment dispersing disease to glaucoma in DBA/2J mice. *BMC genetics*, 15(1), p.42.

Nakatsukasa, M. et al., 2010. Tumor-associated calcium signal transducer 2 is required for the proper subcellular localization of claudin 1 and 7: implications in the pathogenesis of gelatinous drop-like corneal dystrophy. *The American journal of pathology*, 177(3), pp.1344–55.

Nathanson, J.A. & McKee, M., 1995. Alterations of ocular nitric oxide synthase in human glaucoma. *Investigative ophthalmology & visual science*, 36(9), pp.1774–84.

Nathwani, A.C. et al., 2014. Long-term safety and efficacy of factor IX gene therapy in hemophilia B. *The New England journal of medicine*, 371(21), pp.1994–2004.

Nicolson, S.C. et al., 2016. Identification and Validation of Small Molecules That Enhance Recombinant Adeno-associated Virus Transduction following High-Throughput Screens. *Journal of Virology*, 90(16), pp.7019–7031.

Nilsson, S.F., 1997. The uveoscleral outflow routes. *Eye (London, England)*, 11 (Pt 2), pp.149–54.

Nilsson, S.F.E. et al., 2006. The prostanoid EP2 receptor agonist butaprost increases uveoscleral outflow in the cynomolgus monkey. *Investigative ophthalmology & visual science*, 47(9), pp.4042–9.

Nitta, T. et al., 2003. Size-selective loosening of the blood-brain barrier in claudin-5-deficient mice. *The Journal of cell biology*, 161(3), pp.653–60.

Niyadurupola, N. & Broadway, D.C., 2008. Pigment dispersion syndrome and pigmentary glaucoma - a major review. *Clinical & Experimental Ophthalmology*, 36(9), pp.868–882.

Noecker, R.J., 2006. The management of glaucoma and intraocular hypertension: Current approaches and recent advances. *Therapeutics and Clinical Risk Management*, 2(2), pp.193–206.

Noecker, R.S. et al., 2003. A six-month randomized clinical trial comparing the intraocular pressure-lowering efficacy of bimatoprost and latanoprost in patients with ocular hypertension or glaucoma. *American journal of ophthalmology*, 135(1), pp.55–63.

O'Callaghan, J. et al., 2017. Therapeutic potential of AAV-mediated MMP-3 secretion from corneal endothelium in treating glaucoma. *Human Molecular Genetics*, 26(7), pp.1230–1246.

O'Rourke, J., 1970. Studies in Uveal Physiology. *Archives of Ophthalmology*, 84(4), p.415.

Overby, D.R., Zhou, E.H., Vargas-Pinto, R., et al., 2014. Altered mechanobiology of Schlemm's canal endothelial cells in glaucoma. *Proceedings of the National Academy of Sciences of the United States of America*, 111(38), pp.13876–81.

Overby, D.R., Bertrand, J., Schicht, M., et al., 2014. The structure of the trabecular meshwork, its connections to the ciliary muscle, and the effect of pilocarpine on outflow facility in mice. *Investigative Ophthalmology and Visual Science*, 55(6), pp.3727–3736.

Overby, D.R., Bertrand, J., Tektas, O.Y., et al., 2014. Ultrastructural changes associated with dexamethasone-induced ocular hypertension in mice. *Investigative Ophthalmology and Visual Science*, 55(8), pp.4922–4933.

Overby, D.R., Stamer, W.D. & Johnson, M., 2009. The changing paradigm of outflow resistance generation: Towards synergistic models of the JCT and inner wall endothelium. *Experimental Eye Research*, 88(4), pp.656–670.

Park, D.-Y. et al., 2014a. Lymphatic regulator PROX1 determines Schlemm's canal integrity and identity. *The Journal of clinical investigation*, 124(9), pp.3960–74.

Park, D.-Y. et al., 2014b. Lymphatic regulator PROX1 determines Schlemm canal integrity and identity. *The Journal of clinical investigation*, 124(9), pp.1–3.

Parshley, D.E. et al., 1995. Early changes in matrix metalloproteinases and inhibitors after in vitro laser treatment to the trabecular meshwork. *Current eye research*, 14(7), pp.537–44.

Parshley, D.E. et al., 1996. Laser trabeculoplasty induces stromelysin expression by trabecular juxtacanalicular cells. *Investigative ophthalmology & visual science*, 37(5), pp.795–804.

Patel, G.C. et al., 2017. Dexamethasone-Induced Ocular Hypertension in Mice. *The American Journal of Pathology*, 187(4), pp.713–723.

Pattabiraman, P.P. & Rao, P. V., 2010. Mechanistic basis of Rho GTPase-induced extracellular matrix synthesis in trabecular meshwork cells. *AJP: Cell*

Physiology, 298(3), pp.C749–C763.

Pedrigi, R.M. et al., 2011. A model of giant vacuole dynamics in human Schlemm's canal endothelial cells. *Experimental Eye Research*, 92(1), pp.57–66.

Pedrigi, R.M. et al., 2011. A model of giant vacuole dynamics in human Schlemm's canal endothelial cells. *Experimental eye research*, 92(1), pp.57–66.

Perabo, L. et al., 2006. Combinatorial engineering of a gene therapy vector: Directed evolution of adeno-associated virus. *Journal of Gene Medicine*, 8(2), pp.155–162.

Perabo, L. et al., 2003. In vitro selection of viral vectors with modified tropism: the adeno-associated virus display. *Molecular therapy : the journal of the American Society of Gene Therapy*, 8(1), pp.151–7.

Perkumas, K.M. & Stamer, W.D., 2012. Protein markers and differentiation in culture for Schlemm's canal endothelial cells. *Experimental Eye Research*, 96(1), pp.82–87.

Peterson, J.A., Tian, B., Geiger, B., et al., 2000. Effect of latrunculin-B on outflow facility in monkeys. *Experimental eye research*, 70(3), pp.307–13.

Peterson, J.A., Tian, B., McLaren, J.W., et al., 2000. Latrunculins' effects on intraocular pressure, aqueous humor flow, and corneal endothelium. *Investigative ophthalmology & visual science*, 41(7), pp.1749–58.

Promelle, V. et al., 2016. Ocular blood flow and cerebrospinal fluid pressure in glaucoma. *Acta radiologica open*, 5(2), p.2058460115624275.

Rakocevic, J. et al., 2016. Co-expression of vascular and lymphatic endothelial cell markers on early endothelial cells present in aspirated coronary thrombi from patients with ST-elevation myocardial infarction. *Experimental and molecular pathology*, 100(1), pp.31–8.

Rakoczy, E.P. et al., 2015. Gene therapy with recombinant adeno-associated vectors for neovascular age-related macular degeneration: 1 year follow-up of a phase 1 randomised clinical trial. *The Lancet*, 386(10011), pp.2395–2403.

Ramesh, S., Bonshek, R.E. & Bishop, P.N., 2004. Immunolocalisation of opticin in the human eye. *British Journal of Ophthalmology*, 88(5), pp.697–702.

Ramos, R.F. et al., 2007. Schlemm's canal endothelia, lymphatic, or blood vasculature? *Journal of glaucoma*, 16(4), pp.391–405.

Rao, P.V., Pattabiraman, P.P. & Kopczynski, C., 2017. Role of the Rho GTPase/Rho

kinase signaling pathway in pathogenesis and treatment of glaucoma: Bench to bedside research. *Experimental Eye Research*, 158, pp.23–32.

Rasmussen, C.A. et al., 2014. Latrunculin B Reduces Intraocular Pressure in Human Ocular Hypertension and Primary Open-Angle Glaucoma. *Translational vision science & technology*, 3(5), p.1.

Raviola, G. & Raviola, E., 1981. Paracellular route of aqueous outflow in the trabecular meshwork and canal of Schlemm. A freeze-fracture study of the endothelial junctions in the sclerocorneal angel of the macaque monkey eye. *Investigative ophthalmology & visual science*, 21(1 Pt 1), pp.52–72.

Reichstein, D. et al., 2007. Apoptotic retinal ganglion cell death in the DBA/2 mouse model of glaucoma. *Experimental Eye Research*, 84(1), pp.13–21.

Ren, R. et al., 2016. Outflow facility in human eyes through multiple mechanisms. *Investigative Ophthalmology and Visual Science*, 57(14), pp.6197–6209.

Rizzolo, L.J., 2014. Barrier properties of cultured retinal pigment epithelium. *Experimental Eye Research*, 126, pp.16–26.

Rodgers, L.S. et al., 2013. Epithelial barrier assembly requires coordinated activity of multiple domains of the tight junction protein ZO-1. *Journal of Cell Science*, 126(7), pp.1565–1575.

Rodrigues, M.M., Spaeth, G.L. & Donohoo, P., 1982. Electron microscopy of argon laser therapy in phakic open-angle glaucoma. *Ophthalmology*, 89(3), pp.198–210.

Rosenquist, R. et al., 1989. Outflow resistance of enucleated human eyes at two different perfusion pressures and different extents of trabeculotomy. *Current eye research*, 8(12), pp.1233–40.

Rosenthal, R. et al., 2017. Water channels and barriers formed by claudins. *Annals of the New York Academy of Sciences*, 1397(1), pp.100–109.

Roy Chowdhury, U. et al., 2015. Aqueous Humor Outflow: Dynamics and Disease. *Investigative Opthalmology & Visual Science*, 56(5), p.2993.

Russell, S. et al., 2017. Efficacy and safety of voretigene neparvovec (AAV2-hRPE65v2) in patients with RPE65-mediated inherited retinal dystrophy: a randomised, controlled, open-label, phase 3 trial. *Lancet (London, England)*, 390(10097), pp.849–860.

Sabanay, I. et al., 2004. Functional and structural reversibility of H-7 effects on the

conventional aqueous outflow pathway in monkeys. *Experimental Eye Research*, 78(1), pp.137–150.

Sabanay, I. et al., 2000. H-7 effects on the structure and fluid conductance of monkey trabecular meshwork. *Archives of ophthalmology*, 118(July), pp.955–962.

Saccà, S.C. et al., 2016. The Outflow Pathway: A Tissue With Morphological and Functional Unity. *Journal of Cellular Physiology*, 231(9), pp.1876–1893.

Saleh, M., Nagaraju, M. & Porciatti, V., 2007. Longitudinal evaluation of retinal ganglion cell function and IOP in the DBA/2J mouse model of glaucoma. *Investigative ophthalmology & visual science*, 48(10), pp.4564–72.

Samarakoon, R., Goppelt-Struebe, M. & Higgins, P.J., 2010. Linking cell structure to gene regulation: Signaling events and expression controls on the model genes PAI-1 and CTGF. *Cellular Signalling*, 22(10), pp.1413–1419.

Samarakoon, R., Overstreet, J.M. & Higgins, P.J., 2013. TGF-β signaling in tissue fibrosis: Redox controls, target genes and therapeutic opportunities. *Cellular Signalling*, 25(1), pp.264–268.

Samulski, R.J., Salganik, M. & Hirsch, M.L., 2015. Adeno-associated Virus as a Mammalian DNA Vector. *Mobile DNA III*, 2(2), pp.829–851.

Sanka, K. et al., 2007. Influence of actin cytoskeletal integrity on matrix metalloproteinase-2 activation in cultured human trabecular meshwork cells. *Investigative ophthalmology & visual science*, 48(5), pp.2105–14.

Sarra, G.M. et al., 2002. Kinetics of transgene expression in mouse retina following sub-retinal injection of recombinant adeno-associated virus. *Vision Research*, 42(4), pp.541–549.

Scherer, W.J., 2002. A retrospective review of non-responders to latanoprost. *Journal of ocular pharmacology and therapeutics : the official journal of the Association for Ocular Pharmacology and Therapeutics*, 18(3), pp.287–91.

Schlötzer-Schrehardt, U. et al., 2003. Matrix metalloproteinases and their inhibitors in aqueous humor of patients with pseudoexfoliation syndrome/glaucoma and primary open-angle glaucoma. *Investigative ophthalmology & visual science*, 44(3), pp.1117–25.

Schneeberger, E.E. & Karnovsky, M.J., 1976. Substructure of intercellular junctions in freeze-fractured alveolar-capillary membranes of mouse lung. *Circulation*

research, 38(5), pp.404–411.

Schneeberger, E.E. & Lynch, R.D., 2004. The tight junction: a multifunctional complex. *American journal of physiology. Cell physiology*, 286(6), pp.C1213–C1228.

Schuettauf, F. et al., 2002. Effects of anti-glaucoma medications on ganglion cell survival: the DBA/2J mouse model. *Vision research*, 42(20), pp.2333–7.

Schuettauf, F. et al., 2004. Retinal neurodegeneration in the DBA/2J mouse - A model for ocular hypertension. *Acta Neuropathologica*, 107(4), pp.352–358.

Semple, B.D., Frugier, T. & Morganti-Kossmann, M.C., 2010. CCL2 modulates cytokine production in cultured mouse astrocytes. *Journal of neuroinflammation*, 7(1), p.67.

Senatorov, V. et al., 2006. Expression of mutated mouse myocilin induces open-angle glaucoma in transgenic mice. *J Neurosci*, 26(46), pp.11903–11914.

Sharma, A. et al., 2010. AAV serotype influences gene transfer in corneal stroma in vivo. *Experimental Eye Research*, 91(3), pp.440–448.

Sheffield, V.C. et al., 1993. Genetic linkage of familial open angle glaucoma to chromosome 1q21–q31. *Nature Genetics*, 4(1), pp.47–50.

Shen, Q. et al., 2006. Magnetic resonance imaging of tissue and vascular layers in the cat retina. *Journal of magnetic resonance imaging : JMRI*, 23(4), pp.465–72.

Shepard, A.R. et al., 2010. Adenoviral Gene Transfer of Active Human Transforming Growth Factor-β2 Elevates Intraocular Pressure and Reduces Outflow Facility in Rodent Eyes. *Investigative Opthalmology & Visual Science*, 51(4), p.2067.

Shepard, A.R. et al., 2007. Glaucoma-causing myocilin mutants require the Peroxisomal targeting signal-1 receptor (PTS1R) to elevate intraocular pressure. *Human Molecular Genetics*, 16(6), pp.609–617.

Sherwood, J.M. et al., 2016. Measurement of Outflow Facility Using iPerfusion. *PloS one*, 11(3), p.e0150694.

Siah, W.F., Loughman, J. & O'Brien, C., 2015. Lower Macular Pigment Optical Density in Foveal-Involved Glaucoma. *Ophthalmology*, 122(10), pp.2029–37.

Siddiqui, Y. et al., 2003. What is the risk of developing pigmentary glaucoma from pigment dispersion syndrome? *American journal of ophthalmology*, 135(6), pp.794–9.

Siegner, A. et al., 1996. alpha B-crystallin in the primate ciliary muscle and

trabecular meshwork. *European journal of cell biology*, 71(2), pp.165–9.

Srinivasan, B. et al., 2015. TEER Measurement Techniques for In Vitro Barrier Model Systems. *Journal of Laboratory Automation*, 20(2), pp.107–126.

Srivastava, A., 2016. In vivo tissue-tropism of adeno-associated viral vectors. *Current Opinion in Virology*, 21, pp.75–80.

Stamer, W.D. et al., 2015. Biomechanics of Schlemm's canal endothelium and intraocular pressure reduction. *Progress in Retinal and Eye Research*, 44(2), pp.86–98.

Stamer, W.D. et al., 1996. Cultured human trabecular meshwork cells express functional alpha 2A adrenergic receptors. *Investigative ophthalmology & visual science*, 37(12), pp.2426–33.

Stamer, W.D. et al., 1998. Isolation, culture, and characterization of endothelial cells from Schlemm's canal. *Investigative ophthalmology & visual science*, 39(10), pp.1804–12.

Stamer, W.D. et al., 1995. Isolation and culture of human trabecular meshwork cells by extracellular matrix digestion. *Current eye research*, 14(7), pp.611–7.

Stamer, W.D. & Clark, A.F., 2017. The many faces of the trabecular meshwork cell. *Experimental eye research*, 158, pp.112–123.

Stieger, K. et al., 2007. Oral administration of doxycycline allows tight control of transgene expression: a key step towards gene therapy of retinal diseases. *Gene Therapy*, 14(23), pp.1668–1673.

Stone, E.M. et al., 1997. Identification of a gene that causes primary open angle glaucoma. *Science (New York, N.Y.)*, 275(5300), pp.668–70.

Streilein, J.W., 2003. Ocular immune privilege: therapeutic opportunities from an experiment of nature. *Nature reviews. Immunology*, 3(11), pp.879–889.

Stur, M. et al., 1986. Effect of Timolol on Aqueous Humor Protein Concentration in the Human Eye. *Archives of Ophthalmology*, 104(6), pp.899–900.

Sun, X. et al., 2017. Primary angle closure glaucoma: What we know and what we don't know. *Progress in retinal and eye research*, 57, pp.26–45.

Surace, E.M. & Auricchio, A., 2008. Versatility of AAV vectors for retinal gene transfer. *Vision Research*, 48(3), pp.353–359.

Surgucheva, I. & Surguchov, A., 2011. Expression of caveolin in trabecular meshwork cells and its possible implication in pathogenesis of primary open

angle glaucoma. *Molecular vision*, 17, pp.2878–88.

Swaminathan, S.S. et al., 2017. Secreted Protein Acidic and Rich in Cysteine (SPARC) -Null Mice Exhibit More Uniform Outflow. , 54(3), pp.2035–2047.

Swaminathan, S.S. et al., 2014. TGF-β2-mediated ocular hypertension is attenuated in SPARC-null mice. *Investigative Ophthalmology and Visual Science*, 55(7), pp.4084–4097.

Swenson, E.R., 2014. Safety of carbonic anhydrase inhibitors. *Expert opinion on drug safety*, 13(4), pp.459–72.

Takahashi, H. et al., 1998. Mouse myocilin (Myoc) gene expression in ocular tissues. *Biochemical and biophysical research communications*, 248(1), pp.104–9.

Takai, Y., Tanito, M. & Ohira, A., 2012. Multiplex cytokine analysis of aqueous humor in eyes with primary open-angle glaucoma, exfoliation glaucoma, and cataract. *Investigative Ophthalmology and Visual Science*, 53(1), pp.241–247.

Takanosu, M. et al., 2001. Structure, chromosomal location, and tissue-specific expression of the mouse opticin gene. *Investigative ophthalmology & visual science*, 42(10), pp.2202–10.

Tam, A.L.C. et al., 2013. Latanoprost Stimulates Ocular Lymphatic Drainage: An In Vivo Nanotracer Study. *Translational vision science & technology*, 2(5), p.3.

Tam, L.C.S. et al., 2017. Enhancement of Outflow Facility in the Murine Eye by Targeting Selected Tight-Junctions of Schlemm's Canal Endothelia. *Scientific reports*, 7, p.40717.

Tamm, E.R., 2002. Myocilin and glaucoma: Facts and ideas. *Progress in Retinal and Eye Research*, 21(4), pp.395–428.

Tamm, E.R., 2009. The trabecular meshwork outflow pathways: structural and functional aspects. *Experimental eye research*, 88(4), pp.648–55.

Taylor, A.W., 2009. Ocular immune privilege. *Eye (London, England)*, 23(10), pp.1885–9.

Tektas, O.-Y. & Lütjen-Drecoll, E., 2009. Structural changes of the trabecular meshwork in different kinds of glaucoma. *Experimental eye research*, 88(4), pp.769–75.

Testa, F. et al., 2013. Three-year follow-up after unilateral subretinal delivery of adeno-associated virus in patients with Leber congenital Amaurosis type 2.

Ophthalmology, 120(6), pp.1283–91.

Tham, Y.C. et al., 2014. Global prevalence of glaucoma and projections of glaucoma burden through 2040: A systematic review and meta-analysis. *Ophthalmology*, 121(11), pp.2081–2090.

Toris, C.B. et al., 2002. Aqueous humor dynamics in ocular hypertensive patients. *Journal of glaucoma*, 11(3), pp.253–8.

Toris, C.B. et al., 1999. Aqueous humor dynamics in the aging human eye. *American journal of ophthalmology*, 127(4), pp.407–12.

Toris, C.B., Gabelt, B.T. & Kaufman, P.L., 2008. Update on the Mechanism of Action of Topical Prostaglandins for Intraocular Pressure Reduction. *Survey of Ophthalmology*, 53(6 SUPPL.), pp.107–120.

Townsend, K.A., Wollstein, G. & Schuman, J.S., 2008. Clinical application of MRI in ophthalmology. *NMR in Biomedicine*, 21(9), pp.997–1002.

Tripathi, R.C. et al., 1994. Aqueous Humor in Glaucomatous Eyes Contains an Increased Level of TGF-β2. *Experimental Eye Research*, 59(6), pp.723–728.

Trope, G.E. & Clark, B., 1982. Beta adrenergic receptors in pigmented ciliary processes. *The British Journal of Ophthalmology*, 66(12), pp.788–792.

Turner, A.J. et al., 2017. DBA/2J mouse model for experimental glaucoma: Pitfalls and problems. *Clinical and Experimental Ophthalmology*.

Ueda, J., Wentz-Hunter, K. & Yue, B.Y.J.T., 2002. Distribution of myocilin and extracellular matrix components in the juxtacanalicular tissue of human eyes. *Investigative ophthalmology & visual science*, 43(4), pp.1068–76.

Underwood, J.L. et al., 1999. Glucocorticoids regulate transendothelial fluid flow resistance and formation of intercellular junctions. *The American journal of physiology*, 277(2 Pt 1), pp.C330-42.

Vance, M. et al., 2016. AAV Gene Therapy for MPS1-associated Corneal Blindness. *Scientific reports*, 6, p.22131.

Vandenberghe, L.H. & Auricchio, A., 2012. Novel adeno-associated viral vectors for retinal gene therapy. *Gene therapy*, 19(2), pp.162–8.

Vidal-Sanz, M. et al., 2017. Shared and Differential Retinal Responses against Optic Nerve Injury and Ocular Hypertension. *Frontiers in Neuroscience*, 11(APR), pp.1–14.

Vranka, J.A., Kelley, M.J., et al., 2015. Extracellular matrix in the trabecular

meshwork: Intraocular pressure regulation and dysregulation in glaucoma. *Experimental Eye Research*, 133, pp.112–125.

Vranka, J.A., Bradley, J.M., et al., 2015. Mapping molecular differences and extracellular matrix gene expression in segmental outflow pathways of the human ocular trabecular meshwork. *PLoS ONE*, 10(3), pp.1–20.

Wallace, D.M. et al., 2013. Anti-connective tissue growth factor antibody treatment reduces extracellular matrix production in trabecular meshwork and lamina cribrosa cells. *Investigative ophthalmology & visual science*, 54(13), pp.7836–48.

Walton, K.L., Johnson, K.E. & Harrison, C.A., 2017. Targeting TGF-β Mediated SMAD Signaling for the Prevention of Fibrosis. *Frontiers in Pharmacology*, 8.

Wang, J. et al., 2007. Existence of transient functional double-stranded DNA intermediates during recombinant AAV transduction. *Proceedings of the National Academy of Sciences of the United States of America*, 104(32), pp.13104–9.

Wang, J. & Dong, Y., 2016. Characterization of intraocular pressure pattern and changes of retinal ganglion cells in DBA2J glaucoma mice. *International journal of ophthalmology*, 9(2), pp.211–7.

Wang, L. et al., 2017. Single stranded adeno-associated virus achieves efficient gene transfer to anterior segment in the mouse eye K. Stieger, ed. *PLOS ONE*, 12(8), p.e0182473.

Wang, R. & Wiggs, J.L., 2015. Common and Rare Genetic Risk Factors for Glaucoma. *Cold Spring Harbor Perspectives in Medicine*, pp.1–14.

Ward, M.S. et al., 2007. Neuroprotection of Retinal Ganglion Cells in DBA/2J Mice With GDNF-Loaded Biodegradable Microspheres. *Journal of Pharmaceutical Sciences*, 96(3), pp.558–568.

Weinreb, R.N. et al., 2002. Effects of Prostaglandins on the Aqueous Humor Outflow Pathways. *Survey of Ophthalmology*, 47(4), pp.S53–S64.

Weinreb, R.N., Aung, T. & Medeiros, F. a, 2014. The pathophysiology and treatment of glaucoma: a review. *JAMA : the journal of the American Medical Association*, 311(18), pp.1901–11.

Weinreb, R.N. & Khaw, P.T., 2004. Primary open-angle glaucoma. *Lancet (London, England)*, 363(9422), pp.1711–20.

Whitlock, N.A. et al., 2010. Increased Intraocular Pressure in Mice Treated with Dexamethasone. *Investigative Opthalmology & Visual Science*, 51(12), p.6496.

Wiggs, J.L. & Pasquale, L.R., 2017. Genetics of glaucoma. *Human Molecular Genetics*, 26(R1), pp.R21–R27.

Wilson, G.N. et al., 2016. Early cytoskeletal protein modifications precede overt structural degeneration in the DBA/2J mouse model of glaucoma. *Frontiers in Neuroscience*, 10(NOV), pp.1–16.

Wise, J.B. & Witter, S.L., 1979. Argon laser therapy for open-angle glaucoma. A pilot study. *Archives of ophthalmology (Chicago, Ill. : 1960)*, 97(2), pp.319–22.

Wong, A. et al., 2017. Variations in optic nerve head morphology by intraocular pressure in open-angle glaucoma. *Graefe's Archive for Clinical and Experimental Ophthalmology*.

Wooley, D.P. et al., 2017. A directed evolution approach to select for novel Adeno-associated virus capsids on an HIV-1 producer T cell line. *Journal of Virological Methods*, 250, pp.47–54.

Wordinger, R.J., Sharma, T. & Clark, A.F., 2014. The Role of TGF-β2 and Bone Morphogenetic Proteins in the Trabecular Meshwork and Glaucoma. *Journal of Ocular Pharmacology and Therapeutics*, 30(2–3), pp.154–162.

Wostyn, P. et al., 2015. A new glaucoma hypothesis: a role of glymphatic system dysfunction. *Fluids and barriers of the CNS*, 12, p.16.

Xu, Z. et al., 2004. Conservation of critical functional domains in murine plasminogen activator inhibitor-1. *The Journal of biological chemistry*, 279(17), pp.17914–20.

Yan, C. et al., 2016. Targeting Imbalance between IL-1β and IL-1 Receptor Antagonist Ameliorates Delayed Epithelium Wound Healing in Diabetic Mouse Corneas. *American Journal of Pathology*, 186(6), pp.1466–1480.

Yang, H. et al., 2015a. Intracellular cytoskeleton and junction proteins of endothelial cells in the porcine iris microvasculature. *Experimental Eye Research*, 140, pp.106–116.

Yang, H. et al., 2015b. Quantitative study of the microvasculature and its endothelial cells in the porcine iris. *Experimental Eye Research*, 132, pp.249–258.

Yang, X. et al., 2011. Elevated pressure downregulates ZO-1 expression and

disrupts cytoskeleton and focal adhesion in human trabecular meshwork cells. *Molecular vision*, 17(November), pp.2978–85.

Ye, W. et al., 1997. Interendothelial junctions in normal human schlemm's canal respond to changes in pressure. *Investigative Ophthalmology and Visual Science*, 38(12), pp.2460–2468.

Yoshihara, M. et al., 2017. Restricted Presence of POU6F2 in Human Corneal Endothelial Cells Uncovered by Extension of the Promoter-level Expression Atlas. *EBioMedicine*, 25, pp.175–186.

Zhang, Y.E., 2009. Non-Smad pathways in TGF-beta signaling. *Cell research*, 19(1), pp.128–39.

Zhong, Y. et al., 2013. Adenosine, adenosine receptors and glaucoma: An updated overview. *Biochimica et Biophysica Acta - General Subjects*, 1830(4), pp.2882–2890.

Zhou, L.X. & Liu, J.H.K., 2006. Circadian variation of mouse aqueous humor protein. *Molecular vision*, 12(June), pp.639–43.

Zhou, T. et al., 2017. Whole exome sequencing implicates eye development, the unfolded protein response and plasma membrane homeostasis in primary open-angle glaucoma. *PLoS ONE*, 12(3), pp.1–18.

Zhou, X. et al., 2005. Involvement of inflammation, degradation, and apoptosis in a mouse model of glaucoma. *The Journal of biological chemistry*, 280(35), pp.31240–8.

Zhou, Y. & Aref, A.A., 2017. A Review of Selective Laser Trabeculoplasty: Recent Findings and Current Perspectives. *Ophthalmology and therapy*, 6(1), pp.19–32.

Zhou, Y., Grinchuk, O. & Tomarev, S.I., 2008. Transgenic Mice Expressing the Tyr437His Mutant of Human Myocilin Protein Develop Glaucoma. *Investigative Opthalmology & Visual Science*, 49(5), p.1932.

Zhu, D. et al., 2014. Intraocular soluble intracellular adhesion molecule-1 correlates with subretinal fluid height of diabetic macular edema. *Indian Journal of Ophthalmology*, 62(3), p.295.

Zihni, C. et al., 2016. Tight junctions: from simple barriers to multifunctional molecular gates. *Nature Reviews Molecular Cell Biology*, 17(9), pp.564–580.

Zillig, M. et al., 2005. Overexpression and properties of wild-type and Tyr437His

mutated myocilin in the eyes of transgenic mice. *Investigative Ophthalmology and Visual Science*, 46(1), pp.223–234.

Zode, G.S. et al., 2011. Reduction of ER stress via a chemical chaperone prevents disease phenotypes in a mouse model of primary open angle glaucoma. *The Journal of clinical investigation*, 121(9), pp.3542–53.

Appendices

Appendix I: Tam et al., 2017. Enhancement of outflow facility in the murine eye by targeting selected tight-junctions of Schlemm's canal endothelia. *Scientific Reports.*

Appendix II: Campbell et al., 2017. Manipulating ocular endothelial tight junctions: applications in treatment of retinal disease pathology and ocular hypertension. *Progress in Retinal and Eye Research.*

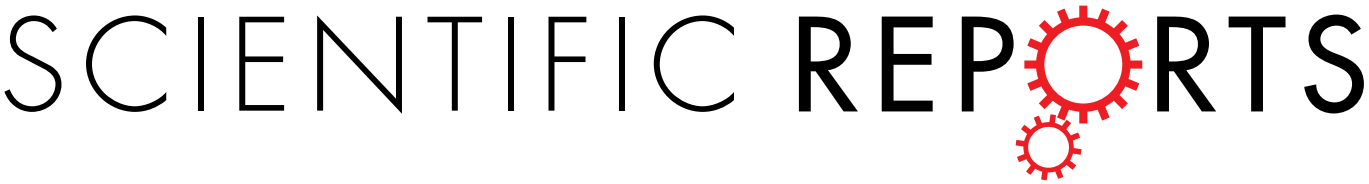

OPEN

Enhancement of Outflow Facility in the Murine Eye by Targeting Selected Tight-Junctions of Schlemm's Canal Endothelia

Received: 05 August 2016
Accepted: 09 December 2016
Published: 16 January 2017

Lawrence C. S. Tam[1,*], Ester Reina-Torres[1,2,*], Joseph M. Sherwood[2], Paul S. Cassidy[1], Darragh E. Crosbie[1], Elke Lütjen-Drecoll[3], Cassandra Flügel-Koch[3], Kristin Perkumas[4], Marian M. Humphries[1], Anna-Sophia Kiang[1], Jeffrey O'Callaghan[1], John J. Callanan[5], A. Thomas Read[6], C. Ross Ethier[7], Colm O'Brien[8], Matthew Lawrence[9], Matthew Campbell[1], W. Daniel Stamer[4], Darryl R. Overby[2] & Pete Humphries[1]

The juxtacanalicular connective tissue of the trabecular meshwork together with inner wall endothelium of Schlemm's canal (SC) provide the bulk of resistance to aqueous outflow from the anterior chamber. Endothelial cells lining SC elaborate tight junctions (TJs), down-regulation of which may widen paracellular spaces between cells, allowing greater fluid outflow. We observed significant increase in paracellular permeability following siRNA-mediated suppression of TJ transcripts, claudin-11, zonula-occludens-1 (ZO-1) and tricellulin in human SC endothelial monolayers. In mice claudin-11 was not detected, but intracameral injection of siRNAs targeting ZO-1 and tricellulin increased outflow facility significantly. Structural qualitative and quantitative analysis of SC inner wall by transmission electron microscopy revealed significantly more open clefts between endothelial cells treated with targeting, as opposed to non-targeting siRNA. These data substantiate the concept that the continuity of SC endothelium is an important determinant of outflow resistance, and suggest that SC endothelial TJs represent a specific target for enhancement of aqueous movement through the conventional outflow system.

Under physiological conditions, the majority of aqueous humour (AH) exits the anterior chamber through the conventional outflow pathway in humans[1–3]. In this pathway, AH filters sequentially through the trabecular meshwork (TM), including the juxtacanalicular tissue (JCT), and the endothelial lining of Schlemm's canal (SC) before entering the SC lumen and draining into the episcleral veins. Electron microscopic evidence has indicated that AH drainage across SC endothelium occurs through micron-sized pores that pass either through (transcellular) or between (paracellular) individual SC cells[4–9]. In particular, a significant fraction of AH crosses the inner wall of SC via paracellular pores[10]. Moreover, the presence of tight-, adherens- and gap-junctions in SC endothelial cells provides a mechanism by which the conventional outflow pathway is dynamically responsive to constantly changing physiological conditions while still preserving the blood-aqueous barrier[11–17]. It has long been recognised that elevated intraocular pressure (IOP) associated with primary open-angle glaucoma (POAG) is due to elevated resistance to AH outflow through the conventional outflow pathway[18], although the cause of elevated outflow resistance in glaucoma remains to be fully elucidated. Previous studies support the concept that outflow

[1]Neurovascular Genetics, Smurfit Institute of Genetics, Trinity College, University of Dublin, Dublin 2, Ireland. [2]Department of Bioengineering, Imperial College London, London, UK. [3]Department of Anatomy, University of Erlangen-Nürnberg, Erlangen, Germany. [4]Department of Ophthalmology, Duke University, Durham, NC, USA. [5]Ross University School of Veterinary Medicine, P. O. Box 334, Basseterre, St. Kitts, West Indies. [6]Department of Ophthalmology and Vision Sciences, University of Toronto, Canada. [7]Coulter Department of Biomedical Engineering, Georgia Institute of Technology and Emory University, Atlanta, USA. [8]Ophthalmology, Mater Hospital, UCD School of Medicine, Dublin, Ireland. [9]RxGen, Hamden, CT, USA. *These authors contributed equally to this work. Correspondence and requests for materials should be addressed to L.C.S.T. (email: lawrenct@tcd.ie) or W.D.S. (email: william.stamer@duke.edu) or P.H. (email: pete.humphries@tcd.ie)

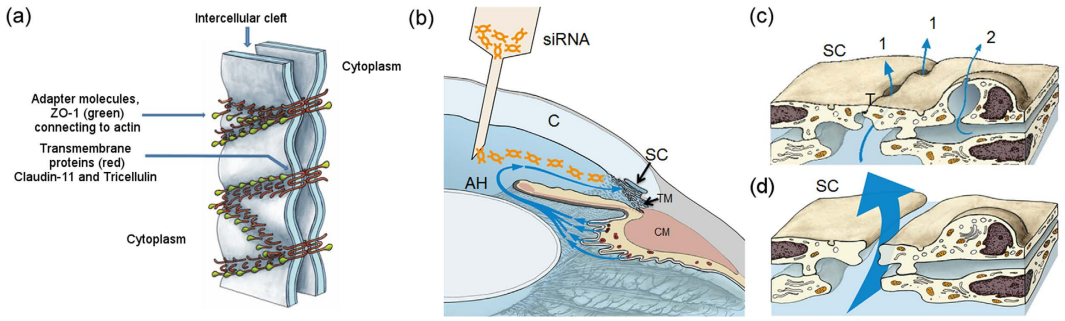

Figure 1. Schematic illustration of the therapeutic strategy addressed in this study. (a) Schematic representation of adapter molecules and transmembrane proteins connecting neighbouring SCEC. **(b)** Intracameral delivery enables siRNAs to be transported towards the conventional outflow pathway by following the natural flow dynamics of aqueous humour in the anterior chamber. AH = aqueous humour; C = cornea; CM = ciliary muscle; SC = Schlemm's canal; TM = trabecular meshwork. **(c)** AH crosses the inner wall endothelium of SC via (1) the intercellular pathway through gaps in tight junctions (T) and, or via (2) the intracellular pathway through a giant vacuole with a pore. **(d)** siRNAs taken up by endothelial cells of the inner wall of SC elicit knockdown of tight junction proteins, resulting in the opening of intercellular clefts with concomitant increase in aqueous outflow facility.

resistance is modulated through a synergistic hydrodynamic interaction between JCT and SC endothelium such that inner wall pore density may influence outflow resistance generation by defining the regions of filtration through the JCT[19–21]. As glaucomatous eyes have reduced SC inner wall pore density, decreased porosity of the inner wall appears to contribute to elevated outflow resistance and increased IOP[22–24].

Prolonged elevation of IOP results in progressive degeneration of retinal ganglion cell axons, and hence to irreversible vision loss. Treatment of POAG by lowering IOP remains the only approach to limiting disease progression. Topically applied medications that either reduce AH production or increase drainage through the unconventional (uveoscleral) outflow pathway are widely used in management of IOP in patients with POAG[25]. However, a proportion of patients do not respond optimally to such medications and, therefore, there is a clear need to investigate novel approaches to reduce outflow resistance by identifying specific targets within the conventional outflow pathway through which this might be achieved. Owing to the fact that a major fraction of AH filtration at the level of SC appears to largely pass through paracellular routes[10], strategies specifically targeting cell-cell junctions between endothelial cells of the inner wall of SC may be effective at decreasing outflow resistance. Hence, we hypothesised that down-regulation of selected tight junction (TJ) components of endothelial cells lining the inner wall of SC may increase the paracellular spaces between these cells, facilitating flow of AH across the inner wall into the SC (Fig. 1), thus reducing outflow resistance and IOP.

In this report, we have identified TJ components in human primary cultures of SC endothelial cells (SCEC), and also in mouse and non-human primate outflow tissues. We show that siRNA-mediated down-regulation of such components increases the paracellular permeability of human primary SCEC monolayers to 70 kDa FITC-dextran, and decreases transendothelial electrical resistance. Furthermore, intracameral delivery of siRNAs targeting selected TJ components is shown to increase intercellular open spaces between SC inner wall endothelial cells as observed by transmission electron microscopy (TEM) and elevates outflow facility (the mathematical inverse of outflow resistance) in normotensive mice. In summary, our findings clearly identify a specific approach to promoting AH outflow by direct manipulation of selected TJs within the conventional outflow pathway.

Results

Characterisation of tight junction expression in human SC endothelial cells. We examined the TJ expression profile in primary cultures of human SCEC isolated from four individual donors, with the objective of determining key junctional components that regulate permeability and selectivity of the inner wall of SC. The mean normalised expression ($2^{-\Delta\Delta Ct}$) of genes encoding claudin and adhesion junctional proteins from four different SCEC strains is shown in Fig. 2a. The complete expression pattern can be found as Supplementary Fig. S1. The expression profile shows that claudin-11 (or oligodendrocyte specific protein) was amongst the highest expressed claudin-based TJ protein in cultured SCEC (Fig. 2a). In addition, zonula-occludens-1 protein (ZO-1, also known as *TJP1*), a key component of junctional complexes that regulate TJ formation, was also expressed at high levels in cultured SCEC. The cell-cell adhesion molecule, junctional adhesion molecule-3 (JAM3) was also highly expressed in human SCEC monolayers. In contrast, occludin and claudin-5, which are major TJ components of human and mouse brain and inner retinal vascular endothelium[26,27] were expressed at low levels in human SCEC. Collectively, these data indicate that claudin-11 is the dominant claudin in the TJs of cultured SCEC, and that ZO-1 is a major junctional associated protein of cultured SCEC. We also compared transcript levels of claudin-11 and ZO-1 in cultured monolayers of human SCEC (SC77) against those of human TM cells (TM93), and observed expression levels of claudin-11 to be 2.52-fold higher in SCEC than in TM cells (Supplementary Fig. S2). However, no significant difference in ZO-1 transcript expression was observed between TM and SCEC.

Claudin-11 and ZO-1 protein expression was detected in cultured SCEC by Western blot (Fig. 2b). In addition, we also detected expression of another TJ protein, tricellulin (also known as MARVELD2) in cultured SCEC,

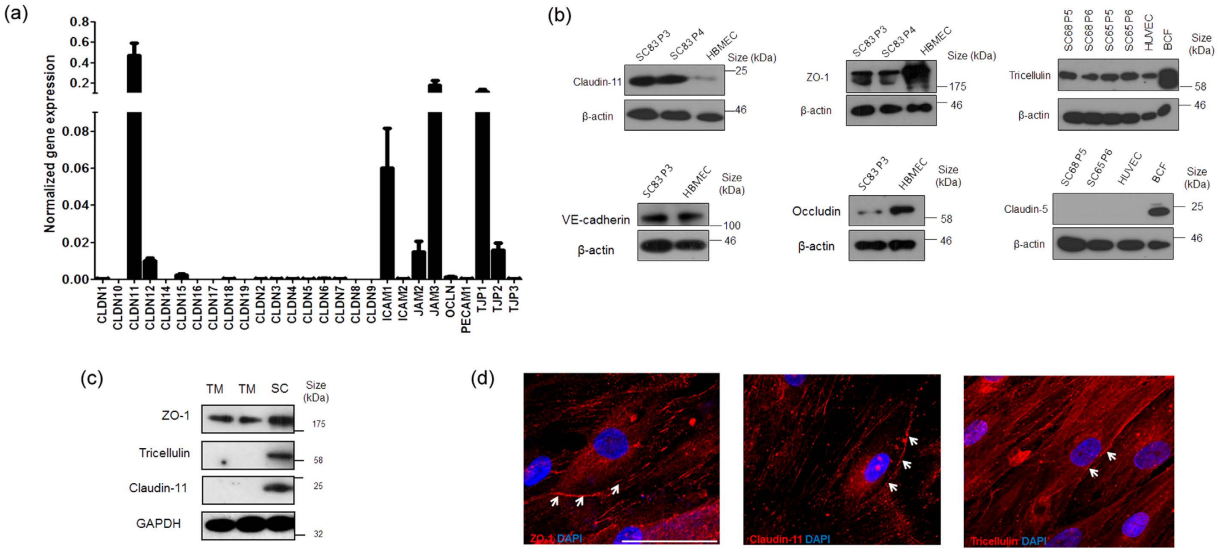

Figure 2. Characterisation of tight junction expression in human Schlemm's canal endothelial cells. **(a)** The human TJs RT^2 Profiler PCR array was used to profile the expression of claudin and adhesion junctional proteins. Bar graphs illustrate average relative gene expression ($2^{-\Delta CT}$) normalised to 5 housekeeping genes from 4 different human SCEC strains. Data are mean ± s.e.m. Note the break in scale for normalised gene expression. **(b)** Protein analysis of claudin-11, ZO-1, tricellulin, VE-cadherin, occludin and claudin-5 in cultured human SCEC. HBMEC = human brain microvascular endothelial cells; BCF = Mouse brain capillary fraction; B-actin as loading control. Different SCEC strains are denoted followed by passage (P) number. **(c)** Tight junction protein expression in TM (TM120 and TM130) and SCEC. GAPDH as loading control. **(d)** White arrow heads illustrate immuno-detection of ZO-1, claudin-11 and tricellulin (Cy3) in cultured human SCEC. Blue = DAPI nuclei staining. Scale bar, 50 μm.

which was not included in the PCR array. Consistent with previous studies[14,28], expression of vascular endothelial (VE)-cadherin was also identified in cultured SCEC (Fig. 2b). However, we did not detect claudin-5 protein expression in cultured SCEC, and only low levels of occludin protein expression were detected, an observation consistent with the PCR array data. Furthermore, we did not detect claudin-11 and tricellulin expression in TM cells (TM120 and 130), whereas both TM and SCEC (SC82) were shown to express ZO-1 protein (Fig. 2c). This is consistent with a previous finding showing that both TM and SCEC express the junction-associated protein, ZO-1[29]. Immunocytochemistry was then undertaken to examine the expression patterns of TJ proteins in confluent SCEC monolayers. We observed discontinuous membrane-specific staining patterns for ZO-1, claudin-11 and tricellulin in cultured SCEC monolayers (Fig. 2d).

Characterisation of expression of tight junction and tight junction associated components in mouse and non-human primate outflow tissues. We performed immunohistochemistry (IHC) on frozen sections of mouse anterior segments to localise the expression of TJ proteins in the outflow region comprising the TM and the inner wall of SC. Immunofluorescent images show tricellulin and ZO-1 staining predominantly localising in the inner wall endothelium of SC (Fig. 3a). In particular, we observed ZO-1 staining to be diffusely distributed in the cytoplasm of SCEC. In regions where part of the endothelium was cut obliquely to the inner wall of SC, continuous junctional strands were displayed around SCEC margins. ZO-1 and tricellulin staining were also detected in the TM region and in the outer wall. In both regions the endothelial cells were connected by TJs. However, we did not detect claudin-11 or claudin-5 staining in the inner wall of SC and TM with the antibodies used in this study (Supplementary Fig. S3). These data indicate that murine outflow tissues may possess a different junctional composition at the inner wall of SC as compared to humans, with the possible absence of claudin-based tight junctional proteins in TM and SCEC. However, the presence of ZO-1 and tricellulin along the inner wall in mice indicates that these proteins may be suitable targets for assessment of effects of TJ down-regulation in mice.

IHC was performed on paraffin sections of African green monkey anterior segments to identify the junctional composition of the outflow region. Hematoxylin and eosin staining (H&E) of the anterior chamber clearly identified the iridocorneal angle and conventional outflow tissues (Fig. 3b). Superimposed immunofluorescent imaging showed strong continuous claudin-11 staining along the endothelial cell margins of the inner wall of SC, highly indicative of TJ barrier function (Fig. 3b). Claudin-11 immunostaining was also present along the outer wall of SC and between TM cells. Similarly, ZO-1 and tricellulin staining were observed in the inner wall endothelium of SC. All three TJ proteins were present between TM endothelial cells, but the staining was less intense than in the inner wall endothelium. In addition, we did not detect claudin-5 expression in SCEC isolated from non-human primates (Supplementary Fig. 4). These data indicate that SCEC in non-human primates possess a similar TJ barrier composition to that found in humans.

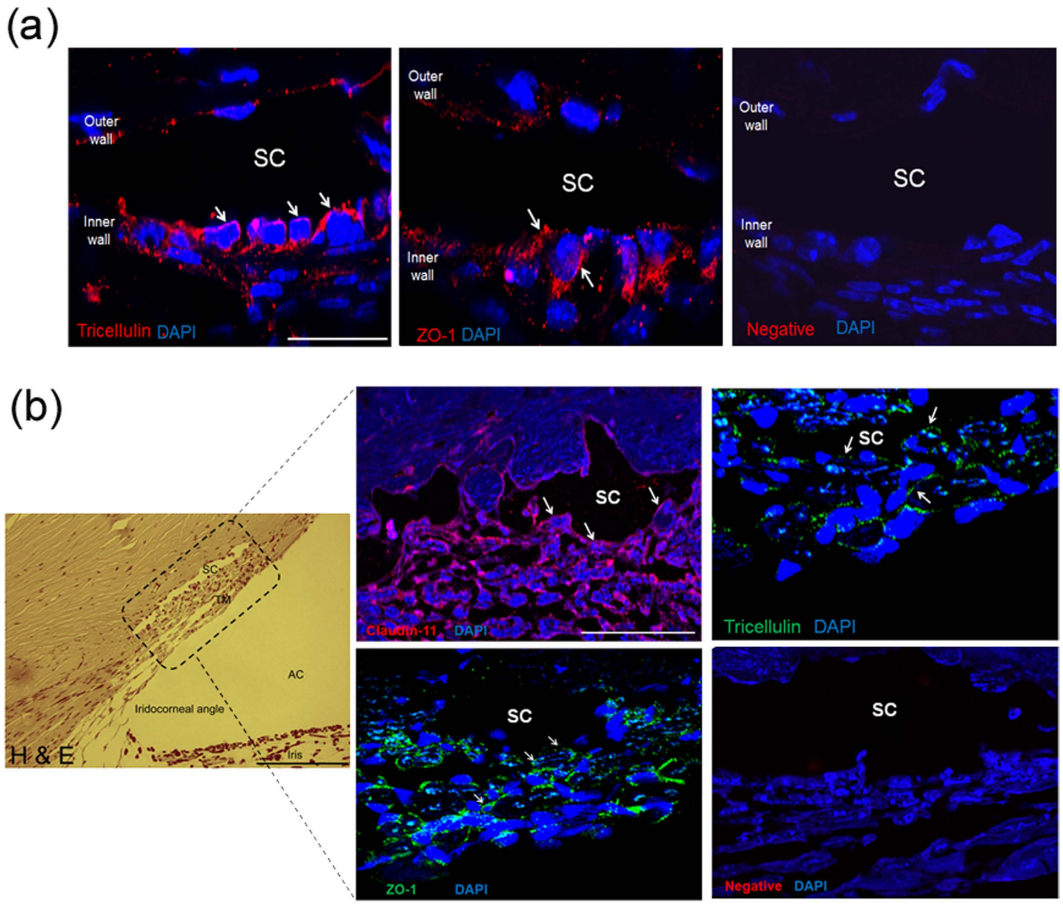

Figure 3. Characterisation of tight junction expression in mouse and non-human primate outflow tissues. (**a**) Immunostaining of tricellulin and ZO-1 in frozen sections of mouse anterior segments. ZO-1 and tricellulin = Cy3 (red); DAPI = blue; SC = Schlemm's canal lumen. Scale bar, 50 μm. (**b**) H&E staining of paraffin monkey anterior segments (left panel). Boxed area depicts superimposed regions shown in immunofluorescence images. AC = anterior chamber; SC = Schlemm's canal lumen; TM = trabecular meshwork. Scale bar, 200 μm. Immunofluorescent images of claudin-11, ZO-1 and tricellulin staining in the inner wall endothelium of SC. White arrows indicate detection of corresponding tight junctions at the inner wall of SC endothelium. Negative = no primary antibody. Scale bar, 50 μm.

Validation of tight junction siRNAs. In order to validate the suppression efficiency of pre-designed siRNAs targeting the human transcripts of claudin-11, ZO-1 and tricellulin, cultured SCEC were separately transfected with 40 nM of each siRNA, and levels of endogenous TJ expression were assessed in a time-dependent manner by Western blot. Time-dependent down-regulation of claudin-11 expression to $5 \pm 3\%$ ($p < 0.0001$), $11 \pm 1\%$ ($p < 0.0001$) and $9 \pm 4\%$ ($p < 0.0001$) (mean ± s.e.m.), was achieved at 24, 48 and 72 h post-transfection respectively, as compared to non-targeting (NT) siRNA (Fig. 4a). ZO-1 expression was reduced to $72 \pm 3\%$ ($p = 0.005$), $64 \pm 4\%$ ($p = 0.0004$) and $49 \pm 18\%$ ($p = 0.02$) at 24, 48 and 72 h post-transfection respectively (Fig. 4b). Furthermore, tricellulin expression was reduced to $75 \pm 0.2\%$ ($p = 0.002$), $81 \pm 6\%$ ($p = 0.012$) and $87 \pm 8\%$ ($p > 0.05$) at 24, 48 and 72 h respectively following siRNA treatment (Fig. 4c). The difference in knockdown efficiencies likely indicates that ZO-1 and tricellulin have slower protein turnover rates than claudin-11 in cultured SCEC. A cell viability assay was performed on transfected SCEC and no change in viability due to siRNA treatment was detected when cells were treated with either 40 or 200 nM of siRNA (Supplementary Fig. S5). siRNAs targeting mouse ZO-1 and tricellulin were also validated and show efficient knockdown of gene expression *in vitro* (Supplementary Fig. S6).

The efficacy of siRNA inhibition *in vivo* was tested in retinas from mice injected intravitreally with siRNA against ZO-1 and tricellulin. RT-PCR carried out on RNA extracted from mouse retinas showed that 12 hr post-injection, tricellulin RNA was significantly reduced to 0.32 fold ($p = 0.049$; Supplementary Fig. S7) compared to eyes injected with NT-siRNA while ZO-1 was reduced to 0.57 fold ($p = 0.048$; Supplementary Fig. S7). This approach using retina was taken because of the difficulty in isolating SC endothelium from mouse eyes to perform a reliable quantification analysis.

We performed cell death assays to assess SCEC viability following siRNA inoculation *in vivo* in mouse outflow tissues. Immunohistochemistry was performed on eyes 48 hours post injection with either targeting or NT siRNA. Approximately 30–40 12 μm sections were each stained by TUNEL and complemented by cleaved

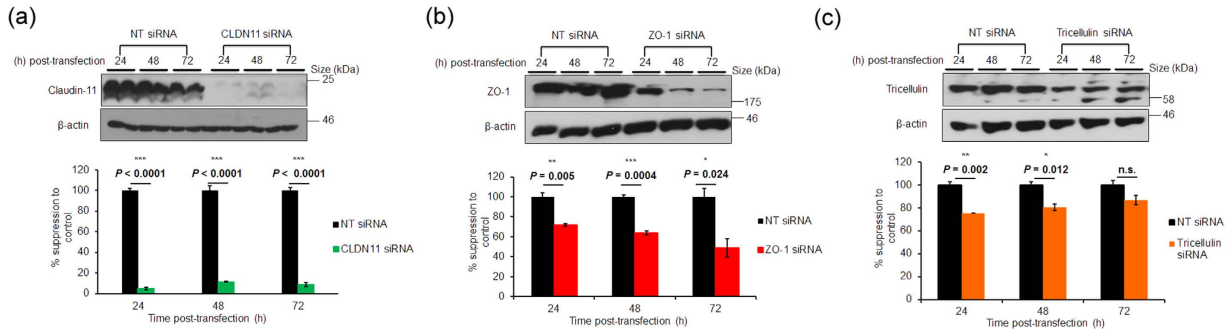

Figure 4. siRNA-mediated down-regulation of tight junction RNA transcripts in cultured human SCEC. Representative Western blots of (**a**) claudin-11, (**b**) ZO-1 and (**c**) tricellulin knockdown in cultured human SCEC over a 72 h period. Corresponding bar graphs depict densitometric analysis of percentage protein normalised to β-actin. NT siRNA = non-targeting siRNA. Data are mean ± s.e.m.; n.s. = $P \geq 0.05$ (n = 4, unpaired *t*-test).

caspase-3 staining as markers of apoptosis for representatives of targeting and non-targeting siRNA. For TUNEL staining, most sections displayed some apoptotic damage in the corneal epithelium. Parts of the ciliary body were also the site of minor labelling, regardless of treatment received. Closer inspection of the angle and outflow tissue itself provided no evidence of any apoptotic cell death in either targeting or NT controls. Cleaved caspase-3 was sparsely detected in the ciliary body, and effectively absent in the angle or outflow tissue in either treatment, correlating with observations by TUNEL (Supplementary Fig. S8).

Effect of down-regulation of tight junctions on SCEC monolayer permeability. In order to address the hypothesis that down-regulation of TJ components in SCEC could be used as a means of modulating the resistance of SC inner wall, transendothelial electrical resistance (TEER) was measured to assess changes in endothelial barrier function in confluent SCEC monolayers following TJ knockdown. SCEC monolayers transfected with claudin-11 or ZO-1 siRNAs showed significant reduction in TEER compared to NT siRNAs at 48 and 72 h post-transfection ($p < 0.001$; Fig. 5a). Furthermore, transfection with a combination of claudin-11 and ZO-1 siRNAs elicited a significant decrease in TEER, and the magnitude of decrease was more profound than those treated with single siRNAs at 48 h post-transfection ($p < 0.001$, Fig. 5a). Similarly, treatment with tricellulin siRNA alone also showed significant reduction of TEER at 48 h post-transfection, and the effect was sustained up to 72 h ($p < 0.001$, Fig. 5b). We next treated SCEC monolayer simultaneously with a combination of three siRNAs targeting claudin-11, ZO-1 and tricellulin, and observed significant reduction in TEER from 24 to 72 h post-transfection as compared to control ($p < 0.001$, Fig. 5c). Measured TEER values can be seen in Supplementary Table S1.

The effect of TJ down-regulation on endothelial permeability was tested in confluent SCEC monolayers using non-ionic macromolecular tracer, FITC-dextran (FD), which can only transverse via the paracellular route. To investigate the size selectivity of paracellular permeability in SCEC monolayers, we first determined the flux of 4, 70 and 150 kDa FD in the basal to apical direction following treatment of monolayers with siRNAs targeting tricellulin. At 24 h post-transfection, we observed no difference between control and treated in apparent permeability co-efficient (P_{app}) to the 4 kDa FD ($\approx 3.66 \times 10^{-6}$ cm/s), which readily passes through the monolayer. In contrast, the 150 kDa FD did not readily cross the monolayer ($\approx 1.23 \times 10^{-8}$ cm/s). The largest decrease in barrier tightness as measured by P_{app} was observed with the 70 kDa FD ($p < 0.0001$, Fig. 5d). These data indicate that down-regulation of tricellulin in SCEC monolayers selectively opens the paracellular route to macromolecules of 70 kDa. Following this, we treated SCEC monolayers with siRNAs targeting other TJs, and observed that down-regulation of claudin-11 ($p < 0.0001$), ZO-1 ($p < 0.0001$), as well as tricellulin ($p < 0.0001$) significantly increased paracellular flux of 70 kDa FD, as compared to controls (Fig. 5e,f). In addition, P_{app} (70 kDa FD) was observed to be significantly greater in monolayers treated with a combination of ZO-1 and tricellulin siRNAs than control ($p < 0.0001$), and compared to those treated singly with either ZO-1 or tricellulin siRNA ($p < 0.001$) (Fig. 5f). Furthermore, treatment with a combination of siRNAs targeting three TJs simultaneously also increased P_{app} of SCEC to 70 kDa FD ($p = 0.0004$ vs. control; Fig. 5g). We used primary SCEC strains from different donor eyes for flux assays in Fig. 5e–g, and as a consequence, we observed natural variability in baseline P_{app} values and responses to TJ down-regulation from different strains. Collectively, these data demonstrate that claudin-11, ZO-1 and tricellulin contribute to the barrier function of cultured human SCEC, and that siRNA-mediated down-regulation of these cellular junctional proteins significantly alters endothelial cell barrier integrity and permeability.

Ultrastructural analysis of the inner wall endothelium of SC following treatment with siRNAs. To examine how siRNA treatment affects the continuity of the inner wall of SC, ultrastructural investigation of TJs between SC cells was performed by TEM. Six wild type C57BL/6J mice were intracamerally injected with a combination of 1 μg ZO-1 siRNA and 1 μg of tricellulin siRNA, and contralateral eyes were injected with 2 μg of NT siRNA. 48 h post-injection, all animals were sacrificed with eyes enucleated immediately after death and immersed for TEM investigation. As can be seen in Fig. 6a,b, the inner wall of SC in both treated and control

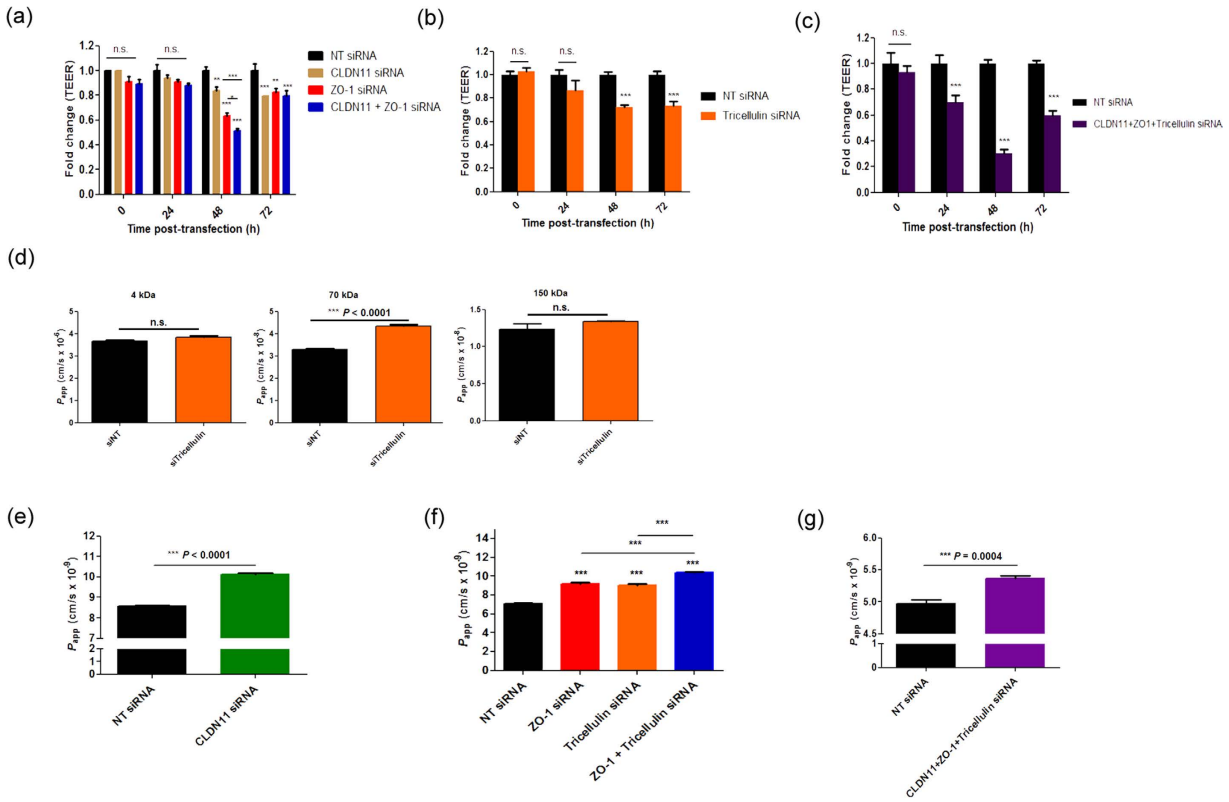

Figure 5. siRNA-mediated down-regulation of tight junction RNA transcripts modulates TEER and paracellular permeability in cultured SCEC monolayers. (**a**) Effect of siRNA-mediated knockdown of TJ RNA transcripts on TEER across human SCEC monolayers. 40 nM of siRNA targeting claudin-11, ZO-1, or in combination were transfected into human SCEC, and TEER was measured 24, 48 and 72 h post-transfection. $^{*}P < 0.05$, $^{**}P < 0.01$, $^{***}P < 0.001$, n.s. $P \geq 0.05$ (n = 3 separate cell transfection, two way analysis of variance (ANOVA) followed by Bonferroni's multiple comparison post-tests). Data are fold change ± s.e.m. (**b**) TEER measurements following treatment with tricellulin siRNAs in cultured SCEC monolayers (n = 5 separate cell transfections, two way ANOVA followed by Bonferroni's multiple comparison post-tests). $^{***}P < 0.0001$. Data are fold change ± s.e.m. (**c**) TEER measurements following treatment of SCEC monolayers with a combination of claudin-11, ZO-1 and tricellulin siRNAs (n = 7 separate cell transfections, two way ANOVA followed by Bonferroni's multiple comparison post-tests). $^{***}P < 0.001$. n.s. = $P > 0.05$. (**d**) Cultured SCEC monolayers demonstrate size selectivity. Apparent permeability co-efficient (P_{app}, cm/s) of 4, 70 and 150 kDa FITC dextrans was determined following treatment with siRNAs targeting tricellulin. ($^{***}p < 0.0001$; n = 3). n.s. = $P \geq 0.05$ (**e**,**f**,**g**) P_{app} of 70 kDa FITC-dextran through human SCEC monolayers following treatment with claudin-11, ZO-1 and tricellulin siRNAs, or in combination. NT = non-targeting. Data are mean ± s.e.m. Note the break in scale for P_{app} (**e**,**f**). (**e**) ***P < 0.0001, n = 6. (**f**) ($^{***}P < 0.0001$, n = 4). (**g**) ***P = 0.0004, n = 6. (unpaired Student's *t*-test for left and right bar graphs; one way ANOVA followed by Bonferroni's *post hoc* test for middle bar graphs).

eyes appeared similar. The inner wall was continuous without loss of cells or apparent cellular damage, and in both control and treated eyes there were no swollen cells that would indicate necrosis. There were also no cellular extensions and nuclear densifications or fragmentations that would indicate apoptosis.

To more clearly visualize cell membranes and junctions, sections were stained with UAR-EMS rather than uranyl acetate (see materials and methods). This staining allowed better visualization of the intercellular junctions and revealed that intercellular clefts between neighbouring SC cells were more often open in eyes treated with targeting siRNAs than in controls, indicating an absence or weakening of the TJ complexes. Open clefts exhibited a typical width of 10–20 nm without any contact between neighbouring cell membranes, while closed clefts exhibited a focal fusion between neighbouring cell membranes often surrounded by small cytoplasmic filaments (Fig. 6c,d). Quantification of intercellular junctions was performed by 2 independent observers, who examined TEM sections at 80,000x along the anterior-posterior extent of the inner wall from 4 regions of each eye (n = 6 treated and 5 control eyes; one control eye was removed as, for technical reasons, not all 4 regions could be evaluated). Each section contained between 10–30 cells, and each region was separated from another by at least several hundred microns, such that each region could be considered an independent sample. This quantification revealed that approximately 33% of intercellular junctions were open in eyes treated with targeting siRNA (Table 1). In contrast, only approximately 2% of intercellular junctions were open in contralateral eyes treated with non-targeting siRNA (Table 2), and this difference was statistically significant (p = 0.004, unpaired Student's

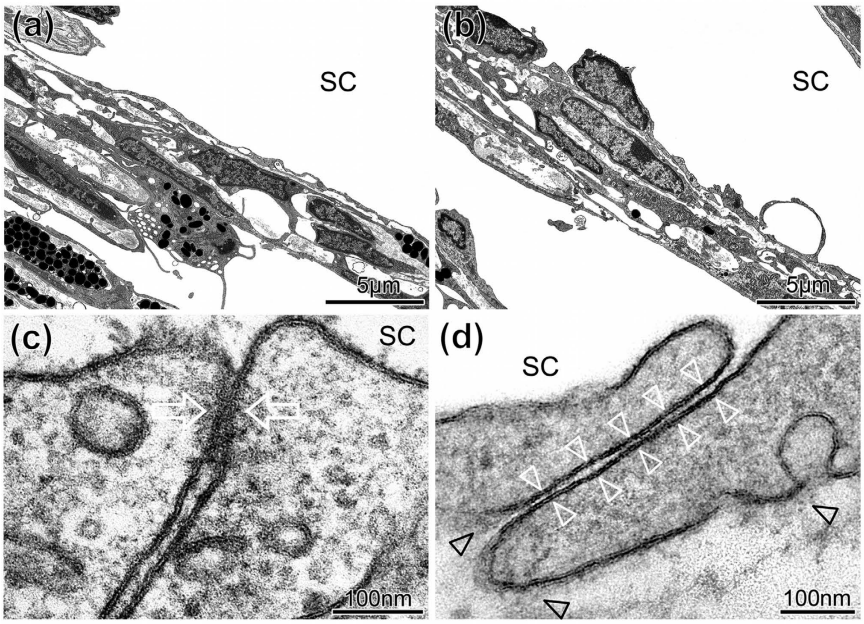

Figure 6. Transmission electron microscopic analysis of sagittal sections of the inner wall of SC following siRNA treatment. (**a**,**b**) Representative sagittal sections through the inner wall of Schlemm's canal (SC) and outer trabecular meshwork (TM) of a mouse eye treated with **(a)** non-targeting (NT) or **(b)** targeting (T) siRNA illustrating intact cells and an intact and continuous inner wall endothelium that appeared similar in both cases. The inner wall endothelium is connected to the underlying ECM so that no ballooning was visible. (**c**,**d**) High magnifications of sagittal sections through intercellular clefts along the inner wall endothelium of SC showing examples for junctions quantitatively evaluated as closed **(c)** with fusion between the neighbouring cell membranes (arrows) or open clefts **(d)** where the cell membranes of adjacent endothelial cells were clearly separated along the entire cleft length (white arrowheads). Despite the open clefts, adhesions to subendothelial matrix (black arrowheads) were preserved. The number of open intercellular clefts was quantified (see Tables 1 and 2).

	Region 1		Region 2		Region 3		Region 4		
Sample	N total	N open	N total	N open	N total	N open	N total	N open	% open
C4 NEP T	15	4	17	3	21	5	24	9	27%
C4 REP T	18	15	14	3	22	17	10	5	63%
C4 LEP T	9	5	26	1	18	9	12	3	28%
C5 LEP T	26	10	15	3	24	4	20	4	25%
C6 LEP T	25	11	31	11	15	4	18	2	31%
C6 NEP T	25	2	29	9	16	4	30	8	23%
								Average	33%
								SD	25%

Table 1. Quantification of total and open intercellular clefts along the inner wall in treated eyes that were immersion fixed immediately after death.

t-test). These data reveal that the siRNA treatment is opening intercellular clefts along the inner wall of SC *in vivo*, presumably by affecting TJs.

It is feasible that siRNA treatment may also have affected adherens or cell-matrix junctions that provide mechanical support between endothelial cells and to the subendothelial tissue. Indeed, TJs and adherens junctions are coupled, and disassembly of adherens junctions often leads to disassembly of TJ[30]. To determine whether siRNA had affected these other junctional types, we examined for disconnections between the inner wall and subendothelial tissue that typically leads to inner wall 'ballooning' as observed following treatment with Na_2-EDTA[31,32]. In none of the 4 regions examined per eye in either case, did we observe any ballooning of the inner wall (Fig. 6a,b). Even in areas with open intercellular clefts, the basal cell membranes of the endothelial cells were still attached to the underlying extracellular matrix (ECM) (Fig. 6d). This implies that the cell-matrix adhesions remained intact. We also examined for adhered platelets, which is a sign of inner wall damage, as platelets often seal endothelial gaps where ECM is exposed to the lumen of SC[31,32]. No adhering platelets were observed in any region of any eye.

Sample	Region 1		Region 2		Region 3		Region 4		% open
	N total	N open	N total	N open	N total	N open	N total	N open	
C4 NEP NT	8	0	22	0	17	2	28	0	3%
C4 REP NT	17	1	20	0	13	0	18	0	1%
C5 LEP NT	21	0	26	0	14	0	19	0	0%
C6 LEP NT	11	1	30	0	26	0	9	0	1%
C6 NEP NT	20	1	17	0	29	0	31	1	2%
								Average	2%
								SD	1%

Table 2. Quantification of total and open intercellular clefts along the inner wall in control eyes that were immersion fixed immediately after death.

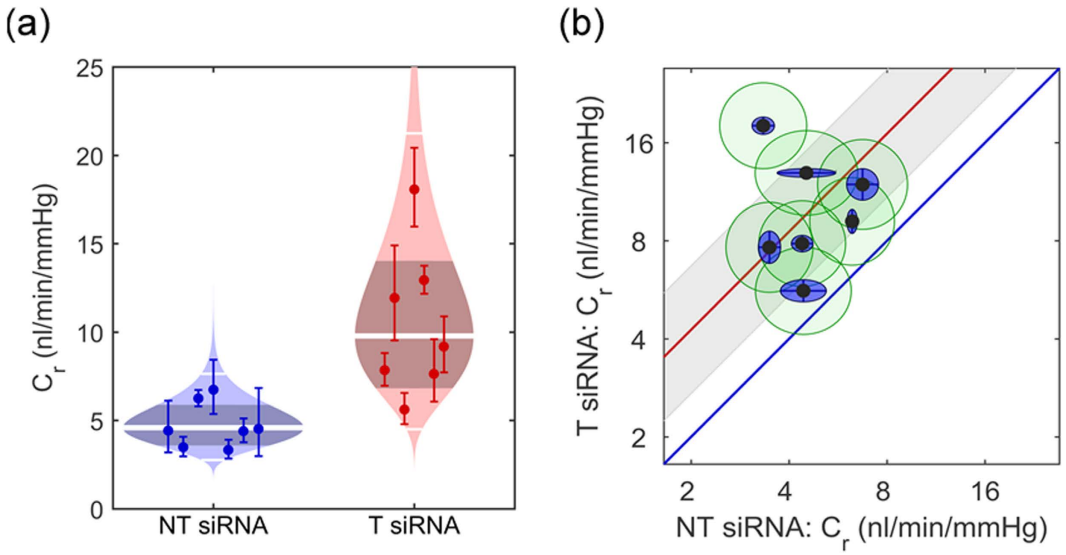

Figure 7. Effect of down-regulation of tight junction RNA transcripts on outflow facility *ex vivo*. (a) 'Cello' plots showing the individual values and statistical distribution of outflow facility at 8 mmHg (C_r) for eyes treated with either non-targeting (NT) siRNA or a combination of ZO-1 and tricellulin targeting (T) siRNA. Each individual point represents a single eye, with error bars showing the 95% confidence intervals on C_r arising from the regression analysis. For each condition, the predicted log-normal distribution is shown, with the thick central white band showing the geometric mean and the thinner white bands showing two geometric standard deviations from the mean. The shaded central region indicates the 95% confidence interval on the mean. **(b)** Paired facility plot: each data point represents one pair of eyes, with C_r for the treated T siRNA eye on the Y-axis and the C_r for contralateral control NT-siRNA eye on the X-axis. The red line shows the average difference between contralateral eyes, with its confidence interval in grey, whilst the blue line represents the case of identical facility between contralateral eyes, corresponding to no effect due to T siRNA. All data points are above the blue unity line, indicating that the facility was higher in the treated eyes compared to the controls; n = 7, p = 0.006. Inner blue ellipses show the 95% confidence intervals on C_r arising from the regression analysis, whilst the green outer ellipses show additional uncertainty due variability between contralateral eyes, estimated from 10 pairs of C57BL/6J eyes perfused only with glucose supplemented PBS[36].

Effect of down-regulation of tight junctions on outflow facility *ex vivo*. In order to evaluate whether down-regulation of TJs increases outflow facility, studies were performed in mouse eyes since the conventional outflow pathway of mice resembles that of human morphologically, physiologically and pharmacologically[33–35]. We targeted ZO-1 and tricellulin based on the IHC data obtained in Fig. 3a. Seven wild type C57BL/6J mice were intracamerally injected with a combination of 1 μg ZO-1 siRNA and 1 μg of tricellulin siRNA, and contralateral eyes were injected with 2 μg of NT siRNA. 48 h post-injection, all animals were sacrificed and enucleated eyes were perfused in pairs using the recently developed *iPerfusion*[36] system to measure outflow facility, calculated from the flow measured over multiple pressure steps (Supplementary Fig. S9). Outflow facility in the siRNA treated eyes was increased compared to eyes receiving NT siRNA (Fig. 7a). Figure 7b shows the paired facility data where the facility of the treated eye is plotted against that of the contralateral control eye. In all cases, the facility of the treated eye was elevated compared to control (n = 7 pairs), exhibiting an average facility increase of 113% (confidence interval [35, 234]%, p = 0.0064, facility values for each pair of eyes are provided in Supplementary Table S2). These data demonstrate that down-regulation of TJ components within the

conventional outflow pathway significantly increases conventional outflow facility in mouse eyes *ex vivo*. To investigate the long-term effect of TJ down-regulation, we perfused eyes from animals 8 weeks post-injection and we observed no difference in outflow facility between treated and control eyes (average facility increase of 9.2%, confidence interval [−14.22, 32.62]%, $p > 0.05$, $n = 4$ pairs, facility values for each pair of eyes are provided in Supplementary Table S2). This observation indicates that a single injection of siRNAs enables transient and reversible modulation of outflow facility in the anterior chamber of murine eyes.

Discussion

AH exiting the anterior chamber via the conventional outflow pathway passes through the tissues of the TM and into the SC lumen by crossing its endothelial barrier. Conceptually, loosening the TJs that bind endothelial cells could render the barrier more permeable resulting in reduced outflow resistance. However, this targeted approach has not been previously assessed in regard to AH outflow. The current study focused on identifying TJ components present in human, murine and non-human primate outflow tissues that might serve as plausible targets for siRNA-mediated down-regulation. A number of such targets were identified in primary cultures of human SCEC, disruption of which has previously been associated with altering endothelial cell permeability in other cell systems[37–39].

The TJ profile found in human SCEC identifies claudin-11 and tricellulin as SC specific TJ related proteins not present in TM cells, while ZO-1 has been found to be present in both SCEC and TM cells as previously reported[29,40]. Previous studies have also reported the identification of specific protein markers that are either exclusively expressed in the inner wall endothelium of SC, or differ appreciably in their expression from TM cells[14,28,41,42]. Owing to the high level of claudin-11 expression found in SCEC as compared to TM cells, this claudin-based TJ may also be used as a specific marker for identifying SC cells.

The association of both claudin-11 and tricellulin with SCEC is of significance because both TJs have been associated with maintenance of barrier function. Several studies on paracellular tightness have demonstrated that claudin-11 modulates paracellular cation permeability[39,43,44] and its knockdown increases TEER in human corpus cavernosum endothelial cells[45]. On the other hand, transcript knockdown studies have shown that the inhibition of tricellulin leads to instability of TJs[46], whereas tricellulin overexpression is associated with reduced permeability to macromolecules[47]. Accordingly, we observed that siRNA-mediated knockdown of selected TJ decreases transendothelial resistance and increases permeability to 70 kDa FD in cultured human SC cell monolayers. In particular, these effects were more profound when a combination of siRNAs was used, suggesting a synergistic effect in increasing paracellular permeability following down-regulation of a range of TJs.

Paracellular pathways have been well established to possess defined values of electrical conductance as well as charge and size selectivity[48]. For example, the junctional complexes comprising of tight and adherens junctions between cerebral endothelial cells enable the blood-brain barrier to regulate the entry of blood-borne molecules and preserve ionic homeostasis within the brain microenvironment[49]. Our size selectivity data indicate that SC endothelial barriers have restrictive properties to regulate paracellular passage, and direct alteration of TJ complex only allows the passage of dextrans of up to 70 kDa, representing a biologically relevant size comparable to albumin (66 kDa), which does not cross the paracellular route readily in unperturbed endothelial monolayers[50]. We have shown that TJ barriers are formed and localised along the endothelial cells of the inner wall of SC *in vivo*. In conjunction with *in vitro* permeability data, TJs in the inner wall endothelium of SC are identified as possibly playing a pivotal role in contributing to paracellular movement of AH and solutes across the endothelial layer. Similarly to human SCEC, non-human primates also express ZO-1, claudin-11 and tricellulin in the inner wall of SC. However, we did not detect claudin-11 expression in the mouse outflow pathway, which suggests differential expression patterns between species.

In order to prove the efficacy of the siRNA in an *in vivo* system, ZO-1 and tricellulin siRNA were injected into the anterior chambers of mice. We show that knockdown of transcripts encoding TJs in the conventional outflow pathway increases AH outflow facility in wild type mice, and that this effect is associated with the presence of an increased number of open intercellular clefts between SCEC. It is therefore reasonable to infer that opening of intercellular clefts is responsible for the increased outflow facility measured *ex vivo*. In contrast to studies using EDTA to disrupt cellular junctions along the inner wall[31,32], no eyes treated with siRNA exhibited signs of necrosis or apoptosis, and there were no platelets adhering to the inner wall. This indicates that the endothelial cell membranes remained intact and the subendothelial ECM was not exposed to the lumen of SC.

Our *in vivo* data also reinforce that the hydraulic conductivity of the inner wall endothelium of SC is maintained by the adhesive forces produced at the endothelial cell-cell junctions between TJ proteins[14,28]. It is therefore correct to propose that factors which change the adhesive properties of TJ proteins in the inner wall of SC may alter the existing behaviour of the outflow pathway. To illustrate this point, we have preliminary data demonstrating higher claudin-11 and ZO-1 expression in glaucomatous SCEC monolayers as compared to healthy controls (Supplementary Fig. S10a). In addition, cultured glaucomatous SCEC strains displayed higher TEER values than healthy strains (Supplementary Fig. S10b). The increase in TJ expression found in glaucomatous SCEC suggests that altered barrier function in the inner wall of SC may negatively impact on conventional outflow behaviour.

While conventional adeno-associated viruses (AAV) have been shown to be inefficient in transducing cells of the outflow tissues, self-complementary AAV have been reported to be effective in such transduction[51,52]. It is of note that AAV expressing inducible short hairpin RNAs (shRNA) targeting claudin-5, or a combination of claudin-5 and occludin have been used to transfect cerebral and retinal tissues, and that down-regulation of these TJ vascular endothelial cell components renders the blood-brain and inner blood-retina barriers reversibly permeable to compounds up to 1 kDa, or 5 kDa respectively[53,54]. Should it prove possible using this technique to periodically activate virus expressing shRNAs within SCEC using an inducible promoter, expression of such shRNA could in principle be used as a means of periodically increasing outflow facility in cases of POAG in which patients fail to achieve target IOP with conventional medications. Alternatively, episcleral delivery of

siRNA, where materials can be delivered non-invasively into the outflow tissues in a retrograde fashion as an outpatient procedure[55], might represent an attractive alternative, thus avoiding the necessity of introducing a viral vector into the anterior chamber to secure viral-mediated shRNA expression. To explore the feasibility of an episcleral delivery approach, we have successfully achieved delivery of biotin conjugated tracer molecules to the conventional outflow pathway via the episcleral route in mice. Taken together, results from this study support the concept that endothelial TJs of the inner wall of SC are an attractive target upon which to base future attempts to increase AH outflow in cases of ocular hypertension.

Materials and Methods

Cell Culture. Human SCEC and TM cells were isolated, cultured and characterised as previously described[56,57]. SCEC strains used in this study were SC65, SC68, SC73, SC76, SC77, SC82 and SC83. TM93 was used for RNA analysis, whereas TM120 and TM130 were used for protein analysis. All SCEC and TM cells were used between passages 2 and 6. SCEC were cultured in low glucose Dulbecco's modified Eagle medium (Gibco, Life Sciences) supplemented with 10% *Performance Plus* foetal bovine serum (FBS) (Gibco, Life Sciences), 1% Pen/Strep glutamine (Gibco, Life Sciences), in a 5% CO_2 incubator at 37 °C. TM cells underwent a differentiation step by plating at full confluency for one week in media containing 10% FBS, and changed over to media containing 1% FBS for an additional week prior to experimentation. Cultured cells were passaged with trypsin-EDTA (Gibco-BRL) to maintain exponential growth.

Human tight junction PCR array. The human TJ RT^2 Profiler PCR array (PAHS-143ZA, Qiagen) was used to profile the expression of 84 key genes encoding proteins that form selective barriers between epithelial and endothelial cells to regulate size selectivity, polarity, proliferation and differentiation. Total RNA was extracted from four different human SCEC strains (SC65, 68, 76 and 77) at passages 3 to 5 using RNEasy Mini Kit (Qiagen) according to manufacturer's protocol. Genomic DNA contamination was eliminated by DNase treatment. Total RNA was reverse-transcribed into cDNA using RT^2 First Strand Kit (Qiagen). The Threshold cycle (Ct) values of different passage numbers from each SCEC strain were determined and averaged using ABI Prism 7700 Sequence Detector. The mean normalised expression ($2^{-\Delta Ct}$) of genes encoding claudin and adhesion junctional proteins was determined and analysed using the online Qiagen RT^2 Profiler PCR Array Data Analysis software. Normalised gene expression was calculated by using the equation: $2^{-\Delta Ct} = 2^{-[Ct(\text{gene of interest}) - Ct(\text{Housekeeping genes})]}$. Normalisation was carried out with five housekeeping genes (*ACTB, B2M, GAPDH, HPRT1 and RPLP0*) included in the PCR array. The $2^{-\Delta\Delta CT} = 2^{-\Delta Ct\ \text{treated}}/2^{-\Delta Ct\ \text{control}}$ method was used to calculate fold changes for each gene as difference in gene expression[58].

Western Blot. Protein lysates were isolated from cultured cells in protein lysis buffer containing 1 M Tris pH 7.5, 1 M NaCl, 1% NP-40, 10% SDS, 1X protease inhibitor cocktail (Roche). The homogenate was centrifuged at 10,000 r.p.m. (IEC Micromax microcentrifuge, 851 rotor) at 4 °C for 20 min and the supernatant was stored at −80 °C until use. Protein concentration was determined by BCA Protein assay kit (Pierce, IL, USA) with bovine serum albumin (BSA) at 2 mg/ml as standards on 96-well plates according to the manufacturer's protocol. 30–50 μg of total protein was loaded in each lane. Protein samples were separated by electrophoresis on 7.5–10% SDS–PAGE under reducing conditions and electro-transferred to PVDF membranes. After blocking with 5% blotting grade blocker non-fat dry milk in TBS for 1 h at room temperature, membranes were incubated overnight at 4 °C with the following Rabbit polyclonal primary antibodies: anti-oligodendrocyte specific protein antibody (1:500; Abcam); anti-ZO-1 antibody (1:250; Invitrogen), anti-tricellulin C-terminal antibody (1:125; Invitrogen), anti-occludin antibody (1:500, Invitrogen) and anti-VE-cadherin antibody (1:1000; Abcam). Blots were washed with TBS and incubated with horse radish peroxidase-conjugated polyclonal rabbit IgG secondary antibody (Abcam). The blots were developed using enhanced chemiluminescent kit (Pierce Chemical Co.) and exposed to Fuji X-ray film. Each blot was stripped with Restore Western Blot Stripping Buffer (Pierce) and probed with rabbit polyclonal to β-actin or GAPDH (Abcam) as loading controls. Protein band intensities were quantified by scanning with a HP Scanjet Professional 10000 Mobile Scanner and analysed using *Image J* (Version 1.50c). The percentage reduction in band intensity was calculated relative to the control non-targeting siRNA, which was standardised to represent 100% and normalised against β-actin.

Immunocytochemistry. Human SCEC were grown on Lab-Tek II chamber slides and fixed in 4% paraformaldehyde (pH 7.4) for 20 min at room temperature and then washed with PBS for 15 min. Cell monolayers were blocked in PBS containing 5% normal goat serum and 0.1% Triton X-100 at room temperature for 20 min. Primary antibodies were diluted at 1:100 in blocking buffer and incubated overnight at 4 °C. Secondary antibodies diluted at 1:500 were then incubated for 2 h at room temperature in a humidity chamber. Following incubation, chamber slides were mounted with aqua-polymount (Polyscience) after nuclei-counterstaining with DAPI. Fluorescent images of SCEC monolayers were captured using a confocal microscope (Zeiss LSM 710), and processed using imaging software ZEN 2012.

Immunohistochemistry for frozen sections. Enucleated mouse eyes were fixed in 4% paraformaldehyde (pH 7.4) overnight at 4 °C on a rotating device. Posterior segments of the eye and the lens were removed and anterior segments were then washed with PBS for 15 min and sequentially submerged in 10, 20 and 30% sucrose. Dissected anterior segments were then suspended in specimen blocks with OCT solution (Tissue-Tek) and frozen in a bath of isopropanol submerged in liquid nitrogen. Frozen anterior segments were sectioned using a cryostat (Leica CM 1900) to 12 μm thickness. Sections were collected on Polysine® slides (Menzel-Glazer). To detect TJ proteins, sections were blocked for 20 min at room temperature in PBS containing 5% goat serum and 0.1% Triton-X, and incubated with the corresponding antibodies at 1:100 dilutions overnight at 4 °C in a humidity chamber. All sections were then washed three times in PBS and incubated with Cy-3 labelled anti-rabbit IgG

antibody at 1:500 (Abcam) for 2 h at room temperature in a humidity chamber. Following incubation, sections were washed with PBS and mounted with aqua-polymount (Polyscience) after nuclei-counterstaining with DAPI. Anterior segments were visualised using a confocal microscope (Zeiss LSM 710).

Immunohistochemistry for paraffin embedded sections. Paraffin sections of African green monkey (*Chlorocebus Sabeus*) anterior segments were rehydrated by immersion in the following solutions: twice for 2 min each in Histoclear solution; 100% ethanol for 1 min; 95% ethanol for 1 min; 70% ethanol for 1 min; deionised water for 1 min; washing twice for 5 min in PBS. For antigen retrieval, paraffin sections were heated to 95 °C for 10 min in citrate buffer (Sodium citrate, pH 6). Paraffin sections were then blocked and stained as described above.

siRNAs. All *in vivo* predesigned siRNAs used in this study were synthesised by Ambion and reconstituted as per manufacturer's protocol. siRNA identification numbers are as follows: human claudin-11 siRNA (ID number: s9925), human ZO-1 siRNA (ID number: s14156), human MARVELD2 siRNA (ID number: s45794), mouse ZO-1 siRNA (ID number: s75175), mouse MARVELD2 siRNA (ID number: ADCSU2H). Silencer Negative control siRNA (Ambion) was used as a non-targeting control in knockdown studies.

Cell viability assay. SCEC were grown to confluency on a 96-well plate. Cells were transfected with siRNA in quadruplicate using Lipofectamine RNAiMax reagent as outlined by the manufacturer (Life Technologies) at both 1 pmol/well (40 nM) and 5 pmol/well (200 nM). Cells were left for 48 hours, apart from a media change after 24 hours. CellTitre 96 AQueous One Solution Reagent (Promega) was thawed and mixed with culture medium at a 1:5 dilution. Cells were incubated with this mixture for a period of 2 hours, before transferring the media to a fresh 96-well plate. Absorbance of each well was recorded at 450 nm on a spectrophotometer (Multiskan FC, THermo Scientific). After blanking against wells with reagent and no cells, each treatment group was presented relative to a negative control containing no siRNA. A positive control was achieved by incorporating 1% SDS into the media-reagent mixture. A one-way ANOVA with a Tukey's post-test was performed on the data set.

Measurement of SCEC monolayer transendothelial electrical resistance (TEER). TEER was used as a measure of TJ integrity by the human SCEC monolayers as previously descrived[54]. In brief, human SCEC (1×10^4 cells per well) were grown to confluency on Costar HTS Transwell-polyester membrane inserts with a pore size of 0.4 μm. The volume of the apical side (inside of the membrane inserts) was 0.1 ml and that of the basal side (outside of the membrane inserts) was 0.6 ml. Confluent cells were then transfected in triplicates with 40 nM of claudin-11, ZO-1 and tricellulin siRNAs, or in combination, using Lipofectamine RNAiMax reagent as outlined by the manufacturer (Life Technologies). Non-targeting siRNA was used as a control. 48 h post-transfection, TEER values were determined using an EVOM resistance meter with Endohm Chamber (World Precision Instruments) and a Millicell-Electrical Resistance System. For measurement of TEER, both the apical and basolateral sides of the endothelial cells were bathed in fresh growth medium at 37 °C, and a current was passed across the monolayer with changes in electrical resistance, which was reported as $\Omega.cm^2$ after correcting for the surface area of the membrane (1.12 cm). Electrical resistance was measured in triplicate wells, and the inherent resistance of a blank transwell was subtracted from the values obtained for the endothelial cells.

Cell permeability assay using FITC-dextran. Human SCEC were prepared and treated using the same method for TEER measurement as described above. Transwell permeability assays were carried out as previously described[54]. In brief, 4 kDa, 70 kDa and 150 kDa fluorescein isothiocyanate (FITC)-conjugated dextran (FD) (Sigma) was applied at 1 mg/ml to the basal compartment of the transwells. Sampling aliquots of 0.1 ml were collected every 15 min for a total of 120 min from the apical side for fluorescence measurements and the same volume of culturing media was added to replace the medium removed. FITC fluorescence was determined using a spectrofluorometer (Optima Scientific) at an excitation wavelength of 485 nm and an emission wavelength of 520 nm. Relative fluorescence units (RFU) were converted to values of nanograms per millilitre using FITC-dextran standard curves, and were corrected for background fluorescence and serial dilutions over the course of the experiment. The apparent permeability co-efficient ($P_{app,}$ cm/s) for each treatment was calculated using the following equation:

$$P_{app} = (dM/dt)/(A \times C_0),$$

where dM/dt (μg/s) is the rate of appearance of FD on the apical side from 0 min to 120 min after application of FD. C_0 (μg/ml) is the initial FD concentration on the basal side, and A (cm^2) is the effective surface area of the insert. dM/dt is the slope calculated by plotting the cumulative amount of (M) versus time.

Animal Husbandry. The use of animals and injections carried out in this study were in accordance with the European Communities Regulations 2002 and 2005 and the Association for Research in Vision and Ophthalmology statement for the use of Animals in Ophthalmic and Vision Research, and was approved by the institutional Ethics Committee. In this case, all procedures carried out at Imperial College London and Trinity College Dublin were approved by the UK Home Office and by the Health Products Regulatory Authority of the Irish Medicines Board (project authorisation AE19136/P017) respectively. Male C57BL/6J mice (Charles River Laboratories, UK) of age 10 to 12 weeks were used. *Ex vivo* perfusions and intracameral injections were done under the UK Home Office Project at Imperial College London. Animals were brought into the animal facility one week prior injections for an acclimatisation period. Mice were housed in individually ventilated cages with 5 mice per cage. They were provided with food and water *ad libitum* and were under 12 h light/dark cycles (7 am to 7 pm) at 21 °C.

Intracameral injection. Adult C57BL/6J mice of 10 to 12 weeks of age were anaesthetised by intra-peritoneal injection of medetomidine hydrochloride (Domitor) and ketamine (0.66 and 66.6 mg/kg body weight, respectively). Pupils were dilated with 2.5% tropicamide and 2.5% phenylephrine eye drops. Glass micro-capillaries (outer diameter = 1 mm, inner diameter = 0.58 mm; World Precision Instruments) were pulled using a micropipette puller (Narishige PB-7). Under microscopic control, a pulled blunt-ended micro-glass needle (tip diameter ~100 μm) was first used to puncture the cornea to withdraw AH. Immediately after puncture, a pulled blunt-ended micro-glass needle attached to a 10 μl syringe (Hamilton, Bonaduz) was inserted through the puncture, and 1.5 μl of PBS containing 1 μg of ZO-1 siRNA and 1 μg of tricellulin siRNA was administered into the anterior chamber to give a final concentration of 16.84 μM. Contralateral eyes received an identical injection of 1.5 μl containing the same concentration of NT siRNA. Following surgery, a reversing agent (1.5 mg/kg body weight, atipamezole hydrochloride) was delivered by intra-peritoneal injection. Fusidic gel was applied topically to the eye as antibiotic and Vidisic gel was also applied topically as a moisturiser. Furthermore, 5 mg/kg enrofloxacin antimicrobial (Baytril; Bayer Healthcare) was injected subcutaneously.

Apoptosis markers staining. IHC was performed on perfused eyes 48 hours post injection with either targeting or non-targeting siRNA. Approximately 30–40 12 μm sections were each stained by TUNEL and complemented by cleaved caspase-3 staining as markers of apoptosis for representatives of targeting and non-targeting siRNA. Eyes were fixed and prepared for cryosectioning as described before. TUNEL staining was performed as per manufacturers protocol (*in situ* Cell Death Detection Kit, POD, Roche), for positive controls, slides treated with Dnase-1 for 10 minutes at room temperature after permeabilisation and prior to antibody labelling. Cleaved caspase-3 staining was performed as described before using cleaved caspase 3 marker antibody (#9661, Cell Signalling Technology), positive controls were obtained by perfusing wild type eyes *ex vivo* for 24 hours at 35 °C with 200 ng/ml of mouse IL-1B and 100 ng/ml of human TNF-α in DMEM to induce apoptosis.

Transmission electron microscopy (TEM). All eyes were immersion fixed in Karnovsky's solution initially and post-fixed in Ito's solution. The eyes were embedded in Epon and semi-thin sagittal sections were cut through the whole globe. Ultrathin sections of SC and TM were cut sagitally from one side of the eye first, and then another ultrathin section approximately 1mm deeper was cut. If possible, this section was taken from the other side of the eye. In the small mouse eye, this process could be repeated four times. In this way, different parts of the circumference of the eye were evaluated. Different staining methods were investigated to visualise cell membranes, and the best results were obtained using UAR-EMS (Science Services, Munich, Germany). In ultrathin sections of the entire anterior posterior length of the inner wall from all four regions of treated eyes and their controls, we investigated whether there was any ballooning of the inner wall endothelium, necrosis or apoptosis of endothelial cells or adherence of platelets to the inner wall endothelium. Intercellular gaps were counted at magnifications of 80.000x by two independent observers (ELD and CFK).

Outflow facility measurements. Mouse eyes were perfused *ex vivo* to measure outflow facility using the *iPerfusion* system[36]. Mice were culled by cervical dislocation and the eyes were enucleated within 10 min post mortem and stored in PBS at room temperature to await perfusion (~20 min). Both eyes were perfused simultaneously using two independent perfusion systems as described previously[36]. Briefly, each eye was affixed to a support using a small amount of cyanoacrylate glue and submerged in a PBS bath regulated at 35 °C. The eye was cannulated via the anterior chamber with a 33-gauge bevelled needle (NanoFil, #NF33BV-2, World Precision Instruments) under a stereomicroscope using a micromanipulator. The *iPerfusion* system comprises an automated pressure reservoir, a thermal flow sensor (SLG64-0075, Sensirion) and a wet-wet pressure transducer (PX409, Omegadyne) in order to apply a desired pressure, measure flow rate out of the system and measure the intraocular pressure respectively. The perfusate was DBG (PBS including divalent cations and 5.5 mM glucose), and was filtered through a 0.22 μm filter (VWR international) prior to use.

Following cannulation, eyes were perfused for 30 min at ~8 mmHg to allow the eye to acclimatise to the environment. Subsequently, nine discrete pressure steps were applied from 4.5 to 21 mmHg, while flow and pressure were recorded. Stability was defined programmatically, and data were averaged over 4 min at steady state. A non-linear model was fit to flow-pressure data to account for the pressure dependence of outflow facility in mouse eyes. This model was of the form $Q = C_r P (P/P_r)^{\beta}$. where Q and P and are the flow rate and pressure respectively, and C_r is the outflow facility at reference pressure P_r which is selected to be 8 mmHg (the approximate physiological pressure drop across the outflow pathway). The power law exponent β quantifies the non-linearity in the Q-P response and thus the pressure dependence of outflow facility. The data analysis methodology described previously[36] was applied in order to analyse the treatment effect, whilst accounting for measurement uncertainties and statistical significance was evaluated using the paired weighted t-test described therein.

Statistical analysis. For real-time PCR, TEER and paracellular permeability measurements, Student's t-tests and ANOVA with Bonferroni post-test were carried out using GraphPad Prism 5.0. For *ex vivo* perfusions, a paired weighted t-test was performed using MATLAB as described[36]. For open clefts quantification, an unpaired t-test was performed. Statistical significance was indicated by $p \leq 0.05$.

References

1. Bill, A. The aqueous humor drainage mechanism in the cynomolgus monkey (Macaca irus) with evidence for unconventional routes. *Invest Ophthalmol Vis Sci* **4,** 911–919 (1965).
2. Toris, C. B., Yablonski, M. E., Wang, Y. L. & Camras, C. B. Aqueous humor dynamics in the aging human eye. *Am J Ophthalmol* **127,** 407–412 (1999).
3. Bill, A. & Phillips, C. I. Uveoscleral drainage of aqueous humour in human eyes. *Exp Eye Res* **12,** 275–281 (1971).

4. Holmberg, A. The fine structure of the inner wall of Schlemm's canal. *AMA Arch Ophthalmol* **62,** 956–958 (1959).
5. Tripathi, R. C. Ultrastructure of Schlemm's canal in relation to aqueous outflow. *Exp Eye Res* **7,** 335–341 (1968).
6. Bill, A. & Svedbergh, B. Scanning electron microscopic studies of the trabecular meshwork and the canal of Schlemm–an attempt to localize the main resistance to outflow of aqueous humor in man. *Acta Ophthalmol (Copenh)* **50,** 295–320 (1972).
7. Grierson, I. & Lee, W. R. Pressure effects on flow channels in the lining endothelium of Schlemm's canal. A quantitative study by transmission electron microscopy. *Acta Ophthalmol* (*Copenh*) **56,** 935–952 (1978).
8. Epstein, D. L. & Rohen, J. W. Morphology of the trabecular meshwork and inner-wall endothelium after cationized ferritin perfusion in the monkey eye. *Invest Ophthalmol Vis Sci* **32,** 160–171 (1991).
9. Ethier, C. R., Coloma, F. M., Sit, A. J. & Johnson, M. Two pore types in the inner-wall endothelium of Schlemm's canal. *Invest Ophthalmol Vis Sci* **39,** 2041–2048 (1998).
10. Braakman, S. T., Read, A. T., Chan, D. W., Ethier, C. R. & Overby, D. R. Colocalization of outflow segmentation and pores along the inner wall of Schlemm's canal. *Exp Eye Res* **130,** 87–96 (2015).
11. Raviola, G. & Raviola, E. Paracellular route of aqueous outflow in the trabecular meshwork and canal of Schlemm. A freeze-fracture study of the endothelial junctions in the sclerocorneal angel of the macaque monkey eye. *Invest Ophthalmol Vis Sci* **21,** 52–72 (1981).
12. Bhatt, K., Gong, H. & Freddo, T. F. Freeze-fracture studies of interendothelial junctions in the angle of the human eye. *Invest Ophthalmol Vis Sci* **36,** 1379–1389 (1995).
13. Ye, W., Gong, H., Sit, A., Johnson, M. & Freddo, T. F. Interendothelial junctions in normal human Schlemm's canal respond to changes in pressure. *Invest Ophthalmol Vis Sci* **38,** 2460–2468 (1997).
14. Perkumas, K. M. & Stamer, W. D. Protein markers and differentiation in culture for Schlemm's canal endothelial cells. *Exp Eye Res* **96,** 82–87 (2012).
15. Braakman, S. T. *et al.* Biomechanical strain as a trigger for pore formation in Schlemm's canal endothelial cells. *Exp Eye Res* **127,** 224–235 (2014).
16. Braakman, S. T., Moore, J. E. Jr., Ethier, C. R. & Overby, D. R. Transport across Schlemm's canal endothelium and the blood-aqueous barrier. *Exp Eye Res* **146,** 17–21 (2015).
17. Stamer, W. D. *et al.* Biomechanics of Schlemm's canal endothelium and intraocular pressure reduction. *Prog Retin Eye Res* **44,** 86–98 (2015).
18. Grant, W. M. Clinical measurements of aqueous outflow. *Am J Ophthalmol* **34,** 1603–1605 (1951).
19. Johnson, M., Shapiro, A., Ethier, C. R. & Kamm, R. D. Modulation of outflow resistance by the pores of the inner wall endothelium. *Invest Ophthalmol Vis Sci* **33,** 1670–1675 (1992).
20. Lütjen-Drecoll, E. Structural factors influencing outflow facility and its changeability under drugs. A study in Macaca arctoides. *Invest Ophthalmol Vis Sci* **12,** 280–294 (1973).
21. Overby, D. R., Stamer, W. D. & Johnson, M. The changing paradigm of outflow resistance generation: towards synergistic models of the JCT and inner wall endothelium. *Exp Eye Res* **88,** 656–670 (2009).
22. Allingham, R. R. *et al.* The relationship between pore density and outflow facility in human eyes. *Invest Ophthalmol Vis Sci* **33,** 1661–1669 (1992).
23. Johnson, M. *et al.* The pore density in the inner wall endothelium of Schlemm's canal of glaucomatous eyes. *Invest Ophthalmol Vis Sci* **43,** 2950–2955 (2002).
24. Overby, D. R. *et al.* Altered mechanobiology of Schlemm's canal endothelial cells in glaucoma. *Proc Natl Acad Sci USA* **111,** 13876–13881 (2014).
25. Zhang, K., Zhang, L. & Weinreb, R. N. Ophthalmic drug discovery: novel targets and mechanisms for retinal diseases and glaucoma. *Nat Rev Drug Discov* **11,** 541–559 (2012).
26. Morita, K., Sasaki, H., Furuse, M. & Tsukita, S. Endothelial claudin: claudin-5/TMVCF constitutes tight junction strands in endothelial cells. *J Cell Biol* **147,** 185–194 (1999).
27. Campbell, M. *et al.* An experimental platform for systemic drug delivery to the retina. *Proc Natl Acad Sci USA* **106,** 17817–17822 (2009).
28. Heimark, R. L., Kaochar, S. & Stamer, W. D. Human Schlemm's canal cells express the endothelial adherens proteins, VE-cadherin and PECAM-1. *Curr Eye Res* **25,** 299–308 (2002).
29. Underwood, J. L. *et al.* Glucocorticoids regulate transendothelial fluid flow resistance and formation of intercellular junctions. *Am J Physiol* **277,** C330–342 (1999).
30. Gumbiner, B., Stevenson, B. & Grimaldi, A. The role of the cell adhesion molecule uvomorulin in the formation and maintenance of the epithelial junctional complex. *J Cell Biol* **107,** 1575–1587 (1988).
31. Bill, A., Lütjen-Drecoll, E. & Svedbergh, B. Effects of intracameral Na2EDTA and EGTA on aqueous outflow routes in the monkey eye. *Invest Ophthalmol Vis Sci* **19,** 492–504 (1980).
32. Hamanaka, T. & Bill, A. Morphological and functional effects of Na2EDTA on the outflow routes for aqueous humor in monkeys. *Exp Eye Res* **44,** 171–190 (1987).
33. Bàràny, E. H. Simultaneous measurement of changing intraocular pressure and outflow facility in the vervet monkey by constant pressure infusion. *Invest Ophthalmol Vis Sci* **3,** 135–143 (1964).
34. Overby, D. R. *et al.* The structure of the trabecular meshwork, its connections to the ciliary muscle, and the effect of pilocarpine on outflow facility in mice. *Invest Ophthalmol Vis Sci* **55,** 3727–3736 (2014).
35. Li, G. *et al.* Pilocarpine-induced dilation of Schlemm's canal and prevention of lumen collapse at elevated intraocular pressures in living mice visualized by OCT. *Invest Ophthalmol Vis Sci* **55,** 3737–3746 (2014).
36. Sherwood, J. M., Reina-Torres, E., Bertrand, J. A., Rowe, B. & Overby, D. R. Measurement of outflow facility using iPerfusion. *Plos One* **11,** e0150694 (2016).
37. Van Itallie, C. M., Fanning, A. S., Bridges, A. & Anderson, J. M. ZO-1 stabilizes the tight junction solute barrier through coupling to the perijunctional cytoskeleton. *Mol Biol Cell* **20,** 3930–3940 (2009).
38. Ikenouchi, J., Sasaki, H., Tsukita, S., Furuse, M. & Tsukita, S. Loss of occludin affects tricellular localization of tricellulin. *Mol Biol Cell* **19,** 4687–4693 (2008).
39. Gow, A. *et al.* CNS myelin and sertoli cell tight junction strands are absent in Osp/claudin-11 null mice. *Cell* **99,** 649–659 (1999).
40. Alvarado, J. A., Betanzos, A., Franse-Carman, L., Chen, J. & Gonzalez-Mariscal, L. Endothelia of Schlemm's canal and trabecular meshwork: distinct molecular, functional, and anatomic features. *Am J Physiol Cell Physiol* **286,** C621–634 (2004).
41. Park, D. Y. *et al.* Lymphatic regulator PROX1 determines Schlemm canal integrity and identity. *J Clin Invest* (2014).
42. Kizhatil, K., Ryan, M., Marchant, J. K., Henrich, S. & John, S. W. Schlemm's canal is a unique vessel with a combination of blood vascular and lymphatic phenotypes that forms by a novel developmental process. *PLoS Biol* **12,** e1001912 (2014).
43. Van Itallie, C., Rahner, C. & Anderson, J. M. Regulated expression of claudin-4 decreases paracellular conductance through a selective decrease in sodium permeability. *J Clin Invest* **107,** 1319–1327 (2001).
44. Morita, K., Sasaki, H., Fujimoto, K., Furuse, M. & Tsukita, S. Claudin-11/OSP-based tight junctions of myelin sheaths in brain and Sertoli cells in testis. *J Cell Biol* **145,** 579–588 (1999).
45. Wessells, H. *et al.* Transcriptional profiling of human cavernosal endothelial cells reveals distinctive cell adhesion phenotype and role for claudin 11 in vascular barrier function. *Physiol Genomics* **39,** 100–108 (2009).
46. Ikenouchi, J. *et al.* Tricellulin constitutes a novel barrier at tricellular contacts of epithelial cells. *J Cell Biol* **171,** 939–945 (2005).

47. Krug, S. M. *et al.* Tricellulin forms a barrier to macromolecules in tricellular tight junctions without affecting ion permeability. *Mol Biol Cell* **20,** 3713–3724 (2009).
48. Bazzoni, G. Endothelial tight junctions: permeable barriers of the vessel wall. *Thromb Haemost* **95,** 36–42 (2006).
49. Stamatovic, S. M., Keep, R. F. & Andjelkovic, A. V. Brain endothelial cell-cell junctions: how to "open" the blood brain barrier. *Curr Neuropharmacol* **6,** 179–192 (2008).
50. Johnstone, M. A. In *Becker-Shaffer's Diagnosis and Therapy of the Glaucomas* (8th Edition) (eds Marc F. Lieberman & Michael V. Drake) 25–46 (Mosby, 2009).
51. Buie, L. K. *et al.* Self-complementary AAV virus (scAAV) safe and long-term gene transfer in the trabecular meshwork of living rats and monkeys. *Invest Ophthalmol Vis Sci* **51,** 236–248 (2010).
52. Bogner, B. *et al.* Capsid mutated adeno-associated virus delivered to the anterior chamber results in efficient transduction of trabecular meshwork in mouse and rat. *Plos One* **10,** e0128759 (2015).
53. Campbell, M. *et al.* Systemic low-molecular weight drug delivery to pre-selected neuronal regions. *EMBO Mol Med* **3,** 235–245 (2011).
54. Keaney, J. *et al.* Autoregulated paracellular clearance of amyloid-beta across the blood-brain barrier. *Sci Adv* **1,** e1500472 (2015).
55. Morrison, J. C. *et al.* A rat model of chronic pressure-induced optic nerve damage. *Exp Eye Res* **64,** 85–96 (1997).
56. Stamer, W. D., Roberts, B. C., Howell, D. N. & Epstein, D. L. Isolation, culture, and characterization of endothelial cells from Schlemm's canal. *Invest Ophthalmol Vis Sci* **39,** 1804–1812 (1998).
57. Stamer, W. D., Seftor, R. E., Williams, S. K., Samaha, H. A. & Snyder, R. W. Isolation and culture of human trabecular meshwork cells by extracellular matrix digestion. *Curr Eye Res* **14,** 611–617 (1995).
58. Schmittgen, T. D. & Livak, K. J. Analyzing real-time PCR data by the comparative C(T) method. *Nat Protoc* **3,** 1101–1108 (2008).

Acknowledgements

Work at the Ocular Genetics Unit at the University of Dublin, Trinity College, was supported by the European Research Council ERC-2012-AdG. The Unit also receives support from Science Foundation Ireland. Work at Duke University was supported by grants from the US National Institutes of Health (EY022359 and EY019696) and at Imperial College London by Fight for Sight UK (Ref 1385), the US National Institutes of Health (EY022359 and EY019696), and the UK Engineering and Physical Sciences Research Council (EP/J010499/1). We would like to thank C. Woods and C. Murray for animal husbandry. We thank Elke Kretshmar, Hong Nguyen and Britta Bäckermann for their technical assistance with TEM, Jörg Pekarsky for preparing the schematic drawing and Marco Gößwein for preparing the final version of Figure 1.

Author Contributions

All authors reviewed the manuscript. L.C.S.T. performed PCR arrays, RNAi knockdown, gene expression analysis in SCEC, IHC, TEER and P*app* measurements, and wrote the main manuscript text; E.R.-T. performed mouse intracameral injections, iPerfusion, gene expression analysis in TM cells and contributed to manuscript preparation; J.M.S. contributed to experimental design, performed statistical analysis for iPerfusion and contributed to manuscript preparation; P.C. performed RNAi knockdown, mouse intracameral injection and assisted with iPerfusion; D.C. performed mouse IHC and protein inhibition analysis in mouse; E.L.-D. performed TEM; C.F.-K. performed TEM; K.P. provided SCEC lines; M.M.H. performed gene sequencing and contributed to siRNA design; A.-S.K. assisted with PCR array analysis and contributed to manuscript preparation; J.O'C assisted with iPerfusion and performed cell viability experiments; J.J.C. provided non-human primate anterior segment paraffin sections; A.T.R. contributed to the interpretation of physiological data and statistical analysis, and provided revisions to the manuscript; C.R.E. contributed to the interpretation of physiological data and statistical analysis, and provided revisions to the manuscript; C.O'B. contributed to manuscript preparation; M.L. contributed to manuscript preparation; M.C. contributed to manuscript preparation; W.D.S. conceived the concept and assisted with experimental design, provided cell lines and contributed to manuscript preparation; D.R.O. assisted with experimental design, iPerfusion and contributed to manuscript preparation; P.H. conceived the concept and contributed to experimental design and writing of the manuscript.

Additional Information

Supplementary information accompanies this paper at http://www.nature.com/srep

Competing financial interests: The authors declare no competing financial interests.

How to cite this article: Tam, L. C. S. *et al.* Enhancement of Outflow Facility in the Murine Eye by Targeting Selected Tight-Junctions of Schlemm's Canal Endothelia. *Sci. Rep.* **7**, 40717; doi: 10.1038/srep40717 (2017).

Publisher's note: Springer Nature remains neutral with regard to jurisdictional claims in published maps and institutional affiliations.

Progress in Retinal and Eye Research xxx (2017) 1–14

Contents lists available at ScienceDirect

Progress in Retinal and Eye Research

journal homepage: www.elsevier.com/locate/prer

Manipulating ocular endothelial tight junctions: Applications in treatment of retinal disease pathology and ocular hypertension

Matthew Campbell**, Paul S. Cassidy, Jeffrey O'Callaghan, Darragh E. Crosbie, Pete Humphries*

Smurfit Institute of Genetics, Lincoln Place Gate, Trinity College Dublin, Dublin 2, Ireland

ARTICLE INFO

Article history:
Received 3 July 2017
Received in revised form
1 September 2017
Accepted 20 September 2017
Available online xxx

Keywords:
Tight junctions
RNAi
Blood-retina barrier (BRB)
Schlemm's canal
Endothelium
Retinal degeneration

ABSTRACT

Protein levels of endothelial tight-junctions of the inner retinal microvasculature, together with those of Schlemm's canal, can be readily manipulated by RNA interference (RNAi), resulting in the paracellular clefts between such cells to be reversibly modulated. This facilitates access to the retina of systemically-deliverable low molecular weight, potentially therapeutic compounds, while also allowing potentially toxic material, for example, soluble Amyloid-β1-40, to be removed from the retina into the peripheral circulation. The technique has also been shown to be highly effective in alleviation of pathological cerebral oedema and we speculate that it may therefore have similar utility in the oedematous retina. Additionally, by manipulating endothelial tight-junctions of Schlemm's canal, inflow of aqueous humour from the trabecular meshwork into the Canal can be radically enhanced, suggesting a novel avenue for control of intraocular pressure. Here, we review the technology underlying this approach together with specific examples of clinical targets that are, or could be, amenable to this novel form of genetic intervention.

Contents

* Corresponding author.
** Corresponding author.
E-mail addresses: matthew.campbell@tcd.ie (M. Campbell), pete.humphries@tcd.ie (P. Humphries).

https://doi.org/10.1016/j.preteyeres.2017.09.003
1350-9462/

1. Introduction

Endothelial cells lining the cerebral and inner retinal microvasculatures, together with those of the Canal of Schlemm, possess tight-junctions. In the brain and retina, tight junctions form an exceedingly tight seal, with very low rates of fluid-phase transcytosis. Such junctions, constituting the blood-brain and inner blood-retina barriers (BBB/iBRB), prevent potentially noxious materials, including for example, low molecular weight blood-borne enzymes, anaphylatoxins, antibodies etc., from entering and damaging neurological tissues (Hawkins and Davis, 2005; Abbott et al., 2010; Campbell et al., 2011, 2012; Campbell and Humphries, 2012). Additionally, in the anterior segment of the eye, Schlemm's Canal (SC) constitutes part of the conventional aqueous humour outflow pathway, aqueous produced by the ciliary body passing into the anterior chamber of the eye and then into the trabecular meshwork, from where it filters into the canal across its endothelial barrier (Stamer and Clark, 2017). While weaker and less well characterised than their counterparts of the inner retinal vessels, the tight junctions of canal endothelia are dynamically responsive to fluctuations in intraocular pressure (see Figs. 1 and 2) (Ye et al., 1997). Since it is well proven and within our capabilities to artificially modulate levels of transcript encoding tight-junctions, a means exists to enhance the permeability of the inner retinal vessels and the Canal for potentially therapeutic purposes.

Here, we provide an overview of the structure of tight junctions and of how levels of transcripts encoding tight junction components can be reversibly modulated both in retinal and SC endothelial cells. We provide examples of how low molecular weight compounds can be systemically delivered to the retina in its 'barrier modulated' state, and speculate on those degenerative retinal conditions in which oedema accumulates in the presence of an essentially intact iBRB and which could, in principle, be targeted using this approach. In the context of glaucoma, up to six percent of cases of open-angle disease are bilaterally sub-optimally responsive to standard topically-applied pressure-reducing medications (Kass et al., 2002) and for the most commonly used prostaglandin analogue, Latanoprost, between 25 and 50% of patients do not achieve greater than a 20% reduction in intraocular pressure (Scherer, 2002; Noecker et al., 2003). These topical formulations act largely by inhibiting aqueous secretion by the ciliary body or to increase aqueous outflow through the unconventional drainage pathway. Down regulation of SC endothelial tight junctions has been shown to increase aqueous humour outflow in experimental animal model systems (Tam et al., 2017) and could form the basis of a radical therapeutic approach targeting the major aqueous humour outflow system of the eye.

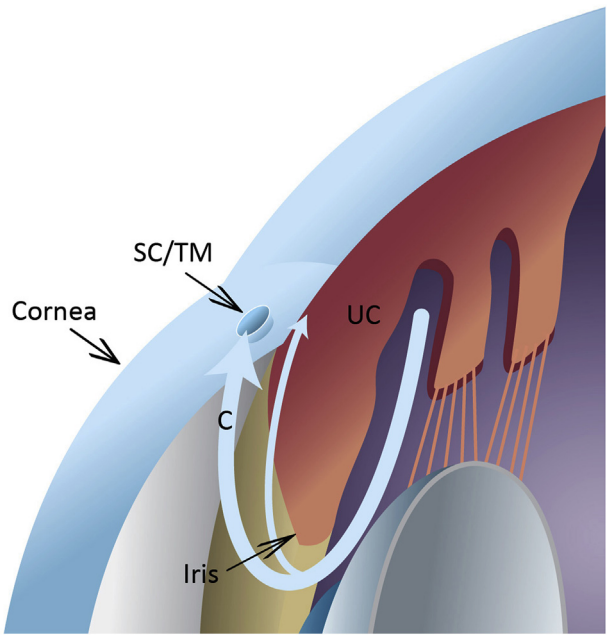

Fig. 1. Aqueous humour is secreted by the ciliary body and moves through the pupil, around the iris. A pressure gradient directs it toward the SC lumen, where most aqueous egresses (red arrow). This is termed the conventional pathway (C). The unconventional pathway (UC) involves the removal of aqueous through the fibres of the ciliary body into the supraciliary and suprachoroidal spaces.

2. Structure and organization of endothelial tight junctions of cerebral and inner retinal vasculatures

Tight junctions (TJs), are essentially contact points between the plasma membranes of adjacent cells, or indeed the point where one endothelial cell contacts itself in a microvessel. TJs are located at the apical periphery of the plasma membrane, and each TJ is paired to and associates with another TJ on the membrane of the adjacent cell. TJs have numerous functions and can act as sites for vesicle targeting, proliferation, transcription signals, mediating cell polarity. Given their molecular complexity, TJs also act as a physical barrier to limit paracellular diffusion of solutes across the BBB/iBRB and indeed the endothelium of Schlemm's canal.

Typically, each TJ consists of at least three different types of protein; 1) occludin, 2) junction adhesion molecule (JAM) family of proteins, and 3) claudin proteins (Ben-Yosef et al., 2003). However, the TJ itself can consist of over 40 individual proteins between support proteins, structural proteins, transport proteins, and other more unique proteins such as tricellulin, a homologue of occludin that concentrates when three cells come together (Anderson and Van Itallie, 2008). In addition, the actin cytoskeleton of the cell is critical for TJ formation, as actin strands bind the PDZ-domain containing scaffolding proteins ZO-1, ZO-2, ZO-3, MAGI-1, PatJ, PALS1 and MUPP1, which can subsequently bind to the TJ proteins that can mediate extracellular interaction with adjacent TJ proteins.

During the assembly stage of the TJ, the proteins Par3, Par6 and aPKC are critical and the TJ is also important for the function of the basolateral-located adherens junctions, which are largely cadherin based junctions. Indeed, the protein VE-cadherin can act as a mediator of intracellular signalling via its interaction with phosphatidylinositol-3-OH kinase or other growth factor receptors. For example, VE-cadherin has been shown to interact directly with β-catenin, which can subsequently regulate cellular homeostasis or responses to cellular stress (Taddei et al., 2008). Paracellular transport of molecules from blood to retina or across the Schlemm's canal endothelium is exclusively passive, driven predominantly by concentration gradients (Van Itallie and Anderson, 2004).

The molecular composition and indeed the overt permeability of TJs varies considerably amongst different tissue types. For example, some tissues display variable electrical conductance, charge selectivity, non-charged solute permeability, and size selectivity, and this is reflected to a large degree on the density of claudin proteins present in their TJs. Importantly, TJs are distinguished from adherens junctions (AJs) in that they are located at the apical periphery of the contact point of endothelial cells, with AJs expressed below them. Additionally, AJs have a different molecular composition, being enriched with cadherins, catenins and nectin amongst others.

Structurally claudins are integral membrane proteins with four transmembrane domains and two extracellular and one intracellular loop. In the first extracellular loop claudins have a common WGLWCC motif, and they also possess a C-terminus PDZ domain. This region binds to the PDZ domains of the TJ support proteins,

Please cite this article in press as: Campbell, M., et al., Manipulating ocular endothelial tight junctions: Applications in treatment of retinal disease pathology and ocular hypertension, Progress in Retinal and Eye Research (2017), https://doi.org/10.1016/j.preteyeres.2017.09.003

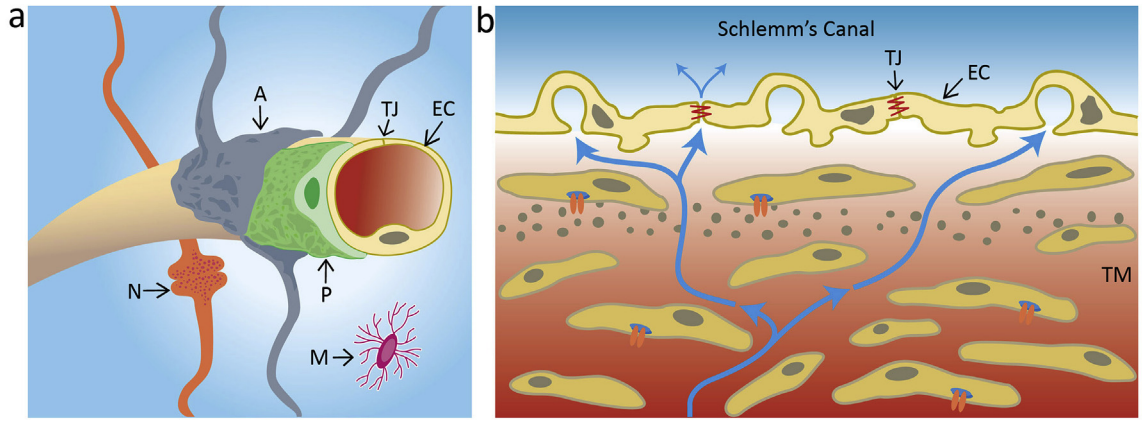

Fig. 2. a) Structure of the neurovascular unit of the inner blood retina barrier (iBRB) comprising endothelial cells (EC), pericytes (P) and atrocyte foot processes (A). The contacting point of an iBRB EC is where the tight junction (TJ) is formed. Neurons (N) and microglia (M) are located on the retina aspect of the iBRB. **b)** Schlemm's canal endothelial cells contain TJs but also manifest giant vacuoles to allow for aqueous humour movement (see arrows for directionality of flow) into Schlemm's canal via the trabecular meshwork (TM).

such as ZO-1, ZO-2, ZO-3 (Itoh et al., 1999) and MUPP-1 (Hamazaki et al., 2002). The C-terminus tail, is also the region which confers stability to claudins, and swapping the C-terminus tails has been found to coincide with a reversal of protein half-lives (Van Itallie et al., 2004).

Various post-translational modifications have also been implicated in claudin function. For example, phosphorylation has been shown to increase claudin1-4 permeability to chloride ions (Yamauchi et al., 2004), and loss of palmitoylation sites on claudin-14 results in reduced localization of the protein to the membrane (Van Itallie et al., 2005).

Some claudins, such as claudin-1, are widely expressed (Van Itallie and Anderson, 2004), whereas other claudin proteins are expressed only in certain cell types or during embryonic development (Turksen and Troy, 2001). This, suggests that claudins play various roles not necessarily limited to the TJs.

Various studies expressing combinations of different claudins in Madin-Darby canine kidney (MDCK) cells found that over-expression of claudin-7 increased paracellular permeability to cations, while reducing it to anions. Additionally, over-expression of claudin-4, -8 and -14 reduced permeability to cations but not anions, while over-expression of claudin-2 decreased barrier integrity without reducing the number of TJ strands (Ben-Yosef et al., 2003; Furuse and Tsukita, 2006).

The finding that claudin-14 reduces permeability to cations aligns with its abundant *in vivo* expression in the outer hair cells of the cochlea in the ear. Here TJs function to separate the K^+-rich endolymph and Na^--rich perilymph, a separation essential for optimal hearing. The importance of claudin-14 for this role is observed in the deafness observed in mice and humans with claudin-14 mutations (Ben-Yosef et al., 2003). Claudin-11-null mice also exhibit deafness, and this is due to a similar role of claudin-11 in maintaining the endocochlear potential in the ear (Kitajiri et al., 2004).

Indeed, mutations in the claudin-16 gene, expressed in the thick ascending limb of the nephron, cause Mg^{2+} reabsorption in humans and cattle, resulting in deficiency of the ion. Claudin-16 contains a number of negatively charged residues in its first extracellular loop, which appear to electrostatically interact with soluble ions, enabling or inhibiting their passage (Simon et al., 1999). Detailed in Table 1, are some key properties of the claudins listed in this section.

As well as mediating selective ion transport across the paracellular pathway, claudins also play a central role in determining the maximum size of molecules that diffuse across an endothelial cell layer. Claudin-1 knockout mice, for example, die within one day of birth due to excessive water loss across the skin. Additionally, mutations in claudin-1 are associated in humans with ichthyosis – a condition manifested by skin dehydration (Hadj-Rabia et al., 2004). These observed phenotypes in humans and other animals lacking claudin proteins demonstrate their importance in regulating TJ function and in controlling passive paracellular diffusion of materials across the TJ. Claudins are distinguished from other tight junction proteins such as occludin in that their extracellular domains have a certain degree of homology and mediate size selectivity and ion flux across the various barriers. Occludin appears to have a more regulatory role at the tight junction.

3. Structure and organization of Schlemm's canal endothelial tight junctions

The endothelial tight junctions of Schlemm's Canal differ from those seen in vascular endothelia in several ways. Early studies using electron microscopy showed electron dense junctions present between endothelial cells of Schlemm's Canal similar to those seen in vascular endothelia (Vegge, 1967). Subsequent freeze fracture studies showed that Schlemm's Canal endothelial cells TJs were composed of parallel junctional strands with minimal branching which did not form complex bi-dimensional networks. The lack of branching between TJ strands in SC endothelial cells leads to the formation of channels between junction strands that are continuous from the juxtacanalicular tissue to the SC lumen. These channels were identified as a potential paracellular route for AH outflow in to the SC lumen through intercellular clefts in the SC inner wall endothelium (Raviola and Raviola, 1981; Bhatt et al., 1995). Early tracer studies using cationised ferritin showed staining of cell membranes lining channels between tight junctions in the SC inner wall endothelium, showing therefore that these channels represented a paracellular pathway across the SC inner wall. Further, these channels were of greater size and number in eyes that were fixed at elevated pressure, (Epstein and Rohen, 1991). Additionally, endothelial tight junctions in perfused human donor eyes were shown by freeze fracture to exist in single and double stranded forms at the majority of TJs, with a minority of TJs having three or more junctional strands. The complexity of these junctions was shown to be responsive to applied pressure in the eye, with the number of junctional strands decreasing as perfusion pressure increased, (Ye et al., 1997). The above features are in

Please cite this article in press as: Campbell, M., et al., Manipulating ocular endothelial tight junctions: Applications in treatment of retinal disease pathology and ocular hypertension, Progress in Retinal and Eye Research (2017), https://doi.org/10.1016/j.preteyeres.2017.09.003

Table 1
Relevant claudins and their chromosomal and tissue expression pattern.

Gene	Protein name	Chromosome	Tissue expression (protein)
CLDN1	claudin 1	3q28	Heart, brain, lung, liver testis
CLDN2	claudin 2	Xq22.3	Liver, kidney
CLDN3	claudin 3	7q11.23	Lung, liver, kidney, testis
CLDN4	claudin 4	7q11.23	Lung, kidney
CLDN5	claudin 5	22q11.21	Brain, heart, lung, liver, kidney, testis, endothelial cells in general
CLDN6	claudin 6	16p13.3	Embryonic tissues
CLDN7	claudin 7	17p13.1	Lung, kidney, testis
CLDN8	claudin 8	21q22.11	Lung, liver, kidney, testis
CLDN10	claudin 10	13q32.1	Liver
CLDN11	claudin 11	3q26.2	Brain, testis
CLDN14	claudin 14	21q22.13	Liver, kidney, ear
CLDN16	claudin 16	3q28	Kidney

contrast to TJs of the inner retinal vascular endothelium, which are composed of complex networks of multiple TJ strands, and do not exhibit dynamic regulation in response to pressure, with no changes to TJ strand structure in response to perfusion pressure (Fujimoto, 1995; Schneeberger and Karnovsky, 1976).

Schlemm's canal endothelial cells also differ from inner retinal vascular endothelial cells in that they have remarkably high hydraulic conductivity, with Schlemm's canal having a hydraulic conductivity of 4000-9000 $\times$ 10^{-11} cm^2 s/g, significantly higher than other ocular barriers, and possibly one of the highest hydraulic conductivities of all body vessel linings (Johnson, 2006). The inner wall endothelium of SC is also permeable to higher molecular weight tracer molecules than other endothelial cells of the eye, with labelled ferritin, 450 kDa, staining the interior of paracellular pores, while the inner blood-retinal barrier (iBRB) excludes molecules as small as 500 Da (Epstein and Rohen, 1991; Campbell et al., 2009). It must be noted that these differences in endothelial permeability cannot be solely apportioned to differences in TJ structure and organization as, in addition to TJ mediated paracellular pores between cells, SCECs possess giant vacuoles containing large intracellular pores. These intracellular pores have an average pore size of approximately 1 μm in diameter, with pores greater than 3 μm reported (see Fig. 3 for an overview of the differences in iBRB and SC endothelia) (Sit et al., 1997).

Human SC endothelial cells have differing TJ protein expression profiles than is seen other endothelial cells. For example, at the iBRB, ZO-1, occludin and claudin-5 are instrumental in maintaining barrier function, with claudin-5 being particularly important in controlling paracellular permeability (Campbell and Humphries, 2012; Morita et al., 1999). Contrastingly, recent studies have shown a more simplistic TJ composition in human SC endothelial cells, with claudin-11 and ZO-1 being the major TJ proteins present, and claudin-5 and occludin being expressed at low levels only (Tam et al., 2017).

4. Induction of inner retinal microvessel permeability: validation of the concept as a potentially therapeutic modality

In the original experimental approach (Campbell et al., 2008, 2009) targeting both the BBB and iBRB simultaneously, 20 μg of siRNA targeting Claudin-5 was hydrodynamically injected into the tail veins of mice in a volume of 10% of the body weight of the animal, a procedure that was well tolerated given the overtly high volumes. Using this approach, maximum suppression of claudin-5 was observed approximately 48 h after each tail injection, levels of claudin-5 returning to normal by 72 h post inoculation. During this period, both the BBB and iBRB became permeable to the perfused nuclear stain, Hoechst H33342 (molecular weight, 563Da). In cryosections of the retina, staining of the inner nuclear

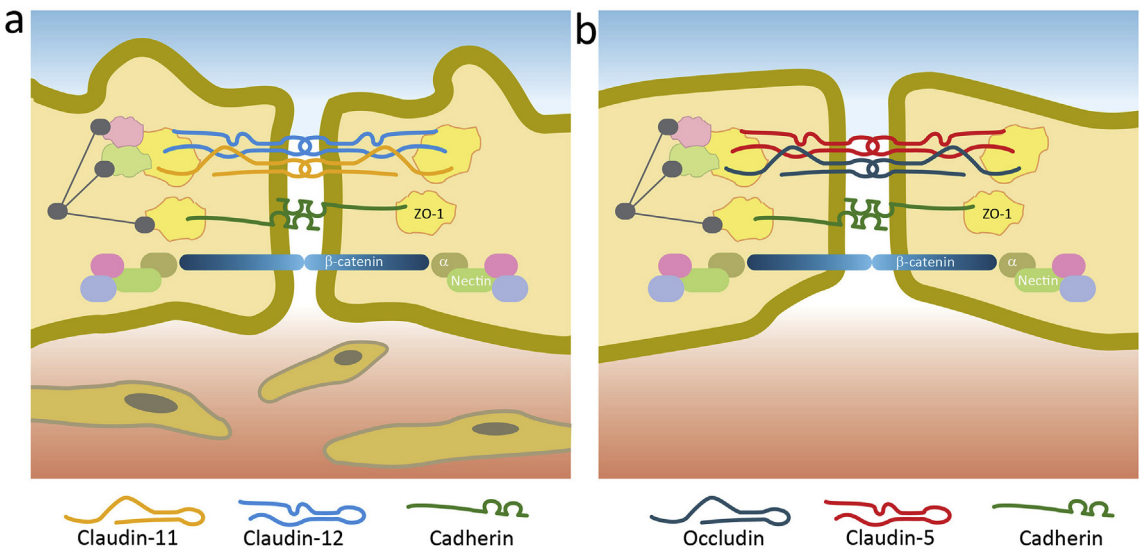

Fig. 3. a) Molecular architecture of the Schlemm's canal endothelial cells shows an enrichment of claudin-11 and claudin-12 at the tight junction. **b)** Tight junctions of endothelial cells associated with the inner blood retina barrier (iBRB) show an enrichment of claudin-5 and occludin at the tight junction.

Please cite this article in press as: Campbell, M., et al., Manipulating ocular endothelial tight junctions: Applications in treatment of retinal disease pathology and ocular hypertension, Progress in Retinal and Eye Research (2017), https://doi.org/10.1016/j.preteyeres.2017.09.003

layer (INL) was evident 24 h post-siRNA injection, while staining of the outer nuclear layer (ONL) became evident at 48 h. However, 72 h after siRNA inoculation, no staining could be detected in any of the nuclear layers (Fig. 4). Under the same conditions, systemically administered FITC-labelled dextran, FD-4 (MW 4,400Da), showed no evidence of being able to access any of the nuclear layers of the retina, these data indicating that down-regulation of claudin-5 facilitates a transient and size-selective enhancement of permeability at the iBRB to compounds of at least 563 Da, but not to those of higher molecular weight. In subsequent studies (Campbell et al., 2012), tail injections were undertaken with siRNA complexed with a clinically enabled polyethylene imine (PEI) carrier, *in vivo*-JetPEI (Polyplus Transfection). 20 μg of claudin-5 siRNA injected in a volume of 0.4 ml with this carrier was shown to be as effective as the hydrodynamic approach in down-regulation of claudin-5. While these initial experiments validated barrier modulation technology as an enabling system for enhancing drug delivery to neural tissues, it was unable to selectively target the retina while leaving the BBB intact.

5. Site-specific modulation of the iBRB

In order to selectively target the retina, claudin-5 shRNA was incorporated into an AAV-2/9 vector, inducible by doxycycline (Campbell et al., 2011). A single once off sub-retinal injection of this vector was required, provision of doxycycline in drinking water (2 mg/ml) being used to induce claudin-5 shRNA expression (viral constructs are now available that are capable of accessing the retina following intravitreal inoculation and there is no reason not to assume that such constructs will act in a similar manner, providing they have tropism for vascular endothelia). The efficacy of this system was initially validated in a light-induced murine model of apoptotic photoreceptor degeneration, in which it has been firmly established that death of photoreceptor cells is calpain-dependent (Perche et al., 2007). N-Acetyl-L-leucyle-L-methioninal; calpain inhibitor II (ALLM), molecular weight 401Da is a potent calpain inhibitor. Albino mice given doxycycline in drinking water, were treated IP with 20 mg/kg ALLM followed by exposure to 7900 lux of white light. After 24 h, photoreceptor cell death was assessed by TUNEL staining of retinal cryosections. As illustrated in Fig. 5, photoreceptor cell viability was extensively preserved in animals systemically treated with the drug which, under conditions where permeability of the iBRB had not been modulated, could not gain sufficiently effective access to the retina to provide therapeutic benefit.

Validating this approach, a murine model of the exudative form of age-related macular degeneration (AMD) was also used (Campbell et al., 2011). Wild type C57BL/6J mice were sub-retinally inoculated in one eye with an AAV-2/9 expressing claudin-5 shRNA and the other eye with an AAV-2/9 expressing a non-targeting shRNA as control. Animals were administered doxycycline (2 mg/kg) for 3 weeks prior to induction of laser burns to the RPE/Bruch's membrane, inducing localized expression of vascular endothelial growth factor (VEGF) and choroidal neovascularisation (CNV) at the site of laser burns. During an interval of 14 days subsequent to laser treatment, mice were administered two systemic (IP) doses either of 17-AAG (30 mg/kg), or sunitinib malate (20 mg/kg), both well characterised and potent inhibitors of VEGFR-2. As shown in Fig. 6, animals having received a claudin-5 targeting vector showed highly significant suppression of CNV compared to the contralateral eye receiving a non-targeting vector.

It is of interest also to note that endothelial tight junctions at the iBRB can be further manipulated in order to increase barrier permeability beyond that achievable using claudin-5 alone. In this regard, Keaney et al. (2015), demonstrated that co-suppression of transcripts encoding claudin-5 and occludin rendered the iBRB reversibly permeable to systemically administered compounds up to approximately 4 kDa in molecular weight. While manipulating permeability to this extent runs the risk of admission into the retina (or brain) of potentially damaging low molecular weight materials such as anaphylatoxins, or low molecular weight enzymes, no observable negative physiological consequences of such modulation were noted. The possible therapeutic implications of this observation will be considered later in this review.

6. On the potential therapeutic utility of manipulation of iBRB permeability

6.1. Experimentally enhancing macular pigment (MP) access to retina

The macular pigments, lutein, zeaxanthin and mesozeaxanthin, act protectively within the retina, acting as filters for short wavelength blue light and also as scavengers of reactive oxygen species (Whitehead et al., 2006). Potentially beneficial effects of dietary supplementation have been investigated in a number of scenarios, including for example, inherited retinal degenerations, specifically retinitis pigmentosa and Usher syndrome (Aleman et al., 2001) and in patients with AMD (Ma et al., 2012; Liu et al., 2014). In the study by Aleman et al. (2001), there was a trend toward more severe progression of disease in those patients who had lower retinal MP levels. In the study by Ma et al. (2012), abnormalities in central retinal function in early AMD were reported to be improved and in the study reported by Liu et al. (2014,2015), a meta-analysis of 1176 AMD patients, both visual acuity and contrast sensitivity were found to improve with supplementation. However, it is well

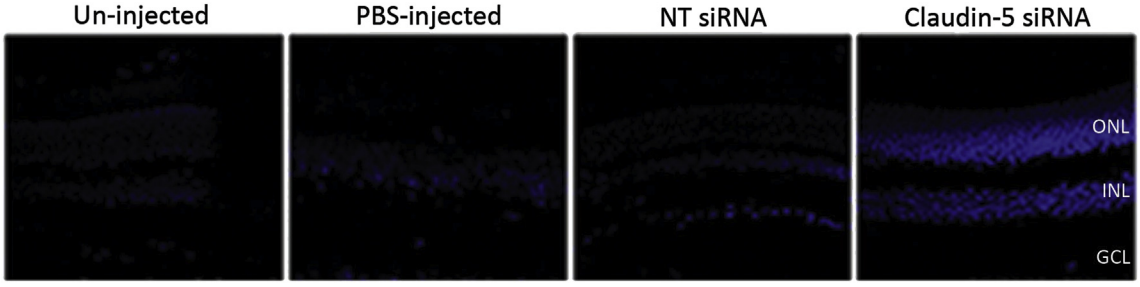

Fig. 4. Extravasation of Hoechst H33342 from the retinal microvessels was manifested by distinct staining of nuclei in the inner nuclear layer (INL) and outer nuclear layer (ONL) 48 h post delivery of claudin-5 siRNA when compared to control groups.
This is part of figure 6 from our paper, Campbell et al., J. Gene Medcine 2008 Aug; 10(8) 930–47

Please cite this article in press as: Campbell, M., et al., Manipulating ocular endothelial tight junctions: Applications in treatment of retinal disease pathology and ocular hypertension, Progress in Retinal and Eye Research (2017), https://doi.org/10.1016/j.preteyeres.2017.09.003

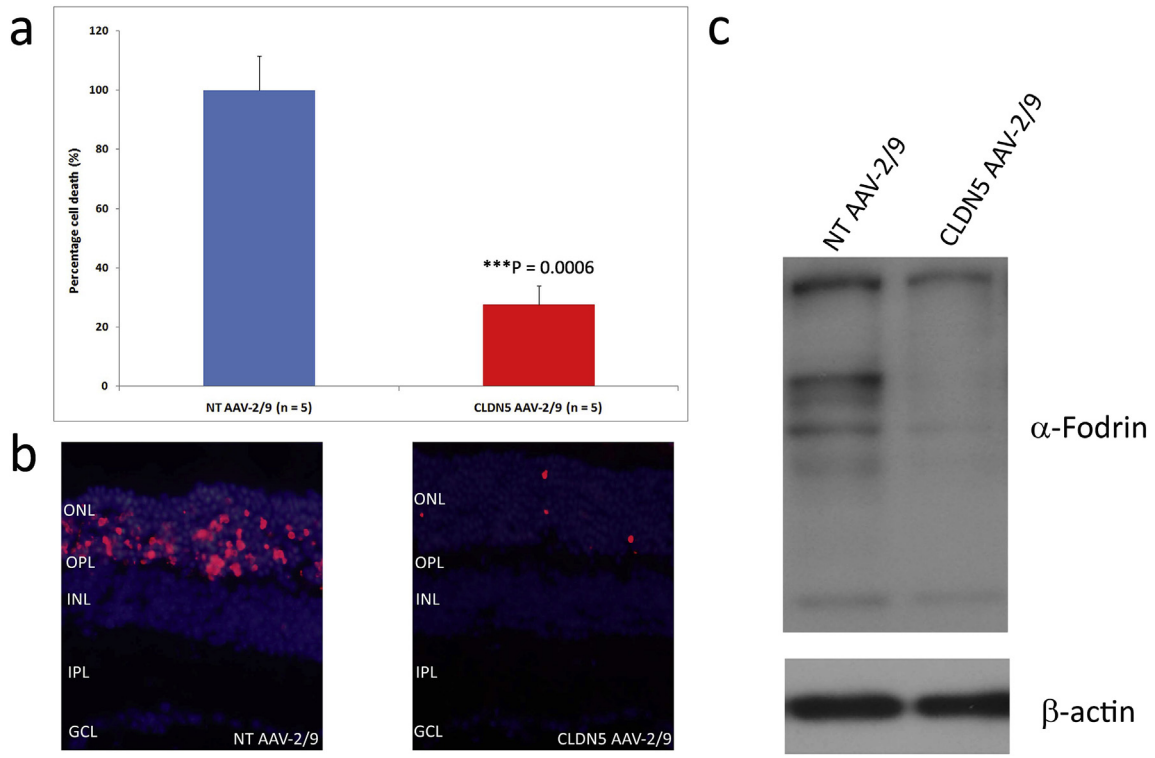

Fig. 5. (a) Albino BalB/c mice were inoculated sub-retinally with either the NT AAV-2/9 in their left eye or the CLDN5 AAV-2/9 in their right eye. Significant protection of photoreceptor cells was observed in the right eyes (CLDN5 AAV-2/9) of mice compared to the left eyes (NT AAV-2/9) (***P = 0.0006). (b) TUNEL positive cells were shown to be consistently localized in large numbers to the outer nuclear layer (ONL) of NT AAV-2/9 injected retinas compared to CLDN5 AAV-2/9 injected retinas. Outer plexiform layer (OPL), inner nuclear layer (INL), inner plexiform layer (IPL), ganglion cell layer (GCL). (c) Extensive cleavage of the calpain substrate α-fodrin was observed in mice receiving the NT AAV compared to mice receiving the CLDN5 AAV with ALLM prior to light ablation.
This is figure 4 from our paper, Campbell et al., EMBO Molecular Medicine 2011, 3, 235–245.

recognised that not all on supplementation show increases in MP density within the retina, a probable reflection of variability in carotenoid transporter efficiency (40, 43, 44).

While mice do not possess a macula, they nevertheless could represent a highly cost efficient avenue for study of the physiological effects of MPs in normal and degenerating retinas. However, wild type mice do not accumulate these carotenoids within retinal tissues even when supplemented in their diet. Recent studies however, have shown that mice with targeted disruptions of β-carotene oxygenases 1 and 2 (*Bco2*−/− in particular) are able to accumulate MPs within the retina (Li et al., 2017). However, a very large amount of carotenoid ~2.6 mg per mouse per day, equivalent to an average human dose of about 635 mg per day, was required to achieve measurable levels of MP within these retinas. Controlled modulation of the permeability of the iBRB of *Bco2*−/− mice, would enable very much smaller systemic doses of MP to be required in order to achieve elevated MP levels within retinal tissues. Given the fact that lutein and zeaxanthin have molecular weights (569Da), well below the cut off for systemic delivery following transient down regulation of claudin-5, *Bco2*−/− mice would likely be rendered a more versatile and useful model for studies of the physiological or protective effects of MPs within the retina. The same system could be used to experimentally enhance MP uptake in primates.

6.2. Alleviation of retinal oedema

Previous studies from this laboratory (Campbell et al., 2012) have shown that siRNA-mediated down regulation of claudin-5 is highly effective in reducing pathological cerebral oedema in a murine model of traumatic brain injury (TBI). In this model, a small ultra-cold probe is placed for a short period of time onto the skulls of anaesthetised animals. This induces a focal necrotic cerebral lesion and breakdown of the BBB, with extensive extravasation of fluid from the cerebral capillaries into the parenchyma of the brain. The barrier then reforms, pathological oedema remaining within penumbral region of the brain, adjacent to the injury site. [It is of interest to note that TBI accounts for about 1% of all adult mortality worldwide and cerebral oedema induced by out-of-hospital cardiac arrest is similarly prevalent. Treatments involving injection of the osmotic diuretic, mannitol, are archaic and inefficient if oedema persists beyond 24 h. This treatment paradigm has hardly changed in over 80 years]. In the current approach, claudin-5 siRNA complexed with the carrier agent *in-vivoJetPEI* was systemically administered. The transiently modulated BBB allowed efficient fluid drainage from the brain, reducing lesion volumes and improving cognitive function (Fig. 7).

It is of interest to note in the above context, that a number of well-defined retinal conditions are characterised by a build-up of intra-retinal oedema and could be targetable using this approach. In general, retinal oedema as a co-morbidity of a range of retinal conditions will involve vasogenic oedema as the initial insult, *i.e.*, oedema derived from a vascular source, with extravasation of fluid from blood to neural tissues. Vasogenic oedema will lead to acute pressure changes within neural tissue and will lead to eventual cytotoxic oedema, where cells within the penumbral region of injury/damage will gradually decline. Bearing in mind that the retina is simply an extension of the central nervous system (CNS), we speculate that in such conditions, it may be possible to counterbalance fluid exudation into retinal tissues, by enhancing fluid

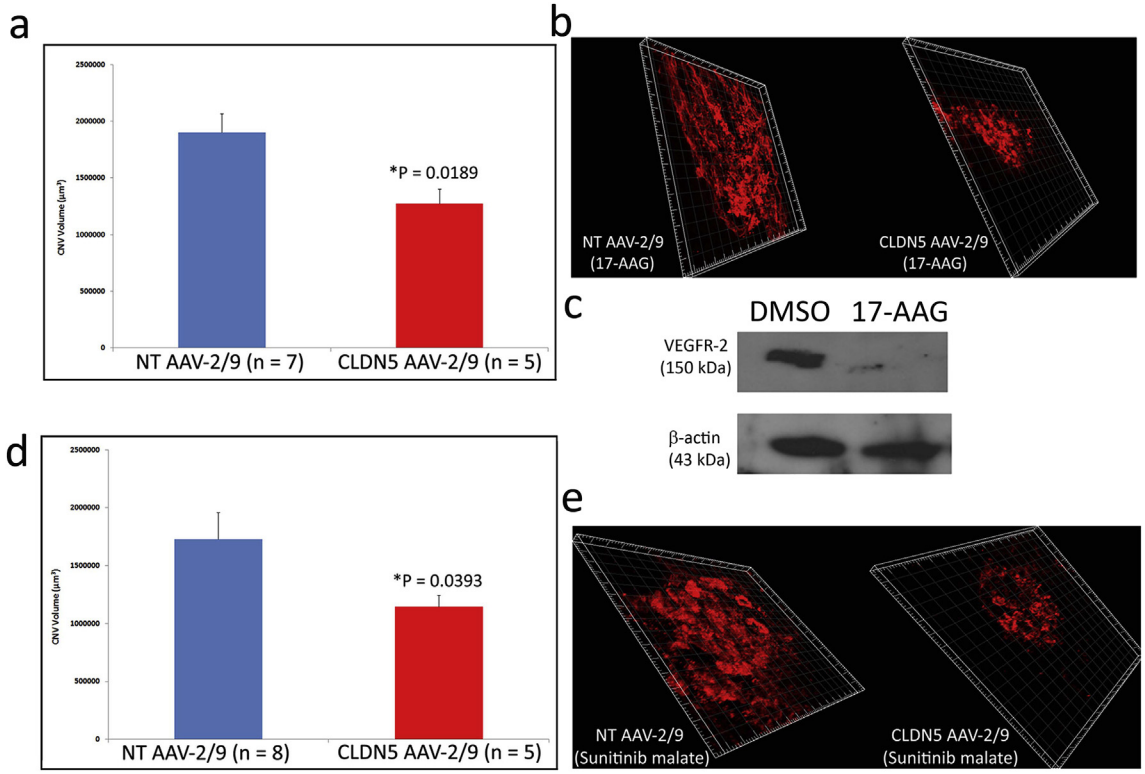

Fig. 6. (a) Albino BalB/c mice were inoculated sub-retinally with either the NT AAV-2/9 in their left eye or the CLDN5 AAV-2/9 in their right eye. Significant protection of photoreceptor cells was observed in the right eyes (CLDN5 AAV-2/9) of mice compared to the left eyes (NT AAV-2/9) (***P = 0.0006). (b) TUNEL positive cells were shown to be consistently localized in large numbers to the outer nuclear layer (ONL) of NT AAV-2/9 injected retinas compared to CLDN5 AAV-2/9 injected retinas. Outer plexiform layer (OPL), inner nuclear layer (INL), inner plexiform layer (IPL), ganglion cell layer (GCL). (c) Extensive cleavage of the calpain substrate α-fodrin was observed in mice receiving the NT AAV compared to mice receiving the CLDN5 AAV with ALLM prior to light ablation.
This is part of Figure 5 from our paper, Campbell et al., EMBO Molecular Medicine 2011, 3, 235–245.

resorption into the inner retinal vasculature by manipulating iBRB permeability. While this may appear counter-intuitive, the approach is now validated in murine models of TBI, where BBB breakdown is a hallmark pathology. The same will apply to retinal oedematous conditions, where penumbral regions are at risk of perpetuating neural damage. Such conditions include, *inter alia,* Non-arteritic Anterior Ischaemic Opthic Neuropathy (NAION), characterised by axoplasmic flow stasis and extracellular oedema at the optic nerve head and X-linked Juvenile Retinoschisis, in which fluid-filled cavities develop as the retina splits, cavities largely forming in the outer/inner plexiform and inner nuclear layers of the retina (fundus images of these conditions, clearly revealing the presence of retinal oedema are shown in Fig. 8). NAION is caused by reduced blood flow in the posterior ciliary artery, which causes ischaemia in the anterior part of the optic nerve head, resulting in a vasogenic oedema and axoplasmic flow stasis in ganglion cell axons, causing them to swell and become damaged (Hayreh, 2013). It is a major cause of visual handicap in older people, with approximately 6000 cases per year in US (the prevalence is higher in diabetics). 25% of patients experience NAION in contralateral eye within five years of developing the disease and loss of vision is often permanent. Most importantly, there are no effective treatments (Hayreh, 2014). Animal models of NAION are controversial. However, given the impelling data that exist on efficient clearance of oedema from the brain, we suggest that claudin-5 suppression within the inner retinal endothelial vasculature could represent a plausible means of alleviation of optic nerve head swelling. In this regard, we tested the efficacy of intravitreal inoculation of GLP grade claudin-5 siRNA in the Vervet (African Green) monkey. Tissues at the optic nerve head were dissected and subjected to RT-PCR analysis. Clearly, claudin-5 levels can be reduced using this approach (see Fig. 9). In the current context it is of note that intravitreal inoculation is widely accepted in routine ophthalmic practice (some patients have now received several hundred intravitreal injections of Lucentis). Moreover, therapy could readily be packaged as lyophilized compound, reconstituted and administered in outpatient facilities and readout of efficacy over days/weeks following therapy would be rapid, using standard clinical techniques (fluorescein angiography, visual acuity, OCT, ERG).

X-linked juvenile retinoschisis, caused by recessive mutations within the RS1 (Retinoschisin) gene, is characterised by splitting of the retina, particularly in the region of the macula, largely occurring in the OPL, INL and IPL layers (Gerth et al., 2008; Yu et al., 2010; Gregori et al., 2009). Retinoschisin is an extracellular matrix (ECM) protein secreted from a number of retinal cell types including photoreceptors, bipolar, amacrine and ganglion cells, and binding strongly to the membranes of photoreceptors and bipolar cells, stabilizing retinal cellular architecture (Vijayasarathy et al., 2012; Molday et al., 2012). AAV-mediated therapeutic intervention involving either CMV or endogenous promoter-driven expression of the RS1 gene, has now progressed from murine models (Zeng et al., 2004; Bush et al., 2016; Byrne et al., 2014; Dalkara et al., 2013) into clinical evaluation (Clinicaltrials.gov.NCT02416622; NCT0231787). It is also of note that regression of retinal cysts in one patient with juvenile XL retinoschisis was induced by oral administration (500 mg/day over four days) of the carbonic anhydrase inhibitor, acetozolmide (Zhang et al., 2015). The latter is used as a topical medication for open angle

Please cite this article in press as: Campbell, M., et al., Manipulating ocular endothelial tight junctions: Applications in treatment of retinal disease pathology and ocular hypertension, Progress in Retinal and Eye Research (2017), https://doi.org/10.1016/j.preteyeres.2017.09.003

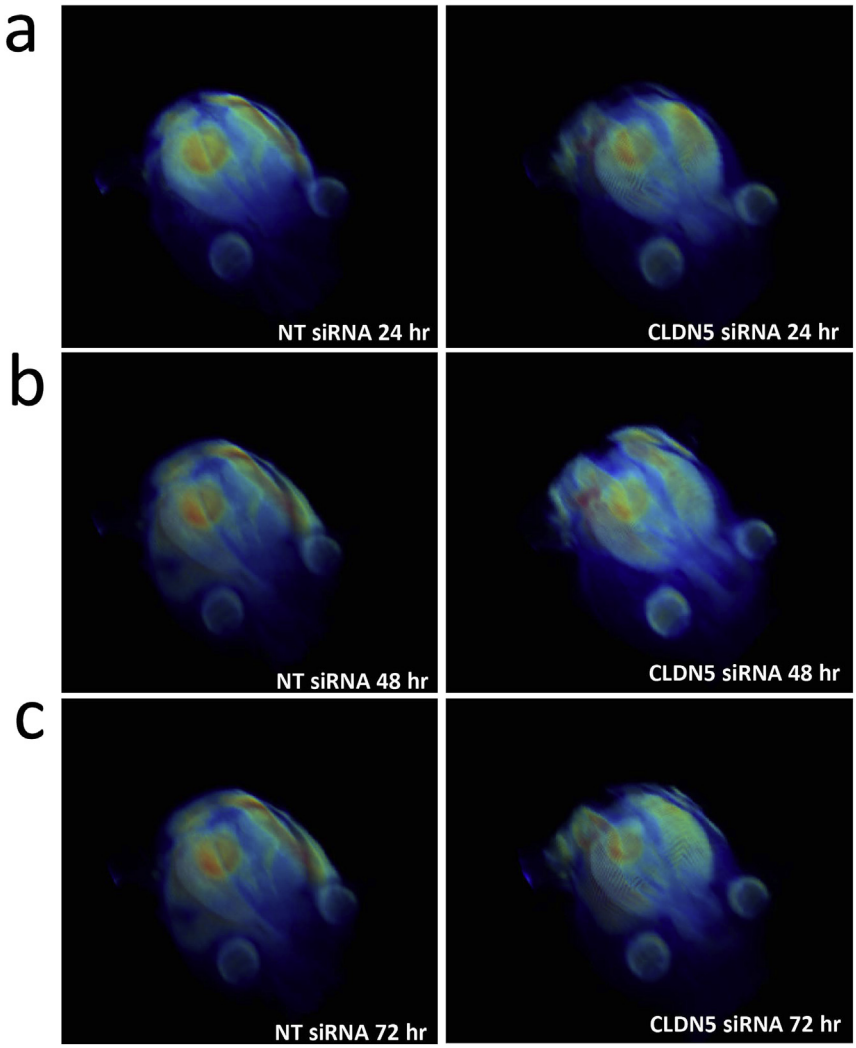

Fig. 7. Three-Dimensional volumetric rendering of MRI data showed lesion volume in red (pseudocolor) with NT siRNA injected mice in the left column and claudin-5 siRNA injected mice in the right column. **a)** NT siRNA and claudin-5 siRNA 24 h post injury. **b)** 48 h post injury. **c)** 72 h post injury.
This is a small part of figure 4 from our paper, Campbell et al., Nature Communications 2012 May 22; 3: 849.

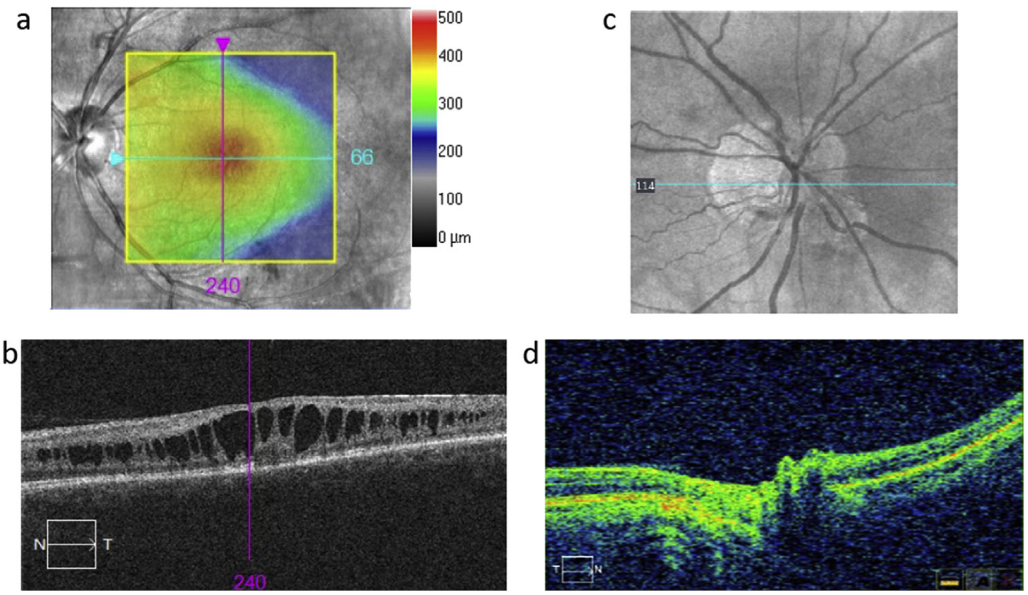

Fig. 8. a) and **b)** Optical coherence tomography (OCT) analysis of X-linked retinoschisis. **c)** and **d)** OCT analysis of non-arteritic ischemic optic neuropathy (NAION).

Please cite this article in press as: Campbell, M., et al., Manipulating ocular endothelial tight junctions: Applications in treatment of retinal disease pathology and ocular hypertension, Progress in Retinal and Eye Research (2017), https://doi.org/10.1016/j.preteyeres.2017.09.003

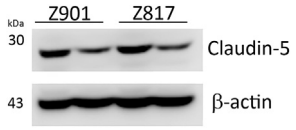

Fig. 9. Claudin-5 suppression in the vasculature associated with the optic nerve head in african green monkeys 48 h post injection of claudin-5 siRNA.

glaucoma and acts by enhancing aqueous outflow through the uveoscleral route. However, it also enhances the pumping activity of the RPE enabling excess fluid accumulating in intra-retinal cysts to be transported into the choroidal circulation. In view of the fact that the inner retinal microvessels innervate the layers of the retina in which schisis most frequently occurs, we speculate that modulation of the permeability of the inner retinal vessels may assist in facilitating fluid clearance from the large cysts that occur within these retinal layers. In this regard, it is noteworthy that intravitreal inoculation is an accepted mode of delivery of siRNA, the following trials serving as an indication: QPI-1007 (Quark): siRNA targeting caspase-2 for suppression of apoptosis in NAAION; AGN211745 (siRNA/Allergan): siRNA targets VEGFR1 (AMD); Bevasiranib (Opko Health): siRNA targets VEGF (diabetic macular oedema); PF-04523655 (Quark): siRNA targets RTP801/REDD1 apoptotic stress response gene; ALY040012 (Sylentis): siRNA targeting ocular hypertension. (Bevasiranib was initially withdrawn from trial owing to lack of efficiency in suppressing VEGF activity. Note however, that in the scenario described above, only partial knockdown of claudin-5 transcript is required to enhance iBRB permeability). This approach could also be envisaged as an adjunct to AAV-mediated therapeutic intervention, where AAV expressing an inducible claudin-5 shRNA is used in conjunction with gene replacement.

6.3. Enhancing clearance of soluble amyloid β1-40 from glaucomatous retinas

Evidence has accumulated over a number of years to suggest a pathological role for amyloid-β (Aβ) in degenerative retinopathies, including AMD and glaucoma. Co-localization of Aβ and drusen in post-mortem human AMD eyes has been observed in a number of studies, including those reported by Dentchev et al. (2003), Anderson et al. (2004) and Johnson et al. (2002), such studies suggesting Aβ as a putative activator of complement cascades. Further evidence for a pathological role for Aβ in AMD was reported by Ding et al. (2011) and Liu et al. (2015). In the former study, systemic anti-Aβ antibody treatment of APOE4 mice, fed on a high fat diet to induce AMD-like retinal symptoms, resulted in an alleviation of disease pathology, while in the latter, sub-retinal inoculation of Aβ into wild type mice produced pathological changes in RPE and photoreceptors. In optic nerve head post mortem tissue from individuals with glaucoma, Gupta et al. (2016) detected elevated levels of soluble Aβ, which has also been detected in aqueous humour from up to 40% of patients with glaucoma (Janciauskiene and Krakau, 2001).

These, and many other studies, strongly suggest that suppression of Aβ accumulation within retinal tissues may be protective in AMD, glaucoma and possibly in inherited retinal degenerations. In this regard, our own studies (Keaney et al., 2015) have shown that siRNA-mediated down regulation of endothelial tight junction transcripts encoding claudin-5 together with occludin, allowed paracellular transport of a soluble Aβ1-40 monomer (MW 4.3 kDa), modified with proline at position 19 and not prone to aggregation into higher molecular weight structures, to readily diffuse across brain endothelial cell monolayers in vitro. However, a dityrosine cross-linked Aβ1-40 dimer (MW 8.6 kDa) did not diffuse in such a manner, these data demonstrating that the paracellular spaces between brain endothelial cells can be widened sufficiently by down regulation of two tight junction components to allow soluble Aβ1-40 dimers to diffuse across them. These observations were confirmed *in vivo* in wild type mice and in a murine AD model (Tg2576) expressing a mutated form of APP, where it was shown that tail vein co-inoculation of claudin-5 and occludin siRNAs rendered the BBB reversibly permeable to biotinylated dextran of 3kD but not of 10kD. Periodic intravenous inoculation of claudin-5

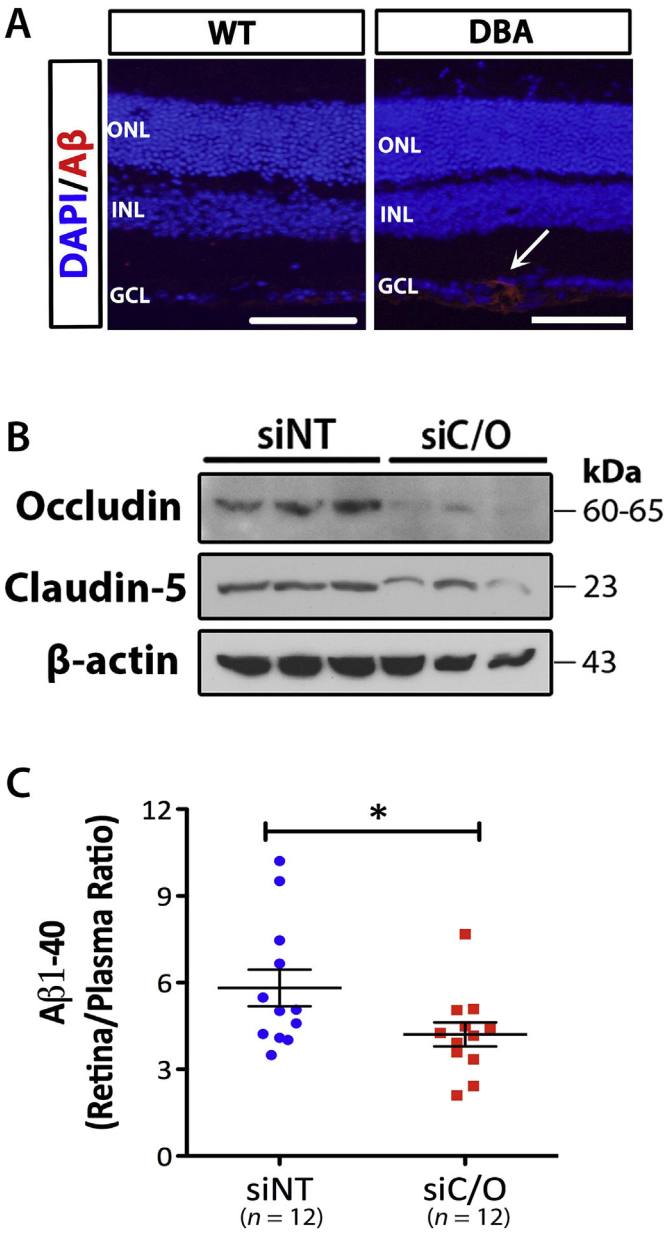

Fig. 10. Aβ in retinas of 8-month old siRNA-treated DBA/2J mice. **a)** Aβ immunostaining in the ganglion cell layer of wild-type (WT) and DBA/2J mouse retinas (ONL: outer nuclear layer, INL: inner nuclear layer, GCL: ganglion cell layer. Scale bar = 50 μm). **b)** Western blot analysis of claudin-5 and occludin in retinas of DBA/2J mice following systemic administration of non-targeting (NT) or claudin-5 and occludin (C/O) siRNAs. **c)** Retina/plasma ratios of Aβ(1–40) (pg/g soluble retina Aβ(1–40) to pg/ml plasma Aβ(1–40)) in DBA/2J mice after a single round of siRNA administration (unpaired Student's *t*-test, n = 12 animals per experimental group, $^{*}P = 0.045$. Data are means ± s.e.m.).
This is supplementary Figure 10 from our paper, Keaney et al., Sci. Adv. 2015 Sep; 1(8) e1500472.

and occludin siRNAs every 21 days into AD mice for a period of 9 months resulted during this period in a significant induction of movement of soluble Aβ1-40 from brain tissue into the peripheral circulation. Furthermore, in a murine model of pseudoexfoliative glaucoma, the DBA/2J mouse, in which Aβ1-40 was clearly detectable in retinal sections, a single intravenous injection of claudin-5 and occludin siRNAs resulted in retina:plasma ratios of Aβ1-40 being significantly reduced (Fig. 10).

These data raise the distinct possibility for an avenue of clearance of neurotoxic Aβ1-40 from retinal tissues as a means of protecting against ganglion cell death in glaucoma. It will be of interest in this context to assess such an approach in additional models more accurately resembling the primary open-angle form of glaucoma, for example in transgenic mice expressing a C437H mutation within the human myocilin gene, a model mimicking primary open angle glaucoma in which there is an intracellular accumulation of ECM material within cells of the Trabecular meshwork, and a decrease in secretion of MMPs, favouring an extracellular accumulation of ECM materials, these animals classically displaying elevations in IOP and reduced outflow facility, with concomitant demise of retinal ganglion cells (Zode et al., 2011).

6.4. Targeting oxidative stress

The brain and retina account for approx. 20% of the body's oxygen consumption, which generates appreciable levels of reactive oxygen species and peroxides, contributing to neurological and retinal degeneration (Ott et al., 2007). For example, oxygen free radicals interact with membrane phospholipids generating MDA (malondialdehyde; HOCH=CH-CHO, or $C_3H_4O_2$). This compound is pro-inflammatory, and has been recently shown (Weismann et al., 2011) to be normally sequestered by complement factor H (CFH). CFH is an inhibitor of the alternative complement pathway and a mutation, His402Tyr within the SCR-7 domain of the protein was the first to be strongly associated with AMD. The risk variant, CC has been shown to have a very much lower affinity for MDA than the non-risk variant TT. People with AMD who are heterozygous for the normal and risk variants have a compromised ability to bind MDA, presumably increasing the risk of disease progression. The Authors conclude: 'We report the identification of CFH as a hitherto unrecognized innate defence protein against MDA, which is a ubiquitously generated pro-inflammatory product of lipid peroxidation'. Reactive oxygen species are also similarly important in contributing to disease pathology in IRDs and in diabetic retinopathy (Kiang et al., 2014).

Mitochondria are a major site of generation of oxygen free radicals in the retina. A recently developed oxygen free radical scavenger, XJB -5-131 (4- hydroxy-2,2,6,6-tetramethyl piperidine-1-oxyl nitroxide chemically linked to a mitochondrial targeting peptide, Leu-D-Phe-Pro-Val-Orn), enables the systemically-administered drug to become localized in the membranes of the mitochondria and it has been shown to be protective against neurological degeneration in a murine model of Huntington's disease (Xun et al., 2012). While this drug, with a molecular weight of 959 Da, can access the brain in the Huntington model, it's systemic access to the retina could be radically enhanced (with concomitant reduction in systemic dosage) by periodic manipulation of iBRB permeability, possibly representing a approach to slowing disease progression in a manner independent of primary mutations in IRDs or other retinopathies.

6.5. Targeting unique IRD molecular pathologies

With over 260 genes having so far been identified in IRDs, with 70 in retinitis pigmentosa, the molecular pathologies associated with these conditions are clearly of immense diversity, genes encoding proteins, or enzymes involved in transport processes, protein deglutamylation, membrane trafficking, ciliogenesis, calcium-sensitive chloride channels, proteins with protective function against apoptosis/oxidative stress, retinal neurotransmission, photoreceptor morphogenesis, fatty acid and steroid metabolism, extracellular proteins of the retina, retinal adhesion proteins, phagocytosis of rod outer segments, transcription factors and activators, semaphorins, protein ubiquitination, actin binding proteins, pre-mRNA processing, the rate-limiting step of the alternative pathway of guanine nucleotide biosynthesis, and about every gene encoding proteins or enzymes of the visual transduction and retinoid cycles, and indeed many more (Jane Farrar et al., 2017). In some cases, molecular pathologies specific to only one, or a limited number of genetic subtypes of disease may offer opportunities to target such uniqueness by systemic drug treatment.

The RP10 form of RP is arguably one of these, accounting for at least 5% of autosomal dominant cases of RP (perhaps 25–30,000 cases world-wide). It is an early onset, aggressive retinopathy, symptoms manifesting within the first decade. The disease is caused by mutations within the inosine monophosphate dehydrogenase 1 (IMPDH1) gene (Jordan et al., 1993; Kennan et al., 2002; Aherne et al., 2004), which, together with IMPDH2, are the rate-limiting enzymes of *de novo* guanine nucleotide biosynthesis. While each enzyme performs the same role in converting IMP to XMP, which is then converted to GMP, levels of expression between tissues vary considerably, the predominant enzyme within the murine retina being IMPDH1 (Aherne et al., 2004). IMPDH1−/− mice (hence having little or no IMPDH activity because of minimal expression of IMPDH2) have only a very slow deterioration in retinal function, the outer nuclear layer (ONL) of these animals remaining largely intact (Aherne et al., 2004). Since both IMPDH1 and IMPDH2 are minimally expressed in these retinas, retinal function appears to be maintained with a sufficient supply of guanine nucleotides generated by the salvage pathway of guanine nucleotide biosynthesis. Mutations identified in RP10, occur within the CBS domain of the IMPDH1 enzyme, a binding site for GDP/GTP inhibition, indicating that mutations within the IMPDH1 gene result in constitutive activation of the enzyme, disturbing guanine nucleotide pools within the retina and thus causing loss of photoreceptor function (Buey et al., 2015). Interestingly however, OCT imaging (unpublished data) of severely affected individuals reveals a remarkably intact outer nuclear retinal layer, indicating that while visual function is lost, photoreceptors appear to remain viable (Fig. 11), thus providing a potentially very robust window of opportunity for therapeutic intervention. These data suggest that suppression of IMPDH in dominant RP10 could result in a restoration of visual function. A number of FDA-approved IMPDH inhibitors (inhibiting both IMPDH1 and 2) are available, including CellCept, Mizorbine and VX-497 and these have been used as

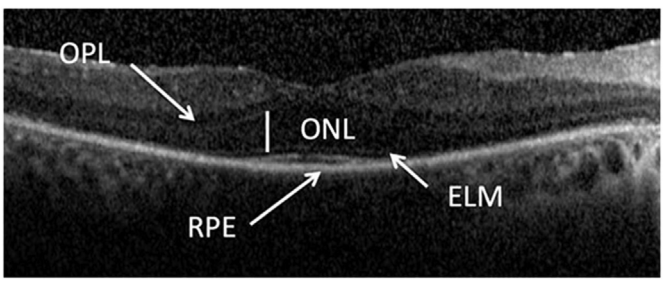

Fig. 11. Preserved outer nuclear layer (ONL) in a patient with the RP10 form of retinitis pigmentosa.

Please cite this article in press as: Campbell, M., et al., Manipulating ocular endothelial tight junctions: Applications in treatment of retinal disease pathology and ocular hypertension, Progress in Retinal and Eye Research (2017), https://doi.org/10.1016/j.preteyeres.2017.09.003

effective immunosuppressive agents (B and T lymphocytes are highly dependent upon the alternative, rather than the salvage pathway of guanine nucleotide biosynthesis). The concept of repositioning such agents as orally-available therapeutics for an IRD, delivery of which could be enhanced (thus reducing systemic dosage) by manipulating ocular endothelial tight junctions is a provocative but potentially realistic concept, dependent on long term tolerability. Given the ease with which systemically-deliverable compounds can access the retina (Fig. 3), tolerable doses may be achievable.

The gene encoding Bestrophin, a calcium-gated chloride channel located in the basolateral region of RPE cells, is mutated in the ciliopathy, autosomal recessive bestrophinopathy (Johnson et al., 2017). Mutated proteins have been shown to mis-localise and end up in proteasomes in the cytoplasm and are degraded (Uggenti et al., 2016). These authors have shown in vitro that proteasomal inhibitors, Bortezomib and 4-phenylbutyrate (4PBA), both approved proteasomal inhibitors, effectively restore the location of mutant bestrophins to the RPE and restore Cl-conductance of the channels in vitro. The Authors comment: "The functional rescue achieved with 4PBA is significant because it suggests that this drug, which is already approved for long-term use in infants and adults, might represent a promising therapy for the treatment of ARB and other bestrophinopathies resulting from missense mutations in BEST1". Again, the degree of enhancement of systemic drug uptake by claudin-5 modulated iBRB could render such compounds (MW 4-PBA 186Da; MW Bortezomib 384Da) systemically tolerable over prolonged periods.

7. Targeting Schlemm's canal endothelial tight junctions: a novel process for enhancement of aqueous outflow through the conventional outflow pathway

Glaucoma in its various forms represents the second most common blinding disease on a global basis after cataract, elevations in IOP being the greatest risk factor (Quigley and Broman, 2006; Tham et al., 2014; Actis et al., 2016). Aqueous humour leaves the eye through the so-called conventional and un-conventional outflow pathways located close together in the periphery of the anterior chamber, at the apex of the narrow angle formed between the iris and the cornea. The conventional outflow pathway comprises the trabecular meshwork, which, as the name suggests, is an interlaced structure of cells embedded in a pressure-responsive ECM through which aqueous flows into the Canal of Schlemm both through paracellular gaps or through cellular pores in the canal's endothelial lining. While a number of genes have been firmly associated with open-angle glaucoma susceptibility, a robust understanding of the molecular pathology of the disease remains to be determined. It should be highlighted, that a balance in the production of matrix metalloproteinases (MMPs) and their tissue inhibitors within the trabecular meshwork is a significant factor in the maintenance of physiological IOP at between 12 and 22 mmHg (De Groef et al., 2013). From the canal, fluid flows through collector channels and eventually into the episcleral veins. Some aqueous also leaves the eye through the bundles of the ciliary muscles – the so-called un-conventional or uveoscleral route. Interestingly, currently used topical medications (including prostaglandin analogues, carbonic anhydrase inhibitors and β-blockers) either slow up aqueous production by the ciliary body, or enhance its clearance via the uveoscleral route, none of these formulations directly and primarily targeting the conventional pathway. Since an appreciable number of those with open angle disease do not respond adequately to currently available pressure-reducing drugs, a large amount of research in recent years has gone into the development of medicines capable of enhancing aqueous outflow through the conventional route. These include Rho kinase inhibitors (Li et al., 2016; Ren et al., 2016), adenosine receptor agonists (Laties et al., 2016; Myers et al., 2016), marine macrolides (Ethier et al., 2006), prostanoid receptor agonists (Kalouche et al., 2016) and AAV-mediated gene therapies involving enhanced MMP expression to remodel the ECM within the Trabecular meshwork (Spiga and Borras, 2010; Gerometta et al., 2010; Borras et al., 2016; O'Callaghan et al., 2017).

The bulk of outflow resistance in the conventional pathway is generated within the juxtacanalicular tissues and the endothelial cells of the canal itself. Aqueous enters Schlemm's canal either through the formation of intra-endothelial fluid-filled vacuoles (so called 'giant' vacuoles) or through the paracellular route, where it passes through pores left between the endothelial tight junctions. Less is known of the nature of the tight junctions joining SC endothelia than those of the cerebral and inner retinal vasculatures. Interestingly claudin-5, a major component of the tight junctions of the cerebral and inner retinal vascular endothelia, is absent from human SC endothelial cells (Tam et al., 2017). However, as outlined earlier, ZO-1, tricellulin and claudin-11 are prominently expressed TJ proteins. In order to explore the hypothesis that down-regulation of SC endothelial TJs might result in an increase in the permeability of the canal, Tam et al. (2017) intracamerally injected siRNA validated against tricellulin and ZO-1 into wild type mice. Injected material followed the natural flow of aqueous through the trabecular meshwork and into the canal's endothelial cells. As illustrated in Fig. 12, transmission electron microscopy revealed reversible opening of the paracellular clefts between endothelial cells as a result of such down-regulation. This was accompanied by a significant elevation in outflow facility in treated eyes *ex vivo*.

In translational terms, a major factor to be considered in this approach is the mode of siRNA delivery. Recent reports have indicated that siRNA can be effectively delivered to the eye in the form of topical drops to the cornea. However, in this approach, while the siRNA (SYL040012, targeting the β2-adrenoceptor) was able to efficiently access the ciliary body which was the primary site of action, little siRNA was found in the aqueous humour using this technique (Martinez et al., 2014; Moreno-Montanes et al., 2014). While periodic intracameral injection of siRNA as indicated by IOP is a realistic option, an alternative and less invasive procedure would involve retrograde introduction of siRNA into Schlemm's canal via the episcleral veins and a device facilitating this approach has been manufactured (Retroject Inc, NC). An alternative would be the use of AAV as a delivery vehicle for shRNAs. While single stranded AAV particles will not transfect tissues of the trabecular meshwork, self-complementary AAV have been reported to do so with high efficiency (Buie et al., 2010). However, it is unclear from this work as to whether AAV directly transfects SC endothelial cells. If this can be demonstrated, an AAV expressing shRNAs under the control of a promoter inducible by a topical eye drop could in principle be used. In this regard, it is of interest to note in a recently reported experimental system, that AAV transfecting the corneal endothelium can be activated to express MMP3 via the use of doxycycline applied to the cornea, the enzyme then being secreted from the corneal endothelia in to the TM, where re-modelling of the ECM resulted in increased outflow facility and decreased IOP in wild type mice (O'Callaghan et al., 2017). Since an inducing agent will travel with the natural flow of aqueous toward Schlemm's canal, there is reason to believe that AAVs transfecting SC endothelia could be periodically activated using such a procedure. A combinatorial AAV-mediated approach, targeting ECM remodelling together with incrementing SC permeability, is a realistic possibility based on observations to date.

Please cite this article in press as: Campbell, M., et al., Manipulating ocular endothelial tight junctions: Applications in treatment of retinal disease pathology and ocular hypertension, Progress in Retinal and Eye Research (2017), https://doi.org/10.1016/j.preteyeres.2017.09.003

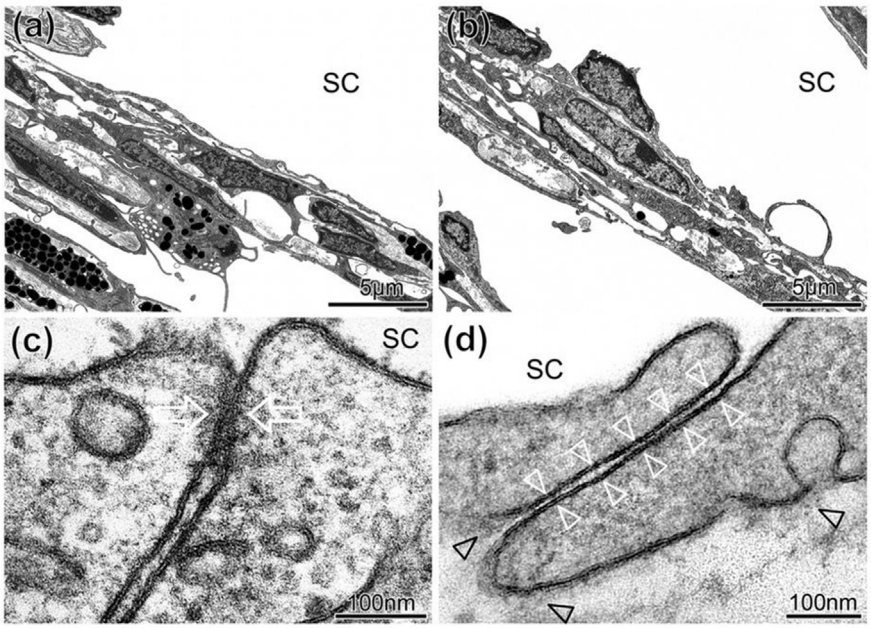

Fig. 12. Representative sagittal sections through the inner wall of Schlemm's canal (SC) and outer trabecular meshwork (TM) of a mouse eye treated with **(a)** non-targeting (NT) or **(b)** targeting (T) siRNA illustrating intact cells and an intact and continuous inner wall endothelium that appeared similar in both cases. The inner wall endothelium is connected to the underlying ECM so that no ballooning was visible. (**c**, **d**) High magnifications of sagittal sections through intercellular clefts along the inner wall endothelium of SC showing examples for junctions quantitatively evaluated as closed **(c)** with fusion between the neighbouring cell membranes (arrows) or open clefts **(d)** where the cell membranes of adjacent endothelial cells were clearly separated along the entire cleft length (white arrowheads). Despite the open clefts, adhesions to sub-endothelial matrix (black arrowheads) were preserved.
This is Figure 6 from our paper Tam et al., Scientific Reports 2017; 7: 40717 (pbl on line Jan 16 2017).

8. Future prospects

Retinal endothelial barrier modulation technologies are, in principle, deployable in a stand-alone sense, or in combination with gene and other molecular therapeutic approaches. There is a significant need for a therapy for one of the more common idiopathic retinopathies, NAION, which is currently incurable and can lead to irreversible blindness. Clearance of oedema from the optic nerve head by intravitreal injection of siRNA targeting claudin-5 could well be effective in this scenario. It is also of note that as yet there are no medicines available for the most common (non-exudative) form of AMD, and yet, clearance of Aβ, or drug-mediated suppression of oxidative stress within the retina, could have utility in slowing down disease progression in this, and indeed other forms of retinal degeneration including glaucoma. It will also be of interest to assess the efficacies of gene therapy for XL-retinoschisis *vis-à-vis* direct facilitation of fluid egress from intraretinal cysts, perhaps the two approaches, each using AAV could be used in a combinatorial sense. Repositioning approved drugs for use as therapies in early stage IRDs where the iBRB is essentially intact, is an interesting possibility, several scenarios having been outlined, including the possibility of IMPDH1 suppression in the RP10 form of RP and the use of proteasome inhibitors for at least one form of bestrophinopathy, but there will be many other examples based on the very extensive range of molecular pathologies that are involved, low molecular weight drug-mediated inhibition of protein misfolding for example, being one. Improved treatment regimens for open-angle glaucoma continue to be a priority. As outlined, much research is currently being directed toward the development of topical formulations targeting the major (conventional) outflow pathway. The fact that siRNA could periodically be delivered in a retrograde fashion into Schlemm's canal endothelia through the episcleral veins, obviating a requirement for intracameral inoculation, is an interesting concept which, in principle, could be deployed as an outpatient procedure. In summary, we suggest that direct manipulation of permeability of both the inner retinal microvasculature and the Canal of Schlemm, may have significant potential clinical utility.

Acknowledgement

We thank Blanca Garcia Sandoval and Carmen Ayuso for provision of unpublished OCT images of RP10; Matthew Lawrence for provision of dissected primate tissues from the optic nerve head and David Keegan for OCT and fundus images of NAION and XL-retinoschisis. Research on modulation of permeability at the blood-brain and inner blood-retina barriers has been supported by grants from the Wellcome Trust, Science Foundation Ireland, the Health Research Board of Ireland, Enterprise Ireland, Bright Focus Foundation and the US Department of Defense. Studies on enhancement of aqueous outflow by modulation of permeability at SC endothelia is supported by the European Research Council (ERC-2012-AdG 322656-Oculus). Primate studies on claudin-5 suppression were supported by the St. Kitt's Medical Research Foundation.

References

Abbott, N.J., Patabendige, A.A., Dolman, D.E., Yusof, S.R., Begley, D.J., 2010. Structure and function of the blood-brain barrier. Neurobiol. Dis. 37, 13–25.

Actis, A.G., Versino, E., Brogliatti, B., Rolle, T., 2016. Risk factors for primary open angle glaucoma (POAG) progression: a study ruled in Torino. Open Ophthalmol. J. 10, 129–139.

Aherne, A., Kennan, A., Kenna, P.F., McNally, N., Lloyd, D.G., Alberts, I.L., Kiang, A.S., Humphries, M.M., Ayuso, C., Engel, P.C., Gu, J.J., Mitchell, B.S., Farrar, G.J., Humphries, P., 2004. On the molecular pathology of neurodegeneration in IMPDH1-based retinitis pigmentosa. Hum. Mol. Genet. 13, 641–650.

Aleman, T.S., Duncan, J.L., Bieber, M.L., de Castro, E., Marks, D.A., Gardner, L.M., Steinberg, J.D., Cideciyan, A.V., Maguire, M.G., Jacobson, S.G., 2001. Macular pigment and lutein supplementation in retinitis pigmentosa and Usher

syndrome. Invest Ophthalmol. Vis. Sci. 42, 1873–1881.
Anderson, J.M., Van Itallie, C.M., 2008. Tight junctions. Curr. Biol. 18, R941–R943.
Anderson, D.H., Talaga, K.C., Rivest, A.J., Barron, E., Hageman, G.S., Johnson, L.V., 2004. Characterization of beta amyloid assemblies in drusen: the deposits associated with aging and age-related macular degeneration. Exp. Eye Res. 78, 243–256.
Ben-Yosef, T., Belyantseva, I.A., Saunders, T.L., Hughes, E.D., Kawamoto, K., Van Itallie, C.M., Beyer, L.A., Halsey, K., Gardner, D.J., Wilcox, E.R., Rasmussen, J., Anderson, J.M., Dolan, D.F., Forge, A., Raphael, Y., Camper, S.A., Friedman, T.B., 2003. Claudin 14 knockout mice, a model for autosomal recessive deafness DFNB29, are deaf due to cochlear hair cell degeneration. Hum. Mol. Genet. 12, 2049–2061. Epub 2003/08/13.
Bhatt, K., Gong, H., Freddo, T.F., 1995. Freeze-fracture studies of interendothelial junctions in the angle of the human eye. Invest Ophthalmol. Vis. Sci. 36, 1379–1389.
Borras, T., Buie, L.K., Spiga, M.G., 2016. Inducible scAAV2.GRE.MMP1 lowers IOP long-term in a large animal model for steroid-induced glaucoma gene therapy. Gene Ther. 23, 438–449.
Buey, R.M., Ledesma-Amaro, R., Velazquez-Campoy, A., Balsera, M., Chagoyen, M., de Pereda, J.M., Revuelta, J.L., 2015. Guanine nucleotide binding to the Bateman domain mediates the allosteric inhibition of eukaryotic IMP dehydrogenases. Nat. Commun. 6, 8923.
Buie, L.K., Rasmussen, C.A., Porterfield, E.C., Ramgolam, V.S., Choi, V.W., Markovic-Plese, S., Samulski, R.J., Kaufman, P.L., Borras, T., 2010. Self-complementary AAV virus (scAAV) safe and long-term gene transfer in the trabecular meshwork of living rats and monkeys. Invest Ophthalmol. Vis. Sci. 51, 236–248.
Bush, R.A., Zeng, Y., Colosi, P., Kjellstrom, S., Hiriyanna, S., Vijayasarathy, C., Santos, M., Li, J., Wu, Z., Sieving, P.A., 2016. Preclinical dose-escalation study of intravitreal AAV-RS1 gene therapy in a mouse model of X-linked retinoschisis: dose-dependent expression and improved retinal structure and function. Hum. Gene Ther. 27, 376–389.
Byrne, L.C., Ozturk, B.E., Lee, T., Fortuny, C., Visel, M., Dalkara, D., Schaffer, D.V., Flannery, J.G., 2014. Retinoschisin gene therapy in photoreceptors, Muller glia or all retinal cells in the Rs1h-/- mouse. Gene Ther. 21, 585–592.
Campbell, M., Humphries, P., 2012. The blood-retina barrier: tight junctions and barrier modulation. Adv. Exp. Med. Biol. 763, 70–84.
Campbell, M., Kiang, A.S., Kenna, P.F., Kerskens, C., Blau, C., O'Dwyer, L., Tivnan, A., Kelly, J.A., Brankin, B., Farrar, G.J., Humphries, P., 2008. RNAi-mediated reversible opening of the blood-brain barrier. J. Gene Med. 10, 930–947.
Campbell, M., Nguyen, A.T., Kiang, A.S., Tam, L.C., Gobbo, O.L., Kerskens, C., Ni Dhubhghaill, S., Humphries, M.M., Farrar, G.J., Kenna, P.F., Humphries, P., 2009. An experimental platform for systemic drug delivery to the retina. Proc. Natl. Acad. Sci. U. S. A. 106, 17817–17822.
Campbell, M., Humphries, M.M., Kiang, A.S., Nguyen, A.T., Gobbo, O.L., Tam, L.C., Suzuki, M., Hanrahan, F., Ozaki, E., Farrar, G.J., Kenna, P.F., Humphries, P., 2011. Systemic low-molecular weight drug delivery to pre-selected neuronal regions. EMBO Mol. Med. 3, 235–245.
Campbell, M., Hanrahan, F., Gobbo, O.L., Kelly, M.E., Kiang, A.S., Humphries, M.M., Nguyen, A.T., Ozaki, E., Keaney, J., Blau, C.W., Kerskens, C.M., Cahalan, S.D., Callanan, J.J., Wallace, E., Grant, G.A., Doherty, C.P., Humphries, P., 2012. Targeted suppression of claudin-5 decreases cerebral oedema and improves cognitive outcome following traumatic brain injury. Nat. Commun. 3, 849.
Dalkara, D., Byrne, L.C., Klimczak, R.R., Visel, M., Yin, L., Merigan, W.H., Flannery, J.G., Schaffer, D.V., 2013. In vivo-directed evolution of a new adeno-associated virus for therapeutic outer retinal gene delivery from the vitreous. Sci. Transl. Med. 5, 189ra76.
De Groef, L., Van Hove, I., Dekeyster, E., Stalmans, I., Moons, L., 2013. MMPs in the trabecular meshwork: promising targets for future glaucoma therapies? Invest Ophthalmol. Vis. Sci. 54, 7756–7763.
Dentchev, T., Milam, A.H., Lee, V.M., Trojanowski, J.Q., Dunaief, J.L., 2003. Amyloid-beta is found in drusen from some age-related macular degeneration retinas, but not in drusen from normal retinas. Mol. Vis. 9, 184–190.
Ding, J.D., Johnson, L.V., Herrmann, R., Farsiu, S., Smith, S.G., Groelle, M., Mace, B.E., Sullivan, P., Jamison, J.A., Kelly, U., Harrabi, O., Bollini, S.S., Dilley, J., Kobayashi, D., Kuang, B., Li, W., Pons, J., Lin, J.C., Bowes Rickman, C., 2011. Anti-amyloid therapy protects against retinal pigmented epithelium damage and vision loss in a model of age-related macular degeneration. Proc. Natl. Acad. Sci. U. S. A. 108, E279–E287.
Epstein, D.L., Rohen, J.W., 1991. Morphology of the trabecular meshwork and inner-wall endothelium after cationized ferritin perfusion in the monkey eye. Invest Ophthalmol. Vis. Sci. 32, 160–171.
Ethier, C.R., Read, A.T., Chan, D.W., 2006. Effects of latrunculin-B on outflow facility and trabecular meshwork structure in human eyes. Invest Ophthalmol. Vis. Sci. 47, 1991–1998.
Fujimoto, K., 1995. Freeze-fracture replica electron microscopy combined with SDS digestion for cytochemical labeling of integral membrane proteins. Application to the immunogold labeling of intercellular junctional complexes. J. Cell Sci. 108 (Pt 11), 3443–3449.
Furuse, M., Tsukita, S., 2006. Claudins in occluding junctions of humans and flies. Trends Cell Biol. 16, 181–188.
Gerometta, R., Spiga, M.G., Borras, T., Candia, O.A., 2010. Treatment of sheep steroid-induced ocular hypertension with a glucocorticoid-inducible MMP1 gene therapy virus. Invest Ophthalmol. Vis. Sci. 51, 3042–3048.
Gerth, C., Zawadzki, R.J., Werner, J.S., Heon, E., 2008. Retinal morphological changes of patients with X-linked retinoschisis evaluated by Fourier-domain optical coherence tomography. Arch. Ophthalmol. 126, 807–811.
Gregori, N.Z., Berrocal, A.M., Gregori, G., Murray, T.G., Knighton, R.W., Flynn Jr., H.W., Dubovy, S., Puliafito, C.A., Rosenfeld, P.J., 2009. Macular spectral-domain optical coherence tomography in patients with X linked retinoschisis. Br. J. Ophthalmol. 93, 373–378.
Gupta, V., Gupta, V.B., Chitranshi, N., Gangoda, S., Vander Wall, R., Abbasi, M., Golzan, M., Dheer, Y., Shah, T., Avolio, A., Chung, R., Martins, R., Graham, S., 2016. One protein, multiple pathologies: multifaceted involvement of amyloid beta in neurodegenerative disorders of the brain and retina. Cell Mol. Life Sci. 73, 4279–4297.
Hadj-Rabia, S., Baala, L., Vabres, P., Hamel-Teillac, D., Jacquemin, E., Fabre, M., Lyonnet, S., De Prost, Y., Munnich, A., Hadchouel, M., Smahi, A., 2004. Claudin-1 gene mutations in neonatal sclerosing cholangitis associated with ichthyosis: a tight junction disease. Gastroenterology 127, 1386–1390.
Hamazaki, Y., Itoh, M., Sasaki, H., Furuse, M., Tsukita, S., 2002. Multi-PDZ domain protein 1 (MUPP1) is concentrated at tight junctions through its possible interaction with claudin-1 and junctional adhesion molecule. J. Biol. Chem. 277, 455–461.
Hawkins, B.T., Davis, T.P., 2005. The blood-brain barrier/neurovascular unit in health and disease. Pharmacol. Rev. 57, 173–185.
Hayreh, S.S., 2013. Ischemic optic neuropathies - where are we now? Graefes Arch. Clin. Exp. Ophthalmol. 251, 1873–1884.
Hayreh, S.S., 2014. Ocular vascular occlusive disorders: natural history of visual outcome. Prog. Retin Eye Res. 41, 1–25.
Itoh, M., Furuse, M., Morita, K., Kubota, K., Saitou, M., Tsukita, S., 1999. Direct binding of three tight junction-associated MAGUKs, ZO-1, ZO-2, and ZO-3, with the COOH termini of claudins. J. Cell Biol. 147, 1351–1363.
Janciauskiene, S., Krakau, T., 2001. Alzheimer's peptide: a possible link between glaucoma, exfoliation syndrome and Alzheimer's disease. Acta Ophthalmol. Scand. 79, 328–329.
Jane Farrar, G., Carrigan, M., Dockery, A., Millington Ward, S., Palfi, A., Chadderton, N., Humphries, M., Kiang, A.S., Kenna, P.F., Humphries, P., 2017 Aug 1. Toward an elucidation of the molecular genetics of inherited retinal degenerations. Hum. Mol. Genet. 26 (R1), R2–R11.
Johnson, M., 2006. 'What controls aqueous humour outflow resistance?'. Exp. Eye Res. 82, 545–557.
Johnson, L.V., Leitner, W.P., Rivest, A.J., Staples, M.K., Radeke, M.J., Anderson, D.H., 2002. The Alzheimer's A beta -peptide is deposited at sites of complement activation in pathologic deposits associated with aging and age-related macular degeneration. Proc. Natl. Acad. Sci. U. S. A. 99, 11830–11835.
Johnson, A.A., Guziewicz, K.E., Lee, C.J., Kalathur, R.C., Pulido, J.S., Marmorstein, L.Y., Marmorstein, A.D., 2017. Bestrophin 1 and retinal disease. Prog. Retin Eye Res. 58, 45–69.
Jordan, S.A., Farrar, G.J., Kenna, P., Humphries, M.M., Sheils, D.M., Kumar-Singh, R., Sharp, E.M., Soriano, N., Ayuso, C., Benitez, J., et al., 1993. Localization of an autosomal dominant retinitis pigmentosa gene to chromosome 7q. Nat. Genet. 4, 54–58.
Kalouche, G., Beguier, F., Bakria, M., Melik-Parsadaniantz, S., Leriche, C., Debeir, T., Rostene, W., Baudouin, C., Vige, X., 2016. Activation of prostaglandin FP and EP2 receptors differently modulates myofibroblast transition in a model of adult primary human trabecular meshwork cells. Invest Ophthalmol. Vis. Sci. 57, 1816–1825.
Kass, M.A., Heuer, D.K., Higginbotham, E.J., Johnson, C.A., Keltner, J.L., Miller, J.P., Parrish 2nd, R.K., Wilson, M.R., Gordon, M.O., 2002. The Ocular Hypertension Treatment Study: a randomized trial determines that topical ocular hypotensive medication delays or prevents the onset of primary open-angle glaucoma. Arch. Ophthalmol. 120 (701–13), 829–830 discussion.
Keaney, J., Walsh, D.M., O'Malley, T., Hudson, N., Crosbie, D.E., Loftus, T., Sheehan, F., McDaid, J., Humphries, M.M., Callanan, J.J., Brett, F.M., Farrell, M.A., Humphries, P., Campbell, M., 2015. Autoregulated paracellular clearance of amyloid-beta across the blood-brain barrier. Sci. Adv. 1, e1500472.
Kennan, A., Aherne, A., Palfi, A., Humphries, M., McKee, A., Stitt, A., Simpson, D.A., Demtroder, K., Orntoft, T., Ayuso, C., Kenna, P.F., Farrar, G.J., Humphries, P., 2002. Identification of an IMPDH1 mutation in autosomal dominant retinitis pigmentosa (RP10) revealed following comparative microarray analysis of transcripts derived from retinas of wild-type and Rho(-/-) mice. Hum. Mol. Genet. 11, 547–557.
Kiang, A.S., Humphries, M.M., Campbell, M., Humphries, P., 2014. Antioxidant therapy for retinal disease. Adv. Exp. Med. Biol. 801, 783–789.
Kitajiri, S., Miyamoto, T., Mineharu, A., Sonoda, N., Furuse, K., Hata, M., Sasaki, H., Mori, Y., Kubota, T., Ito, J., Furuse, M., Tsukita, S., 2004. Compartmentalization established by claudin-11-based tight junctions in stria vascularis is required for hearing through generation of endocochlear potential. J. Cell Sci. 117, 5087–5096.
Laties, A., Rich, C.C., Stoltz, R., Humbert, V., Brickman, C., McVicar, W., Baumgartner, R.A., 2016. A randomized phase 1 dose escalation study to evaluate safety, tolerability, and pharmacokinetics of trabodenoson in healthy adult volunteers. J. Ocul. Pharmacol. Ther. 32, 548–554.
Li, G., Mukherjee, D., Navarro, I., Ashpole, N.E., Sherwood, J.M., Chang, J., Overby, D.R., Yuan, F., Gonzalez, P., Kopczynski, C.C., Farsiu, S., Stamer, W.D., 2016. Visualization of conventional outflow tissue responses to netarsudil in living mouse eyes. Eur. J. Pharmacol. 787, 20–31.
Li, B., Vachali, P.P., Shen, Z., Gorusupudi, A., Nelson, K., Besch, B.M., Bartschi, A., Longo, S., Mattinson, T., Shihab, S., Polyakov, N.E., Suntsova, L.P., Dushkin, A.V., Bernstein, P.S., 2017. Retinal accumulation of zeaxanthin, lutein, and beta-

Please cite this article in press as: Campbell, M., et al., Manipulating ocular endothelial tight junctions: Applications in treatment of retinal disease pathology and ocular hypertension, Progress in Retinal and Eye Research (2017), https://doi.org/10.1016/j.preteyeres.2017.09.003

carotene in mice deficient in carotenoid cleavage enzymes. Exp. Eye Res. 159, 123–131.
Liu, R., Wang, T., Zhang, B., Qin, L., Wu, C., Li, Q., Ma, L., 2014. Lutein and zeaxanthin supplementation and association with visual function in age-related macular degeneration. Invest Ophthalmol. Vis. Sci. 56, 252–258.
Liu, C., Cao, L., Yang, S., Xu, L., Liu, P., Wang, F., Xu, D., 2015. Subretinal injection of amyloid-beta peptide accelerates RPE cell senescence and retinal degeneration. Int. J. Mol. Med. 35, 169–176.
Ma, L., Dou, H.L., Huang, Y.M., Lu, X.R., Xu, X.R., Qian, F., Zou, Z.Y., Pang, H.L., Dong, P.C., Xiao, X., Wang, X., Sun, T.T., Lin, X.M., 2012. Improvement of retinal function in early age-related macular degeneration after lutein and zeaxanthin supplementation: a randomized, double-masked, placebo-controlled trial. Am. J. Ophthalmol. 154, 625–634 e1.
Martinez, T., Gonzalez, M.V., Roehl, I., Wright, N., Paneda, C., Jimenez, A.I., 2014. In vitro and in vivo efficacy of SYL040012, a novel siRNA compound for treatment of glaucoma. Mol. Ther. 22, 81–91.
Molday, R.S., Kellner, U., Weber, B.H., 2012. X-linked juvenile retinoschisis: clinical diagnosis, genetic analysis, and molecular mechanisms. Prog. Retin Eye Res. 31, 195–212.
Moreno-Montanes, J., Sadaba, B., Ruz, V., Gomez-Guiu, A., Zarranz, J., Gonzalez, M.V., Paneda, C., Jimenez, A.I., 2014. Phase I clinical trial of SYL040012, a small interfering RNA targeting beta-adrenergic receptor 2, for lowering intraocular pressure. Mol. Ther. 22, 226–232.
Morita, K., Sasaki, H., Furuse, M., Tsukita, S., 1999. Endothelial claudin: claudin-5/TMVCF constitutes tight junction strands in endothelial cells. J. Cell Biol. 147, 185–194.
Myers, J.S., Sall, K.N., DuBiner, H., Slomowitz, N., McVicar, W., Rich, C.C., Baumgartner, R.A., 2016. A dose-escalation study to evaluate the safety, tolerability, pharmacokinetics, and efficacy of 2 and 4 Weeks of twice-daily ocular trabodenoson in adults with ocular hypertension or primary open-angle glaucoma. J. Ocul. Pharmacol. Ther. 32, 555–562.
Noecker, R.S., Dirks, M.S., Choplin, N.T., Bernstein, P., Batoosingh, A.L., Whitcup, S.M., 2003. Bimatoprost/Latanoprost Study G. A six-month randomized clinical trial comparing the intraocular pressure-lowering efficacy of bimatoprost and latanoprost in patients with ocular hypertension or glaucoma. Am. J. Ophthalmol. 135, 55–63.
O'Callaghan, J., Crosbie, D.E., Cassidy, P.S., Sherwood, J.M., Flugel-Koch, C., Lutjen-Drecoll, E., Humphries, M.M., Reina-Torres, E., Wallace, D., Kiang, A.S., Campbell, M., Stamer, W.D., Overby, D.R., O'Brien, C., Tam, L.C.S., Humphries, P., 2017. Therapeutic potential of AAV-mediated MMP-3 secretion from corneal endothelium in treating glaucoma. Hum. Mol. Genet. 26, 1230–1246.
Ott, M., Gogvadze, V., Orrenius, S., Zhivotovsky, B., 2007. Mitochondria, oxidative stress and cell death. Apoptosis 12, 913–922.
Perche, O., Doly, M., Ranchon-Cole, I., 2007. Caspase-dependent apoptosis in light-induced retinal degeneration. Invest Ophthalmol. Vis. Sci. 48, 2753–2759.
Quigley, H.A., Broman, A.T., 2006. The number of people with glaucoma worldwide in 2010 and 2020. Br. J. Ophthalmol. 90, 262–267.
Raviola, G., Raviola, E., 1981. Paracellular route of aqueous outflow in the trabecular meshwork and canal of Schlemm. A freeze-fracture study of the endothelial junctions in the sclerocorneal angel of the macaque monkey eye. Invest Ophthalmol. Vis. Sci. 21, 52–72.
Ren, R., Li, G., Le, T.D., Kopczynski, C., Stamer, W.D., Gong, H., 2016. Netarsudil increases outflow facility in human eyes through multiple mechanisms. Invest Ophthalmol. Vis. Sci. 57, 6197–6209.
Scherer, W.J., 2002. A retrospective review of non-responders to latanoprost. J. Ocul. Pharmacol. Ther. 18, 287–291.
Schneeberger, E.E., Karnovsky, M.J., 1976. Substructure of intercellular junctions in freeze-fractured alveolar-capillary membranes of mouse lung. Circ. Res. 38, 404–411.
Simon, D.B., Lu, Y., Choate, K.A., Velazquez, H., Al-Sabban, E., Praga, M., Casari, G., Bettinelli, A., Colussi, G., Rodriguez-Soriano, J., McCredie, D., Milford, D., Sanjad, S., Lifton, R.P., 1999. Paracellin-1, a renal tight junction protein required for paracellular Mg2+ resorption. Science 285, 103–106.
Sit, A.J., Coloma, F.M., Ethier, C.R., Johnson, M., 1997. Factors affecting the pores of the inner wall endothelium of Schlemm's canal. Invest Ophthalmol. Vis. Sci. 38, 1517–1525.
Spiga, M.G., Borras, T., 2010. Development of a gene therapy virus with a glucocorticoid-inducible MMP1 for the treatment of steroid glaucoma. Invest Ophthalmol. Vis. Sci. 51, 3029–3041.
Stamer, W.D., Clark, A.F., 2017. The many faces of the trabecular meshwork cell. Exp. Eye Res. 158, 112–123.
Taddei, A., Giampietro, C., Conti, A., Orsenigo, F., Breviario, F., Pirazzoli, V., Potente, M., Daly, C., Dimmeler, S., Dejana, E., 2008. Endothelial adherens junctions control tight junctions by VE-cadherin-mediated upregulation of claudin-5. Nat. Cell Biol. 10, 923–934.
Tam, L.C., Reina-Torres, E., Sherwood, J.M., Cassidy, P.S., Crosbie, D.E., Lutjen-Drecoll, E., Flugel-Koch, C., Perkumas, K., Humphries, M.M., Kiang, A.S., O'Callaghan, J., Callanan, J.J., Read, A.T., Ethier, C.R., O'Brien, C., Lawrence, M., Campbell, M., Stamer, W.D., Overby, D.R., Humphries, P., 2017. Enhancement of outflow facility in the murine eye by targeting selected tight-junctions of Schlemm's canal endothelia. Sci. Rep. 7, 40717.
Tham, Y.C., Li, X., Wong, T.Y., Quigley, H.A., Aung, T., Cheng, C.Y., 2014. Global prevalence of glaucoma and projections of glaucoma burden through 2040: a systematic review and meta-analysis. Ophthalmology 121, 2081–2090.
Turksen, K., Troy, T.C., 2001. Claudin-6: a novel tight junction molecule is developmentally regulated in mouse embryonic epithelium. Dev. Dyn. 222, 292–300.
Uggenti, C., Briant, K., Streit, A.K., Thomson, S., Koay, Y.H., Baines, R.A., Swanton, E., Manson, F.D., 2016. Restoration of mutant bestrophin-1 expression, localisation and function in a polarised epithelial cell model. Dis. Model Mech. 9, 1317–1328.
Van Itallie, C.M., Anderson, J.M., 2004. The molecular physiology of tight junction pores. Physiol. (Bethesda) 19, 331–338.
Van Itallie, C.M., Colegio, O.R., Anderson, J.M., 2004. The cytoplasmic tails of claudins can influence tight junction barrier properties through effects on protein stability. J. Membr. Biol. 199, 29–38. Epub 2004/09/16.
Van Itallie, C.M., Gambling, T.M., Carson, J.L., Anderson, J.M., 2005. Palmitoylation of claudins is required for efficient tight-junction localization. J. Cell Sci. 118, 1427–1436. Epub 2005/03/17.
Vegge, T., 1967. The fine structure of the trabeculum cribriforme and the inner wall of Schlemm's canal in the normal human eye. Z Zellforsch Mikrosk Anat. 77, 267–281.
Vijayasarathy, C., Ziccardi, L., Sieving, P.A., 2012. Biology of retinoschisin. Adv. Exp. Med. Biol. 723, 513–518.
Weismann, D., Hartvigsen, K., Lauer, N., Bennett, K.L., Scholl, H.P., Charbel Issa, P., Cano, M., Brandstatter, H., Tsimikas, S., Skerka, C., Superti-Furga, G., Handa, J.T., Zipfel, P.F., Witztum, J.L., Binder, C.J., 2011. Complement factor H binds malondialdehyde epitopes and protects from oxidative stress. Nature 478, 76–81.
Whitehead, A.J., Mares, J.A., Danis, R.P., 2006. Macular pigment: a review of current knowledge. Arch. Ophthalmol. 124, 1038–1045.
Xun, Z., Rivera-Sanchez, S., Ayala-Pena, S., Lim, J., Budworth, H., Skoda, E.M., Robbins, P.D., Niedernhofer, L.J., Wipf, P., McMurray, C.T., 2012. Targeting of XJB-5-131 to mitochondria suppresses oxidative DNA damage and motor decline in a mouse model of Huntington's disease. Cell Rep. 2, 1137–1142.
Yamauchi, K., Rai, T., Kobayashi, K., Sohara, E., Suzuki, T., Itoh, T., Suda, S., Hayama, A., Sasaki, S., Uchida, S., 2004. Disease-causing mutant WNK4 increases paracellular chloride permeability and phosphorylates claudins. Proc. Natl. Acad. Sci. U. S. A. 101, 4690–4694.
Ye, W., Gong, H., Sit, A., Johnson, M., Freddo, T.F., 1997. Interendothelial junctions in normal human Schlemm's canal respond to changes in pressure. Invest Ophthalmol. Vis. Sci. 38, 2460–2468.
Yu, J., Ni, Y., Keane, P.A., Jiang, C., Wang, W., Xu, G., 2010. Foveomacular schisis in juvenile X-linked retinoschisis: an optical coherence tomography study. Am. J. Ophthalmol. 149, 973–978 e2.
Zeng, Y., Takada, Y., Kjellstrom, S., Hiriyanna, K., Tanikawa, A., Wawrousek, E., Smaoui, N., Caruso, R., Bush, R.A., Sieving, P.A., 2004. RS-1 gene delivery to an adult Rs1h knockout mouse model restores ERG b-wave with reversal of the electronegative waveform of X-linked retinoschisis. Invest Ophthalmol. Vis. Sci. 45, 3279–3285.
Zhang, L., Reyes, R., Lee, W., Chen, C.L., Chan, L., Sujirakul, T., Chang, S., Tsang, S.H., 2015. Rapid resolution of retinoschisis with acetazolamide. Doc. Ophthalmol. 131, 63–70.
Zode, G.S., Kuehn, M.H., Nishimura, D.Y., Searby, C.C., Mohan, K., Grozdanic, S.D., Bugge, K., Anderson, M.G., Clark, A.F., Stone, E.M., Sheffield, V.C., 2011. Reduction of ER stress via a chemical chaperone prevents disease phenotypes in a mouse model of primary open angle glaucoma. J. Clin. Invest 121, 3542–3553.

Please cite this article in press as: Campbell, M., et al., Manipulating ocular endothelial tight junctions: Applications in treatment of retinal disease pathology and ocular hypertension, Progress in Retinal and Eye Research (2017), https://doi.org/10.1016/j.preteyeres.2017.09.003